

Understanding how ABI3 contributes to the aetiology of Alzheimer's Disease

Elena Simonazzi

Thesis presentation for the degree of Doctor of Philosophy
(Medicine)

2022

Acknowledgments

“Per me si va ne la città dolente, / per me si va ne l'eterno dolore, / per me si va tra la perduta gente. / [...] Lasciate ogne speranza, voi ch'entrate.”

This is what Dante found inscribed above the gates of Hell¹ (or, most likely, as a footnote on his studentship acceptance form): a more befitting description for trying to complete a PhD during a pandemic will never be found.

And exactly like in Dante's experience, this journey would have not been possible without a Virgil. So first and foremost, I want to thank Professor Phil Taylor, for guiding me with his incredible support, suggestions and constructive criticisms, and for the patience and understanding shown during the most challenging times. And – most importantly – for encouraging me to grow, personally and professionally.

I also want to thank my co-supervisor, Professor Paul Morgan, for the helpful insight he provided during the course of this work, and Professor Valentina Escott-Price, without whom my understanding of statistics would be considerably poorer. My gratitude also goes to Professor Frank Sengpiel, who made my two-photon experiments possible, and Professor Mark Good, for his guidance on the behavioural assays. Finally, I want to thank Dr Adam Ranson, who helped with the two-photon data processing, and Fangli Chen, for her astounding surgical abilities and her crucial help with the two-photon imaging, as well as Dr Ariadni Kouzeli and Joshua Stevenson-Hoare, for their crucial support during image processing and analysis.

I am also hugely grateful for having been blessed with the most incredible group of travelling companions. So my first “thank you” goes to Ryan, Magda, Emily, Diogo, Valentina and every other past or present member of the Myeloid Cell Biology Group and Cardiff DRI that crossed my path during the past four years, for helping and encouraging me, or simply being there to share my joys and frustrations. To Marieta and Megan, who ended up as unwilling witnesses of my monologues more

¹ Dante Alighieri, Divine Comedy, Inferno, Canto III

times than I can remember (sorry!), for their patience. To Dina and Sarah, for their amazing kindness. And finally, to Nikoleta, for making me feel less lonely and being always ready to share a laugh with me at the most improbable hours in a deserted lab. While I shouldn't have preferences, three people merit a special mention. Mark, who somehow managed to simultaneously be the most irritatingly competitive (but incredibly helpful) colleague and the most wonderful friend, without whom this adventure would have been unbearably duller. Ruth, whose efforts to give me diabetes can only be rivalled by the amazing support she showed me during the years, at work and outside. And finally Elisa, who – since the very beginning – has been a tiny, living piece of home away from home and was there for me when I need it the most. Thank you all, for showing me that even if this job can sometimes feel like a soul-crushing, life-sucking black hole, it is absolutely worth it when surrounded by the right people.

And since I was lucky enough to find just as many amazing people outside my workplace, my gratitude goes to everyone that stuck around despite years of being forced apart, endless work-related tirades, or a combination of both. So a massive “Thank you!” to my extraordinary parents (and annoying brothers), for supporting me however they could, no matter the distance; to Will's family, for making me feel like I belonged, and especially to those two gems of his grandparents, who never failed to ask if my mice were behaving; to Valentina, Eva, Irina and Cecilia, for always believing in me; to all my friends scattered around the world, for not hating me despite monstrous lags in our conversations; and to the 33HDS gang, for forcing me to put work apart and enjoy life every now and then.

And last but not least, the biggest and most heartfelt thank you goes to Will, for being my pillar throughout this odyssey and being a constant reminder that even on the longest, most tiring, most discouraging days, everything is going to be just fine.

Summary

Neuroinflammation in Alzheimer's Disease (AD) is not a simple by-product of β -amyloidosis and neurofibrillary tangles, but it rather plays a crucial role in AD pathogenesis. However, we are still far from understanding how exactly microglia influence disease progression. A rare missense variant, S209F, associated to an increased risk of AD has been identified in Abi3 (Abl-interactor-3), a poorly investigated member of the Abi family, which is involved in Rac-dependent regulation of the actin cytoskeleton. Within the brain, Abi3 is considered a core human microglial signature gene. Given that a flexible actin cytoskeleton is key to many microglia – and more broadly, macrophages – functions, the precise role of Abi3 in these cells in health and pathology, such as AD, needs to be clarified.

In order to investigate Abi3 biological functions, a combination of cellular assays, histology, live imaging and behavioural paradigms was employed. In an actin-mediated spreading assay, Abi3 knock-out (KO) BMDM-like cells – derived from conditionally-immortalized macrophage precursors – showed increased cellular surface and solidity. These findings have been validated by histological analyses of brains of healthy Abi3-WT and -KO mice as well as in the APPNL-G-F AD model. Microglial cells lacking Abi3 present reduced ramifications accompanied by an increase in cell density and CD68 expression. Young Abi3-KO mice also show impaired surveyance activity *in vivo*. In addition, Abi3 ablation leads to an elevated astrocytic density from a young age, as well as a reduction in Amyloid β deposition in the hippocampus, but not in the prefrontal cortex, of 16-week-old mice. Behavioural assays highlighted a potential impact of Abi3 ablation on the emotional domain but not on cognitive ability. These results support the hypothesis of a critical role of Abi3 in microglial homeostasis, and suggest that its rare variant may promote AD development by altering microglia homeostatic functions.

Contributions

Dr D. Fathalla generated lentiviral vectors for human ABI3, which were then used by Dr R. Jones to generate hABI3 overexpressing cell lines (Chapter 2).

Dr A. Kouzeli and Dr R. Jones helped with image acquisition and analysis for some of the samples shown in Chapter 4 and 5.

Fangli Chen performed all the cranial window surgeries required for the *in vivo* imaging experiments and helped to operate the microscope during the imaging sessions.

Dr A. Ranson developed the MATLAB code (shown in Appendix 2) required to convert raw images acquired with the two-photon microscope into TIFF files for downstream analysis (Chapter 4).

Joshua Stevenson-Hoare wrote a Python code used to extract parameters of interest for the in-depth morphological analysis (Chapter 4) out of individual Excel files in order to obtain a single spreadsheet comprising all the samples for the downstream analysis. He also helped with the R code development in order to perform the linear mixed model analysis on the aforementioned dataset.

Contents

1. Chapter 1 – Introduction.....	18
1.1. Microglia.....	2
1.1.1. Microglia ontogenesis.....	2
1.1.2. Regulation of microglial turnover in the adult brain	6
1.1.3. Role of microglia in physiological and pathological conditions	8
1.1.3.1. Immune surveillance and phagocytosis in the adult brain.....	8
1.1.3.2. Microglia and CNS development: neurogenesis, axonal growth and neurotransmission.....	10
1.1.4. Maintenance of microglial homeostasis	12
1.1.4.1. Microglial homeostasis.....	12
1.1.4.2. Microglia activation.....	13
1.1.4.3. Interplay among glial populations.....	14
1.1.5. Microglia heterogeneity and sexual dimorphism	15
1.1.5.1. Spatial heterogeneity	15
1.1.5.2. Microglia and aging	17
1.1.5.3. Sexual dimorphism	18
1.2. Alzheimer’s Disease.....	20
1.2.1. Aetiopathogenesis of AD.....	21
1.2.1.1. Amyloid- β plaques.....	21
1.2.1.2. Neurofibrillary Tau tangles.....	22
1.2.2. Genetic risk factors	23
1.2.3. Neuroinflammation and role of microglia in AD.....	26
1.2.4. Transgenic mouse models of AD	29
1.3. Abi3.....	33
1.3.1. Role and regulation of the WRC.....	33
1.3.2. Abi3 structure and functions.....	35
1.3.3. Proposed role in AD	39
1.4. Project aims and hypothesis.....	43
2. Chapter 2 – Materials and methods.....	46

2.1.	Buffers and solutions	47
2.2.	Animals.....	48
2.2.1.	Genotyping	50
2.2.1.1.	Abi3-KO mice.....	51
2.2.1.2.	App-KI mice	52
2.2.1.3.	Cx3cr1-GFP mice	53
2.3.	Cell culture	54
2.3.1.	NIH 3T3 cell lines	54
2.3.2.	Macrophage Precursor (MØP) cell lines	54
2.3.3.	Bone-Marrow Derived MØs (BMDMs)	55
2.3.4.	Incubation and media preparation	55
2.3.5.	Cell counting.....	56
2.3.6.	Cryopreservation and thawing	56
2.3.7.	Human ABI3 overexpression	57
2.4.	Functional cell assays.....	58
2.4.1.	Spreading assay.....	58
2.4.2.	Phagocytosis assay.....	61
2.4.3.	ROS detection via DHR 123 staining	65
2.4.4.	Griess Nitrites quantification assay	66
2.5.	Quantitative PCR (qPCR).....	69
2.5.1.	Ribonucleic Acid (RNA) Extraction.....	69
2.5.2.	Reverse transcription.....	69
2.5.3.	qPCR reaction	70
2.6.	Histological analyses	71
2.6.1.	Brain extraction and preparation for immunostainings	71
2.6.2.	Immunofluorescent staining of free floating sections.....	72
2.6.3.	Thioflavin-S staining	76
2.6.4.	Image acquisition and analysis	76
2.6.4.1.	Image acquisition and z-stack processing.....	76

2.6.4.2.	Iba1 and GFAP analysis.....	77
2.6.4.3.	Iba1/CD68 co-localisation analysis.....	79
2.6.4.4.	Morphometric analysis of single cells	80
2.6.4.5.	Whole-section A β -plaques evaluation	82
2.6.4.6.	Individual A β -plaques microgliosis assessment	83
2.7.	Two-photon microscopy	85
2.8.	Behavioural assays	88
2.8.1.	Elevated Plus Maze (EPM) paradigm.....	91
2.8.2.	Open Field (OF) paradigm	92
2.8.3.	Novel Object Recognition (NOR) paradigm.....	93
2.8.4.	Sucrose Preference (SP) paradigm.....	96
2.8.5.	Nest Scoring	97
2.9.	Statistics and analysis softwares.....	99
2.9.1.	Cell assays.....	99
2.9.2.	qPCR data	99
2.9.3.	Flow Cytometry data	99
2.9.4.	Immunofluorescence and two-photon data.....	99
2.9.5.	Behavioural paradigms data.....	100
2.9.6.	Graphs and statistics.....	100
3.	Chapter 3: Role of Abi3 on macrophages and microglia physiological activity	101
3.1.	Introduction	102
3.2.	Results.....	104
3.2.1.	Overexpression of Abi3 impacts actin-mediated cell spreading in NIH 3T3 cell lines	104
3.2.2.	Alterations in Abi3 levels cause defective spreading ability in Macrophages	114
3.2.3.	Abi3 ablation does not seem to impact the phagocytic activity of BMDMs	132
3.2.4.	The lack of Abi3 may cause alteration in ROS and NO production in BMDMs	142

3.3.	Discussion	148
3.4.	Conclusion and future work	156
4.	Chapter 4: How does Abi3 influence microglia physiological activity?	159
4.1.	Introduction.....	160
4.2.	Results	162
4.2.1.	Basic characterisation of microglia in young Abi3-KO mice brain.....	162
4.2.2.	In-depth morphological characterisation of individual Abi3-KO microglia	164
4.2.3.	Evaluation of microglia dynamics <i>in vivo</i> through two-photon imaging on Abi3-KO mice	170
4.2.4.	Histological evaluation of phagocytosis and astrocytosis in young Abi3-KO mice brain.....	173
4.3.	Discussion	177
4.4.	Conclusion and future work	181
5.	Chapter 5: What is the effect of Abi3 on the development of Alzheimer's disease-like pathology?	185
5.1.	Introduction.....	186
5.2.	Results	188
5.2.1.	Basic characterisation of adult Abi3-KO mice crossed with the App ^{NL-G-F} AD model.....	188
5.2.2.	Amyloid burden and peri-plaque microgliosis assessment on adult Abi3-KO App-KI mice.....	196
5.2.3.	Evaluation of Abi3 impact on adult mice behaviour	202
5.3.	Discussion	219
5.4.	Conclusion and future work	228
6.	Chapter 6: General discussion.....	231
6.1.	Introduction.....	232
6.2.	Main findings	234
6.2.1.	<i>In vitro</i> assessment of Abi3 impact on macrophage functionality	234

6.2.2.	<i>In vivo</i> evaluation of Abi3 role in the healthy brain.....	237
6.2.2.1.	Loss of Abi3 causes alterations in microglia number and distribution and severely impact microglial morphology and functionality.....	237
6.2.2.2.	Abi3 knock-out leads to increased astrocytic burden in young healthy mice	239
6.2.3.	Investigation of Abi3 impact on AD.....	240
6.2.3.1.	Loss of Abi3 increases gliosis in adult mice.....	240
6.2.3.2.	Abi3 ablation differently impacts amyloid burden in PFC and hippocampus without affecting microglia recruitment around plaques.....	242
6.2.3.3.	Genetic ablation of Abi3 appear to cause emotional, but not cognitive, changes in adult mice.....	244
6.3.	Conclusions	248
6.4.	Future work.....	249
7.	Bibliography	252
8.	Appendices	300
	Appendix 1.....	300
	Appendix 2.....	300
	Appendix 3.....	309
	Appendix 4.....	309

List of figures

Figure 1.1	Schematic representation of the developmental origin of microglia and other tissue-resident macrophages.....	5
Figure 1.2	Schematic representation of APP processing.....	22
Figure 1.3	Manhattan plot of the results of a metanalysis for genome-wide association in Alzheimer's disease.....	25
Figure 1.4	Visual summary of the main features and disadvantages of some of the available AD mouse models.....	32
Figure 1.5	Schematic representation of the Wave Regulatory Complex (WRC).....	35
Figure 1.6	Graphical representation of mouse Abi3 exon and protein structure.....	36

Figure 1.7 Abi3-KO model.	37
Figure 1.8 Abi3 and Gngt2 expression in mouse whole cortex and hippocampus, compared to Aif1 (Iba1) and Gfap as shown by scRNAseq.....	38
Figure 1.9 Time course of Abi3 and Spi1 expression in mouse microglia during development.	39
Figure 2.1 Touchdown PCR program used for Abi3-KO genotyping, based on standard Jackson Laboratory protocol.	52
Figure 2.2 PCR program used for App-KI genotyping, based on the protocol provided by the RIKEN Center.....	53
Figure 2.3 Touchdown PCR program used for Cx3cr1-GFP genotyping, based on standard Jackson Laboratory protocol.	53
Figure 2.4 Schematic representation of the spreading assay analysis performed using Fiji software.	60
Figure 2.5 Representative images of single colour controls for the phagocytosis assay.	63
Figure 2.6 Schematic representation of the automated workflow of the Fiji analysis performed on the phagocytosis assay images.	64
Figure 2.7 Visual representation of the nuclei count analysis used for the normalisation of nitrite measurements.	68
Figure 2.8 Schematic representation of the High-Capacity cDNA Reverse Transcription Kit PCR protocol.....	69
Figure 2.9 Schematic representation of the temperature and cycling times used to generate the qPCR data.	70
Figure 2.10 Selected regions of the Prefrontal Cortex (PFC) and the hippocampus used for the Iba1 staining.....	72
Figure 2.11 Representative images of the isotype and secondary only compared to the real staining for all the antibodies used for histological analyses in this thesis. .	75
Figure 2.12 Schematic representation of Iba1 analysis performed using Fiji software.	78
Figure 2.13 Schematic representation of 6E10 analysis performed using Fiji software.....	83

Figure 2.14 Schematic representation of peri-plaques microgliosis analysis performed using Imaris software.	84
Figure 2.15 Representative images of EGFP expression in microglia and two-photon microscopy set up.	86
Figure 2.16 Schematic representation of the analysis pipeline performed on 2-photon videos through Fiji software.	88
Figure 2.17 Visual summary of the behavioural schedule.	90
Figure 2.18 Elevated Plus Maze (EPM) layout.	92
Figure 2.19 Open Field (OF) arena layout.	93
Figure 2.20 Visual representation of the additional habituation phase mice underwent before performing NOR task.	94
Figure 2.21 Representative images of the NOR assay set-up.	95
Figure 2.22 Sucrose Preference (SP) test set-up.	97
Figure 2.23 Representative images of the nest scoring set-up and scoring system.	98
Figure 3.1, part I. Representative images of NIH 3T3 cells during the first of three repetitions of the actin-mediated spreading assay.	106
Figure 3.2 Detection of GFP in NIH 3T3 cells transduced with a lentiviral construct containing either of the human ABI3 variants.	114
Figure 3.3. Confirmation of Abi3 knock-out at genomic and transcriptional level in Abi3-KO mice and cell lines.	117
Figure 3.4, part I. Representative images from the single spreading assay experiment performed on Abi3-overexpressing M-CSF differentiated MØs.	119
Figure 3.5 Detection of GFP in MØs derived from MØPs cells overexpressing either of the human ABI3 variants.	122
Figure 3.6, part I. Representative images from the second spreading assay experiments performed on M-CSF differentiated MØs derived from the original Abi3-WT and KO precursors cell lines.	124
Figure 3.7, part I. Representative images from the single spreading assay experiment performed at longer time points on M-CSF differentiated MØs derived from Abi3-WT or KO precursors cell lines.	130

Figure 3.8 QPCR analysis of App-KI and App-KI Abi3-KO BMDMs to confirm Abi3 knock-out.	134
Figure 3.9, part I. Representative images from selected time points of a phagocytosis assay performed on BMDMs.	136
Figure 3.10 Quantification of pHrodo™ Red Zymosan area and mean intensity within App-KI and App-KI Abi3-KO BMDMs during a live-imaging phagocytosis assay...	139
Figure 3.11. Representative images of App-KI cells with and without CytoD treatment.	141
Figure 3.12 Assessing ROS production in App-KI and App-KI Abi3-KO BMDMs by flow cytometric analysis of DHR 123 staining.....	143
Figure 3.13 Alternative gating on stimulated BMDMs to focus on the DHR ^{high} population.	144
Figure 3.14 Evaluation of nitrite quantification with Griess reagent after LPS stimulation.	147
Figure 3.15. Schematic representation of the proposed model for Abi3 action on actin cytoskeleton.	150
Figure 3.16 Abi3 expression in primary murine microglia compared to pMØs and BMDMs as shown by Micro-array.	156
Figure 4.1 Representative images and quantification of the Iba1 staining for microglia in Abi3-WT and -KO mice brain sections.	163
Figure 4.2 Representative images of single microglia obtained from Abi3-WT and -KO mice brain sections, stained with Iba1 antibody and traced using Imaris software.....	165
Figure 4.3 Quantification of ramification length, mean diameter, area and volume of Abi3-WT and -KO microglia.	166
Figure 4.4 Evaluation of complexity of the ramification apparatus and overall cell size.....	168
Figure 4.5 Sholl analysis of Abi3-WT and -KO microglial cells.	169
Figure 4.6 Quantification of microglia surveillance activity through two-photon imaging.....	172
Figure 4.7 Representative images and quantification of the Iba1-CD68 co-staining in Abi3-WT and -KO mice.....	174

Figure 4.8 Representative images of GFAP ⁺ astrocytes in the hippocampus of Abi3-WT and -KO mice.....	176
Figure 5.1 Representative images of Thioflavin-S (Th-S) staining for Amyloid β (A β) plaques in Abi3-WT and App-KI mice brain sections.	190
Figure 5.2, part I. Representative images of a microglial immunostaining in 16-week-old Abi3-WT, Abi3-KO, App-KI and App-KI Abi3-KO mice.....	192
Figure 5.3 Representative images of GFAP ⁺ astrocytes, and relative quantification, in the hippocampus of 16-week-old mice.....	195
Figure 5.4 Representative images of A β plaques stained with a 6E10 antibody and relative quantification in the PFC of 16-week-old App-KI and App-KI Abi3-KO mice.	197
Figure 5.5 Representative images and relative quantification of the 6E10 staining performed on hippocampal sections of adult Abi3-deficient mice and App-KI controls.	200
Figure 5.6, part I. Representative images of individual plaques analysis.	201
Figure 5.7 Representative images of the heatmaps automatically generated by EthoVision for every individual mouse.	203
Figure 5.8 Graphical representation of selected parameters to assess anxiety-like behaviours during the EPM task.....	205
Figure 5.9 Quantification of locomotor activity in the EPM arena.....	207
Figure 5.10 Representative heatmaps from the OF task.....	208
Figure 5.11 Quantification of anxiety-like behaviour in the OF arena.....	210
Figure 5.12 Graphical representation of locomotor activity quantified in the OF arena.....	211
Figure 5.13 Graphical representation of the NOR task results.....	214
Figure 5.14 Graphical representation of the percentage of sucrose preference after 24 hours.....	215
Figure 5.15 Schematic description and representative images of nest scoring assessment.....	217
Figure 5.16 Quantification of nest building score for male and female mice of all the strains of interest in this thesis.....	218

Figure 5.17. Summary table of the behavioural tasks performed on 40-week-old mice.....	224
--	-----

Figure 6.1 Graphical representation of Gngt2 expression in human and mouse. ...	233
---	-----

List of Tables

Table 2.1 List of Buffers and Solutions used in the thesis.	48
Table 2.2 Official and abbreviated names of the transgenic mice strains used in this thesis.	50
Table 2.3 PCR primers used for genotyping of transgenic mice strains used in this thesis and corresponding expected product size in base-pair (bp).	51
Table 2.4 Summary table of standards preparation for nitrite quantification during the Griess assay.	66
Table 2.5 List of the qPCR primers used to quantify Abi3 expression in BMDMs.	70
Table 2.6 List of all antibodies used for immunostainings and their specifications.	74
Table 2.7 Definition of selected parameters obtained from Imaris 3D tracing of microglia.	81
Table 2.8 Summary table of the animals tested for the scope of this thesis.	89
Table 3.1part I. Detailed report of descriptive statistics and ANOVA results for the shortest time points of all three repetitions of the NIH 3T3 spreading assay.	110
Table 3.2 Detailed report of descriptive statistics and ANOVA results for the spreading assay performed on Abi3-overexpressing MØs.	121
Table 3.3, part I. Detailed report of descriptive statistics and Mann-Whitney test results for the shortest time points of all repetitions of the spreading assay performed on Abi3-WT and -KO MØs.	127
Table 3.4 Detailed report of descriptive statistics and Mann-Whitney test results for each time point of the long-term spreading assay performed on Abi3-WT and -KO MØs.	132
Table 4.1 Summary table of the t- and p-values calculated for the genotype and sex effects for segment-related data generated by Imaris analysis.	166
Table 4.2 Summary table of the t- and p-values calculated for the genotype and sex effects for the whole-cell parameters analysed.	168

Table 4.3 Summary table of the t- and p-values calculated for the Sholl intersections and the Sholl Area Under the Curve values..... 170

Chapter 1 – Introduction

1.1. Microglia

In the course of the past century, our appreciation of the crucial role played by microglia in health and disease has expanded exponentially. We now recognise that these brain resident macrophages – who represent between 10 % of the glial population in the brain parenchyma (1) – are essential for the maintenance of the central nervous system (CNS) homeostasis as well as for the immune defence of the brain.

For the longest time, however, microglia were considered secondary players, only passively involved in brain physiology. When the non-neuronal compartment was firstly identified, at the end of the 1800's, the Late Greek term for “glue” (“glía”) was chosen to describe what, at the time, was perceived simply as a “simil-connective” tissue of the CNS and was later revealed to include astrocytes and oligodendrocytes (also known as “macroglia”) (2). W. Ford Robertson later introduced the concept of “mesoglia”, while Santiago Ramon y Cajal reported the existence of a “third element”: both men, however, were in fact primarily describing what we now know as oligodendrocytes. It was only in the 1939 that the term “microglial cell” was coined by Pío del Río Horteiga (3), who provided the first description of microglia as an individual population (4).

In the following decades, a critical role for microglial cells in both health and disease slowly started to delineate, despite some long-lived dogmas that were only recently overcome and contributed to enduring misconceptions regarding the actual function of these cells in the CNS. The crucial aspects of microglial biology will be addressed in the following sections, as well as any major gap in our current understanding of these cells.

1.1.1. Microglia ontogenesis

It is only recently that a consensus has been reached over the developmental origin of microglia.

Since their discovery, and almost till the end of the twentieth century, microglia were mostly believed to derive from the neuroectoderm together with neuronal and macroglial cells (4). This theory was supported by multiple lines of evidence, including a study by Hao and colleagues, that demonstrated they were able to obtain, *in vitro*, macrophage-like cells from either embryonic neuroepithelium or

astrocytes after depriving them of nutrients by not replacing the media for prolonged periods of time (5). Parallel work from De Groot *et al.* demonstrated that cells from a donor bone marrow were not able to majorly contribute to microglial population in new-born mice (6), coherently to what had been observed by Matsumoto and Fijiwara five years before employing adult bone marrow chimeras (7), seemingly supporting the interpretation that microglia did not derive from myeloid progenitors but rather from local precursors of neuroectodermal origin.

At the end of the 1980s, however, the body of evidence in support to Rio-Hortega's theory of a mesodermal origin (3) started to grow. By means of light- and electron microscopy, Murabe and Sano identified morphological similarities between white matter "amoeboid microglia" and macrophages (8) and they were able to stain microglial cells using an antisera against monocyte/macrophage antigens (9). Soon after, Perry and colleagues demonstrated that microglia expressed macrophage-specific markers such as F4/80, CD11b and Fc receptors (10), and this was confirmed in humans by Akiyama and McGeer in 1990 (11). The following identification of a crucial role in microglia of the myeloid transcription factor PU.1 (12–14) finally led the scientific community to accept the hypothesis of microglia as myeloid lineage cells.

The identification of microglial precursors did not happen till 2010, when Ginhoux and colleagues published a first, complex fate mapping study employing multiple mice models to clarify the exact stage of myeloid cells recruitment in the brain (15). Until then, the relative contribution of each of the two hematopoietic waves to microglial recruitment had still been a matter of controversy. In rodents, a primitive wave takes place in the yolk sac (YS) at embryonic day 7-7.5 (E7-7.5) and is responsible for the establishment of erythrocytes and macrophages (16). The following hematopoietic wave (the so called "definitive" one) only starts at E8.5, and generates firstly the erythromyeloid and lympho-myeloid progenitors and finally the hematopoietic progenitors, which migrate from the aorta, gonads, and mesonephros (AGM) region to the fetal liver at E10.5 (17). The fetal liver then becomes the main hematopoietic organ and originates all the hematopoietic lineages until birth, when it is replaced as source of hematopoiesis by the bone marrow (17). Ginhoux and colleagues were finally able to put an end to the debate employing a conditional reporter strain, in which Enhanced Yellow Fluorescent Protein (eYFP) expression could be controlled in YS- or AGM-derived progenitors by precisely timed injection of Tamoxifen at different developmental stages. The authors observed a higher relative number of eYFP-tagged microglia compared to blood monocytes after performing

injections at E7.5, while tagged microglia were almost undetectable following E8.5 injections, thus proving that definitive hematopoiesis does not contribute to microglial population (15). Following this study, Kierdorf and colleagues further characterised microglia precursors and reported that, as early as at E8, CD45⁻ c-kit⁺ erythromyeloid progenitors emerge in the YS and eventually develop into CD45⁺ c-kit⁻ Cx3cr1⁺ cells (18). Between E8.5 and E10, these primitive macrophages enter the circulatory system, through which they reach the brain (15,19), followed by a second wave of YS-derived Hoxb8⁺ cells (20), before the closure of the blood-brain barrier (BBB) at E13.5-14.5 (21,22) (Figure 1.1). Interestingly, in 2016 Matcovitch-Natan et al. defined three distinct phases in microglia development, linked to chromatin remodelling (23), later shown to be at least partially connected to Hdac1 and Hdac2 activity (24). These consecutive stages appeared characterised by expression of genes associated with cell cycle and proliferation in the earliest stage, followed by genes related to neurogenesis and cytokines secretion and finally by canonical mature microglia genes involved in microglia homeostasis (23). Overall, the combined work of Ginhoux, Kierdorf and Matcovitch-Natan identified PU.1, colony stimulating factor 1 receptor (CSF-1R) and interferon regulator factor 8 (IRF8) as crucial regulators of early microglial development (15,18), while in later stages microglial maturation appeared to be dependent on genes such as Sal1, transforming growth factor β (TGF- β) and Mafk (23).

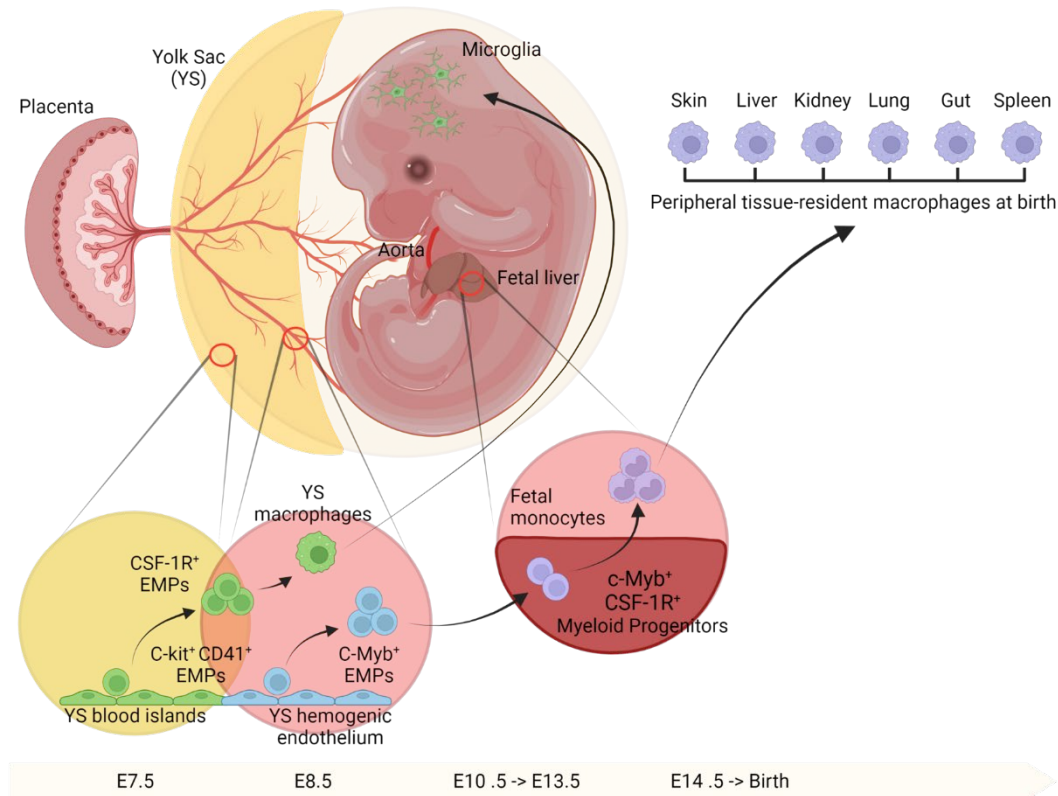


Figure 1.1 Schematic representation of the developmental origin of microglia and other tissue-resident macrophages.

Erythro-myeloid progenitors (EMPs) are generated in the yolk sac (YS) during primitive haematopoiesis, starting at E7. These cells are CD41⁺ and later begin to express CSF-1R. When blood circulation is established at E8.5, additional C-Myb⁺ EMPs are generated by the YS hemogenic endothelium. EMPs then differentiate into primitive macrophages, which through the blood circulation populate all fetal tissues. Primitive macrophages deriving from the C-Myb-independent lineage reach the brain, where they will differentiate into adult microglia. The C-Myb⁺ EMPs seed the remaining tissues and generate the various tissue-resident macrophages. Image adapted from (25) and generated with BioRender.com.

An additional source of confusion was the contribution of perinatal and postnatal hematopoiesis to microglia population. Before Ginhoux and colleagues findings, the use of chimeras had provided contrasting results in this regard (6,7,26–28). Even when donor-derived microglia were identified in the brain, these constituted only a small percentage (5-15 %) of microglia and CNS insults appeared to noticeably contribute to the engraftment (28). Employing a combination of bone marrow reconstitution and parabiosis experiments, Ginhoux *et al.* were also able to prove that the recruitment of donor-cells to the CNS observed in previous works was

biased due to the irradiation protocol, and that bone marrow-derived monocytes are not likely to significantly impact microglia numbers in the steady state (15).

In the recent years, a growing interest has emerged towards border-associate macrophages (BAMs) present in perivascular space, meninges and choroid plexus. A recent study by Utz *et al.* identified two distinct macrophage population (CD206⁺ and CD206⁻, which then develop into BAMs and microglia respectively), deriving from the same erythromyeloid progenitors, already in the YS at E10.5 (29). At E12.5, BAMs and microglia already showed discrete molecular and morphological signatures. Interestingly, deletion of *Tgfb2* in BAMs did not cause any obvious alteration, while microglia lacking TGF- β R signalling displayed an immature phenotype and reduced proliferation (29). Despite the reduction in microglia number, no compensatory conversion from BAMs to microglia was observed, supporting the theory of two separate and stable developmental trajectories (29).

1.1.2. Regulation of microglial turnover in the adult brain

We now know that in the healthy brain, once YS-derived microglia progenitors have reached the brain, they proliferate and populate the CNS without the intervention of other myeloid cells (26,30) and are able to repopulate the brain in less than week following a semi-total ablation (31,32). For years, microglia were considered extremely long-lived cells, maintained with a slow turnover (33,34). A study by Askew *et al.* showed that, instead, a complete renewal of the microglia population would occur in the mouse brain in an estimate of 95 days, with 0.69 % of cells in S-phase at any given time (35) compared to the 0.05 % previously reported by Lawson *et al.* (33). This percentage was estimated to be as high as 2 % in humans (35), albeit a contrasting report from Réu *et al.* suggested that the actual rate could be as low as 0.08 % (36). Askew *et al.* also described a temporal and spatial bond between microglial proliferation and apoptosis (which they found happened at a rate of 1.23 % per day for resident microglia), with an increase of proliferation close to dying cells (35).

The use of a multicolour reporter mouse, which allows stochastic labelling of ~ 14 % of total microglia with one of four fluorescent reporter proteins (thus facilitating the visualisation of the fate of each cell and their progeny in terms of apoptosis and proliferation), led to the detection of brain region-dependant variability in the turnover rate and overall cell density, with olfactory bulb, hippocampus and

cerebellum resulting the regions with the highest turnover (37), similar to what had been noted by Askew and colleagues in the Dentate Gyrus (DG) (35). Recent work by Zhan *et al.* confirmed Tay's observations that microglia re-colonisation of the brain parenchyma through clonal expansion, as well as the parallel need for apoptosis and cell egression to maintain microglial density at homeostatic levels (37,38). This view was later challenged by Eyo *et al.* who instead suggested microglia translocation was the major factor contributing to brain landscape changes on a daily bases, rather than coupled proliferation-apoptosis, due to the marked difference between proliferation rates and landscape rearrangements they observed (39).

Thus, to date the actual rate of microglial self-renewal is still a matter of debate (34,36), as well as the exact mechanisms that regulate microglial proliferative or quiescent states. Zhan and colleagues highlighted that conditional deletion of IKK β (one of the two kinases involved in nuclear factor kappa- light- chain- enhancer of activated B cells (NF- κ B) activation (40)) caused a significant impairment in microglial density following ablation, highlighting the necessity of NF- κ B signalling in the early phases of microglia re-population of the brain (38). This finding was an important addition to the previous understanding of microglial density regulation, which had mostly focused on the role of neuronal-derived CSF-1 and IL-34 (41,42), as well as on the importance of IL-1 signalling as described by Bruttger (31). More recently it was reported that P2Y₁₂R did not appear to influence repopulation and maturation of newly born microglial cells (43), despite its role of on baseline translocation of microglia (39). Instead, Harley *et al.* outlined a possible function of microglial-derived brain-derived neurotrophic factor (BDNF) in the positive regulation of microglial density in homeostatic condition as well as following CNS insult, suggesting that this could be due to an autocrine mechanism involving NF- κ B pathway (44). Despite these advancements, further work is required to further clarify which pathways regulates microglia renewal in the adult brain.

Interestingly, the molecular signature of newly born microglia was found to resemble the one of early post-natal cells described by Matcovitch-Natan *et al.* (23), although they appeared to return to a mature homeostatic signature within 14 days of repopulation (38). Contrasting with Zhan's results, morphological evaluation performed by Mendes and colleagues highlighted a hyper-ramified morphology exhibited by new-born microglia up to a month following depletion, suggesting that YS-derived microglia and cells generated in the adult brain after repopulation may present subtle difference still to be clarified (43). The lack of a visible amoeboid

state in early phases of repopulation, as well as the ability of the new cells to quickly start to perform baseline brain surveillance characteristic of microglia cells (43), despite the changes in gene expression (38), led Mendes and Majewska to suggest that in the adult CNS microglia morphology may be dissociated from their molecular phenotype and that epigenetic mechanisms could partially account for this phenomenon (45).

1.1.3. Role of microglia in physiological and pathological conditions

As previously mentioned, microglia are the brain resident macrophages. It is now accepted that these cells play a crucial role both in the developmental brain and in the adult CNS and in the past years deregulation of microglial homeostasis has been linked to multiple diseases. The following sections will briefly explore some of the main roles of microglia in the healthy CNS (for a complete review see (2,46)). A more detailed account of microglia in AD will be provided in section 1.2.3.

1.1.3.1. Immune surveillance and phagocytosis in the adult brain

The long-accepted concept of “resting” microglia was challenged in 2005, when Nimmerjahn *et al.* and Davalos *et al.* concurrently demonstrated that even in an healthy brain microglia are constantly surveying the parenchyma with their processes, which were shown to extend and contract at an average rate of $\sim 1.47 \mu\text{M}/\text{minute}$ (47,48). A recent study by Madry and colleagues demonstrated that tonic activity of the TWIK-related Halothane-Inhibited K^+ (THIK-1) channel is essential for the maintenance of microglial surveillance activity (49).

These extremely dynamic processes are essential for the maintenance of CNS homeostasis, since they allow microglia to detect debris, protein aggregates, pathogens and injury sites despite their fairly static soma. Through their processes, microglia interact with other brain cells as well as with blood vessels (50,51). Microglia have also been shown to constitutively express low levels of Major Histocompatibility Complex class II (MHC-II), as well as to upregulate various markers of antigen presentation such as MHC-I and MHC-II, CD40, CD80, CD86, proving their ability to activate T cells in pathological contexts (52).

Interestingly, microglia are known to follow a mosaic-like distribution across the parenchyma (35,37), with cells in the neocortex located roughly 50-60 μm apart (47) so that each cell is responsible for the monitoring of a fairly limited territory. Their tiled disposition is maintained after cellular proliferation, when new-born cells have been shown to migrate $\sim 40 \mu\text{m}$ away from their mother (34). However, an increase in microglial density, concurrent to a decrease in process motility, was described in aged mice, suggesting a link between these observations and the progressive decline of brain homeostasis with aging (53).

Following recognition of pathogens or distress signal from surrounding cells, quiescent microglia rapidly become “activated” and react to the stimulus by releasing cytokines and other inflammation mediators such as reactive oxygen species (ROS) or nitric oxide (NO) (2), as well as through phagocytosis. This process consists in the receptor-mediated engulfment of relatively large particles ($\geq 0.5 \mu\text{m}$) that are then digested in specialised acidic compartment (phagolysosomes) (54). In neurogenic areas of the adult brain, TAM receptors (55) (in particular Axl and Mer) are essential for effective clearance of apoptotic cells following recognition of their ligands, Gas6 and Protein S (56). Recent work by Li *et al.* identified a subset of microglia, which the authors named “proliferative-region-associated microglia” (PAMs), in the white matter, where they were seen to specifically phagocyte apoptotic oligodendrocytes (57).

One of the main phagocytic receptors in microglial is the triggering receptor expressed on myeloid cells 2 (TREM2), which has also been involved in Alzheimer’s Disease (AD) (58,59). TREM2 has been shown to stimulate microglia phagocytic activity without parallel inflammation (60). Instead, downregulation of TREM2 caused an increase in TNF- α and nitric oxide synthase-2 (NOS2) transcription *in vitro*, highlighting the importance of this receptor for the maintenance of an immunosuppressive CNS microenvironment following homeostatic clearance of cellular debris (60). A later study by Hsieh *et al.* clarified that specific TREM2-dependant phagocytosis of apoptotic neurons is facilitated by the upregulation of TREM2-ligand on these cells (61).

Conversely, recognition of pathogen-associated molecular patterns (PAMPs, such as LPS) or danger-associated molecular patterns (DAMPs, including amyloid β ($A\beta$) in AD) by Toll-like receptors (TLRs) leads to activation of pro-inflammatory pathways (62,63). These receptors have been shown to be upregulated in the brain of AD patients, in particular in plaque-associated microglia (both in human and mouse),

and their contribution to AD pathogenesis has been proven controversial, as reviewed in (64).

Fc Receptor- (FcRs) mediated phagocytosis involves both Rac and cdc42, two Rho family GTPases of particular interest in this thesis due to their role in the WAVE Regulatory Complex (WRC) as discussed in section 1.3.1. This particular type of phagocytosis is enhanced by recognition of immunoglobulins (IgGs) coating the target particles. The FcRs are expressed at extremely low levels on microglia in homeostatic conditions, but can be upregulated in the presence of pathological insults(65). Conversely, phagocytosis mediated by complement receptor type 3 (CR3) recognises C3b-opsonised targets (66). This mechanism is especially important for synapse refinement during development (67,68) (as it will be discussed more in detail in the next session), and it has been involved in synaptic stripping in AD (69).

1.1.3.2. Microglia and CNS development: neurogenesis, axonal growth and neurotransmission

In the pre-natal stage, microglia are essential for the correct establishment of the neuronal network in the developing brain. A first crucial step is the clearance of dying neuronal progenitor cells that, after a first wave of proliferation, undergo programmed cell death (70,71). Moreover, microglia have been shown to actively promote apoptosis induction in Purkinje cells in the developing cerebellum (70). Even in the post-natal brain, microglial phagocytic activity is required for the correct development and differentiation of neurons in the subgranular layer of the hippocampus (72). Microglia are also responsible for insulin-like growth factor 1 (IGF-1) secretion, which is fundamental for cortical neurons survival (73).

Long-term potentiation (LTP) of post-synaptic neurons is dependent on the concerted action of AMPA and N-methyl-D-aspartate receptors (AMPA and NMDARs, respectively) in response to glutamate release from the pre-synaptic terminal (74). Microglial-dependant secretion of BDNF regulates AMPAR and NMDAR expression on neurons, thus playing a crucial role in learning-induced synaptic plasticity (75). Microglia also secrete Tumour Necrosis Factor α (TNF α), which has been seen to control AMPARs trafficking (76,77). For these reasons, Cx3cr1-deficient mice were shown to present impaired LTP, with consequent deficit in motor learning and spatial learning and memory (78). Interestingly,

CD200-deficient mice, that presented more activated microglia due to the loss of CD200-mediated homeostatic signal, also showed LTP impairment (79).

Multiple studies have also proved that microglia are essential for synapse refinement. Microglia involvement in synaptic pruning had been surmised since Davalos's and Nimmerjahn's studies (47,48), followed by observations of synaptic stripping after microglial activation by Trapp *et al.* (80). Wake and colleagues were among the first to concretely report interactions between microglia and synapses through two-photon imaging and electron microscopy experiments, demonstrating that a reduction in the length of microglial contact with synapses correlated with lower neuronal activity (81). Similar observations were described by Tremblay and colleagues in the visual cortex (82). Later work from Squarzoni *et al.* demonstrated that Cx3cr1 deletion caused severe impairments in synapse pruning and maturation (83), confirming earlier reports of electrophysiological alterations caused by impaired synaptic maturation in Cx3cr1-KO mice (84). Through the use of knock-out mice, it has been recently demonstrated that TREM2 is essential for synaptic stripping during development (85). Coherent with a crucial role of microglial phagocytic activity in synaptic pruning, this process has been shown to also be impaired following the loss of CR3, due to the observation that C3 is used as a molecular tag to mark synapses destined to be removed (67). This confirmed previous observations of a similar function ascribed to C1q in the visual cortex (68). More recently, CD47 has been shown to represent a "don't eat me" signal, specifically protecting more active synapses in order to ensure microglial-dependent removal of the weaker ones (86).

Finally, microglia have been implicated in the regulation of axon fasciculation (the process through which developing axons form bundles) in the corpus callosum through the adaptor protein DAP12 (87). Microglial DAP12 is also involved in the modulation of dopaminergic axons outgrowth and in the positioning of cortical interneurons in conjunction with Cx3cr1 (83). It has been suggested that activated microglia can inhibit axonal growth in a contact-dependent manner through the expression of repulsive guidance molecule a (RGMa) (88).

1.1.4. Maintenance of microglial homeostasis

1.1.4.1. Microglial homeostasis

Alterations in microglial gene expression profile have been observed mere hours after microglial isolation due to the loss of microenvironment-dependent signals (89), although Bohlen *et al.* showed that it is possible to revert these changes by transplanting microglia from short-term cell cultures to genetically microglia-depleted P0-P2 brains (90), thus confirming the necessity for niche-related cues in order to maintain microglial identity.

A first level of control is exerted by neuronal electrical activity, which has been seen to inhibit MHCII expression on the surrounding glial cells (91). Imperative for microglia homeostasis is also the impact of specific circuits involving transcription factors such as Sall1, that in 2016 was shown by Buttgerit and colleagues to be responsible for silencing genes involved with inflammatory response (92). Similarly, Deczkowska *et al.* demonstrated a role of myocyte-specific enhancer factor 2C (Mef2C) in the downregulation of microglial activation, lost in aging due to prolonged exposure to IFN-I (93). Two other major regulators of microglial quiescence have been identified in CD200/CD200R and Cx3cl1/Cx3cr1 (94,95).

Microglia are the only cells in the brain to express CD200R, which interacts with ligand present on the membrane of neuronal and macroglial cells (96,97). A first report of the importance of the CD200-CD200R axis came by Hoek *et al.*, who observed a reduction in microglia ramification, concurrent with upregulation of baseline levels of CD11b and CD45, in CD200-deficient mice, suggesting a more reactive state of these cells (94). Since then, a decline in CD200 levels, accompanied by an increased expression of pro-inflammatory genes, has been reported in the substantia nigra and the hippocampus in the aged brain (98,99). Similarly, CD200 downregulation has been noted in AD patients (100) and in mice challenged with A β (101). In rats, the administration of CD200 fusion protein in the hippocampus caused a decrease in microglia activation as well as an amelioration of LTP deficits associated with aging and LPS-treatment (102) supporting previous observations.

Cx3cl1 can instead be either expressed on the membrane of neuronal cells or be secreted by neurons in the surrounding space, but – similarly to CD200 – leads to inhibition of microglial activation following recognition by Cx3cr1 (95,103). This axis has been reported to be impaired in aging as well as in the presence of AD-like

pathology (104–106) and microglia from Cx3cr1-KO mice were found more sensitive to systemic LPS challenge (107). An *in vivo* study by Rogers *et al.* employing Cx3cr1-deficient mice demonstrated the presence of dose-dependent cognitive deficits associated with impaired hippocampal functionality, ascribed at least in part to elevated expression of IL-1 β (78). In agreement, Cribbs and colleagues reported a reduction in neurogenesis in the hippocampus of aged mice following age-related downregulation of Cx3cl1 (106).

However, one of the most studied factors involved in the maintenance of microglial homeostasis is TGF- β . Initial *in vitro* studies by Paglinawan and colleagues reported reduced transcriptional changes in microglial culture following TNF- α /IFN- γ stimulation in the presence of pre-treatment with TGF- β (108). Coherently, Butovsky *et al.* identified several genes representing a “freshly-isolated” microglial signature (including Tmem119, P2ry12 and Siglech), which appeared quickly downregulated in culture unless TGF- β was added to the media (109). Later work by Bohlen and colleagues further clarify microglial requirements for culturing, recognising the importance of IL-34, M-CSF, TGF- β and cholesterol in the maintenance of microglial homeostatic phenotype (90).

1.1.4.2. Microglia activation

Davalos *et al.* demonstrated that microglia quickly respond to traumatic injury by extending their processes towards the injury site within minutes (48). Activated microglia then proceed to acquire an amoeboid morphology, characterised by short and thick processes and enlarged soma (110). These phenotypical changes are reflected by alterations in the expression of surface markers accompanied by the release an array of different cytokines, chemokines and/or trophic factors, depending on the nature of the stimuli.

For decades, activated microglia have been categorised in a “M1” (neurotoxic) or “M2” (anti-inflammatory and thus neuroprotective) type, in a similar manner to other macrophages. This classification was mostly based on the observation of a combination of morphology and surface markers expression (111). For instance, “M1” microglia are supposed to be characterised by the release of pro-inflammatory mediators such as TNF α , IL-6 and IL-1 β , as well as by the expression of NADPH oxidase, iNOS and MHCII, whereas “M2” cells secrete IL-10 and TGF β , growth factors and neurotrophic factors (111). While the M1/M2 paradigm is still in use, the increase in transcriptomic studies observed in the last decade has highlighted the

severe limitations of this approach (112). An expanding body of evidence supports the idea of extreme microglial heterogeneity both in homeostatic conditions and upon stimulation (89,113–117), which will be discussed more in details in section 1.1.5 and 1.2.3.

Following activation, microglia respond by migrating towards the site of the insult in a matter of minutes, as shown by two-photon laser injury experiments (48). Microglial migration is mediated, among other factors, by purines released by other brain cells during and after an insult (118,119) and detected by a number of purinergic receptors, including P2Y₁₂ (120). While this receptor is not involved in basal “resting state” dynamics, it appears instead to be crucial for microglia movement following alterations of brain homeostasis (120). Other chemoattractants, including astrocyte-derived chemokines, can stimulate microglial chemotaxis through signals that converge on intracellular calcium pathways (121), which in turn regulate the formation of podosomes (122).

Another noteworthy consequence of microglial activation is reactive microgliosis, defined as an increase in number following a pathological stimulus. Upon stimulation, microglia undergoes a phase of elevated proliferation, leading to microgliosis (26). This in turn causes deep alterations of the tiling pattern usually exhibited by microglia in homeostatic conditions (35,37).

1.1.4.3. *Interplay among glial populations*

Multiple studies have highlighted the deeply interconnected nature of cells in the brain. Thus, while neuronal- and astrocyte-derived signals are crucial for maintenance of microglia in quiescent state, this is not an unidirectional relationship.

For instance, microglia release IL-1 β , IL-6 and NO, which are essential for astrocyte proliferation and maturation during brain development (123–125). In addition, microglia contribute to astrocyte activation, which – in a similar way to microglia – can acquire either an “A1” (neurotoxic) or “A2” (neuroprotective) phenotype. IL-1 α , C1q and TNF- α secreted by activated microglia have been shown to be sufficient to induce a shift towards an A1 phenotype (126). This in turn leads astrocytes to lose their homeostatic synaptogenic and phagocytic functionality and cause death of surrounding neurons and oligodendrocytes (126). Moreover, activated microglia secrete ATP, which recruits more astrocytes and induces glutamate release by these cells (127). Glutamate stimulates neuronal activity and, if prolonged, can

cause neuronal damage by excitotoxicity due to the over-stimulation of NMDARs and the consequent abnormal influx of Ca^{2+} ions in post-synaptic neurons (128).

On the other hand, the ability of microglia to scan the parenchyma and extend their processes or migrate towards injury sites or distressed neurons is at least in part mediated, as discussed before, by purines. Astrocytes are not the sole cell responsible for ATP release, however Davalos et al. reported a reversible downregulation of microglia response following inhibition of connexin channels (48), particularly enriched in astrocytes (129). Following this observation, Haynes et al. suggested a role of astrocytes as crucial mediators between damage and microglia response to β -amyloidosis (120). Moreover, astrocytes-derived TGF- β can increase C1q expression in neurons, tagging them for microglial clearance (130), while astrocytic IL-33 regulates microglia-mediated synapse engulfment (131).

Interestingly, microglia have also been seen to interact with oligodendrocytes both during development and in the adult brain. Microglia were found responsible for the correct development of oligodendrocytes progenitors and following myelination process, as well as for the maintenance the progenitor pool in the adult stage (132). In agreement, Wlodarczyk and colleagues identified a CD11c⁺ subset of microglia enriched in primary myelinating areas during development and essential for the correct completion of primary myelination (133).

These are only a few examples of the delicate equilibrium maintained in the brain. However, it is possible to appreciate the extent of potential repercussions on both physiological and pathological brain environment in case of a severe impairment of microglia activity. Fine regulation of microglial homeostasis is therefore critical both in developmental and adult brain.

1.1.5. Microglia heterogeneity and sexual dimorphism

1.1.5.1. Spatial heterogeneity

Evidences of diverse microglial distribution and morphology in various brain regions emerged as early as in 1990 (134). Verdonk and colleagues developed an automatic imaging system and quantified ramification complexity and covered parenchyma area for microglia in different brain regions. This highlighted, in the cerebellum, the presence of microglia characterised by a small soma and low arborisation complexity (135). Instead, microglia located in regions devoid of a

complete BBB, such as the subventricular zone or the circumventricular organs, exhibited an amoeboid morphology in healthy adult mice (134,136,137). As well as morphological difference, microglia residing in different brain regions also displayed variable surveillance ability, which was shown to be reduced in the cerebellum (138), while microglia in the brain cortex reacted faster to ATP injection compared

The advent of single cell transcriptomic (scRNAseq) brought with it an increased awareness of microglial heterogeneity. What had been till then considered as a fairly homogeneous entity – despite a growing body of literature suggesting that microglial subsets differ not just in regards to morphology but also to cell turnover or immunoregulatory proteins expression (35,37,139–142) – revealed itself to instead comprise multiple subpopulations, each characterised by distinct morphological, molecular and therefore functional signatures (143–147).

Given the impact of neuronal and astrocytic feedbacks on microglia, as discussed in the previous section, it is hardly surprising that diverse niche-specific requirements were found to influence microglia (142). Tay *et al.* suggested that the difference in microglial renewal among different brain regions was likely to be functionally relevant, based on the observation of analogous rates of turnover in other cell types (37). Genome-wide analysis highlighted the presence of a higher energy metabolism and a more immune-alerted nature of microglia in the cerebellum, and in lesser measure in the hippocampus, compared to the cerebral cortex and the striatum (142). Coherently, Ayata *et al.* identified morphological and gene expression markers of phagocytic activity in cerebellar microglia, which the authors ascribed to the higher levels of neuronal death in the cerebellum (and therefore increased need for debris removal) (148). In another study, Hammond and colleagues investigated regional diversity across different stages of brain development and aging, as well as in pathological conditions (specifically, in a mouse model of demyelination) (146). The authors reported a region-specific expression of Secreted Phosphoprotein 1 (Spp1), which resulted restricted to the subcortical axon tracts of the corpus callosum in the forebrain and in the axon tracts of the cerebellum in the pre-myelinated brain (146). Spp1+ microglia presented an activated phenotype and were enriched in genes associated to phagocytic activity, which led to speculations regarding their involvement in material engulfment during axonal growth and fasciculation in the early postnatal brain (P4/P5) (146). De Biase and colleagues, while analysing microglia in the basal ganglia, identified a set of genes – including microglia enriched genes such as *Csf1r*, *Cx3cr1*, *Tmem119*, *P2ry12* and *Trem2* – which were conserved among different regions, most likely due to their role in

microglia homeostasis and core immune functions (143). On the other hand, region-specific subsets differed for their expression of genes connected to mitochondrial and lysosomal functionality, metabolism and oxidative stress, which reflected on microglial functionality and morphology (143). Li *et al.* instead did not observe significant region-specific variability in adult microglia, suggesting that Ayata's results may have been connected to Tmem119^{low/-} microglia excluded by their analysis, while previous report from Grabert *et al.* may have been biased by the inclusion of non-microglial CD11b⁺ cells (57).

1.1.5.2. Microglia and aging

Another factor that clearly emerged as a crucial determinant of microglial heterogeneity was aging, albeit different works reported contrasting findings. For instance, Matcovitch-Natan *et al.*, whose observation of a stepwise developmental program was based on whole brain analysis, showed highly homogeneous microglia during development (23), potentially due to a bias introduced by the use of surface markers for the isolation of microglial cells before the transcriptomic experiments (57). A later study by Li *et al.* however, described a notable heterogeneity in early post-natal microglia, with a particular focus presence of PAMs, a transient subpopulation associated to the white matter. The cells resembled the pattern of expression of microglia clustered around A β plaques, leading to the suggestion of a functional role of this subset in the clearance of dying oligodendrocytes or the creation of functional brain circuits (57). Hammond *et al.* confirmed Li's report of an increased heterogeneity in the earliest stages of development, while they identified subpopulations of pro-inflammatory, interferon-responsive cells in the aged brain (146). Finally, Grabert and colleagues showed that, in aged mice, cerebellar microglial exhibited a marked increase in already elevated immune-response genes, while the opposite phenomenon occurred in the hippocampus, leading to an augmented similarity to other forebrain regions (142). Recent work from Masuda *et al.* employed a massively parallel scRNAseq approach to dissect multi-region differences across various developmental phases (E16.5, 3 weeks and 16 weeks) as well as pathological contexts and found that post-natal cells were enriched in homeostatic genes, including Tmem119, while embryonic microglia strongly expressed lysosome-related genes (145). While bulk- and scRNAseq studies have considerably increased our understanding of microglial biology, they do still present

notable limitations, in particular the variability in cell isolation protocols employed by different teams, which could account for the discrepancies discussed in this section.

In 2013, Hickman and colleagues described for the first time what has been since then known as microglial “sensitive” (116). This comprises a set of the 100 murine genes mostly expressed in adult homeostatic microglia and essential for their ability to sense the surrounding microenvironment. These include, among others, receptors for cytokines, chemokines, purines, Fc fragments and ECM, as well as proteins involved in inter-cellular interactions and transporters (116). The expression of these genes was reported to be lowered in a number of pathological conditions (149) as well as in aging (116). Among the genes downregulated during aging, Hickman *et al.* highlighted purinergic receptors (including P2y12) as well as receptors involved in the recognition of apoptotic cells (e.g. Siglech). Taken together, these observations suggest that a reduced ability to interact with the microenvironment could contribute to an ineffective response to insults and accelerate neurodegeneration. However, in aging, the downregulation of purinergic receptors could be also seen as a defence mechanism aimed at limiting microglia activation following enhanced neuronal death in the aged brain (116). This hypothesis is supported by the maintenance of stable levels of phagocytic markers and genes involved in microbial recognition (116). Transcriptomic changes in aged microglia are also accompanied by parallel changes in morphology – namely an increase in cell body volume and a reduction of the ramification apparatus(150) – as well as in functionality, with a drastic decrease in their processes extension/retraction velocity (151).

1.1.5.3. Sexual dimorphism

One last known source of microglial heterogeneity – apart from the obvious health/disease comparison that will be discussed more in details in section 1.2.3 – is sex. We now know that autoimmune diseases, such as multiple sclerosis, as well as AD have a higher occurrence in females, while males are more affected by neurodevelopmental disorders (e.g. autism) (152). While genetics, hormones and environment play a role in this phenomenon, there is evidence of a direct involvement of microglial sexual dimorphism (152,153). This phenomenon is connected to the surge in testosterone production that in male rodents is seen during the late stage of pre-natal period (154), although chromatin remodelling

through DNA methylation and histone modifications have been implicated as well (153).

A first difference has been observed in the number of cells present in adult (13-week-old) mice brain, with males consistently showing a higher number of Iba1+ cells, which also presented a bigger soma size, in hippocampus, cortex and amygdala (155). Similarly, Guillot-Sestier et al. described the identification of more amoeboid microglia in aged males, with consequent increase in their soma area and reduced overall area (156). Results were more variable in the amygdala and the hippocampus of 3-week-old mice, while striatum and cerebellum did not appear affected at either age (155). In a previous study, instead, Hanamsagar et al. reported the presence of a more complex arborisation apparatus in baseline conditions in the CA3 region of the hippocampus in P60 males, and only observed morphological (and transcriptional) changes after intraperitoneal injection of LPS in animals of this sex (157).

Moreover, cells from male animals displayed higher levels of MHCI and -II in the cortex and the hippocampus and exhibited higher responsivity to ATP stimulation in cortical slices (155). Variable results were reported regarding sex impact on phagocytic activity based on age and disease status: Guneykaya and colleagues did not determine any significant difference in the healthy adult brain after P17 (155), whereas Guillot-Sestier et al. employed a model of AD and reported a significantly impaired phagocytosis in aged females. Weinhard et al. also observed a faster increase in volume and CD68 expression (which the authors employed as an indirect marker of phagocytic potential), followed by a corresponding faster reduction, in female microglia two weeks after birth (158).

Other functional differences still to clarify may include reduced lifespan of male microglia as well as an increase in their motility (due to higher levels of P2Y12 receptor on males, which could increase their ability to migrate) and immune response as seen by increased baseline levels of S100a8 (which has been linked to TLR4-dependent regulation of proinflammatory mediators (159)) (155). Conversely, Thion et al. reported higher expression of S100a8, and overall of genes involved in immune response – in females (160). Villa et al. demonstrated an increased expression of NF- κ B-related genes in males, which resulted more prone to activation than females (161).

Discrepancies in activation status of microglia among studies could be explained by the employment of different protocols for cell isolation, as discussed before, but also

by the exposure of animals to non-identical microbiomes, which Thion and colleagues showed to differently impact microglial in a sex-related way (160). Therefore, while consensus has been reached regarding the presence of sexual dimorphism in microglia, the effective impact of sex-driven divergence on microglia biology need further clarification and it is thus imperative to include animals of both sexes in future studies.

1.2. Alzheimer's Disease

According to the 2019 World Alzheimer Report, over 50 million people are estimated to live with dementia across the globe, expected to increase to 152 million by 2050 (162).

Described for the first time by Alois Alzheimer in 1907 (163), Alzheimer's Disease (AD) currently account for at least 60-70 % of the total dementia cases, affecting approximately 10 % of the population aged ≥ 65 years (164). In the pre-clinical stage, patients manifest mild memory impairment, a reflection of initial changes in the cortex and hippocampus. This phase can last for years, but patients eventually start manifesting loss of concentration and memory associated to disorientation and mood changes, often accompanied by depression. Symptoms progress in parallel to the disease spreading across the cortex, with severe worsening of memory loss as well as increased impulsivity and speech difficulties. In the late-stage, patients are often bedridden and eventually die due to complications related to severe impairment of daily functions (165). To date, AD is incurable and the only two classes of FDA-approved drugs – cholinesterase inhibitors, prescribed in the early stages, and NMDA antagonists, for patients with advanced AD – can only temporarily improve symptoms (165). In 2021, the Food and Drug Administration (FDA) granted accelerated approval for Aduhelm (aducanumab) . This human monoclonal antibody is reportedly able to reduce amyloid PET signal in a dose- and time-dependant manner (166). However, to date the only available data available on the outcome of Aduhelm treatment are controversial and the real efficacy of this drug is yet to be determined (167).

1.2.1. Aetiopathogenesis of AD

The two main pathological hallmarks of AD are A β plaques and neurofibrillary Tau tangles (NFTs), which are often accompanied by diffuse gliosis and synaptic loss (165).

1.2.1.1. Amyloid- β plaques

A β is generated by a two-step cleavage of the transmembrane amyloid precursor protein (APP), as shown in Figure 1.2. In the nonamyloidogenic pathway, the first cut is operated by α -secretase. This produces an extracellular domain (APP α), which gets released, and the α -CTF, retained in the membrane. This fragment is then cleaved by a second enzyme, γ -secretase, which produces a 3 kDa fragment (p3) at the N-terminus, released outside the cells, and a cytoplasmic APP intracellular domain (AICD) (168). In the amyloidogenic pathway, however, the first cut is operated by a β -secretase, with the consequent formation of an APP β ectodomain and a transmembrane β -CTF carboxy-terminal fragment, available for further processing via γ -secretase (168). This pathway can generate A β peptides of variable length (38 to 43 amino acids), however the most abundant species are A β 40 and A β 42, which is the most hydrophobic and thus fibrillogenic (169).

The ratio between A β 42:A β 40 is significantly increased in AD patients, while the clearance results reduced (170). Thus, according to the Amyloid Cascade Hypothesis, amyloid plaques are generated by progressive aggregation of A β monomers into various species of oligomers. These are considered the most toxic form of A β for multiple reasons reviewed in (171), including their ability to inhibit LTP and decrease synaptic spines (172,173). Oligomers, in turn, are prone to further aggregate into protofibrils, that eventually become long enough to form insoluble fibres (164).

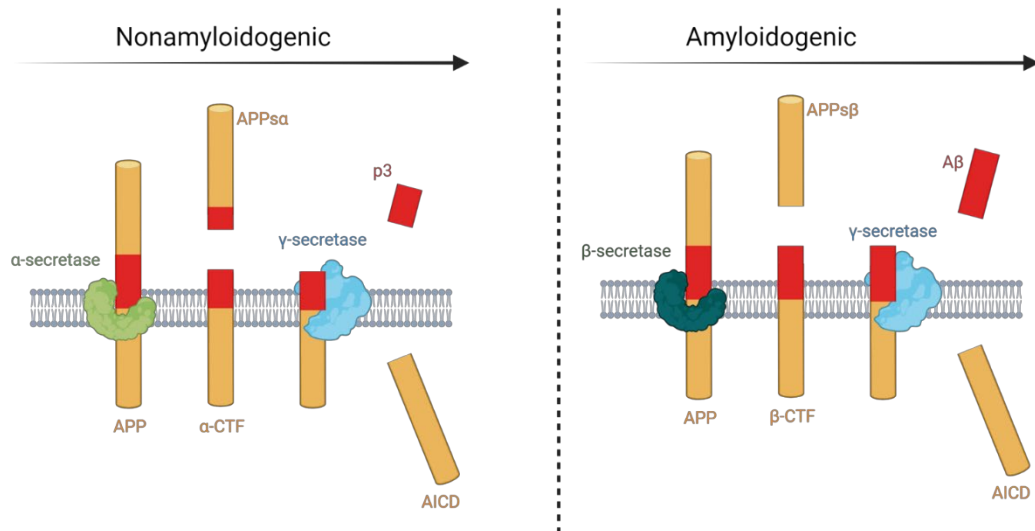


Figure 1.2 Schematic representation of APP processing.

The nonamyloidogenic pathway of APP processing (left) involves two successive cuts, operated by α - and γ -secretase, in order. Instead, in the amyloidogenic pathway (right) the first cut is performed by a β -secretase. Both processes generate soluble extracellular domains (APP_{sa} and $APP_{s\beta}$) and intracellular fragments (AICD) at the C-terminus. However, in the nonamyloidogenic pathway, the cleavage by γ -secretase leads to the formation of $A\beta$ peptides, that can then accumulate in the extracellular space. Image adapted from (168) and generated with BioRender.com.

1.2.1.2. Neurofibrillary Tau tangles

NFTs, the second major hallmark of AD, are caused by pathological alterations in the Tau protein. This is normally involved in microtubules stabilisation and regulation of axonal transport. However, in pathological conditions hyper-phosphorylated Tau (pTau) can detach from microtubules, causing neuronal dysfunction and accumulation of Tau aggregates (174). Accumulation of pTau in the neocortex has been proven to better correlate to AD progression compared to β -amyloidosis (175).

The MAPT gene, encoding for Tau, can originate up to six different isoforms due to alternative splicing. In particular, the so called 3R and 4R are characterised by the presence of either 3 or 4 microtubule-binding repeats at the C-terminus (176). Alterations of the ration 3R:4R from the physiological 1:1 has been observed in the brain of AD patients (174). However, the real impact of this ratio is still unclear. A recent study has shown that increase in 4R in a mouse model of tauopathy exacerbates pathological hyperphosphorylation (177). Notably, excitatory neurones

are particularly sensitive to Tau-induced death (178) due to their increased activity, which has been shown to concurrently increase Tau release (179). This is

1.2.2. Genetic risk factors

AD cases can be classified in early-onset (EOAD) and late-onset (LOAD) based on the age at the diagnosis: symptoms manifestation before the age of 65 classify as early-onset (165). It is estimated that EOAD accounts for a very small percentage of cases (approximately 1 %) and it is connect to highly penetrant familial autosomal dominant mutations (fAD) in three genes: APP, Presenilin 1 (PSEN1) or Presenilin 2 (PSEN2), which encodes for subunits of the γ -Secretase complex (180–182). Mutations in these last two genes are considered responsible for an increased production in A β 42 (183) and their identification contributed to the success of the Amyloid Cascade Hypothesis over the past decades. However, anti-A β therapies and β - and γ -secretase inhibitors have been repeatedly proven unsuccessful in AD treatment, challenging the validity of such a model (184).

LOAD accounts for the majority of AD cases and presents an estimated approximately 70 % of heritability (165). Patients manifest clinical features mostly overlapping with those of EOAD but they develop symptoms after the age of 65 (165). Genetics underlying LOAD risk are extremely complex and have not been fully unravelled yet. The most well-known risk gene in LOAD is Apolipoprotein E (APOE), which presents three polymorphic alleles – ϵ 2, ϵ 3 (considered the common allele) and ϵ 4 – each associated to different risk levels (165,185). In particular, the ϵ 4 allele is associated with the highest AD risk in a dose-dependent manner (186). Conversely, ϵ 2 appears to exert a marginally protective effect. ApoE is believed to contribute to lipid transport in the brain (187), however after decades of studies the mechanisms underlying its role in AD are still far from understood. Notably, Kraseman and colleagues suggested that APOE acts in collaboration with TREM2 to suppress TGF- β signalling, leading to the upregulation of genes characteristic of the Disease-Associated Microglia (DAM) signature (which will be discussed in the next section) (188).

In the past years, the advent of genome-wide association studies (GWAs) led to the identification of over 40 risk loci for common variants (minor allele frequency [MAF] > 0.01) (189) (Figure 1.3). These are often characterised by small effect size (apart for those in APOE) and are preferentially found in intergenic or intronic regions

(190), increasing the challenges involved in understanding the underlying molecular mechanisms (191). Despite this, almost 60 % of genetic variance in sporadic AD is unaccounted for (192). It is likely that at least part of this variability is linked to rare coding variants ($[MAF] \leq 0.01$), whose identification has proven more challenging due to the need of extremely large samples to account for the decrease in power of association test concurrent to that of the MAF value for that variant. However, rare variants preferentially affect protein-coding regions of the genes, which can facilitate their modelling *in silico* and *in vitro* in order to develop novel therapeutic approaches (193).

Among the first identified common variants were those within CR1, CLU and PICALM loci (194,195). Of particular interest, CR1 is the main receptor for the complement factor C3b (196) and binds to C1q, which has been shown to be upregulated in the presence of A β (197–200). Thus CR1 is crucial for A β uptake by microglia (198). Two AD-risk variants mapped in this locus result in low CR1 expression in the brain but higher expression on monocytes (201). Other risk variants of interest have been identified in the SPI1 gene, which codes for the key microglial transcriptional factor PU.1 (202). These have been mapped within PU.1 binding sites as well as in miR-569 binding site on SPI1, which would suggest an effect on gene expression (202). In particular, PU.1 binds, among others, TYROBP, MS4As, INPP5D, TREM2, and CD33 (202): thus, alterations in its levels could lead to severe repercussions for microglia homeostasis.

Several rare variants have been identified in genes involved in microglia biology. For instance, multiple variants have been identified in TREM2 and appear to cause an increased risk of AD due to a partial loss of function of this receptor, which in turn impacts microglial phagocytosis and alters microglial gene expression (203–207). Variants in CD33 (expressed exclusively by microglia in the brain (208) and involved in their phagocytic activity (209)) were originally identified by early GWAS studies and resulted associated with alternative splicing and reduced CD33 expression (210). However, they did not reach genome-wide significance in recent meta-analyses (211). A protective variant has been identified in PLC γ 2, which in the brain is predominantly expressed by microglia (192). This gene encodes for an enzyme responsible for Phosphatidylinositol 4,5-bisphosphate (PIP $_2$) cleavage into the secondary messengers Inositol trisphosphate (IP $_3$) and diacylglycerol (DAG) and is essential for the activation of NF- κ B and MAPK pathways (192). In the same work, the S209F variant in Abi3 was identified (192), leading to the commencing of this study.

It is therefore apparent that AD is a complex, polygenic disease (212). While individual disease-associated alleles only marginally contributes to disease risk, taken together they can provide a useful tool for the prediction of AD susceptibility. The development of a tool to analyse polygenic risk score (PRS) currently allows the evaluation of an overall risk score that comprises all the identified SNPs across the entire genomes, weighted according to their estimated effect size (213). Escott-Price and colleagues proved that the combined use of PRS together with predictors such as APOE, gender and age provides a model with a predictive ability of approximately 78% (212). In the case of individuals with more than 2 standards deviation from the PRS, the distinction between low and high PRS reaches an accuracy of up to 90% (214). Hence, PRS represents an enormous advantage when trying to identify individuals in high risk group during the earliest stages of life.

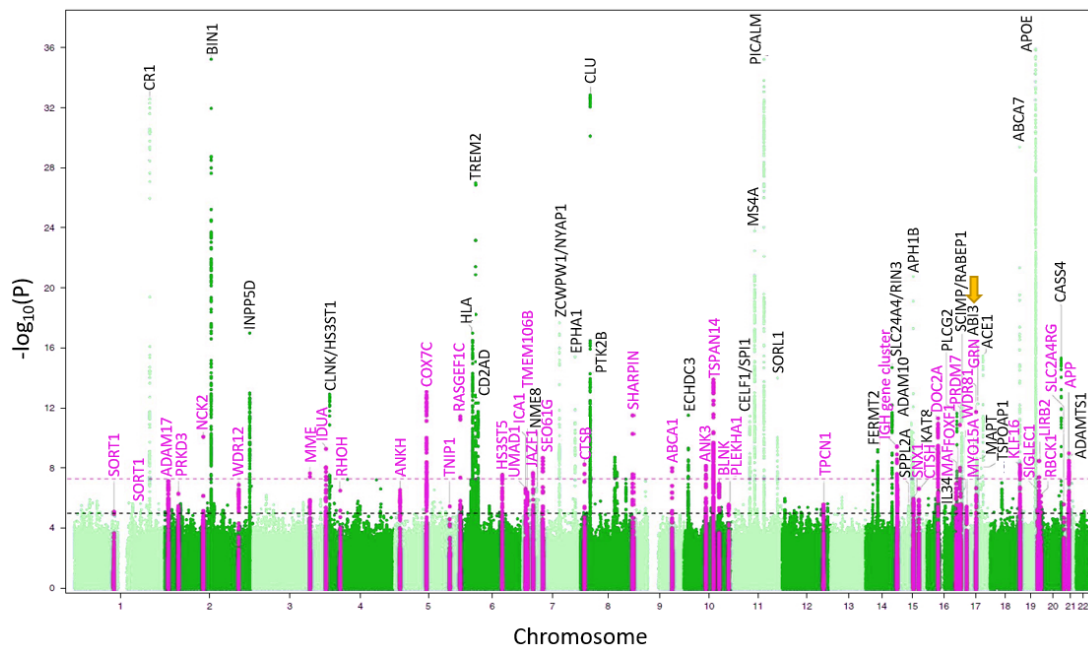


Figure 1.3 Manhattan plot of the results of a metanalysis for genome-wide association in Alzheimer's disease.

Loci with genome-wide significance are reported on the plot, with the newest identified ones highlighted in pink. Variants with p-value below 1×10^{-36} are not shown. The top dotted line represents genome-wide significance level ($p = 5 \times 10^{-8}$), while the bottom dotted line indicates the suggestive significance level ($p = 1 \times 10^{-5}$). ABI3 is indicated by the yellow arrow. Adapted from (215).

1.2.3. Neuroinflammation and role of microglia in AD

The first report of a glial involvement in Alzheimer's Disease (AD) goes back to Alzheimer's original paper, dated 1907 (163). However, it was not until the second half of the 20th century that more detailed accounts of microglia association with Amyloid β (A β) plaques began being published (216–219). The relatively recent interest of the scientific community on this subject was sparked by a series of publications that reinforced the idea of a crucial – albeit still controversial – role of the brain immune system in AD pathogenesis (58,59,220,221).

Microglia activation contributes to early response to amyloid deposition through the secretion of high levels of IL-1 β in order to stimulate astrocytes (222). Nlrp3 inflammasome is essential for the activating cleavage of IL-1 β operated by caspase-1 following A β phagocytosis (223). Using both Nlrp3- and Casp1-deficient mice crossed to a model of familial AD, in 2013 Heneka and colleagues demonstrated that the inhibition of this pathway led to better performance in the Morris Water Maze and the Novel Object Recognition test (220) (two well-established memory paradigms used to assess spatial and recognition memory (224,225)). The lack of Nlrp3 or caspase-1 also resulted in a marked reduction of amyloidosis in both the cortex and the hippocampus of these mice, ascribable to a concomitant increase in microglia phagocytic activity (220).

Following the identifications of TREM2 variants connected to an increased risk of AD (58,59), Wang et al. further investigated the mechanistic basis of these observations (226). They found that the lack of this transmembrane receptor, typically present on the surface of myeloid cells (including microglia in the brain (227)), aggravated A β accumulation in the brain. As the authors demonstrated, this was due to a link between TREM2 ability to bind specific lipids, associated with A β deposits and dead cells, and microglial migration towards A β plaques, which was severely impaired in TREM2 deficient mice (226,228).

Expression levels of CD33 (a transmembrane lectin expressed on multiple immune cells including microglia (208)) were shown to be increased in post mortem samples of AD brains (229). However, higher expression of CD33 appeared to correlate with increased accumulation of A β due to CD33 negative impact on microglia phagocytosis (229). Similarly, Bradshaw *et al.* reported that human monocytes from individual bearing the CD33 risk allele showed a decreased uptake of dextran and A β ₄₂ when tested *in vitro* (230). Moreover, in the same study, the presence of the risk allele (rs3865444C) was shown to cause an increase in fibrillar amyloid burden

in the brain of patients (230). Instead, individuals bearing the rs12459419T variant exhibited increased A β clearance, which was related to the lack of the IgV domain, involved in CD33 functionality (230) as well as its purely intracellular localisation (with no mobilisation to the cellular surface observed even after stimulation) (231). This has been more recently ascribed to the identification of a negative modulation of TREM2 by CD33, supported by the observation of a loss of beneficial effects of CD33 ablation when TREM2 was also knocked-out (232). However, a following study on murine cell lines and primary mouse microglia showed no difference in phagocytosis between CD33-WT and -KO cells (209). Similarly, no difference was observed in a CD33-KO human pro-monocytic cell line following overexpression of murine CD33, whereas the expression of the long isoform of human CD33 (preferentially generated by the risk allele) successfully inhibited phagocytosis (209). Therefore, mouse CD33 may not represent the correct surrogate for the study of CD33 role in AD and further work is required to confirm the putative interactions between CD33 and TREM2.

In line with the previous findings, that suggest a beneficial role of neuroinflammation in AD, Chakrabarty and colleagues proved that the increase in IL-10-related proteins observed in AD brains (233) aggravates brain amyloidosis and memory deficits due to a combination of increased production of ApoE and reduced microglial phagocytosis of the plaques (234). Indeed, IL-10^{-/-} mice showed markedly reduced amyloid burden, decreased synaptic loss and better performance during behavioural assessments (233).

Conversely, it was demonstrated that mice lacking TNF- α type 1 death Receptor, crossed with a model of AD, presented reduced A β secretion and accumulation and microgliosis (235). These mice also displayed a decrease in neuronal death and a parallel amelioration of behavioural scores (235). In addition, Hong et al. showed that microglia are responsible for complement-mediated synaptic loss in the early stage of the pathology in J20 mice (overexpressing two human App mutations (236)) following accumulation of C1q and C3 on synapses (69). Inhibition of CSFR-1 in the adult brain, resulting in microglia ablation, did not affect A β deposition, but it led to a reduction in memory impairment and prevented neuronal and synaptic loss in 5XFAD mice (237). In a more recent study employing the 5XFAD model, Sosna and colleagues inhibited CSFR-1 for a 3-month period starting from the age of two months (when neuritic plaque deposition begins in this model) and observed a marked reduction in intraneuronal amyloid, neuritic plaques and soluble oligomers (238). Likewise, Son *et al.* recently reported an amelioration of dopaminergic

signaling, parallel to a reduction in β -amyloidosis, following a 30-day-long inhibition of CSFR-1 (239).

These sources of evidence seem to indicate a diametrically opposite effect of microglia action compared to the one discussed above. Moreover genetic ablation of either Cx3cl1 or Cx3cr1 also led to a decrease in A β deposition concurrent with increase in microglia activation and cytokine production (240,241). However, Cx3cr1-deficiency also caused a severe worsening of neuronal and memory deficits in a hAPP mouse model, regardless of amyloid burden (242) and it was shown to exacerbate Tau pathology (243). Taken together, these evidences support the hypothesis of a very thin balance between a protective microglial response and a detrimental exacerbation of neuroinflammation.

Interestingly, epidemiological studies reported that the use of Non-Steroidal Anti-Inflammatory Drugs (NSAIDs) correlated with a decreased risk of developing Alzheimer's (244,245). However, all the clinical trials based on this assumption failed to provide any consistent benefit and, instead, were detrimental for some of the most vulnerable patients (246), highlighting the necessity for deeper understanding of neuroinflammation mechanisms in AD.

In 2017, Keren-Shaul et al. described for the first time what they referred to as "disease-associated microglia (DAM)" in the 5XFAD model, as well as in human AD brain tissue (247). This subtype of microglia cells, localised around A β plaques, appeared to become activated in a two-step manner. According to the authors, in the first stage core microglia genes (including Cx3cr1 and P2ry12) are downregulated, while the expression levels of AD risk factors (e.g. Tyrobp, Apoe and B2m) are increased. A further Trem2-dependent activation step causes upregulation of genes connected to lipid metabolism and phagocytosis (247). At the same time, Mathys and colleagues identified two additional microglia populations exclusively associated to pathological conditions such as neurodegeneration (248). The two groups, defined as "early-response stage" and "late-response stage" were isolated at different time points in Ck-p25 mice (an inducible model that presents most of AD hallmarks (249)). Interestingly, whilst late-response cell showed a partial overlapping with DAM, they also manifested a significant upregulation of genes involved in antiviral and interferon response (250). Early-response cells, instead, showed a smaller similarity to stage 1 DAM. Based on these observations, it was proposed that all the different microglia populations represented activation states with an increasing neurotoxic activity, going from the early-response to the late-response ones, with the two subpopulation of DAM representing the middle

steps (251). A parallel work from Krasemann and colleagues identified a specific disease-associated microglial signature, characterized by the upregulation of 28 inflammatory molecules – including ApoE, Csf1 and Clec7a – in microglia surrounding amyloid plaques (MGnD) (188). This change, ascribed to the phagocytosis of apoptotic neurons, is consistent with changes observed in senescent microglia observed in aging and AD, including the downregulation of key immune genes (such as the TGF β signalling) (188). Finally, a more recent work from Chen *et al.* employing a spatial transcriptomic approach identified a network of 57 plaque-induced genes (PIGs), divided in three clusters enriched in microglial and astrocytic genes (including ApoE, C1q, TREM2 and Tyrobp/Dap12) (252). These genes presented a low connectivity in WT animals, but it was shown to increase concurrently to amyloid deposition, leading to speculation about their role in coordinating a response to A β between astrocytes and microglia (252).

1.2.4. Transgenic mouse models of AD

Over the course of the years, a vast number of mouse models have been generated for the study of AD, in an attempt to recapitulate the complex clinical and molecular manifestations of the human disease. Several limitations need to be taken into account. Apart from issues related to poor reproducibility across studies and the problematic inbred genetic background of these mice, a considerable issue is that, in order to obtain results within useful timeframes, most models present particularly early onset of symptoms and fast disease progression. This in turn prevents an accurate evaluation of interaction between age-dependant factors (for instance, increased reactivity of glial cells) and the disease. It also impacts the therapeutic window which is considerably reduced when working with these mice, further reducing the translatability of the available studies to humans (253).

Some of the most commonly employed transgenic (Tg) models, relevant for this thesis, will be briefly described in this section and the main features of each model are summarised in Figure 1.4. For a complete review, please see (254,255).

First-generation models include single, double and triple App-Tg mice, overexpressing APP with or without mutations associated to fAD.

Among these, the TgCRND8 mice were developed by expressing both the double APP Swedish mutation (K670N-M671L) and the Indiana mutation (V717F) (256). A β accumulation is seen starting at 3 months of age and by 8-9 months of age it has

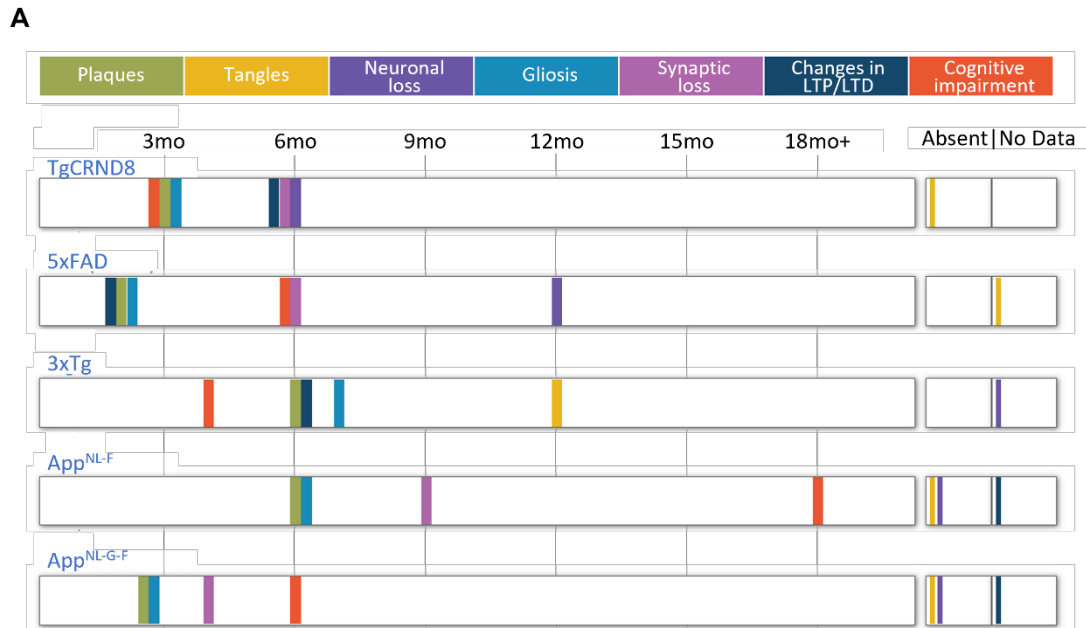
spread to hippocampus, brainstem and cerebellum with parallel gliosis and increase in neuroinflammation. Cognitive impairment has been seen to coincide with plaque deposition (257). Among the main disadvantages of single APP-Tg mice there is the presence of artifacts related to overexpression of APP and random insertion of the transgene. These mice also do not recapitulate NFTs pathology (254).

An example of double APP-Tg mice is instead represented by the 5XFAD model. These mice were generated by (258) by crossing APP-Tg mice to animals bearing mutations in PSEN1, resulting in accelerated amyloid deposition. They manifest high levels of intraneuronal A β 42 starting from 1.5 months of age and extracellular deposits from 2 months (together with parallel gliosis), which reach the hippocampus approximately at 6 months of age. Synaptic degeneration begins at 4 months of age, followed by neuronal loss and moderate behavioural changes (258). These mice present similar drawbacks to those described for the TgCRND8 model, most notably the lack of NFTs accumulation and the risk of potential bias caused by the accumulation of non-A β APP fragments (254). However, compared to other first-generation models, these mice present a preferential deposition of A β ₁₋₄₂ rather than A β ₁₋₄₀, therefore bearing a closer resemblance to the amyloid plaques observed in patients (258).

The 3xTgAD was instead developed through co-injection of two transgenes – encoding the Swedish mutation as well as a mutation in the MAPT gene – into embryonic cells carrying a mutation in the PSEN1 gene (259). These mice present elevated A β 40 and A β 42 levels, with plaque deposition from 3 month of age, as well as NFTs starting at 12 months of age. They present progressive synaptic function and spatial memory impairments 6 months of age (257). As all the other APP-Tg models, they present artifacts due to overexpression and random integration of the transgenes (254).

In order to overcome the problematic overexpression of APP, second-generation models were generated by humanizing murine APP by introducing two (for the APP^{NL-F} model) or three (for the APP^{NL-G-F}, used in this thesis) fAD mutations, namely the Swedish and the Beyreuther/Iberian (I716F; with the addition of the Arctic, in APP^{NL-G-F} mice) (260). These mice present increased A β 42 production, higher A β 42/A β 40 ratio and, in the case of APP^{NL-G-F} mice, increased oligomerisation. APP^{NL-G-F} in particular show plaque deposition in the cortex from 2 months of age, followed by spreading across other brain regions until saturation at around 7 months of age (260). These mice also manifest increase gliosis, synaptic deficits (260) and behavioural alterations summarised in (261). One of the major

drawbacks of this model is the unknown effect of interactions between three separate fAD mutations, as well as fairly moderate cognitive deficits and lack of NFTs (254). However, these mice present amyloid plaques more similar to those observed in patients compared to App-Tg mice, where the plaques result excessively large and mainly composed of $A\beta_{1-40}$ instead of the $A\beta_{1/3pE-42}$ more commonly observed in patients (254).



B

		Strains	General Features	Potential disadvantages
First generation	Single transgenic (App-Tg)	PDAPP Tg2576 APP23 J20 TgCRND8 C57B6	<ul style="list-style-type: none"> Moderate behavioral phenotype. Neuronal loss in some models. 	<ul style="list-style-type: none"> Random integration of transgenes. Artificial expression pattern controlled by exogenous promoters. APP overexpression-related artifacts.
	Double transgenic (App-Tg x PSEN1-Tg or KI)	APPS1 5XFAD	<ul style="list-style-type: none"> Moderate behavioral phenotype Aβ accumulation from early stage. Neuronal loss in some models. 	<ul style="list-style-type: none"> Cognitive impairment often preceding Ab accumulation (potentially due to APP overexpression). No NFTs in single and double Tg. Presence of Aβ species different from those presented by the patients.
	Triple transgenic	3xTg-AD	<ul style="list-style-type: none"> Moderate-severe behavioral phenotype. NFT formation. Neuronal loss. 	<ul style="list-style-type: none"> Atypical region specificity of β-amyloidosis. Increased premature death in some lines (including TgCRND8).
Second generation	Single App knock-in	NL-F NL-G-F	<ul style="list-style-type: none"> No overexpression of APP and by-products (except for CTFβ). Endogenous App promoter-driven gene expression. Amyloid plaques mainly consisted of pathogenic Ab1/3pE-42 similar to the brains of AD patients. 	<ul style="list-style-type: none"> Unknown interactions between multiple fAD APP mutations. No severe behavioral phenotypes. No NFTs or neuronal loss. Overproduction of CTFβ (total amount of CTF same as in wild-type mice + proven to exert no effects on the pathology or cognitive function of the mice).

Figure 1.4 Visual summary of the main features and disadvantages of some of the available AD mouse models.

A) Visual representation of the timescale of the appearance of key pathological hallmarks in some of the most commonly used mouse models of AD. Adapted from the Research Model Database of Alzforum (<https://www.alzforum.org/research-models/alzheimers-disease>). B) Summary table of the main features and disadvantages of first and second generation models. The most relevant positive or negative traits are highlighted in green or red respectively. Adapted from (254).

1.3. Abi3

Numerous cellular processes, including polarisation, adhesion and movement, require a fine control of the cortical actin cytoskeleton, which is localised immediately underneath the plasma membrane. This is especially true for immune cells, including macrophages and microglia, which rely on extremely rapid actin remodelling in order to exert their normal functions as scavengers, described in section 1.1.3. Indeed, actin disruption has been shown to reduce macrophages and microglial chemotaxis and phagocytosis (262–264) as well as microglial production of Nitric Oxide (NO) and pro-inflammatory cytokines, such as Tumour Necrosis Factor α (TNF α) and Interleukin 6 (IL-6) (264).

Members of the Ablason-interacting (Abi) protein family, which includes Abi3, play a crucial role in the tight regulation of actin dynamics through the WRC.

1.3.1. Role and regulation of the WRC

Members of the Rho family, in particular RhoA, Rac and Cdc42, regulate actin reorganisation following extracellular stimuli (265,266). These small GTPases control different aspects of actin dynamics, respectively guiding the formation of stress fibres, lamellipodia and filopodia (267). Therefore, a coordinated action is essential in order to allow cell movement.

The downstream effectors of this cascade are the members of the Wiskott-Aldrich syndrome protein (WASP) family. In particular, WASP-family verprolin homologous (WAVE) proteins are amongst the component of the pentameric WRC (268,269), which plays a crucial role in the activation of the Actin-Related Protein (Arp) 2/3 complex. This is, in turn, essential for the induction of *de novo* actin nucleation (270–273). While the cytoplasm is rich in actin monomers, which can combine

relatively easily with pre-existing actin filaments, initiation of the nucleation process requires the help of this catalytic complex in order to stabilise dimers and trimers (274). This process leads to new actin polymers branching out the pre-existing filaments (272,275,276), inducing membrane ruffling and lamellipodia formation (271,277).

Amongst the different WAVE proteins, WAVE2 is the one preferentially expressed by hematopoietic cells (269). Contrary to WAVE1, it is essential for lamellipodia formation in fibroblasts (278) and CSF-1-dependant membrane ruffling and consequent migration in macrophages (279). It is part of the WRC together with Specifically Rac-Associated (Sra) 1, NCK-Associated Protein (Nap) 1, Hematopoietic Stem Progenitor Cell 300 (HSPC3000) and Abi1 (280,281).

As the other members of the WASP family, WAVE2 presents a VCA region, formed by a Verprolin homology domain (V), a hydrophobic Central or Cofilin homology domain (C) and Acidic domain (A). This region is responsible for binding the Arp2/3 complex (282) and changing its tertiary and quaternary structure (283), thus allowing interaction with globular actin (G-actin) monomers and actin nucleation (284). The interaction of the VCA region with other WAVE2 residues and with Sra1 surface leads to the inhibition of the WRC (281).

When Rac-GTP binds Sra1 following growth factor or substrate stimulation, it causes a conformational change that leaves the VCA region free to interact with Arp2/3 complex and actin (281). Another level of control of the WRC is represented by its binding to negatively-charged phospholipids forming the cell membrane, in particular Phosphatidylinositol(3,4,5)-triphosphate. Indeed, this interaction allows the WRC to reach the cell periphery, where it then becomes able to interact with the actin-related proteins-2/3 (Arp2/3) complex (285). WAVE2 phosphorylation on different residues further increases the complexity of actin polymerisation regulation. In particular, the tyrosine-kinase c-Abl specifically targets WAVE2 Tyr150 (286,287), allowing the release of the VCA region (281). Finally, ERK (a mitogen-activated protein kinase functioning downstream Ras-GTPase) is responsible for the phosphorylation of different Serine and Threonine residues in the Polyproline-Rich Domain (PRD) of WAVE2 (288–290), increasing WRC interaction with Arp2/3 (288).

Abi1 is the most represented member of the Abi family in the WRC, and as such, the most studied. However, particular cell types – including macrophages (291) and microglia in the brain (292,293) – highly express Abi3 in a mutually exclusive way with Abi1 within the WRC (294). Abi3 forms a functionally different WRC than Abi1

(294), due to its inability to bind c-Abl and therefore enable Tyr150 phosphorylation on WAVE2 (Figure 1.5) (295). Thus, the presence of Abi3 in the WRC lead to a reduction in WAVE2 translocation to the cell edge and in lamellipodia formation (294,295).

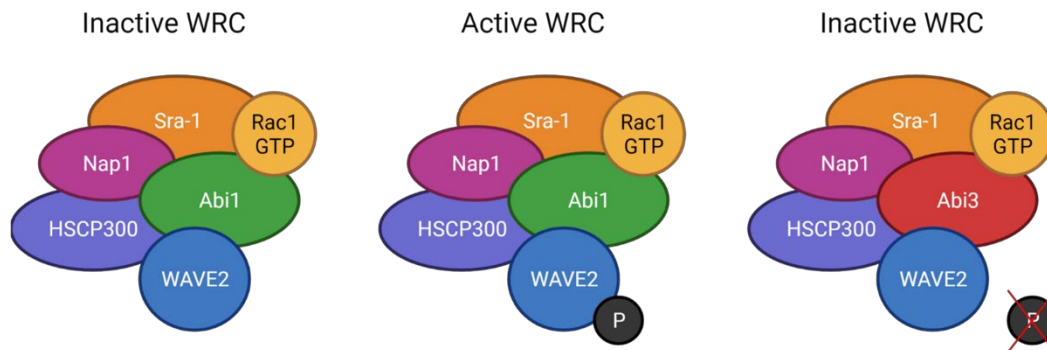


Figure 1.5 Schematic representation of the Wave Regulatory Complex (WRC).

The WRC is composed of 5 subunits: Rac1-GTP (yellow), Rac1-associated protein 1 (Sra-1, orange), Nck-associated protein 1 (Nap1, pink), Haematopoietic Stem/Progenitor Cell Protein 300 (HSCP300, purple) WAVE2 (blue) and Abi1 (green) or Abi3 (red). In the presence of Abi1, the WRC is activated by c-Abl-mediated phosphorylation (P, black) and is thus able to translocate to the cell surface and activate the downstream Arp2/3 complex. Instead, if Abi1 is replaced by Abi3, WAVE2 cannot be phosphorylated and is therefore unable to reach cell periphery (287,294). Adapted from (296).

1.3.2. Abi3 structure and functions

ABI3 gene, comprising 8 exons (Figure 1.6A), was firstly identified in 2000 by Miyazaki and colleagues, who identified an SH3 domain at the C-terminus (Figure 1.6B), as well as proline- and serine-rich regions, in the deduced amino acid sequence (297). ABI3 also presents an amino-terminal homeo-domain homologous region (HHR; Figure 1.6B), homologous to the HHR of other members of the Abi family (298). Of particular relevance is the SH3 domain, considered critical for ABI3 function due to its ability to bind to proline-rich sequences of other proteins (297), including p21-activated kinase (PAK) (299). Phosphorylation of human ABI3 on the S342 residue by PI3K/AKT has been suggested to negatively modulate ABI3 ability to bind the WRC (300).

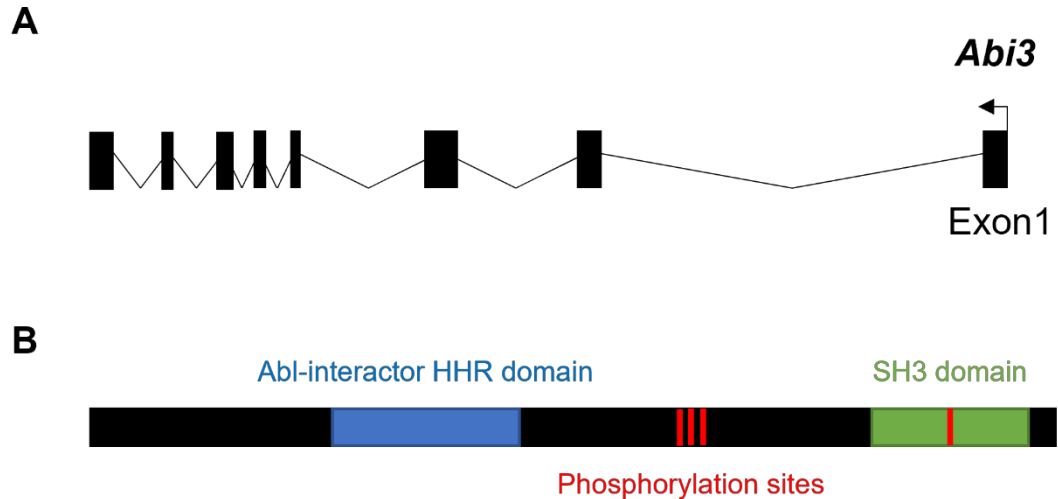


Figure 1.6 Graphical representation of mouse *Abi3* exon and protein structure.

A) *Abi3* is comprised of 8 exons, 6 of which are replaced with a *LacZ* reported in the *Abi3*-KO mice. B) *Abi3* protein structure (based on RefSeq ID NP_079935.1). Similar to other members of the *Abi* family, *Abi3* presents a HHR domain (blue) and Src Homology 3 (SH3) domain (green). Known phosphorylation sites at position 213, 216, 219 and 343 are marked in red.

The B6N(Cg)-*Abi3*^{tm1.1(KOMP)Vlcg}/J strain (hereafter referred to as “*Abi3*-KO”) was generated shortly before the commencing of this study by the Jackson Laboratory (301). The *Abi3*-KO model was created by replacing a 9515 base pair (bp) fragment of *Abi3*, corresponding to exons 2-7, with a *LacZ* reporter gene (Figure 1.7). Notably, these mice have been very recently reported to express extremely low levels of *Gngt2* as well, potentially due to its localisation next to *Abi3* on chromosome 17 (302,303). Mouse and human protein sequences show an elevated homology as seen by BLAST comparison (82 % of identity).

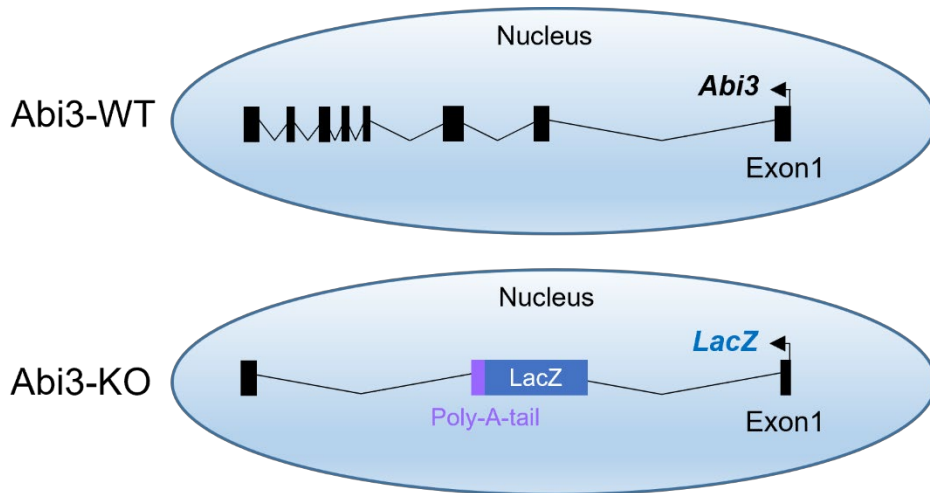


Figure 1.7 Abi3-KO model.

A fragment of *Abi3* comprising exons 2-7, as well as part of exon 1 (for a total of 9515 bp), was replaced with a *LacZ* sequence (blue) followed by a Poly-A-tail (purple). The sequence for the *Abi3*-KO mice is ENSMUST00000059026.

Very little is known about *Abi3*, in particular in the context of physiological levels of expression such as in macrophages. Ectopic expression of *ABI3* in cancer cells was shown to lead to a decrease in cellular motility and metastatic potential *in vivo* (304). Similarly, a study by Latini *et al.* demonstrated that re-expression of *ABI3*-binding protein (*ABI3*-BP) in malignant thyroid cancer cells was sufficient to inhibit invasion (305). The same authors later showed that a similar result could be obtained through forced overexpression of human *ABI3*, which caused arrest of the cell cycle in G0/G1 phase (306). This was ascribed to *ABI3*-dependant increase of p21^{WAF1} and parallel reduction of E2F1, which ultimately induced cell senescence (306).

In addition to various cancer models, *ABI3* has also been studied in cultured hippocampal neurons. Bae and colleagues described a direct interaction between *ABI3* and F-actin (307) and reported alterations of dendritic spines morphogenesis as well as synapse formation following either overexpression or knock-down of *ABI3* *in vitro* (308). However, *Abi3* expression in the brain has been shown to be largely restricted to microglia (Figure 1.8), to the point of now being accepted as a core human microglial gene (293). Notably, single-cell sequencing data shows that *Gngt2* is also expressed in the same cells in the mouse brain (Figure 1.8).

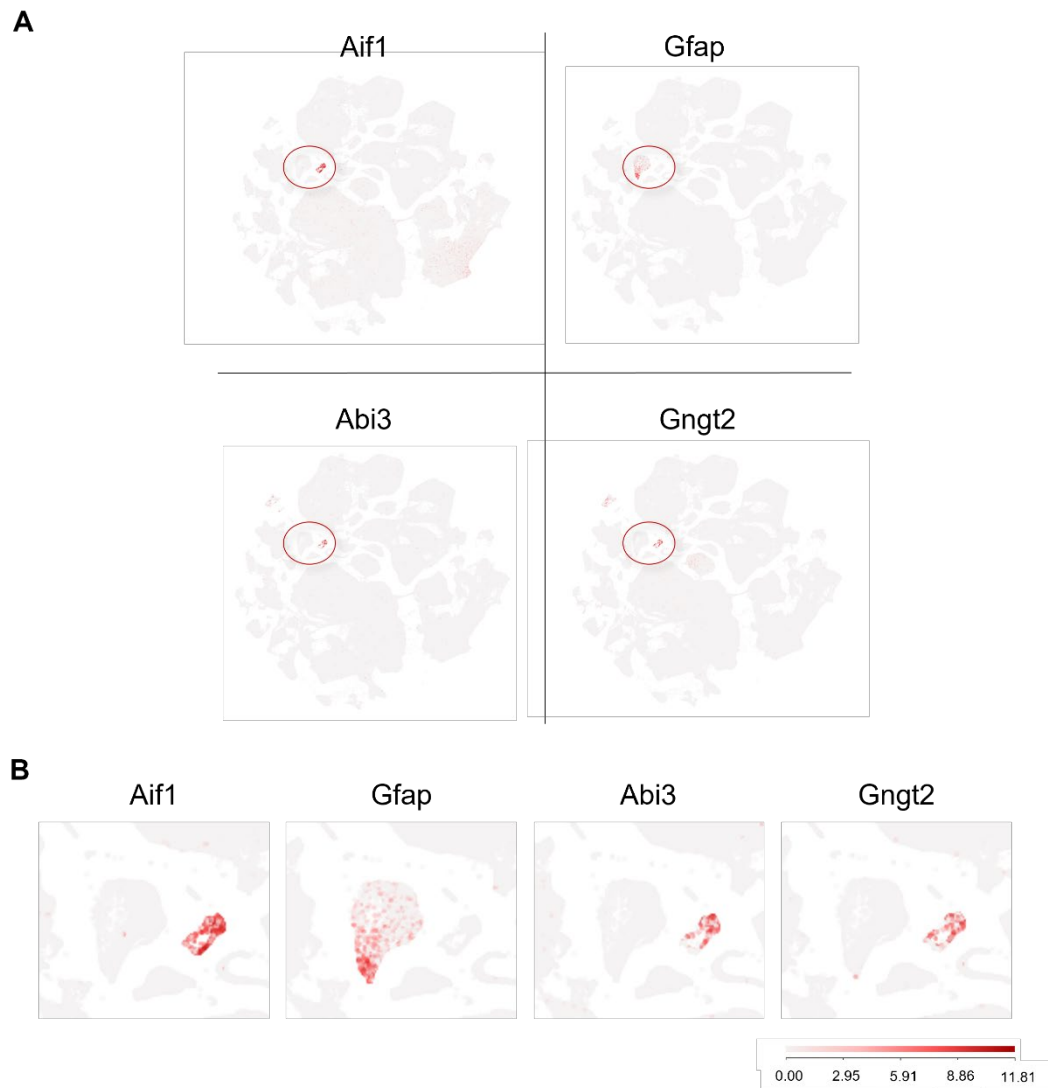


Figure 1.8 *Abi3* and *Gngt2* expression in mouse whole cortex and hippocampus, compared to *Aif1* (*Iba1*) and *Gfap* as shown by scRNAseq.

A) scRNAseq data obtained with 10x Genomics technology in the whole mouse cortex and hippocampus. For ease of visualisation, the region comprising microglia and astrocyte populations (in red circles) is presented enlarged in **B**). Both *Abi3* and *Gngt2* appeared to colocalise with the *Aif1/Iba1*+ cluster indicating microglia, while almost no expression was observed in GFAP+ astrocytes. The scale for all the plots in the bottom right corner indicates the Unique Molecular Identifier counts for *Abi3* per cell. Data and plots from the Allen Brain Map project (309).

While *Abi3* has not been studied during development yet, available transcriptomic datasets (115,310) on murine microglia have shown that it is expressed in the cortex

as early as at E17 and it is increasingly expressed with development (Figure 1.9 A). By the P60 stage, *Abi3* levels appear comparable to those of *Spi1*, which encodes an essential macrophage transcription factor (Figure 1.9B).

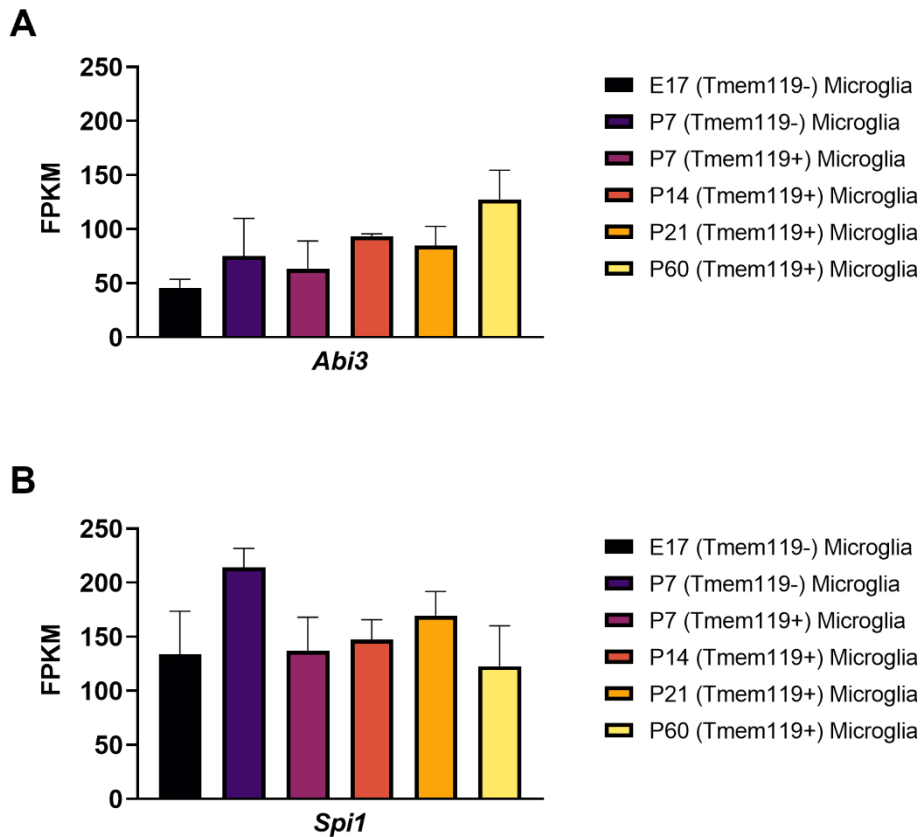


Figure 1.9 Time course of *Abi3* and *Spi1* expression in mouse microglia during development.

RNAseq data for A) *Abi3* and B) *Spi1* (encoding *PU.1*) expression in cortical microglia across different stages of development, from E17 to P60. *Abi3* appear expressed in mouse microglia from early development, although the highest levels are visible in adult cells, at comparable level to those of *Spi1*. Values reported as fragments per kilobase of transcript per million fragments mapped (FPKM). RNAseq data from the Ben Barres GLIA-seq database (115,310).

1.3.3. Proposed role in AD

ABI3 was firstly implicated in AD in 2017, when GWAS studies identified a non-conservative amino-acidic change – from Serine to Phenylalanine – in position 209 (S209F) associated with an increased LOAD risk (MAF=0.011 in cases, MAF=0.008

in healthy controls) (192). This rare variant, recorded as SNP rs616338, has recently been suggested to cause functional inactivation of ABI3 following phosphorylation on the S209 residue (303).

As discussed before, until recently very little was known about Abi3 role in microglia. Following the identification of the rare variant, Satoh and colleagues analysed Abi3 protein expression in a small cohort of post-mortem human brain samples, finding a non-significant difference between AD patients and controls, although the authors reported an increased expression in microglia clustered around amyloid plaques. This led them to speculate about a potential Abi3 role in microglia migration (311).

Two publications, both employing the same Abi3-KO model as this study, emerged during the final phases of this thesis completion, in November 2021 (302,303). While both works investigated the role of Abi3 in AD, the authors utilised two different AD models – 5XFAD and TgCRND8 mice respectively, both described in section 1.2.4 – and reported contrasting results following Abi3 deficiency.

Karahan and colleagues (302) revealed a significant increase in A β plaque load in the cortex of both male and female 8-month-old mice following homozygous deletion of Abi3. The authors also analysed soluble and insoluble A β 40 and A β 42 levels in both the cortex and the hippocampus of these mice, finding increased levels of both species in Abi3-deficient mice, coherently with histological observations. The same phenotype was observed in 4.5-month-old mice, despite no significant difference in the levels of APP (which was significantly higher in the aged cohort) or any other protein involved in A β processing, suggesting that the increase in A β deposition in the absence of Abi3 is not caused by excessive APP levels. No significant difference was observed between genotypes when assessing microgliosis, but the authors noted a reduction in plaque-associated microglia in Abi3-KO brains.

Gene-expression analyses on aged 5XFAD mice, based on predefined LOAD- and neuroinflammation-relevant panels, highlighted a significant upregulation of genes involved in complement system (such as C1qa, C4a, C3ar1) and immune response (including Cd74, Il-3, and Tlr7), as well as autophagy and lipid metabolism, in the absence of Abi3. Following GO analyses identified several enriched pathways involved in inflammatory response, but also in phagocytosis and downregulation of cell proliferation, as well as TGF- β signalling. Significant alterations were also detected in the secretion of multiple chemokines including CXCL10 and CCL3, which resulted upregulated in Abi3-KO 5XFAD mice. CXCL10 expression had been previously shown to be particularly elevated in astrocytes in AD (312,313). Instead CCL3 levels are significantly increased in plaque-associated microglia in the 5XFAD

model compared to healthy controls (314). Given its role as a ligand of CCR5, which has been implicated in the infiltration of peripheral immune cells in the brain during AD (315), it has been suggested that such increase could contribute to the recruitment of T cells, monocytes and microglia (316). The suggestion of a dysregulated inflammatory response in Abi3-KO mice was supported by a single-cell RNA-seq analysis, which found most of Abi3-deficient microglia constituted a cluster enriched in immune-response genes and highlighted an increase expression of DAM marker genes in Abi3-KO mice, potentially explained by the increased A β accumulation (302). Finally, when assessing synaptic function in 6-month-old animals, the authors observed a significant reduction in LTP in Abi3-KO 5XFAD mice. They were however unable to clarify whether this was directly correlated to Abi3 deficiency in neurons, or rather a secondary effect associated to increase neuroinflammation and amyloid deposition. Taken together, the data presented by Karahan and colleagues supported the hypothesis of an exacerbated pathological progression in the absence of Abi3 (302).

In stark contrast, Ibanez *et al.* (303) reported an amelioration of amyloid burden at both 3 and 6 month of age in Abi3-KO TgCRND8 mice. The authors also reported variable levels of micro- and astrogliosis in healthy Abi3-KO mice as well as in mice crossed with the AD model. They described an increase in astrogliosis already at 3 months in healthy Abi3-KO animals, still present in 6-month-old mice, while no obvious difference in microgliosis was noted between Abi3-WT and -KO mice. Interestingly, bulk RNAseq on forebrains of 3-month-old mice detected increased expression of DAM (317), MGnD (188) and PIG (252) signature genes, despite the absence of β -amyloidosis. Abi3-KO mice crossed with the TgCRND8 strain did not display major alterations in micro- or astrogliosis by histological analyses, however bulk RNAseq identified once again upregulation of DAM, MGnD and PIG, as well as A1 (126), signature genes, despite the reduced amyloidosis. Ibanez and colleagues also described alterations in synaptic markers, with increased levels of Synaptophysin and reduced vGlut, suggesting alterations in synapse plasticity. Finally, neonatal Abi3-WT and -KO mice were injected with control vector, wild-type human tau or P301L/S320F human tau, and examined at 3 and 6 months. Conversely to what they had observed in the TgCRND8 model, despite comparable tau expression Abi3-KO mice injected with the mutant tau presented a marked increase in p-tau and misfolded pre-tangle tau at 3 months and increased levels of p-tau (both WT and mutant) at 6 months. Changes in mutant tau levels were accompanied by increased GFAP immunoreactivity in Abi3-KO mice, while Iba1

levels were increased only at the 6-month time point. Overall, in contrast with (302), Ibanez and colleagues reported a dichotomy in response to A β and tau, with Abi3 ablation proving partially beneficial in the first model while leading to an aggravation of tau pathology (303).

A recent PhD thesis abstract from Cambridge University provided additional evidence in support of a beneficial effect of Abi3 ablation in AD (318). Karahan and colleagues employed a human microglia cell line (HMC3) to perform a scratch-wound assay, and reported a detrimental effect of Abi3 knock down on microglia migration in vitro (302). Conversely, Ghaffari described a significant increase in microglia migration following Abi3 knock-down in the BV2 cell line, as well as in Abi3-KO primary microglia (318). The abstract also reported a significant decrease in A β plaques size and number in the brain of Abi3-KO crossed with a TgCRND8 mouse model of AD. Interestingly, TgCRND8 mice showed a significant increase in Abi3 protein levels compared to the controls, especially in plaques-associated microglia (280). This results appear to collide with Karahan *et al.* observation of ABI3 mRNA expression in human cortex samples, as well as of ABI3 protein levels in para-hippocampal samples (from a proteomics dataset provided by Mount Sinai Brain Bank study (319)), which appeared to be increased simply due to the microgliosis observed in the LOAD group compared to controls (302). However, the full text of Ghaffari manuscript is currently under embargo, preventing further evaluation of these results.

While these recent works provided novel insights regarding the impact of Abi3 ablation, much is left to be clarified. For instance, the use of microglial cell lines poses several caveats to the interpretation of the published observations due to their notoriously problematic discrepancies in gene expression (114) and immune response (320) compared to primary cells. Therefore, additional *in vitro* functional assays are required to clarify the role of Abi3 on microglia and macrophages. Another essential aspect, yet to clarify, is the extent of morphological alterations likely caused by Abi3 ablation in microglia. This in turn may limit the validity of the gliosis evaluation performed by Ibanez and colleagues, since they did not evaluate cell count and simply relied on Iba1 immunoreactivity (303). Karahan *et al.*, instead, did not assess microglia distribution in the brain of young, healthy mice, but only focused on adult mice on the 5XFAD background by means of Western Blots (302). Moreover, both works employed different AD mouse models than the one in this manuscript which could explain the contrasting findings reported by the authors in regards to amyloid burden. As such, it is crucial to assess the effects of Abi3

ablation in additional models, such as the App^{NL-G-F} mice used in this thesis, in order to provide further insights on the matter. Finally, to date there is no available information regarding behavioural changes observed in Abi3-KO mice, either healthy or crossed with any AD mouse model. Given the impact of amyloidosis and neuroinflammation on cell death, and therefore on synaptic disruption and behavioural changes, amyloid burden assessment ought to be complemented by behavioural assessment of these mice, in order to fully understand the extent of the repercussions of Abi3 deletion on brain physiology.

1.4. Project aims and hypothesis

To date, limited studies have addressed the role of Abi3 in macrophages and microglia and little is known about the impact of its inhibitory effect of WRC-mediated actin regulation. Abi3 expression is mostly restricted to microglia within the brain (293). It has also been identified as a component of a 56-gene interaction network enriched in immune-response genes related to microglia functionality and AD risk, such as TREM2, SP1 and CSF-1R (192). Thus, given the imperative need for finely tuned actin dynamics for microglial functionality, it was hypothesized that the newly identified S209F rare coding variant in Abi3 would promote AD development through disruption of normal microglial function. As such, a combination of *in vitro* and *in vivo* approaches, based on an Abi3-KO model, were employed to clarify the role of Abi3 on macrophage and microglia phenotype and functionality, both in health and disease.

More specifically, the aims of this thesis were:

- **Chapter 3:**

To date, our knowledge of the impact of Abi3 on actin polymerisation is restricted by the use of non-physiologically relevant cellular models, such as tumour cell lines and NIH 3T3 fibroblasts (294,295,299,307,308,321). Recent work from Karahan *et al.* and Ibanez *et al.*, instead, provided contrasting results about functional alterations in microglial cells (302,303), which were only published in the final writing stages of this manuscript completion. As such, the overall aim of the first result chapter was to functionally investigate the role of Abi3 in the WRC by employing more physiological *in vitro* models.

Given the identification of the S209 variant of Abi3, a first aim was to replicate published results by Sekino *et al.* (294), which were only focused on the common F209-ABI3, including NIH 3T3 overexpressing the rare human variant in order to expand our understanding on the role of ABI3 on actin polymerisation. Oestrogen-regulated Hoxb8 conditionally-immortalised bone marrow precursors (MØPs) were also employed in order to overcome the limitations imposed on results interpretation by the use of a fibroblast cell line.

A second aim of this chapter was to clarify the role of Abi3 on key macrophage functions, such as phagocytosis and release of inflammatory mediators, which have been shown to be impacted by alterations in actin turnover (264,302,322,323). To do so, bone marrow derived macrophages (BMDMs), derived from Abi3-deficient and control mice, were employed in a series of assay aimed to measure particles uptake and inflammatory response to immunological stimuli, such as the release of ROS and NO.

- **Chapter 4:**

At the commencing of this thesis, the Abi3-KO mouse model employed in this study was still entirely uncharacterized and little was known about Abi3 role in microglia (311). Moreover, while MØPs and BMDMs derived from Abi3-deficient animals can be useful *in vitro* models, they cannot recapitulate the complexity of the interactions between microglia and the brain microenvironment.

For this reason the first aim of this chapter was to evaluate microglia morphology and distribution in young healthy Abi3-KO by means of histological analyses of brain sections.

While immunofluorescence images can provide useful indications of Abi3 ablation impact on microglia, they cannot account for the extremely dynamic nature of these cells. Given the putative inhibitory role of Abi3 on filopodia formation, a second aim of this chapter was to assess microglial process motility in Abi3-deficient mice by means of *in vivo* two-photon imaging.

Motile ramifications are also essential for microglia phagocytic activity and interact with surrounding cells. Moreover, alterations in actin cytoskeleton had been previously reported to affect microglial activation status (264), which could in turn affect other glial cells. As such, a third aim was to evaluate the phagocytic activity of Abi3-KO microglial by immunostaining of brain sections, as well as to assess the impact of Abi3 ablation on astrocytes in young, healthy mice.

- **Chapter 5:**

While microglial contribution to disease progression in AD is extremely complex and not fully clarified yet, as discussed in details in section 1.2.3, it is now established that these cells are deeply involved in Alzheimer's pathogenesis. Published works on TREM2 highlighted the importance of a correct translocation of microglia towards amyloid plaques and their ability to clear amyloid deposits (324–326). Recognition of A β , however, triggers a cascade of pro-inflammatory events that ultimately leads to severe neuroinflammation (374).

Upon discovery of the rare S209F ABI3 variant, it was hypothesized that the risk variant could affect microglial functionality, leading to a dysfunctional response to A β and therefore to an increase in brain inflammation. Thus, a first aim of this chapter was to evaluate microgliosis and astrogliosis in adult mice crossed with a mouse model of AD by means of histological techniques.

Given the necessity of a concerted action between microglia and astrocytes in response to amyloid deposition, a second aim was to assess whether any observed change in gliosis and in microglial morphology and functionality (investigated in the previous chapter) affected amyloid deposition. Moreover, microglia ability to migrate towards A β plaques was assessed by means of immunostainings due to the potential impact of Abi3 ablation on microglial motility.

Finally, Abi3-KO mice with and without amyloid pathology were aged and tested with various behavioural paradigms in order to establish whether any alteration in gliosis and plaque burden observed via histological analyses led to parallel changes in anxiety, motility, memory and depression, based on alterations in these behaviours observed in AD patients (328).

Chapter 2 – Materials and methods

2.1. Buffers and solutions

Buffer/Solution name	Ingredients
Mammalian Cell Lysis Buffer	100 mM Tris pH 8.5
	5 mM EDTA
	200mM NaCl
	0.2% (v/v) Sodium Dodecyl Sulfate
Tris-Acetate-EDTA (TAE) Buffer	50X TAE stock solution
	Distilled water
MUSE Staining Solution	625 ng/ml Propidium Iodide (PI)
	500 ng/ml LDS 751
	1X DPBS
Freezing Media	10 % (v/v) Dimethyl Sulfoxide (DMSO)
	90 % (v/v) Heat-Inactivated filtered FBS
4 % Paraformaldehyde (PFA)	4 % (w/v) Paraformaldehyde powder
	1X PBS
10X TBS (pH 7.6)	200 mM Tris base
	1.5 M NaCl
	Sufficient HCl to get pH 7.6
	Distilled water
	0.5 % (v/v) Triton-X 100

Immunofluorescence permeabilization and blocking buffer	1 % (w/v) BSA
	0.3 M Glycine
	1x TBS
Immunofluorescence staining buffer	0.5 % (v/v) Triton-X 100
	1 % (w/v) BSA
	1x TBS
Thioflavin S solution	0.02% (w/v) Thioflavin S
	70% (v/v) Ethanol
	Distilled water
Brain storage solution	0.1 % (w/v) Sodium Azide
	1x DPBS

Table 2.1 List of Buffers and Solutions used in the thesis.

All reagents were provided by ThermoFisher Scientific or Sigma-Aldrich.

2.2. Animals

All animal work in this thesis was conducted in accordance with UK Home Office Guidelines and Animal [Scientific Procedures] Act 1986 which encompasses EU Directive 2010/63/EU on the protection of animals used for scientific purposes. Animal work was undertaken by trained staff under a Home Office approved establishment licence, project licences (P7B7153B9, PP9138610, 3003313 and P92CA01DA) and individual's personal licences at Cardiff University's Biological Services (BIOSERV) Unit, in a specific pathogen free (SPF) unit which undergoes quarterly bespoke health screens.

Animals were housed in conventional open top ventilated cages in racks with shaded tops, or alternatively in scintainers, under controlled conditions (humid

20-24 °C environment, 12-hour light/dark cycle, food and water ad libitum). Cages exceeded the minimum space allocations specified in Annex III of Directive 2010/63/EU and Appendix A to the Council of Europe Convention ETS 123. A maximum of 5 mice under 30g in weight were housed in each cage. Whenever possible, mice were co-housed with appropriate sex- and age-matched controls animals from weaning.

The solid floor polycarbonate cages were provided with an appropriate depth of Eco 6 premium dust-free softwood bedding substrate (Datesand). Environmental enrichment provided consisted in Bed-r'Nest nesting material (made of compacted dust-free virgin kraft paper; Datesand) or nestlets (made of dust-free and pulped virgin cotton fibre; Datesand), along with 50 mm Ø polycarbonate (Datesand) or recycled fibreboard tunnels (International Produc Supplies Limited). Animals were also provided with 30 mm Ø aspen balls or 5 x 1 x 1 cm aspen chew blocks (Datesand) for added cage complexity and as gnawing material. In addition, sunflower seeds were provided for variation and foraging when animals were not undergoing procedure.

Cage cleaning procedures took place regularly, providing fresh bedding substrate, chow and water; scent-marked nesting material was refreshed only when required and more often transferred between cages to reduce stress. Welfare-related assessments and interventions, if required, were performed by the Named Animal Care and Welfare Officers (NACWOs) and the Named Veterinary Surgeon (NVS).

For bone marrow harvest, animals were culled according to approved Schedule 1 methods by asphyxiation due to exposure to increasing CO₂ concentration, followed by confirmation of death by dislocation of neck. For histological analyses, mice were culled with intraperitoneal overdose of Euthatal® (Merial Animal Health Ltd) followed by intracardial perfusion-fixation after confirmation of permanent cessation of the circulation. Details of the age, gender and number of mice used in each experiment can be found in the figure legends.

Table 2.2 lists all the transgenic mice lines used in this thesis.

B6N(Cg)-Abi3tm1.1(KOMP)Vl1cg/J and B6.129P2(Cg)-Cx3cr1tm1Litt/J mice were originally purchased from The Jackson Laboratory. Instead, APPNL-G-F mice were kindly provided by the RIKEN Center for Brain Science (Japan). All lines were bred inhouse.

Official strain name	Thesis abbreviation
B6N(Cg)-Abi3 ^{tm1.1(KOMP)Vlcg/J}	Abi3-KO
APP ^{NL-G-F}	App-KI
B6.129P2(Cg)-Cx3cr1 ^{tm1Litt/J}	Cx3cr1-GFP

Table 2.2 Official and abbreviated names of the transgenic mice strains used in this thesis.

2.2.1. Genotyping

BIOSERV staff provided ear-punch biopsies from which genomic DNA (gDNA) was isolated for animal identification. Biopsies were digested in 1.5 ml microcentrifuge tubes (Starlab) for 1 hour at 52 °C in 50 µl of mammalian lysis buffer and 100 µg/ml of proteinase K (from *Tritirachium album*; Sigma-Aldrich). Proteinase K was inactivated at 72 °C for 30 minutes. During the whole digestion step, samples were continuously shaken at 800 rpm in a Thermoshaker (Grant-bio). After cooling the tubes to room temperature, 400 µl of nuclease free water (ThermoFisher Scientific) was added to each sample prior to vortexing. Genotyping was performed by PCR using GoTaq® Green Mastermix (Promega) as per manufacturer's instructions. Briefly, each reaction was conducted in a 0.2 ml PCR tube or 0.2 ml PCR 96-well plate (Starlab) with the addition of 0.5 µl of gDNA. For each sample, 12 µl of reaction mix (comprised of 6.25 µl of 2X GoTaq® Green Master Mix, 0.0625 µl of 100uM of each primer and enough nuclease-free water to reach the desired volume) were added to each well. Specific DNA primer sequences for targets of interest listed in Table 2.3, provided by The Jackson Laboratory and the RIKEN Center, were purchased through Sigma-Aldrich.

Mouse		Forward Primer (5' to 3')	Reverse Primer (5' to 3')	Product Size (bp)
Abi3 KO	WT	ACCCAGATCCCTGAGAATTTG	CAAGTCCTGAAGGGAGAACG	334
	KO	CGGTCGCTACCATTACCAGT	CAGCCCAAGAGGTAGACAGG	473
Cx3cr1-GFP	WT	GTC TTC ACG TTC GGT CTG GT	CCC AGA CAC TCG TTG TCC TT	410
	KI	CTC CCC CTG AAC CTG AAA C		500
App-KI	WT	ATCTCGGAAGTGAAGATG	TGTAGATGAGAACTTAAC	700
	KI	ATCTCGGAAGTGAATCTA	CGTATAATGTATGCTATACGAAG	400

Table 2.3 PCR primers used for genotyping of transgenic mice strains used in this thesis and corresponding expected product size in base-pair (bp).

The plate was then sealed using appropriate PCR seals (STARLAB) and placed in a Mastercycler® Nexus Gradient (Eppendorf) PCR machine. The final products of the PCR reaction were electrophoresed on a 2 % (w/v) agarose (ThermoFisher Scientific) gel in 1X Tris-Acetate-EDTA (TAE) buffer (ThermoFisher Scientific). SYBR™ Safe (ThermoFisher Scientific) was added at 1:20,000 dilution to the dissolved agarose solution to allow DNA visualisation. Once the agarose gel was hardened inside an appropriately sized Fisherbrand™ gel mould, samples were loaded alongside 100 base pair (bp) DNA ladder (Promega) in individual wells (formed with the addition of a comb (Fisher Scientific) to the mould while the agarose solution was still warm) and run using the Biorad PowerPac™ HC High-Current Power Supply at 100 V for ~25 minutes. The gels were then transferred to a G:BOX Chemi XX6 gel doc system (SynGene) where they were imaged.

In the case of gDNA isolated from MØP cells by Dr R. Jones, 2 x 10⁶ undifferentiated or differentiate cells were lysated in accordance with the instructions of the GenElute™ Mammalian Genomic DNA Miniprep Kit (Sigma). For full details, please refer to (329).

2.2.1.1. Abi3-KO mice

Male and female transgenic Abi3-KO mice purchased from The Jackson Laboratory as heterozygous were inter-crossed to generate lines of Abi3-WT and -KO mice derived on a C57BL/6NJ background. To generate Abi3-KO mice, a 9515 base pair

(bp) fragment comprising exons 2-7 of *Abi3* was replaced by a LacZ reporter gene encoding β -Galactosidase, followed by a poly-A-tail to terminate transcription.

Separate PCR reactions were prepared for *Abi3*-WT and -KO primers and were amplified using the touchdown PCR protocol described by Figure 2.1.

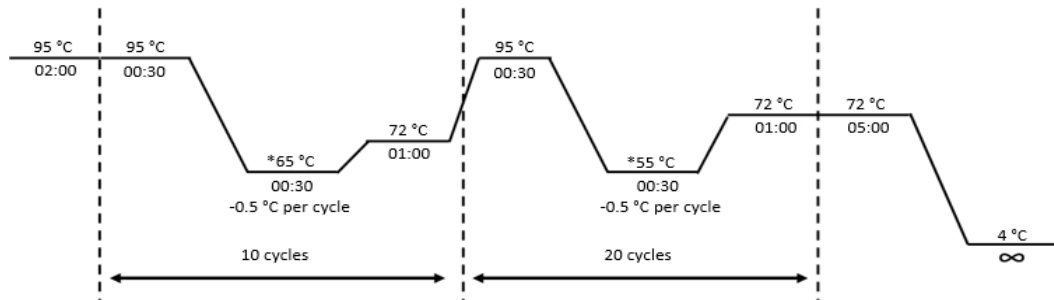


Figure 2.1 Touchdown PCR program used for *Abi3*-KO genotyping, based on standard Jackson Laboratory protocol.

2.2.1.2. *App*-KI mice

Male and female *App*-KI mice obtained from the RIKEN Centre were crossed to *Abi*-KO animals, in order to obtain double-homozygous *App*-KI *Abi3*-KO mice, whilst an independent homozygous *App*-KI line was maintained to be used as control. To generate *App*-KI mice, Swedish, Beyreuther/Iberian and Arctic mutations were introduced into exon 16 (in the case of the first mutation) and exon 17 (for the other two) of the humanized A β sequence, together with a pgk-neo gene cassette with a lox/FRT sequence (placed in intron 16) for positive selection (260).

PCR reactions for *App*-WT and -KI primers were performed independently and were amplified using the PCR protocol described by Figure 2.2.

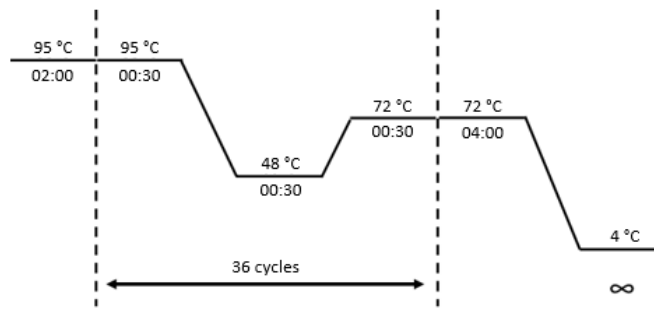


Figure 2.2 PCR program used for App-KI genotyping, based on the protocol provided by the RIKEN Center.

2.2.1.3. Cx3cr1-GFP mice

For two-photon experiments, Abi3-WT and -KO mice were crossed to the Cx3cr1-GFP reporter mice strain. This particular strain expresses eGFP under the Cx3cr1 promoter, so that the fluorescent signal in the brain is limited to microglia cells. Specifically, the first 390 bp of the only coding exon (exon 2) of Cx3cr1 were replaced by a sequence encoding green fluorescent protein (GFP), which prevented Cx3cr1 expression (330). Only mice that were heterozygous for Cx3cr1-GFP were used, in order to ensure continuous Cx3cr1 expression on microglia due to its crucial role in microglia morphology and function (331). Genotyping was performed on using a standard touchdown PCR protocol as shown in Figure 2.3 in separate reactions for Cx3cr1-WT and -KI primer pairs.

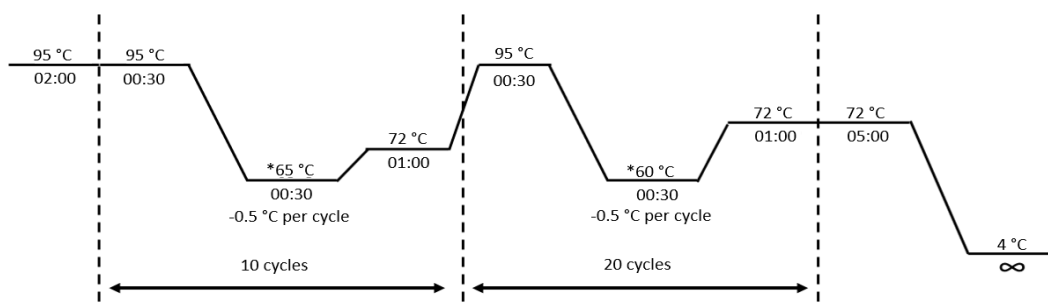


Figure 2.3 Touchdown PCR program used for Cx3cr1-GFP genotyping, based on standard Jackson Laboratory protocol.

2.3. Cell culture

2.3.1. NIH 3T3 cell lines

The NIH 3T3 cell line was originally derived from a NIH Swiss mouse embryo fibroblasts (332). Cells were cultured in standard DMEM and were passaged every 3-4 days at a 1:10 dilution. In order to detach the cell monolayer, media was aspirated and cells were gently washed with Dulbecco's Phosphate Buffered Saline (DPBS). The monolayer was then covered with 0.05 % Trypsin-EDTA (Thermofisher Scientific) and incubated at 37 °C for 5 minutes. Two volumes of DMEM were added to neutralise the Trypsin-EDTA and the cell suspension was then transferred to a 50 ml falcon tube, centrifuged at 350 x g for 5 min and, after removing the supernatant, the pellet was resuspended in fresh DMEM and plated in a new flask.

2.3.2. Macrophage Precursor (MØP) cell lines

CD117⁺ enriched bone-marrow cells, harvested from individual 8-week-old animals following CO₂ asphyxiation, were conditionally-immortalised using a retroviral vector containing an oestrogen-regulated Hoxb8 gene as previously described (333) in order to obtain Macrophage Precursor (MØP) cell lines. During the course of this thesis, Dr R. Jones generated six MØP lines using sex- and age-matching pairs of Abi3-WT and -KO animals (an initial pair derived from 8-week-old females was followed by 2 additional pairs, one for each sex).

MØP cells were cultured in standard RPMI media supplemented with 1 µM oestrogen (10 mM β-estradiol (w/v) in absolute ethanol; Sigma) and 10 ng/ml recombinant murine Granulocyte-Macrophage Colony Stimulating Factor (GM-CSF; Peprotech). Cells were passaged every 2-3 days at a 1:20 dilution.

Three or four days before an experiment, cells were depleted of oestrogen by three consecutive washes with 10 ml of standard RPMI media. Cells were centrifuged at 350 x g for 5 minutes in between washes. After the final wash, the cell pellet was resuspended in RPMI media supplemented with 20 ng/ml Macrophage Colony Stimulating Factor (M-CSF; Peprotech). Cells were counted as described above and seeded in multi-well plates as required. The differentiation media was replenished on day 2. On day 3 or 4, differentiated cells were harvested using Accumax™

(Sigma-Aldrich). The media was discarded, and cells were gently washed with DPBS before sufficient Accumax™ was added to ensure the bottom of the well was fully covered. Cells were incubated at 37 °C for 20 min and then lifted with a cell scraper. Cell suspension was then transferred to a falcon tube, centrifuged at 350 x g for 5 minutes and resuspend in medium according to the requirement of the downstream assay.

2.3.3. Bone-Marrow Derived MØs (BMDMs)

Femur and tibia bones were harvested from individual 6-week-old male App-KI and App-KI Abi3-KO mice following CO₂ asphyxiation and placed into 15 ml falcon tube filled with ice-cold DPBS. After removing the epiphyses of each bone, a 27-gauge needle on a 10 ml syringe containing standard RPMI media was used to flush the bone marrow out of the medullary cavity into a 70 µM strainer placed on a 50 ml falcon tube. Cells were pushed through the strainer using a 5 ml syringe plunger and centrifuged at 350 x g for 5 minutes and resuspended in freezing media in order to cryopreserve them as described in Section 2.3.6.

Upon thawing, bone-marrow cells were resuspended in 10 ml of high-glucose DMEM with GlutaMAX™ (Gibco®, ThermoFisher Scientific), supplemented with 10 % (v/v) heat-inactivated FBS, 100 U/ml Penicillin, 10 µg/ml Streptomycin (henceforth referred to as “standard BMDM media”). Cells were then counted as described in details in Section 2.3.5, seeded at 1x10⁷ per plate in 25 ml of BMDM media supplemented with 20 ng/ml of M-CSF and incubated for 7 days at 37 °C. Differentiation media was refreshed every 2 days before being harvested with 8 mg/ml Lidocaine, 5mM EDTA in DPBS (sterile filtered). The media was discarded, cells were washed once with DPBS, covered with Lidocaine-EDTA and incubated 3-4 minutes at 37 °C. Following the addition two volumes of BMDMs media (to inactivate the Lidocaine-EDTA), cells were moved into a 50 ml falcon tube and centrifuged at 350 x g for 5 minutes.

2.3.4. Incubation and media preparation

All cells used in this thesis were maintained in a humid incubator at 37 °C with 95 % air, 5 % CO₂. Unless stated otherwise, Dulbecco's Modified Eagle Medium (DMEM; Gibco®, ThermoFisher Scientific) and Roswell Park Memorial Institute 1640 (RPMI;

Gibco®, ThermoFisher Scientific) were supplemented NIH 3T3 cells were maintained in T175 cm² flasks with filter caps (Greiner Bio One); undifferentiated MØPs were cultured in multi-well plates, T75 cm² or in T175 cm² flasks with filter caps according to the need (Greiner Bio One) with 10 % (v/v) heat-inactivated Foetal Bovine Serum (FBS, Gibco®, South America) and 100 U/ml Penicillin, 10 µg/ml Streptomycin (Gibco®, ThermoFisher Scientific); finally, BMDMs were plated in 145 mm x 20 mm (diameter x height) culture dish (Greiner Bio One).

2.3.5. Cell counting

Cells were counted utilising a Muse® Cell Analyzer (Luminex), which also allowed viability assessment due to the presence of LDS 751 (a cell-permeant nucleic acid dye that enables the count of nucleated cells) and propidium iodide (a membrane impermeant nucleic acid dye which allows exclusion of non-viable cells). Cells were diluted 1:20 in Muse staining solution, incubated at room temperature for 5 min and run on the Muse® Cell Analyzer as per manufacturer's instructions.

2.3.6. Cryopreservation and thawing

Before freezing, cells were counted as described above and centrifuged at 350 x *g* for 5 min. The supernatant was discarded and the cell pellet was then resuspended in freezing media at a concentration of ~3 x 10⁶ cells in 1 ml. 1 ml aliquots of the cell suspension were then frozen down overnight in a Mr. Frosty™ (ThermoFisher Scientific), or alternatively in a CoolCell® LX (Biocision), at -80 °C in a New Brunswick ULT freezer. Cells were then moved into liquid nitrogen for long term storage.

In order to defrost cells, aliquots were thawed into a water bath at 37 °C until visible disappearance of the ice crystals. Cells were then quickly added to 10 ml of the required media and centrifuged at 350 x *g* for 5 minutes. Finally, after discarding the supernatant, the pellet was resuspended in the appropriate culture media below.

2.3.7. Human ABI3 overexpression

Before the commencing of this thesis, Dr D. Fathalla generated lentiviral vectors containing either of the two variants of human ABI3, which Dr R. Jones then employed to generate hABI3 overexpressing NIH 3T3 and MØP cell lines.

A SFEW cloning vector, previously established in the lab and derived from the SFRW plasmid (7), was utilised for the overexpression of the sequences of interest. The SFEW vector contains the coding sequence for ampicillin resistance, Simian Virus 40 (SV40) promoter and an enhanced green fluorescent protein (eGFP) reporter (335). The eGFP reporter was placed under the control of the spleen focus forming virus (SFFV) promoter (336) and the woodchuck hepatitis virus posttranscriptional regulatory element (WPRE). The use of a T2A peptide sequence (337) allowed the generation of multiple separate proteins from a single mRNA sequence (under the control of a single promoter). Gene insertion was enabled by the presence of the *XhoI* restriction enzyme cut site, positioned between the SFFV promoter and T2A peptide sequence.

A second-generation HIV-1 vector system was employed for the creation of the ABI3-overexpressing lines, to ensure increased safety of lentivirus production (338). Specifically, the genes necessary for an efficient generation of the viral particles were expressed in two separate packaging constructs: the pCMV-Δ8.91 plasmid (comprising viral capsid components of group antigens, *gag*; reverse transcriptase-polymerase, *pol*; trans-activator of transcription, *tat*; and regulator of expression of virion particles, *rev*) and the pMD2.G plasmid (encoding the vesicular stomatitis virus G envelope), both under a cytomegalovirus (CMV) enhancer and promoter (339).

Lentiviral production and cell transduction were then performed following established protocols (329). Briefly, custom primers were used to amplify the desired hABI3 sequence (NM_016428, purchased from Origene; Cytosine residue in position 1124 was replaced by a Thymine in the case of the rare variant) by PCR and the resulting products were purified after gel-electrophoresis. The *XhoI* restriction enzyme was used to linearise the plasmid, prior to combining it to an hABI3 insert to generate the final overexpression plasmids per the Clontech In-Fusion (Takara) manual. Clones positive for the insert, as confirmed by a PCR band of the predicted size, were selected and grown for 24 hours before purifying the plasmid using PureLink® Quick Plasmid Miniprep Kit according to manufacturer's instructions (Invitrogen) and sending samples to Eurofins Genomics

(Wolverhampton, UK) for Sanger sequencing. Primers specific to the vector located on either side of the insert site were used for sequencing and the resulting sequences were checked against the predicted template for confirmation.

HEK 293T cells were then transfected with the two lentiviral packaging plasmids and the desired SFEW plasmid (340) using Effectene[®] transfection reagent (Qiagen), a cationic non-liposomal lipid reagent that allowed transfer of DNA into the cells (341). After 48 hours, the virus was harvested by centrifugation on 20 % (w/v) sucrose gradient and titrated using human Jurkat leukemic T-cell line (342) to determine the best viral concentration for downstream applications. An optional 72-hour titre was used, after adding fresh media to the cells at 48 hours. For the complete protocol, please refer to Dr R. Jones thesis (329) and to detailed lentivirus production described in (343).

2.4. Functional cell assays

2.4.1. Spreading assay

Sterile 13 mm coverslips were coated with 50 µg/ml fibronectin (Sigma) in Hank's Balanced Salt Solution (HBSS; Gibco®, ThermoFisher) for a minimum of 40 minutes at room temperature. Triplicate coverslips were prepared for each experimental group. NIH 3T3 fibroblasts or M-CSF differentiated MØPs-derived macrophages were detached from the bottom of the flask/plate (as described in sections 2.3.4 and 2.3.5), counted (see section 2.3.2) and plated onto 24-well plates containing the FN-coated coverslips and 500 µl per well of complete DMEM or RPMI media (supplemented with 20 ng/ml M-CSF) respectively. In the case of the long-term spreading assay on MØs, M-CSF was replenished every 48 hours to maintain cell viability. Four time points after replating were chosen for the analysis: two short ones (15 and 30 minutes) and two longer ones (2h and 4h). The first two allowed evaluation of the impact of ABI3 alteration immediately after substrate stimulation, while the longer incubations were crucial to assess the ability of the cells to assume their physiological elongated morphology. For the two short timepoints, 15 and 30 minutes, 104 cells were plated in each well while for the longer incubations (2 and 4 hours) 5x10³ cells were used to prevent overcrowding.

At each time point the media was discarded and cells were washed once with DPBS, before being fixed with 4 % PFA for 10 minutes at room temperature. Cells were then washed with DPBS, permeabilised for 3 minutes at room temperature with 0.1 % Triton-X-100 (Sigma) in DPBS, washed again as before and blocked with 1 % Bovine Serum Albumin (BSA; Sigma) in DPBS for 20 minutes at room temperature. F-actin was stained for 20 minutes at room temperature with fluorescent Phalloidin (Invitrogen, ThermoFisher Scientific) conjugated to Alexa Fluor (AF) -555 or -647 at a 1:40 dilution in 1% BSA in DPBS. Finally, cells were washed, incubated 5 minutes with at room temperature with 500 ng/ml 4',6-Diamidino-2-Phenylindole Dilactate (DAPI; ThermoFisher Scientific) in DPBS and mounted in ProLong® Gold Antifade Mountant (ThermoFisher Scientific) on Superfrost Plus Microscope Slides (ThermoFisher Scientific).

Coverslips were imaged using a Zeiss Apotome Axio Observer microscope (Zeiss) or an EVOS™ FL Auto 2 Imaging System (ThermoFisher Scientific) microscope with a 20x objective. Slides were independently blinded and 15-30 random fields were analysed for each experimental group (10 for each coverslip) using Fiji software (Fiji is just ImageJ, version 1.52p(344)) as shown in Figure 2.4. After a first step of brightness and contrast optimisation, manual separation of cells in close contact was performed using a 2 µm-thick black line. After carefully adjusting the threshold and generating a binary file, the “Fill holes” tool automatically filled any gap within the particles, which were then analysed using the “Analyse Particles” function.

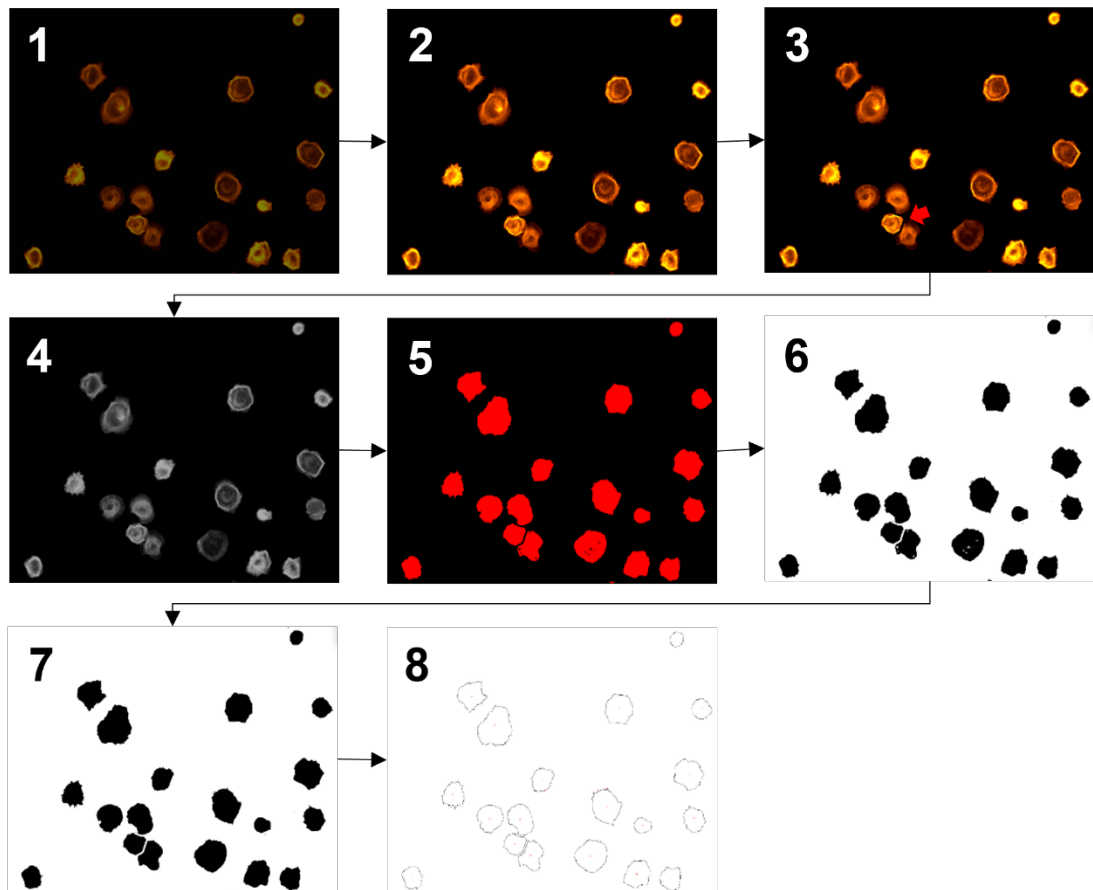


Figure 2.4 Schematic representation of the spreading assay analysis performed using Fiji software.

The same workflow, here shown on NIH 3T3 fibroblasts, was applied to MØPs-derived macrophages. **1)** The original TIFF images of the Phalloidin staining (orange) were imported into Fiji. **2)** Images were then processed by adjusting brightness and contrast **3)** in order to facilitate the following manual separation of adjacent cells with a 2 µm-thick black line (red arrow). **4)** Following conversion to the 8-bit format, **5)** a threshold was manually adjusted taking care to exclude the background and include all the cellular processes. **6)** This led to binary images, to which **7)** the “Fill holes” function was applied in order to fill up any artificial gap inside the particles. A minimum area of 20 µm² was chosen to avoid including debris and any particle present on the borders was excluded from the following analysis. In experiments including DAPI staining, bigger debris were manually removed based on visual comparison to the relative DAPI/Phalloidin co-stained image, to increase accuracy. **8)** The “Analyse particles” tool finally provided an outline image of each picture and the values of cell area and circularity/solidity used for the subsequent statistical analysis.

Cell area was evaluated for both cell lines. In the case of NIH 3T3 cells, which should physiologically assume an elongated morphology, the second parameter assessed was cell circularity (the circularity value of a true circle is 1), calculated

using the following formula: $4\pi \times \frac{[Area]}{[Perimeter]^2}$ (345). Instead, due to the ramified nature of macrophages, in the case of MØPs-derived macrophages cell circularity was replaced by cell solidity (described by the equation: $[Area]/[Convex Area]$). The area or circularity/solidity values obtained from all the images obtained by the 3 coverslip of any given sample were then pooled to perform the final statistical analysis.

The experiment was repeated three times on the same set of NIH 3T3 cell lines, but only once in the case of ABI3-overexpressing MØPs-derived macrophages. Instead, in the case of Abi3-WT and -KO MØP cells, the experiment was repeated twice on the original pair of cell lines, and one more time on the two additional pairs generated in a later occasion, in order to exclude cell line-specific artefacts. Spreading assay data on over-expressing cells (sections 3.2.1 and 3.2.2.) were analysed via Kruskal-Wallis test to compare the medians, and wherever a significant difference was found, the individual p-values were calculated using Dunn's multiple comparison test. Instead, the results of the spreading assays performed on Abi3-WT and -KO MØPs (section 3.2.2) were analysed via Mann-Whitney test. In both instances, the choice of the test was dictated by the elevated number of cells analysed and the non-normal distribution of the data, as well as by the number of samples being compared. All of the above experiments were analysed in blinded conditions to avoid operator bias.

In the case of ABI3-overexpressing cells, aliquots of each NIH 3T3 or MØP-derived macrophage cell line were centrifuged at 350 x g for 5 min, fixed with 1 ml 4 % (w/v) PFA for 10 min, washed twice with DPBS and stored in DPBS at 4 °C, shielded from light. GFP reporter levels were then assessed on an Attune NxT flow cytometer (Thermo Fisher Scientific). Photo multiplier tube (PMT) voltage settings were kept constant between experiments.

2.4.2. Phagocytosis assay

Before the beginning of the assay, 1 vial of pHrodo™ Red Zymosan (ThermoFisher Scientific) was resuspended in 8 ml of Live Cell Imaging (LCI) solution (ThermoFisher Scientific) and sonicated using the ice bath attachment of a Vibra-Cell™ sonicator (Soncis). The Zymosan suspension underwent 15 30-second-long cycles of sonication at 50% amplitude, followed by 10 cycles of 30 seconds at 60% amplitude, to ensure full dissociation of the clumps.

The day before the assay, BMDMs were detached from the culturing dish as described in section 2.3.6, counted and re-seeded at 3×10^4 in a flat bottom 96-well-plate (Greiner Bio One). Each sample was plated in 9 wells (3x non-treated control, 3x Zymosan + DMSO, 3x Zymosan + Cytochalasin D); spare cells of either genotype were plated in additional wells and later used as unstained or single colour controls. Cells were plated in 200 μ l of standard BMDMs media (see 2.3.6) supplemented with 10 ng/ml M-CSF and incubated overnight to ensure adhesion.

On the day of the assay, media was replaced with 100 μ l/well of standard BMDM media supplemented with 10 ng/ml M-CSF and either 5 μ M Cytochalasin D (CytoD, 1:2000 dilution from a 25 mg/ml stock in DMSO; Sigma-Aldrich) for the negative control wells, or DMSO in a 1:2000 dilution for all the remaining wells. Cells were incubated for 45 min at 37 °C, and the media was then replaced with 100 μ l/well of LCI solution supplemented with 10 ng/ml M-CSF and 1:2000 DMSO or CytoD, as required, as well as a 1:1000 dilution of CellMask™ Green (ThermoFisher Scientific) and 2 drops/ml of NucBlue Hoechst 33342 (ThermoFisher Scientific). Care was taken to prepare appropriate solutions for unstained or single colour controls. Following a 10 min incubation at 37 °C, cells were washed twice with LCI solution, and media was replaced with 100 μ l/well of LCI solution additioned with 10 ng/ml M-CSF and 1:2000 DMSO or CytoD, as appropriate.

Baseline images (T-1) were obtained for each well on an Opera Phenix Plus High-Content Screening System (set at 37 °C and 5 % CO₂, in order to ensure cell viability throughout the assay) using a 20x water immersion objective in non-confocal mode. The optimal focal point was selected following a test z-stack and a single plane was imaged across 12 fields for each well. The plate was then ejected and the media was replaced with 120 μ l/well of wither LCI (for the untreated wells) or Zymosan solution supplemented with 10 ng/ml M-CSF and 1:2000 DMSO or CytoD. For the unstained and single colour controls (with the exception of the Zymosan only control), 120 μ l of LCI solution with 10 ng/ml M-CSF and 1:2000 DMSO were added to the wells; a positive control was obtained by adding 120 μ l of pH 4 solution to the pHrodo™ Red Zymosan in a well with no cells (Figure 2.5). The plate was then returned to the Opera Phenix and all the selected wells were imaged every 20 minutes for 2 hours, for a total of 7 time points (T0 to T6).

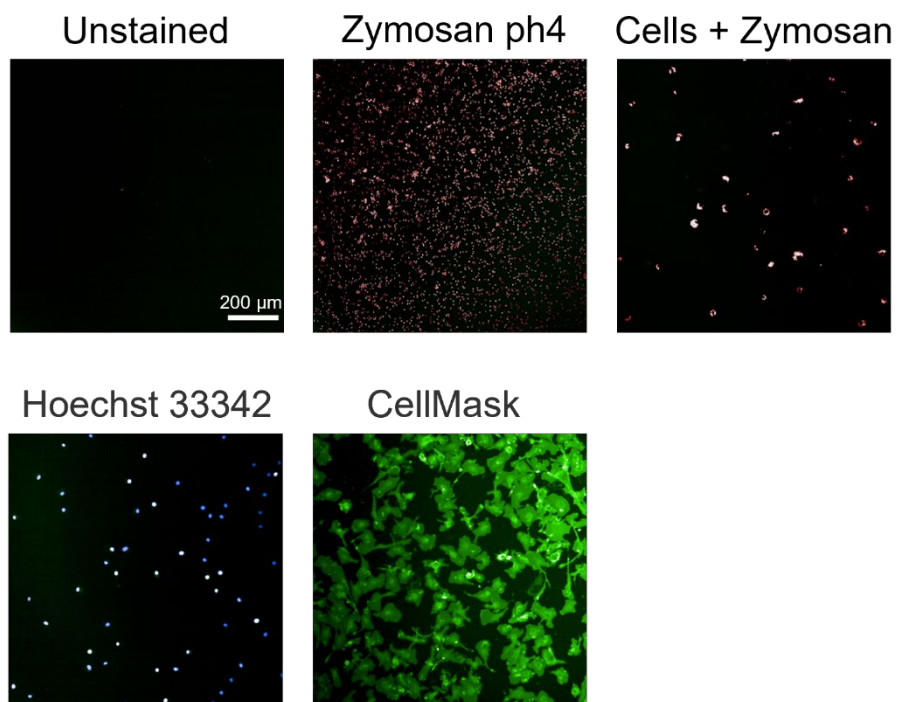


Figure 2.5 Representative images of single colour controls for the phagocytosis assay.

All images were exported, but only files deriving from treated wells (with and without CytoD) were automatically analysed on Fiji as shown in Figure 2.6. All the fixed values selected for any brightness/contrast and thresholding step were tested on random images to ensure high accuracy, before running the macro in a fully automated way on the whole experiment. Briefly, after a first step to increase the brightness of the CellMask™ Green channel and remove the background, an automated threshold was applied in order to generate binary images. After filling any artificial gap within the cells, a mask was generated excluding unwanted background pixels and the deriving ROI was used to select only Zymosan particles co-localizing with cells. Finally, after generating a binary image of the Zymosan channel, CellMask™/Zymosan colocalization and mean Zymosan intensity were measured for each image.

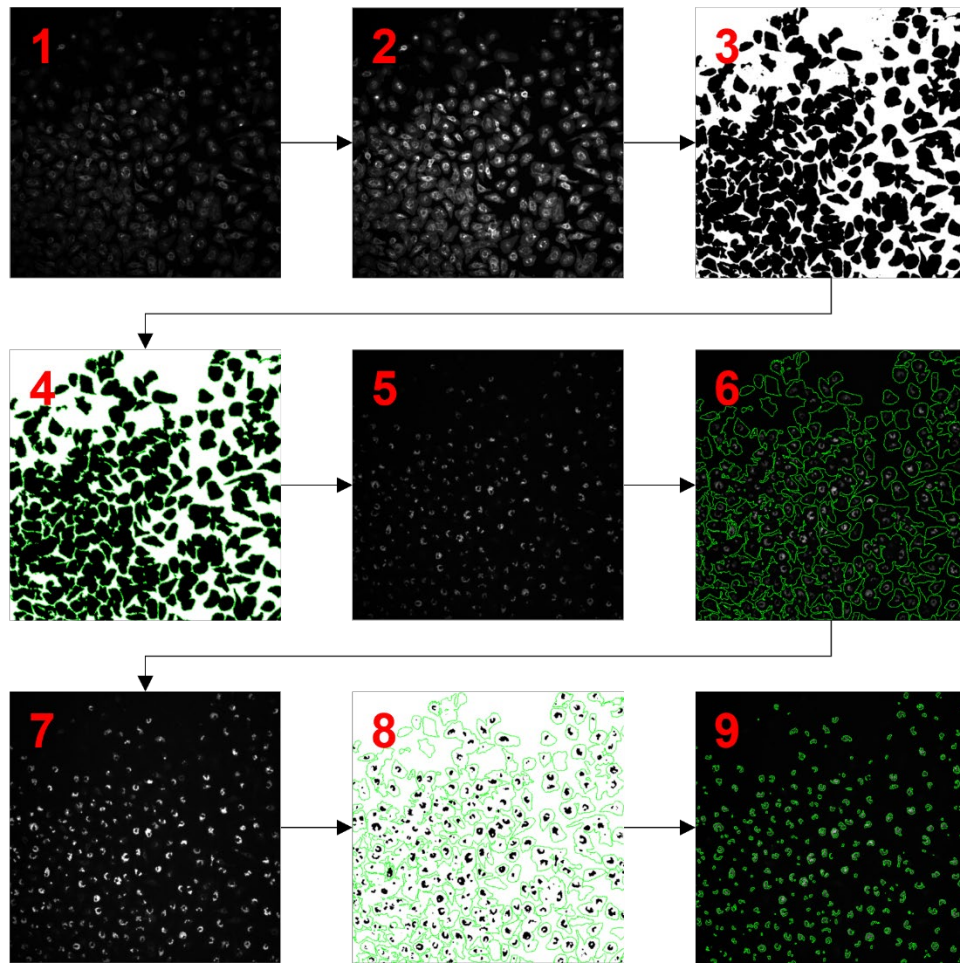


Figure 2.6 Schematic representation of the automated workflow of the Fiji analysis performed on the phagocytosis assay images.

1) CellMask™ Green channel was imported into Fiji and 2) brightness and contrast were automatically adjusted with a fixed value ("Enhance Contrast", "saturated=0.35") to facilitate the downstream analysis. Background was removed with the "Subtract Background" tool, and 3) an automated threshold ("setThreshold=5500, 65535") was applied. Holes were filled with the "Fill holes" option and particles with surface ≥ 0.02 pixels (enough to ensure removal of background pixels and small debris) were analysed to generate a mask. 4) The resulting binary image was then used to create an ROI that 5-6) was applied to the relative pHrodo™ Red Zymosan channel image, before selecting the "Clear Outside" option to ensure inclusion of only co-localizing pixels. 7) Brightness and contrast were automatically increased ("setMinAndMax=75, 3500") and an automated threshold was applied (setThreshold=11000, 65535). 8) The ROI from the CellMask™ Green channel was applied again to the mask obtained from the pHrodo™ Red Zymosan image and the average percentage of colocalization in each image was calculated using the "Measure" tool, set on the "Area fraction" option. 9) Finally, an ROI was obtained from the binary image of the Zymosan particles and applied to the original (not brightness-corrected) image of the same channel, to measure the average Zymosan intensity ("Mean gray value" option) of the "Measure" tool).

All the values obtained from triplicates of the same sample were pooled together for the final statistical analysis. This experiment was repeated three times, using three distinct pairs of sex- and age-matched mice. Data was analysed via Three-way ANOVA tests, followed by Tukey's multiple comparison test wherever appropriate.

2.4.3. ROS detection via DHR 123 staining

After 7 days in differentiation media, BMDMs were detached, counted and re-seeded at 2×10^5 in 24-well ultra-low adherence plates (ThermoFisher Scientific). Each sample was plated in 6 wells (3x non-treated control, 3x Zymosan); spare cells of either genotype were plated in one additional well to be used as unstained control. Cells were plated in 300 μ l of standard BMDMs media (see 2.3.6) supplemented with 10 ng/ml M-CSF and incubated overnight.

The next day, cells were detached by gently pipetting and transferred to round-bottom low-adherence 96-well plates (ThermoFisher Scientific). The plate was centrifuged at 350 x g for 5 min, supernatant was discarded and cells were resuspended with 200 μ l/well RPMI without Phenol Red (Gibco®, ThermoFisher Scientific) supplemented with 10 % (v/v) FBS and 100 U/ml Penicillin, 10 μ g/ml Streptomycin, with or without unlabelled Zymosan (Sigma-Aldrich) in a 1:1 ratio to cells. Following a 30-minute incubation at 37 °C, cells were centrifuged at 350 x g for 5 min, washed once with DPBS and centrifuged again. The cell pellet was then resuspended in 100 μ l/well DPBS and 100 μ l of 10 μ M Dihydrorhodamine 123 in DPBS were added to each well, except for the unstained control. Cells were incubated 15 min at 37 °C, washed once with ice cold DPBS, centrifuged one last time at 350 x g for 5 min, resuspended in 200 μ l/well ice cold DPBS and transferred to 1.5 ml microcentrifuge tubes. Samples were kept on ice and shielded from light until they were run on the Attune NxT flow cytometer to evaluate the percentage of cells showing fluorescent Rhodamine 123 signal (derived from DHR oxidation in the presence of ROS). PMT voltage settings were kept constant between experiments. Results were analysed using a Two-way ANOVA tests (section 3.2.4).

2.4.4. Griess Nitrites quantification assay

On day 7, differentiated BMDM cells were detached from the culturing dish as described in section 2.3.6, counted and re-seeded with 300 µl/well standard BMDMs media (supplemented with 10 ng/ml M-CSF) at 2×10^5 in 2x 24-well plates, 6 wells/plate for each genotype (3x non-treated control, 3x stimulated).

After an overnight incubation to ensure adherence, media was replaced with 600 µl/well of RPMI without Phenol Red supplemented with 2 % (v/v) FBS, 100 U/ml Penicillin, 10 µg/ml Streptomycin, and 10 ng/ml M-CSF, with or without the addition of 100 ng/ml LPS (Sigma-Aldrich) and 20 ng/ml Interferon-γ (BioLegend). Cells were incubated 24 or 48 hours at 37 °C.

Immediately before each time point, the 1 mM sodium nitrite standard solution provided in the Griess Reagent Kit (ThermoFisher Scientific) was diluted with distilled H₂O to obtain calibration solutions with concentrations between 1–100 µM, as shown in Table 2.4.

	Final concentration	Volume of standard (µl)	Volume of water (µl)
A	100 µM	15 of stock	135
B	80 µM	24 of stock	276
C	60 µM	9 of stock	141
D	40 µM	150 of B	150
E	20 µM	150 of D	150
F	10 µM	100 of E	100
G	1 µM	20 of F	180

Table 2.4 Summary table of standards preparation for nitrite quantification during the Griess assay.

At the chosen time points, from each well 3x 150 µl of the supernatant were transferred to 3 individual wells of a flat bottom 96-well plate (for a total of 450 µl of supernatant evaluated for each original well). The supplied reagents A (N-(1-naphthyl)ethylenediamine dihydrochloride, 1 mg/ml) and B (Sulfanilic acid, 10 mg/ml) were mixed in equal volumes and 20 µl of this reagent solution were added to each well together with 130 µl/well of distilled H₂O. The same volume of

reagent mix and water was also added to 3x blank wells (containing 150 µl of complete RPMI without Phenol Red) and to the calibration wells (comprising 150 µl/well of standard solutions prepared as described above). Following a 30-min incubation at room temperature, shielded from light, the absorbance at 548 nm was measured with a FLUOstar Omega microplate reader (BMG Labtech).

During the incubation, 200 µl/well of DPBS additioned with 2 drops/ml NucBlue Hoechst 33342 were added to the cells, before a 10-min incubation at 37 °C. Stained nuclei were then imaged on the EVOS™ FL Auto 2 Imaging System using a 20x objective. A single focal plane was then acquired for 20 pre-selected random field (Figure 2.7A) per well using the “large object” autofocus mode. Imaged were then imported on Fiji and converted to the 8-bit format to be analysed as shown in Figure 2.7B. Briefly, after a background subtraction step, followed by a fixed brightness/contrast adjustment (“saturated=0.35”), binary images were generated using a standardised threshold (“setThreshold=25, 255”). After applying the “Fill Holes” tool, adjacent nuclei were automatically separated using the “Watershed” tool and counted with the “Analyse Particles” option. The results obtained from all 20 images of each well were averaged before being used to normalise the relative absorbance value.

Data was analysed via Three-way ANOVA tests, followed by Tukey’s multiple comparison test wherever appropriate.

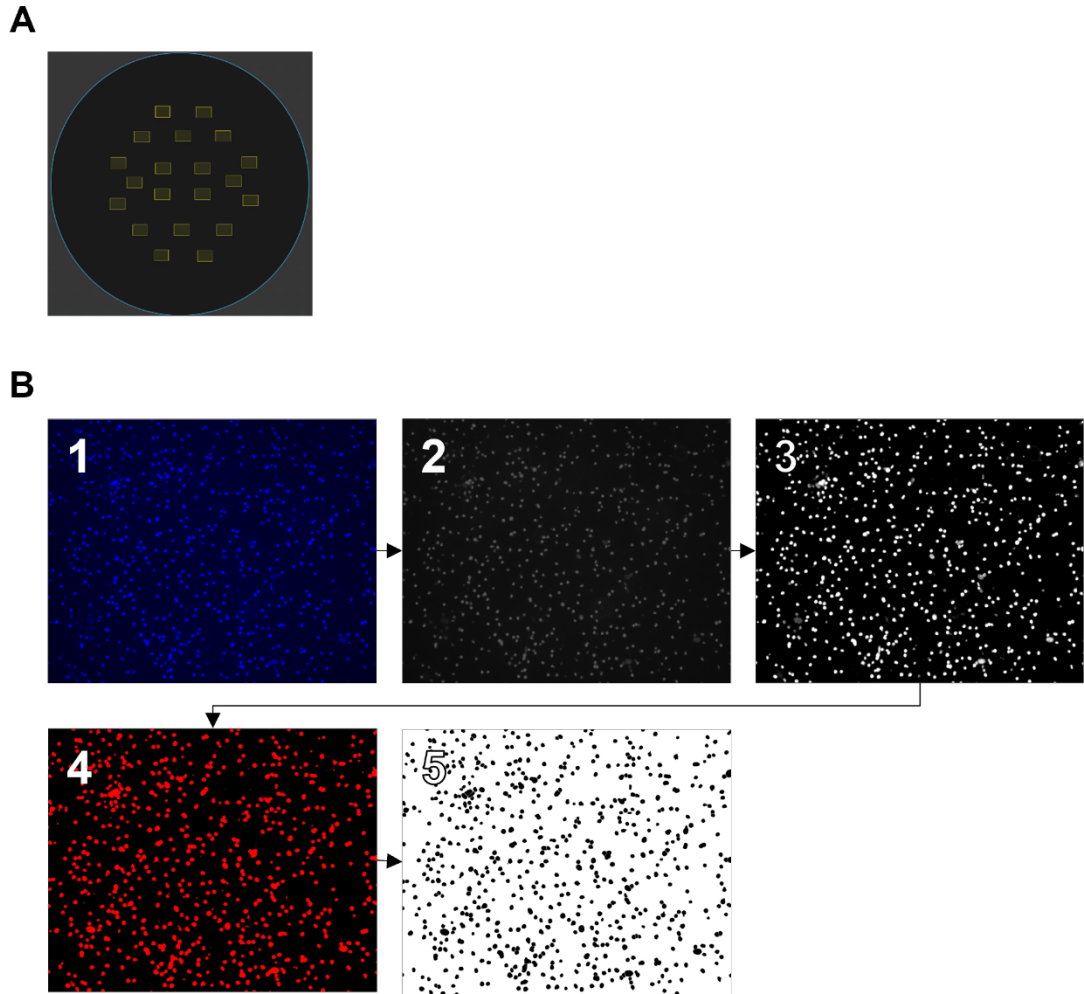


Figure 2.7 Visual representation of the nuclei count analysis used for the normalisation of nitrite measurements.

A) Representation of the 20 pre-selected fields imaged on the EVOS™ FL Auto 2 Imaging System for every sample, in all replicates of this experiment. It was chosen to avoid borders due to the consistent low number of cells present in that area across multiple repeats of the assay during the set up phase. B) Workflow of the automated nuclei count on Fiji. 1) The original TIFF images of the nuclei staining (blue) were imported into Fiji. 2) Images were converted to 8-bit format and 3) processed by subtracting the background and adjusting brightness and contrast to a fixed value (“saturated=0.35”). 4) An automatic threshold (“setThreshold=25, 255”) was applied, followed by the “Watershed” option to separate overlapping nuclei. 5) The deriving binary images were analysed with the “Analyse particles” function to obtain the number of nuclei in the image.

2.5. Quantitative PCR (qPCR)

2.5.1. Ribonucleic Acid (RNA) Extraction

RNA isolation from approximately 2×10^6 MØPs or M-CSF differentiated MØP cells was performed by Dr R. Jones using the RNeasy Mini Kit (Qiagen). Instead, for this thesis, the RNeasy Micro Kit (Qiagen) was preferred due to less than 5×10^5 BMDMs available for each sample. Cells were lysed in the required volume of RLT buffer and samples were stored at -80°C for a few days before the RNA was extracted. The samples were then defrosted on ice and then processed in accordance with manufacturer's instructions (Qiagen). Finally, spin columns were eluted in $30\ \mu\text{l}$ (for MØPS) or $15\ \mu\text{l}$ (for BMDMs) nuclease-free water.

2.5.2. Reverse transcription

Isolated RNA was measured using a DS-11 FX+ spectrophotometer (DeNovix®), which provided both concentration of nucleic acid and 260:280 ratio (used as an index of purity of nucleic acid to protein). Samples were normalised based on their RNA concentration and processed as per manufactures instruction of High-Capacity cDNA Reverse Transcription Kit (ThermoFisher Scientific) to generate complementary DNA (cDNA) for qPCR (Figure 2.5.1).

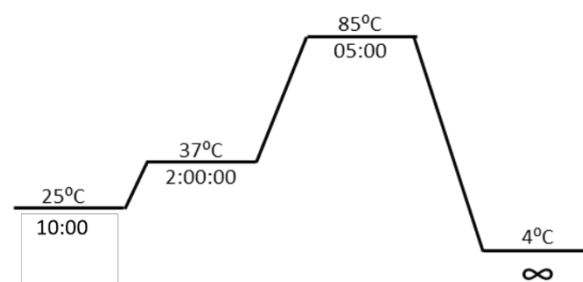


Figure 2.8 Schematic representation of the High-Capacity cDNA Reverse Transcription Kit PCR protocol.

2.5.3. qPCR reaction

All qPCR reactions were performed using the Fast SYBR™ Green Master Mix (ThermoFisher Scientific) according to manufacturer's instructions. qPCR reactions were conducted in a 96 well plate format with a 20 µl reaction on a QuantStudio™ 7 Flex Real-Time PCR Systems (Applied Biosystems™), using the protocol shown in Figure 2.9.

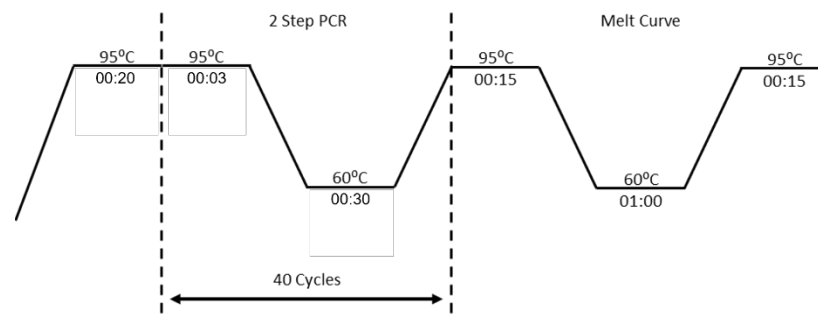


Figure 2.9 Schematic representation of the temperature and cycling times used to generate the qPCR data.

All qPCR primers (Table 2.5) were designed to be intron spanning, checked using NCBI Primer-BLAST, and generated by Sigma-Aldrich.

Target	Forward Primer (5' to 3')	Reverse Primer (5' to 3')
<i>Abi3</i>	TCAAACCCAGCAGGCTCCC	CTTGTCTGTGGCCTGCAAGTAGT
<i>Ywhaz</i>	TTGAGCAGAAGACGGAAGGT	GAAGCATTGGGGATCAAGAA

Table 2.5 List of the qPCR primers used to quantify *Abi3* expression in BMDMs.

Abi3 mRNA expression data was assessed using the x40 cycle and $\Delta\Delta$ CT method where *Ywhaz* was used as an endogenous control gene using the QuantStudio™ Real Time PCR software. The choice of *Ywhaz* as endogenous control was validated for mouse peritoneal macrophages, bone marrow derived macrophages and MOPS by both Dr. Luke Davies and Dr. Ruth Jones (independently) using a

geNorm™ Reference Gene Selection Kit (Primerdesign) and has been since used in published works from members of our research group such as (333).

No template controls (NTC), where nuclease free water was used to replace the RNA, were utilised in all qPCR reactions to control of contamination. BMDMs derived by three separate animals were assessed for each genotype (n=3 per group). qPCR data for Abi3 expression in both MØPs and BMDMs (sections 3.2.2 and 3.2.3) were analysed by One-Way ANOVA followed by Tukey's multiple comparison test to compare all means.

2.6. Histological analyses

2.6.1. Brain extraction and preparation for immunostainings

To ensure preservation of the original brain structure and avoid artifacts during the following histological analyses, 8-9 week-old mice were euthanised with intraperitoneal overdose of Euthatal® (Merial Animal Health Ltd) followed by intracardial perfusion-fixation with 20 ml ice cold DPBS and 50 ml ice cold 4 % PFA. Brains were removed from the skull taking care not to damage the cortex while doing so, and they were left over-night in 4 % PFA at 4 °C to allow appropriate fixation. The next day, the brains were then transferred and stored in DPBS with 0.1 % Sodium Azide (Sigma) at 4 °C until further processing. The addition of Sodium Azide is crucial to prevent microbial contamination.

Brains were cut using a Leica VT1200S vibratome (Leica Biosystems) in order to obtain free-floating coronal sections thick enough (50µm) to ensure the inclusions of microglia cells with their entire ramification apparatus. To do so, each brains was cut at the level of the Inferior Colliculus using a disposable scalpel (ThermoFisher Scientific) in order to provide a stable and flat surface, which was then glued to the magnetic specimen holder of the vibratome. If required, due to tissue damage, the region near the Superior Colliculus was embedded in 3 % Agarose (ThermoFisher Scientific) which had been previously dissolved in DPBS and let cool down in order to avoid heat-induced damage of the tissue. The specimen holder was then moved to the buffer tray filled with enough DPBS to entirely cover the sample and a double-edger razor blade was used to cut the sample using a fully automated cutting mode at a speed of 1 mm/s. Whenever possible, all the sections comprised between

the beginning of the Prefrontal Cortex and the end of the Ventral hippocampus region were collected using a thin-tip paint brush and moved in sequential wells of 24-well plates full of DPBS. 12 wells were used to accommodate each brain. Sections were stored long-term in 24-well plates at 4 °C in 1 ml of DPBS with 0.1 % Sodium Azide.

2.6.2. Immunofluorescent staining of free floating sections

Coronal sections from two regions of interest, the Prefrontal Cortex (between 3.08 mm to 2.58 mm from the bregma, the anatomical intersection of the coronal and the sagittal sutures of the skull) and the hippocampus (-1.34 mm to -2.18 mm from the bregma), were selected for each mouse using Images from the Mouse Brain atlas (346) as a visual reference (Figure 2.10).

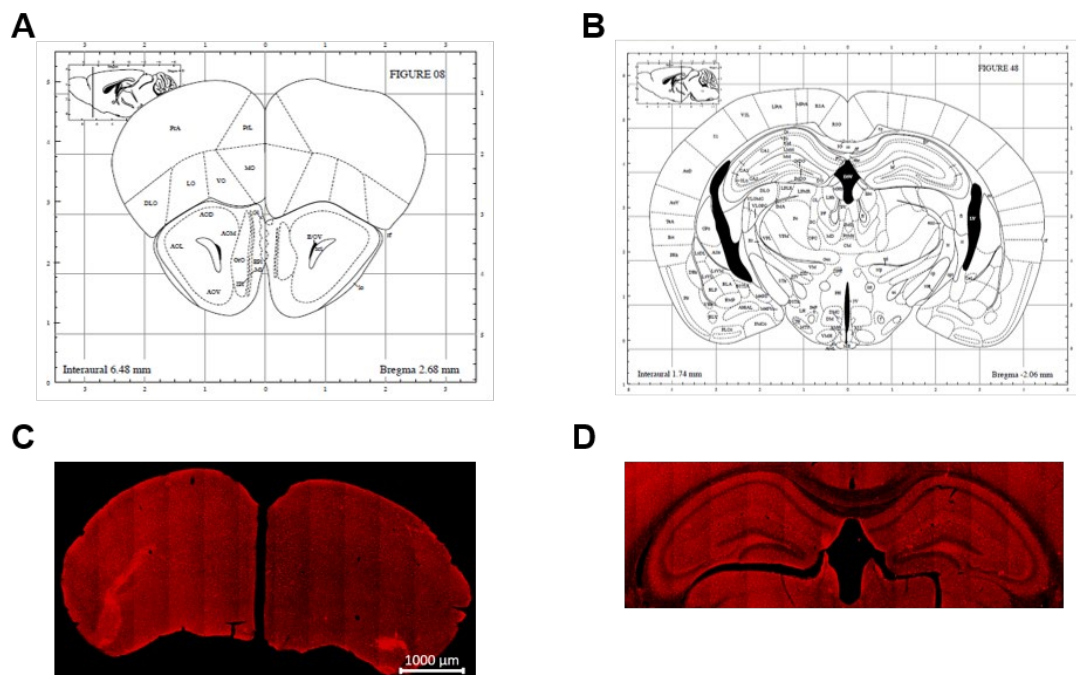


Figure 2.10 Selected regions of the Prefrontal Cortex (PFC) and the hippocampus used for the *Iba1* staining.

*A) and B) Schematic representation of a section comprising the PFC (A) or the hippocampus (B) obtained (reproduced with permission of Elsevier, see Appendix 1) from the Mouse Brain Stereotaxic Atlas (346). The anteroposterior distance from the bregma is indicated in the bottom right corner. C) and D) Exemplar images of *Iba1* staining (red) for microglia on regions comprising the PFC (C) and the hippocampus (D). Images were acquired with a 20x objective using a Zeiss Axioscanner Z1 slide scanner microscope and represent the result of*

the tiling of multiple fields. Sections were selected using the tables provided by the atlas as a visual reference.

In order to perform immunostainings, sections were moved between different wells of 24-well plates using a paint brush. In order to ensure appropriate exposure of the whole section to any given solution, no less than 200 µl were added to each well (up to 500 µl for washing steps) and plates were kept in constant movement on a Cole-Parmer™ Stuart™ Orbital Shaker (Fisher Scientific) on a low speed (40-50 rpm). No more than 4 slices of the same sample were incubated in the same well to stop them from adhering to each other, which could have compromised the quality of the staining.

Upon removal from the 0.1 % Sodium Azide in DPBS solution, sections were washed once for 5 min with 1x Tris-buffered saline. They were then permeabilized and blocked in immunofluorescence blocking buffer for 1 hour at room temperature. Brain slices were then moved to a different well and incubated overnight (or for 48 hours, in the case of 6E10 antibody) at 4 °C in 0.5 % Triton X-100, 1 % BSA in 1x TBS with one or more of the following antibodies:

Type	Target	Conjugation	Host specie	Catalog and lot numbers	Company	Final concentration / dilution
Primary (polyclonal)	Iba1	AF635	Rabbit	013-26471 (lots PTP4892 and CAH5022)	Wako	2.5 µg/ml (1:200)
Primary (polyclonal)	GFAP	Unconjugated	Chicken	ab4674 (lots GR3201333-4 and GR3354276-2)	Abcam	1 µg/ml (1:1000)
Primary (monoclonal)	CD68	Unconjugated	Rat	MCA1957 (lot 1807)	BioRad	10 µg/ml (1:100)
Primary (monoclonal)	β-Amyloid, 1-16 (6E10)	Unconjugated	Mouse	803001 (lots B247600 and B293112)	BioLegend	1 µg/ml (1:1000)
Secondary	Chicken IgY	FITC	Goat	ab46969 (lot GR3179274-11)	Abcam	1:200
Secondary	Rat IgG	AF488	Goat	112-546-143 (lot 138053)	Jackson ImmunoResearch Laboratories	1:200
Secondary	Mouse IgG	AF647/AF488	Donkey/Goat	715-606-151 (lot 138837) / 115-545-146 (lot 138610)	Jackson ImmunoResearch Laboratories	1:200
Isotype control	N/A	AF633	Rabbit (IgG)	A21063 (lot 1986960)	Invitrogen	2.5 µg/ml (1:800)
Isotype control	N/A	Unconjugated	Chicken (IgY)	ab37382 (lot GR3182361-2)	Abcam	1 µg/ml (1:5000)
Isotype control	N/A	Unconjugated	Rat (IgG2a, κ)	14-4321-82 (lot 4346403)	Invitrogen	10 µg/ml (1:50)
Isotype control	N/A	Unconjugated	Mouse (IgG1, κ)	14-4714-82 (lot 1957953)	Invitrogen	1 µg/ml (1:500)

Table 2.6 List of all antibodies used for immunostainings and their specifications.

All the washes following the addition of any fluorescent antibody were performed as quickly as possible to reduce tissue exposure to the light, and the plates were thereafter covered in foil during all the incubation steps. At the end of primary antibodies incubation, the sections were washed 3 times for 10 min with 1x TBS at room temperature and incubated for 2 hours at room temperature with appropriate secondary antibodies in 0.5 % Triton X-100, 1% BSA in 1x TBS. Samples were washed 2 more times for 10 min in 1x TBS at room temperature and they were then counterstained for 10 minutes at room temperature with 500 ng/ml DAPI in 1x TBS. After a last wash in 1x TBS (10 min at room temperature), the samples were rinsed in dH₂O and mounted on Superfrost Plus Microscope Slides using ProLong® Gold mounting media, covered with a 24 x 50 mm coverslip (ThermoFisher Scientific) and stored in the dark at 4 °C.

Isotypes controls were used only during the optimisation process of each staining, together with secondary-only controls, to ensure signal specificity (Figure 2.11), and were not further employed after a protocol was established. Before changing lot of

any antibody, a visual comparison between the new and the old batch was performed to ascertain reproducibility (data not showed). Abi3 deficient samples were always stained at the same time, and with the same solutions, as age- and sex-matched controls, to exclude any artefact caused by differences in the tissue preparation.

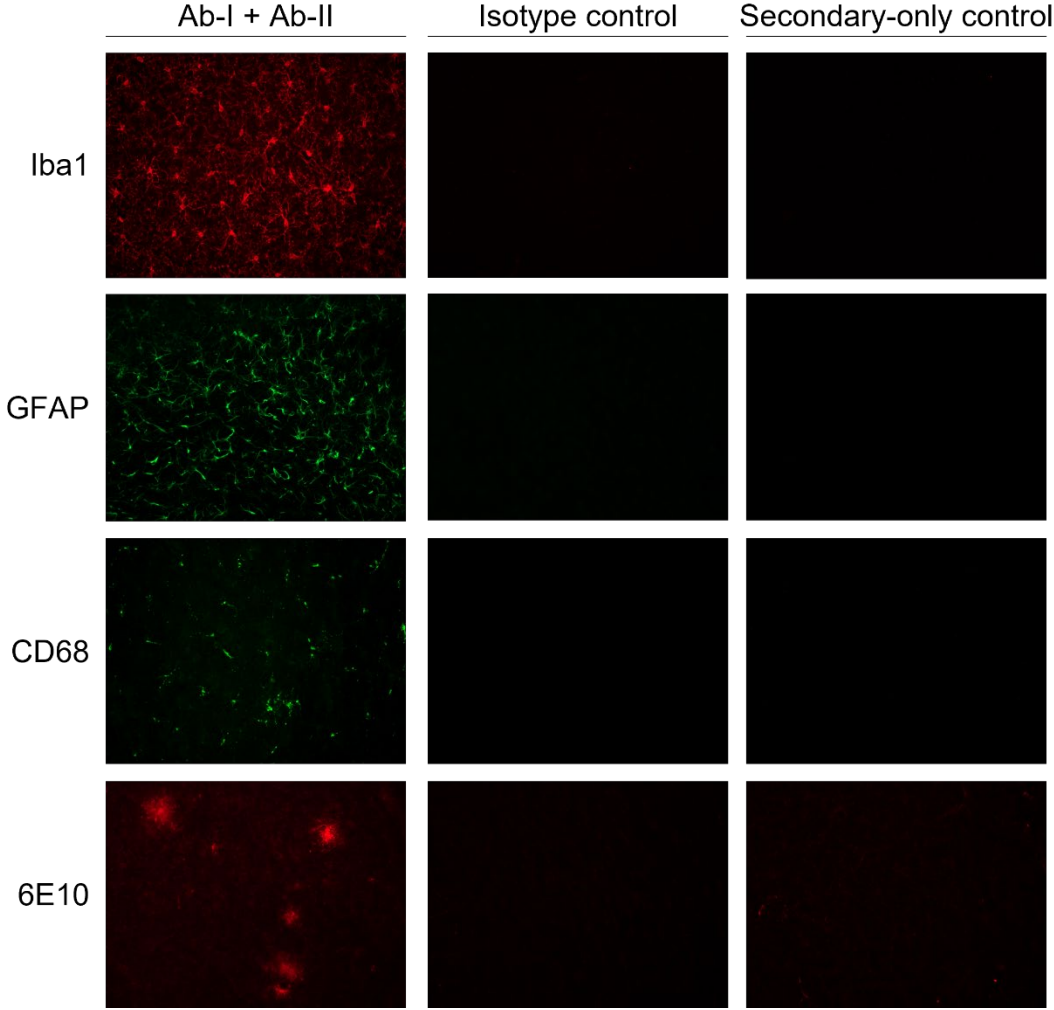


Figure 2.11 Representative images of the isotype and secondary only compared to the real staining for all the antibodies used for histological analyses in this thesis.

Controls were imaged at the same time, with identical laser power and gain and exported with the same brightness levels as the real staining images, to ensure the validity of the protocol.

2.6.3. Thioflavin-S staining

Two coronal sections, including the PFC and the hippocampus, per mouse were stained with 400 μ l of freshly prepared Th-S staining solution for 20 min at room temperature inside 24-well plates, kept in constant movement as described in the previous section. Sections were then washed for 5 min in 50 % EtOH, and finally washed 3 times for 5 min with distilled water. During all these steps, sections were shielded from light by covering the plates in foil. Once stained, sections were mounted on Superfrost Plus Microscope Slides (ThermoFisher Scientific) as described above and stored in the dark at 4 °C for up to two weeks. Due to the potential batch-dependant variability in the Th-S solution, as well as to the high photosensitivity of this staining, all the samples were stained in a single occasion and imaged in the shortest timeframe possible to avoid loss of fluorescent signal.

2.6.4. Image acquisition and analysis

2.6.4.1. Image acquisition and z-stack processing

For basic Iba1, GFAP and CD68 analyses, brain sections were imaged using a Zeiss Cell Observer Spinning Disk confocal microscope (Zeiss) with a 20x objective. For Iba1 and CD68 staining, 8 z-stacks were acquired for the PFC and 14 for the hippocampus region, due to the presence of different sub-regions inside this structure. For GFAP staining, instead, only 14 images were acquired in the hippocampus, due to the extremely low expression level of this astrocytic marker in the cortex (347). The central 30 optical sections of each z-stacks (for a total thickness of $\sim 15 \mu$ m) were transformed into a frontal maximum-intensity orthogonal projection using the “Maximum” option in the Zen Blue Lite software (Zeiss, version 2.6). Due to the relatively limited power of the 20x objective and the thickness of the section, there may have been a slight difference in z-stack thickness even amongst images acquired from the same sample. However, any bias due to this difference was prevented by analysing the same number of planes for each image.

To obtain Iba1 images for the morphometric analysis of individual microglia, hippocampal sections stained with an anti-Iba1 antibody were imaged using the same Zeiss Cell Observer Spinning Disk confocal microscope (Zeiss) with a 40x oil immersion objective. All images were acquired in the CA1 region to avoid any bias

due to region-specific morphological diversity (134,348). Between 4 and 6 z-stacks of random fields were acquired for each mouse.

In the case of the whole-section A β -plaques analysis, as well as for the pilot Th-S staining, images were acquired using the EVOS™ FL Auto 2 Imaging System with a 20x objective. A single plane was acquired for each section, using the “large structures” Autofocus mode to automatically focus on plaques within each individual field. The final stitched image was used for the subsequent Fiji analysis.

Finally, for the evaluation of microgliosis around individual plaques, 10 random fields comprising at least one A β -plaque each were acquired per mouse across the PFC region using a Leica TCS SP8 confocal microscope (Leica Microsystem) with a 40x oil immersion objective. The whole thickness of the tissue was acquired to ensure the most accurate count of peri-plaques microglia. Only plaques that were visibly fully comprised in the z-stack were analysed, and areas with high density of overlapping amyloid deposits were excluded to avoid biases in the microgliosis analysis. The full z-stack was then used for the ensuing Imaris analysis.

All experiments were performed in blinded conditions starting from the image acquisition stage, in order to avoid any operator bias. In case of contribution to the analysis from other members of the group, processed images were briefly inspected to ensure consistency across operators.

2.6.4.2. *Iba1 and GFAP analysis*

The orthogonal projections were then analysed with Fiji Software (Fiji is just ImageJ, version 1.52p (344)) as shown in Figure 2.12. After utilising the “Background subtraction” tool, Iba1 or GFAP positive cells were manually counted using the “Cell Counter” plugin. Care was taken not to include cells with their cell body partially outside the edges of the image. After assessing the number of Iba1+ or GFAP+ cells in the acquired field and calculating the number of cells per square mm (cell/mm²), each image was converted to the 8-bit format. A brightness and contrast adjustment was then performed to allow an easier identification of cell bodies and ramifications. A threshold was then applied to select the positive pixels, taking extreme care to avoid artefacts and trying to select even the thinnest ramifications, although a minimal loss was unavoidable. The resulting binary image was then analysed using the “Measure” tool to obtain the numerical value of area percentage covered by Iba1+ or GFAP+ pixels.

In the case of the microglial staining, the 8-bit image was further processed to obtain Nearest Neighbour Distance (NND) values. Two sequential filters from the MorphoLibJ plugin library were applied to the images: first, a Gray Scale Attribute filter was applied to isolate the cells from the background (Operation = “Opening”, Attribute = “Area”, Minimum Value = 25 pixels, Connectivity = 8), followed by an opening Morphological filter (Operation = “Opening”, Element = “Octagon”, Radius = 1 pixel) in order to separate the cell body from the ramifications. The plugin “Entropy Threshold” was used to obtain binary images, which were then inspected to correct any potential bias originated from missing cell bodies or wrongly included ramifications. The final binary was then analysed to obtain Centroids coordinates, which were used by the “NND” plugin to calculate the relative values for all the identified cell bodies. Finally, the ROIs obtained from the analysis were applied on the original image to prove the quality of the analysis.

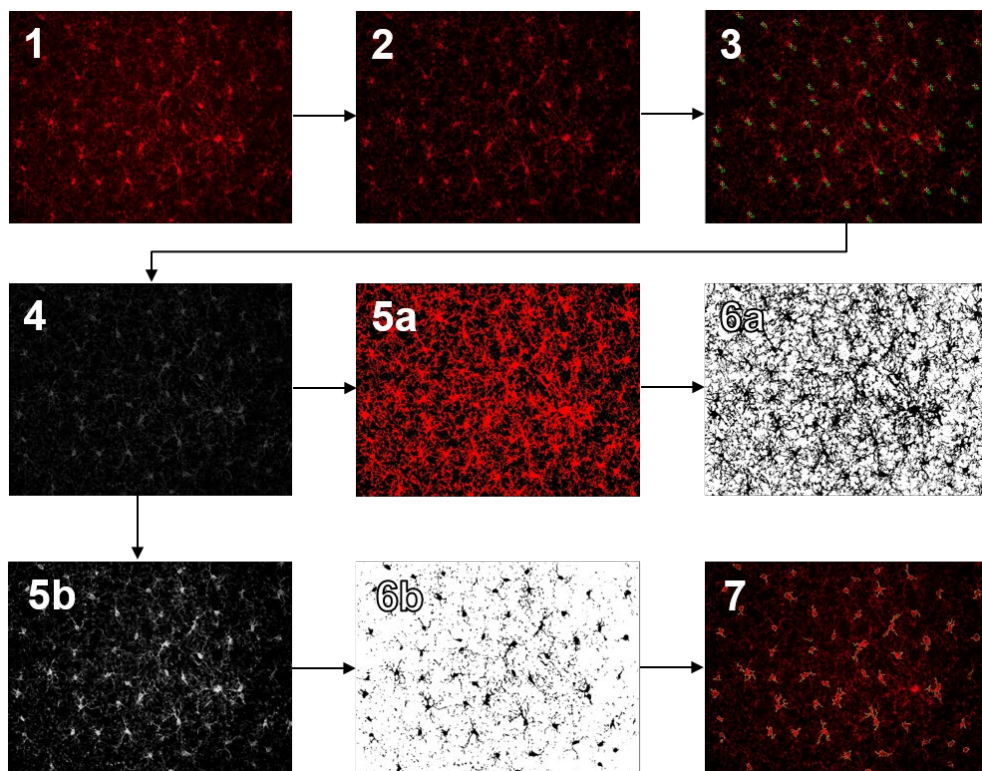


Figure 2.12 Schematic representation of Iba1 analysis performed using Fiji software.

Workflow of the Fiji analysis of brain sections stained with an anti-Iba1 antibody (red). 1) The original TIFF images of the Iba1 staining were imported into Fiji. 2) They were then processed by subtracting background using the “Subtract background” option in order to reduce any potential bias during the subsequent thresholding step. 3) Cell bodies were manually quantified using the “Cell counter” plugin. 4) The images were then converted to the 8-bit

format and a fixed brightness and contrast adjustment (min displayed value = 3, max displayed value = 25) was performed to facilitate the following steps. **5a)** For the area percentage analysis, the threshold was manually adjusted taking care to exclude any artefact and include all the cellular processes. **6a)** This led to binary images, which were then used to assess the area fraction covered by the Iba1+ particles thanks to the “Measure” tool. **5b)** For the NND analysis, instead, the 8-bit image went through a first step of filtering using two MorphoLibJ plugins. A Gray Scale Attribute Filtering (“Operation = Opening”, “Attribute = Area”, “Minimum Value = 25 pixels”, “Connectivity = 8”) and a Morphological Filter (“Operation = Opening”, “Element = Octagon”, “Radius = 1 pixel”) were applied to obtain cell bodies isolated from both the background and the cell ramifications. **6b)** The “Entropy Threshold” plugin was used to convert the filtered images in binary ones. Centroids were calculated for each cell body selecting a 30µm minimum size filter in the “Analyse Particles” tool. **7)** Finally, Nearest Neighbour Distance (NND) values were calculated using the homonymous plugin and the ROIs of the cell bodies were applied to the original image to evaluate the accuracy of the selection.

Data resulting from both microglia and astrocyte characterisation was analysed via Two-way ANOVA for 8-week-old mice (sections 4.2.1 and 4.2.4), while adult samples (section 5.2.1) were analysed via Three-way ANOVA, followed by Šidák’s multiple comparison test wherever appropriate.

Three-way ANOVA tests were employed for the analysis of the phagocytosis and Griess assay (sections 3.2.3 and 3.2.4), and for all behavioural data (section 5.2.4), followed by Šidák’s multiple comparison test wherever appropriate .

2.6.4.3. Iba1/CD68 co-localisation analysis

In the case of CD68 and Iba1 co-localisation analysis, for each image the Iba1 and CD68 channels were analysed separately as described above (see Figure 2.12, steps 4-6a) to obtain binary images of either Iba1+ cells or CD68 staining. ROIs generated from the Iba1 channel when then applied to the respective CD68 binary image before using the “Measure” tool set on the “Area fraction” option, in order to make sure only colocalizing pixels were comprised in the analysis.

Data shown in section 4.2.4 was analysed via Two-way ANOVA.

2.6.4.4. Morphometric analysis of single cells

Each image was carefully cropped to isolate single cells. Only cells that were entirely comprised within the z-stack and whose cell body was not overlapping with adjacent cells were used for the analysis. A total of 5 cells per animal was then analysed using the Filament Tracer module of Imaris software (Bitplane, Oxford Instruments, version 9.3.1). The “AutoPath (no loops)” algorithm was used to trace the cells. Both the starting point and the seed point threshold were manually adjusted to make sure the starting point corresponded to the cell body and the seed points included most if not all the ramifications. After the filament was automatically generated, wrong connections and duplicate branches were manually deleted. At the same time, any branch that had been ill- or partially-traced was manually edited and any small process missed by the algorithm was added to the structure. Due to the elevated level of editing required, and the consequent time consuming nature of this process, technical help was provided by Dr. R. Jones and Dr. A. Kouzeli, who processed a portion of the samples (which were then reviewed to avoid additional bias due to different operators). The chosen parameters to carry on statistical evaluations included those showed in Table 2.7, whose definition here reported has been adapted for microglia from the original software reference manual (349). For the purpose of this work, an increment in radius of 3 μ m was selected for the Sholl analysis and to evaluate data at specific branch levels.

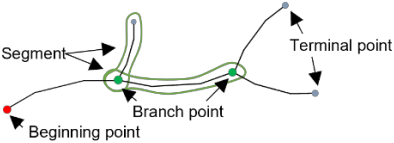
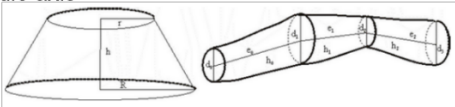
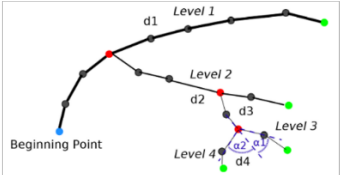
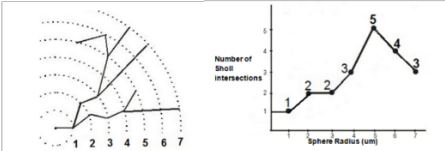
Parameter	Definition
Segment length	<p>Sum of all edges between two branch points or between a branch point and a terminal point, respectively.</p> 
Segment mean diameter	<p>Average value of the diameters measured at each vertex of the branch middle axis</p> 
Segment area	<p>Sum of the areas of all the segment edges, where the area of an edge is defined as a surface area of a frustum (truncated cone).</p> $A = \sum A(i)_{i=0, \dots, n-1, n}$ <p>n = number of edges of a segment</p>
Segment volume	<p>Sum of all (frustum) volumes composing a branch.</p> $V(i) = \left(\frac{\pi}{3}\right) * h(i) * (r(i)^2 + r(i) * r(i+1) + r(i+1)^2)$ $V = \sum V(i) \quad i=0, \dots, n-1, n$
Total number of branching points	<p>Number of branching points in the entire ramification graph.</p>
Full branch level	<p>Highest value of Branching Level. The initial Branch Level at the beginning point is 1. At each branching point, the ramification segment with smaller mean diameter sequentially increases Branch Level, while the ramification segment with a greater diameter maintains the same Branch Level. In the case of two branch segments with the same diameter, the segment with a smaller Branching Angle (angle between the extending lines from the branch point and its peripheral neighbour) keeps the Branch Level, while the branch segment with a greater Branching Angle sequentially raises its Branch Level.</p> 
Cell area	<p>Sum of the areas of all edges within the entire ramification graph.</p>
Cell volume	<p>Sum of all frustum volumes within the entire ramification graph.</p>
Sholl intersections	<p>Number of branch intersections on concentric spheres centered at the beginning point.</p> 

Table 2.7 Definition of selected parameters obtained from Imaris 3D tracing of microglia.

Data shown in section 4.2.2 was analysed using linear mixed-model analysis in R. To account for possible confounders, in addition to the genotype the regression models included sex and mice IDs, as well as radius or branch level wherever appropriate; genotype, sex and radius/branch level were included as fixed effects, while the animal's ID was included as a random effect to account for the animal-specific variability.

2.6.4.5. Whole-section A β -plaques evaluation

As shown in Figure 2.13, regions of interest (PFC and hippocampus) were carefully cropped out of the original stitched images, converted to the 8-bit format and used to generate a mask. After subtracting the background and adjusting brightness and contrast to facilitate plaques detection, a manual threshold was applied to the section taking care to include as much plaque surface as possible without creating artefacts due to the inclusion of background pixels. The resulting binary images were then manually edited, by visual comparison to the original file, to remove any obvious artefact (such as blood vessels, folds in the tissue, out of focus areas etc.) and plaque number and area were obtained using the “Analyse particles” tool. After different trials, a minimum size threshold of 200 μ m was selected to avoid including any remaining background pixels or small artefacts not removed during the previous manual assessment. Furthermore, the previously created mask was used to evaluate the percentage of tissue covered in plaques using the “Measure” tool set on the “Area fraction” option. Finally, the ROIs created from the particles analysis were flattened onto the original section to visually assess the quality of the selection. Statistical analysis was performed via Two-way ANOVA (as shown in section 5.2.2).

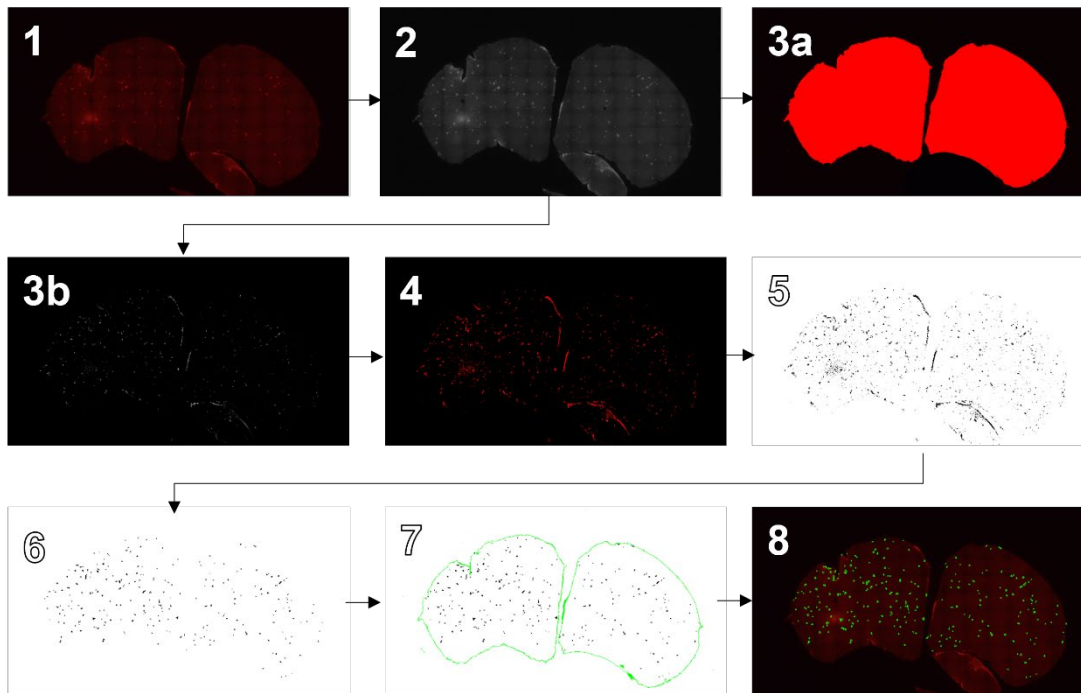


Figure 2.13 Schematic representation of 6E10 analysis performed using Fiji software.

Brain sections comprising either the PFC (shown here) or the hippocampus were stained with a commercial 6E10 antibody (red), specific for residues 1-16 of A β (350). **1)** The stitched TIFF files obtained were imported in Fiji and **2)** converted to 8-bit images. **3a)** A mask was created taking care to exclude any rip in the tissue as well as the Olfactory Nuclei (in PFC-comprising sections) due to their absence in most of the samples. Similarly, at this stage the hippocampus was isolated from the corpus callosum, the hippocampal fimbria and any other adjacent structure to avoid biases. **3b)** The same 8-bit image was also processed using the “Subtract Background” tool and brightness/contrast were adjusted to allow easier identification of the plaques. **4)** A threshold was then applied, taking care to include as much of the plaque area as possible without selecting non-specific background. **5)** The resulting binary images were manually edited to remove obvious artefacts and **6)** the remaining particles were analysed using the “Analyse particles” tool, with a size threshold of 200 μm minimum to avoid including background pixels. This step provided the total number of plaques and the area of each of them within the section. **7)** The mask created during step 3b was then applied to measure the total area of the section and the percentage of area covered by plaques. **8)** Finally, a ROI was created based on the identified plaques and overlaid to the original image to assess the quality of the selection.

2.6.4.6. Individual A β -plaques microgliosis assessment

Each 3D image was opened with Imaris a and analysed as shown in Figure 2.14. Plaques comprised within the stack, sufficiently far from the image border and not overlapping with other A β aggregates were manually rendered using the “Surface”

creation module on “Absolute intensity” mode, with surface detailing set to 0.910 μm to avoid artefacts due to the high background of the staining (any higher detailing was observed to cause artefactual indentations in rendering due to the inclusion of background pixels into the surface). The volume of the plaque was then calculated and exported for the downstream analysis.

The “Spots” creation module, with an estimated volume of 8 μm^3 , was then employed to automatically locate microglial cell bodies across the whole z-stack.

Miss-assigned spots and unrecognised cell bodies were manually amended as required. Finally, the “Find spots close to surface” extension was used to count the number microglial cells within 15 and 30 μm radius from the plaque. Despite every effort to avoid extremely small or big deposits, imaging plaques of different volume was unavoidable; for this reason, following Imaris analysis plaques were divided in 3 groups based on size, to avoid bias in the subsequent analysis. Specifically, a first group of “small” plaques included all the aggregates with a volume of 9,000-20,000 μm^3 ; plaques of >20,000 and <30,000 μm^3 were considered “middle-sized”, and finally any aggregate with a volume comprised between 30,000 and 39,000 μm^3 was categorised as “big”.

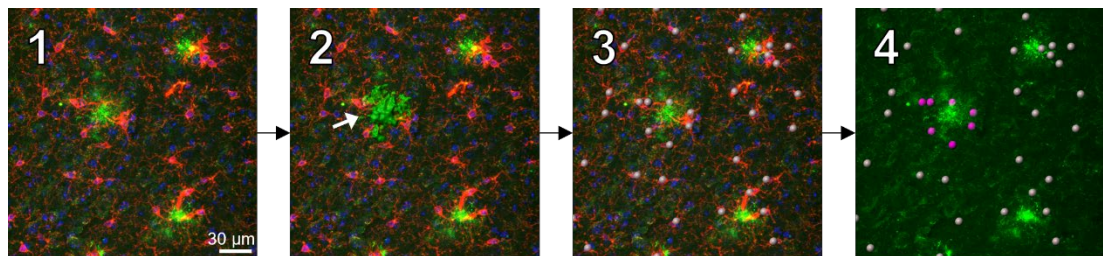


Figure 2.14 Schematic representation of peri-plaques microgliosis analysis performed using Imaris software.

1) The 3-channels z-stack, including Iba1 staining for microglia (red), 6E10 staining for A β plaques (green) and DAPI staining for nuclei (blue), were imported into Imaris software. **2)** Any plaque fully comprised in the z-stack, not overlapping with others and not too close to the borders was rendered in 3D using the “Surface” creation module (white arrow). **3)** The “Spots” creation tool was then used to automatically identify microglial cell bodies across the whole image. If needed, spots were then manually edited to remove incorrect cell bodies and add any missing one. **4)** Finally the “Find spots close to surface” extension was used to automatically identify cell bodies within 15 and 30 μm from the plaque (pink spots).

Peri-plaque microgliosis analysis (section 5.2.3) was conducted using a linear mixed model in R, in order to analyse the effect of genotype and sex (as fixed effects) on microgliosis, while the animal's ID was included as a random effect, for each of three size classes of A β -plaques.

2.7. Two-photon microscopy

Prior to commencing surgical procedures on Cx3cr1-GFP animals, the specificity of EGFP staining was assessed on brain slices. Two brains were extracted without perfusion-fixation, to avoid any impact of PFA on EGFP signal, and were then snap-frozen embedded in Tissue-Tek® Optimal Cutting Temperature™ compound (Sakura Finetek). 16 μ m-thick slices were obtained using a ThermoFisher Scientific CryoStar NX50 cryostat, mounted on Superfrost Plus Microscope Slides using ProLong® Gold mounting media and immediately imaged on a Zeiss Cell Observer Spinning Disk confocal with a 20x objective (Figure 2.15A).

Before being imaged, mice underwent a craniotomy in order to make brain tissue accessible. Following the indications from Goldey et al. (351), a 3 mm-large circular portion of skull was removed and replaced with two 3 mm cover glasses and one 5mm cover glass on the top, together with a metal head plate (fixed by dental cement) to allow head immobilisation during the imaging session. The cranial window was centred over the primary visual cortex (V1), which is located in the left hemisphere of the brain (Figure 2.15B). The V1 region was identified by using coordinates 3.00 mm lateral to lambda and 1.6 4mm anterior to the lambdoid suture (351). All the surgical procedures were performed by Ms. F. Chen.

A week after the surgery – during which the mice entirely recovered from the craniotomy – mice were imaged using a customised two-photon resonant scanning microscope (Thorlabs, B-Scope; Figure 2.15C). Mice were awake during the imaging session and placed on a cylindrical treadmill to try reduce anxiety and therefore head movements due to stress, which would not only impair the image quality but could also lead to detachment of the head plate.

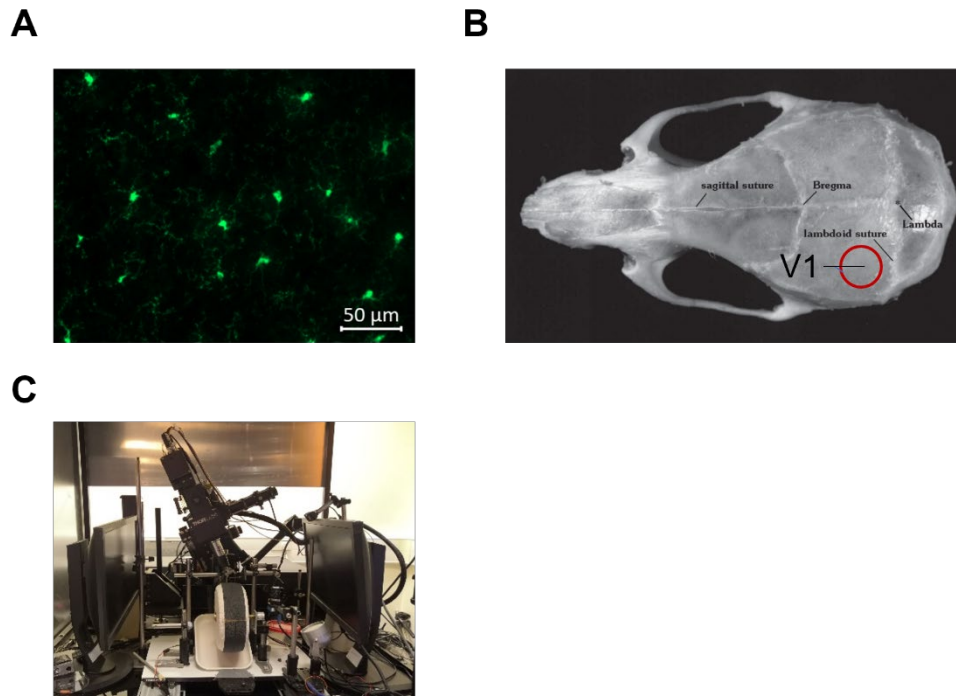


Figure 2.15 Representative images of EGFP expression in microglia and two-photon microscopy set up.

A) Representative picture of EGFP expression (green) in the brain of an *Abi3-KO Het x Cx3cr1-GFP Het* mouse, obtained with a 20x objective on a Zeiss Cell Observer Spinning Disk confocal microscope. Even with a low magnification it was possible to appreciate the specificity of the staining and the presence of a ramification network. **B)** Schematic representation of primary visual cortex (V1) location projected on the overlying skull. V1 was identified using the lambda and the lambda suture as reference (3.00mm lateral to lambda, 1.64mm anterior to the lambda suture). Image of the skull was obtained (reproduced with permission of Elsevier, see Appendix 1) from the Mouse Brain Stereotaxic Atlas (346). **C)** Image shows the customized setup utilized for two-photon imaging. A resonant scanning microscope (Thorlabs, B-Scope) with a 16x 0.8 NA objective with 3-mm working distance (Nikon) was used to obtain two-photon data. During the imaging sessions, mice were clamped in place through the head place, but they were left free to run on a spinning wheel to try reducing the unavoidable anxiety generated by the restriction of head movements. A plastic cone was adjusted on top of the cranial window and filled with water to allow imaging of the underlying tissue. Finally, the mobile tray on which the wheel is located was moved in position and the water-immersion objective was lowered at the adequate starting depth within the cone. A black curtain was then lowered to protect the operator from the lasers. Animals were constantly monitored throughout the session by means of a camera.

Laser power was set to 30mW (at the sample) for all recordings. Each mouse underwent a single imaging session, for a total of 45 minutes, with 50μm-thick z-

stacks (comprised of 25 sections, for a total a 2 μ m step size) acquired every 90 seconds. A 7x zoom was used allow visualisation of the thin processes. Each focal plane of the z-stack was imaged 10 consecutive times before moving to the next one. Following the acquisition, a custom written software in MATLAB® (R2019 and following; MathWorks) (reported in Appendix 2 and developed by Dr. A. Ranson) allowed image registration and therefore the alignment and merging of all 10 images constituting a single focal plane. This step was crucial to obtain a higher signal/noise ratio and be able to visualize most if not all the thin microglia ramifications. Other than providing registered z-stacks for each of the 30 time points, this pipeline produced a single time-stack, where each z-stack resulted merged in a maximum intensity orthogonal projection and then collated with all the others, in chronological order.

The resulting file was then used to perform a quantification of the area covered by Abi3-WT and -KO microglia using Fiji software as shown in Figure 2.16 below. Each TIFF file was appropriately cropped to remove artefacts due to the registration step, more prominent in some animals due to higher stress-related movements. The time stack was then flattened into a single orthogonal projection and brightness and contrast were adjusted to facilitate the downstream analysis. Different thresholds were applied to the resulting 8-bit image to obtain two binary images: a first one comprising all the ramifications and a second one including exclusively the brightest objects, which resulted mostly cell bodies. The percentage of “dynamic area” – i.e. the area covered only by dynamic structures – was measured after subtracting the second binary image from the first one. The quality of the selection was assessed by overlaying the ROI of the dynamic surveillance area to the orthogonal projection of the time stack. Finally, a rainbow LUT was applied to the time stack and the resulting image, showing ramifications color-coded on the basis of their chronological appearance in the time stack, was used to visualise changes in processes length and position.

Data was analysed via Two-way ANOVA (section 4.3.2).

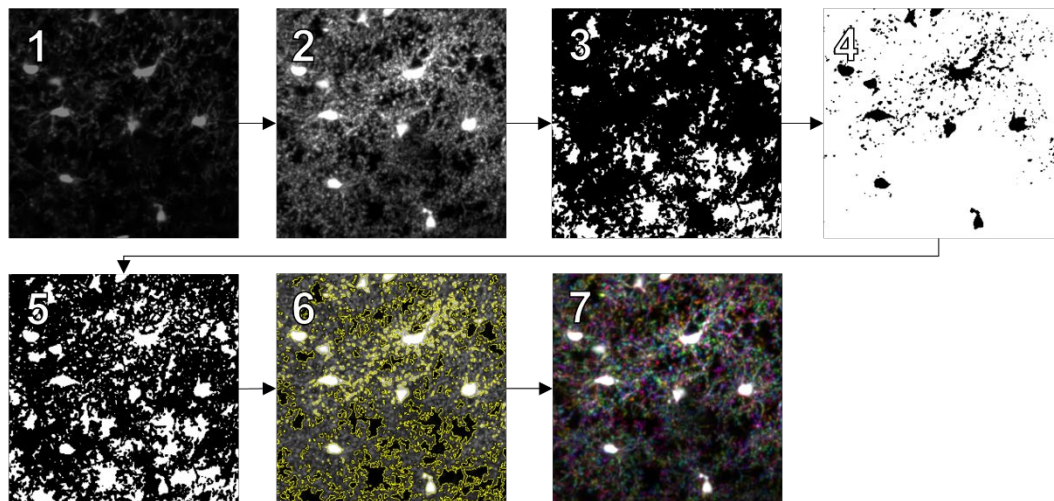


Figure 2.16 Schematic representation of the analysis pipeline performed on 2-photon videos through Fiji software.

Each original file comprises 25 optical planes, with a 2 μm step size; 30 z-stacks were acquired in one session for each animal. A first step of registration was performed on Matlab using the code reported in Appendix 1 in order to maximise the signal/noise ratio. Each registered z-stack, representing a single time point, was then flattened into a single orthogonal projection image and collated to the remaining ones in order to obtain single TIFF file. **1)** These files were then imported into Fiji software. **2)** Images were cropped to remove artefacts due to the registration step and the time stack was flattened by applying a maximum intensity orthogonal projection, to then adjust brightness and contrast in order to facilitate the following analysis. **3)** A first threshold was applied taking care to include all the ramifications, **4)** while a second threshold was used to select only the regions with highest intensity, which mostly coincided with the cell bodies. **5)** The latter, defined as “static” region, was then subtracted from the first binary image, in order to obtain a binary including only dynamic structures. The area percentage covered by the dynamic structures and the one never surveyed by microglia ramifications were both quantified using the “Measure” tool. **6)** Finally, the ROI of the dynamic area was applied to the orthogonal projection in order to assess the quality of the analysis. **7)** In addition, a LUT was applied to the original time stack in order to assign to each frame a different colour: the resulting orthogonal projections allows visualization of changes in position or length of the processes.

2.8. Behavioural assays

Before any task, mice were allowed at least 30 min habituation inside the testing room prior to being assessed. All animals were tested in the same room, using the same equipment and in temperature conditions comparable to those in the holding

room. To reduce light-induced stress, lights in the room were partially shielded to ensure that the centre of the arena was illuminated at no more than 30 lux as measured with a light meter. Moreover, arenas and objects were wiped between animals using 20 % (v/v) EtOH in order to reduce olfactory cues. The operator sat in the room – more than one meter away from the arena – through all the assays, avoiding loud noises or excessive movements.

Whenever possible, age- and sex-matched mice of two different genotypes were cohoused from weaning and each behavioural cohort included animals of all four genotypes tested, as shown in Table 2.8. All behavioural tasks were performed during the 12-hour light cycle, taking care to alternate genotypes (cycling through groups of the two sexes), to reduce biases due to the influence of the circadian rhythm on mice behaviour. For instance, a group of 4 females (one of each genotype), was followed by an equivalent group of males, repeated until all mice had been tested.

	Abi3-WT	Abi3-KO	App-KI	App-KI Abi3-KO
Cohort 1	5M + 4F	4M + 2F	4M + 5F	5M + 3F
Cohort 2	6M + 3F	2M	7M + 3F	3M + 3F
Cohort 3	4M + 4F	11M + 11F	4M + 5F	3M + 2F
Cohort 4	6M + 9F	5M + 3F	3M + 5F	7M + 7F
Cohort 5	4M + 5F	3F	3M + 5F	3M + 7F

Table 2.8 Summary table of the animals tested for the scope of this thesis.

Any effort was made to include mice of both sexes for all four genotypes tested in every cohort, although this was not always possible due to difficulties with breeding.

Animals were aged to 40 weeks, and were handled for approximately a minute each five times during the week preceding the commencing of the behavioural tasks, in order to reduce the stress caused by the operator during testing. Animals were then tested with multiple paradigms as shown in Figure 2.17. In case of particularly big cohorts, animals were split as equally as possible between two sub-cohorts, tested with a 24-hour delay. Anxiety was first assessed with the Elevated Plus Maze (EPM) paradigm, followed by two consecutive days of the Open Field (OF) task, which

provided additional information regarding animal anxiety as well as allowing the animals to get accustomed to the arena. After one habituation day in the presence of a single object (not used in the successive tasks), mice memory was assessed using two paradigms, the Novel Object Recognition (NOR) and the Object In Place (OIP). Each animal was tested twice for each paradigm – with two separate sets of objects for each task – with a day of rest in between sessions; the two repeats of each task were completed before moving to the next one. Each cohort (or sub-cohort, when present) was divided in two balanced groups in order to allow both memory tasks to be performed on the same day to avoid biases caused by the habituation to the arena.

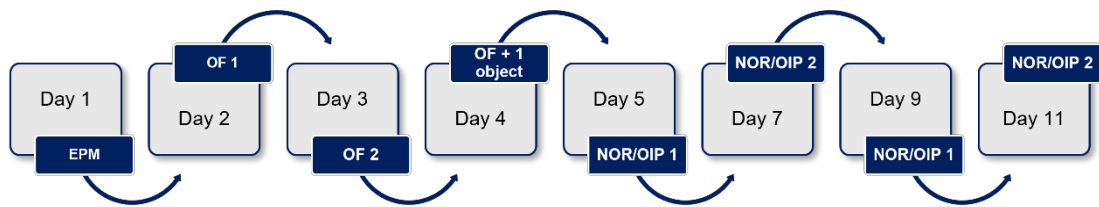


Figure 2.17 Visual summary of the behavioural schedule.

Mice of each cohort were tested over the span of 11 days, starting with the Elevated Plus Maze (EPM) paradigm, on day 1, and the Open Field (OF) paradigm, on day 2, to measure anxiety. They were then given another habituation day in the empty arena (OF2), and an additional one in the presence of a single object (OF + 1 object). Finally, starting from day 5, animals were tested twice with each memory paradigms, the Novel Object Recognition (NOR) and the Object In Place (OIP), with a day of rest in between testing sessions. Each cohort was split in two, maintaining wherever possible a balanced mix of sexes and genotypes, with half cohort tested on the NOR and half on the OIP every day; each mouse was tested with the same paradigm in two consecutive occasions before switching to the remaining one. Due to time constraints, the analysis of the OIP videos will be performed after the completion of this thesis and will therefore not be shown in this manuscript.

Mice were tested again, following the same schedule (but with different sets of objects) at 50 months of age to follow the disease progression. However, due to the elevated manual scoring required and the high number of animals tested, this second time point will not be part of this thesis; the OIP tasks at 40 weeks will be analysed after submission for the same reason.

Four weeks after the completion of the second time point, mice were isolated in large cages with full enrichment and tested with a Sucrose Preference (SP)

paradigm and, after assessing the Nest Score for each animal, mice were culled by an approved Scheduled 1 method and tissue was harvested for future experiments.

The EPM and OF videos were automatically analysed using the EthoVision video-tracking system (v. XT 13; Noldus Information Technology Inc), while NOR videos, requiring manual assessment, were analysed in blinded conditions.

Statistical analysis for all behavioural data (section 5.2.4) was performed using Three-way ANOVA tests, followed by Šidák's multiple comparison test wherever appropriate.

2.8.1. Elevated Plus Maze (EPM) paradigm

The EPM apparatus consisted of a cross-shaped raised platform, 70 cm above the floor. As shown in Figure 2.18A, the maze presented four equally-sized arms (6 x 39 cm), two opposing open arms, surrounded by a 1 cm-high transparent plastic wall to avoid falls, and two closed arms encircled by a 15 cm-high opaque black wall, with a central area of 6 x 6 cm. The maze was placed in a rat open field arena (100 x 100 cm) to stop any animal from escaping after falling from the open arms.

Mice were placed individually in the centre of the arena, facing a closed arm. The recording was started before each mouse was placed in the arena and animals were left free to explore the maze for 10 minutes before being returned to their home cage. The arena was cleaned with 20 % EtOH and thoroughly dried in between animals.

Videos were analysed automatically using EthoVision software after dividing the arena in areas of interest as shown in Figure 2.18B, in order to measure: latency to the first entry and the number of entries in the open arms, time spent in the open arms, total distance travelled in both types of arms as well as average speed in either the open or closed arms. The percentage of time spent moving in either type of arm ($[\text{time spent moving in \{open/close\} arms} / \text{total time spent in \{open/closed\} arms}] * 100$) were also calculated for each animal.

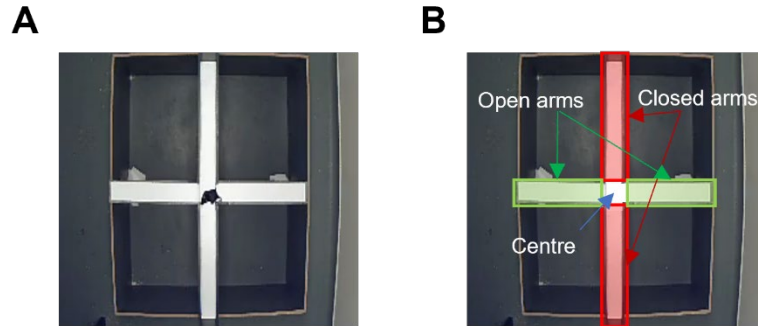


Figure 2.18 Elevated Plus Maze (EPM) layout.

A) The elevated arena is formed by two opposing open arms, where mice are free to dip their head over the 1 cm-high wall to explore the surrounding environment, and two closed arms, surrounded by high black walls that provide shelter to the animals. Mice were placed at the intersection of the four arms and left free to explore the arena for 10 minutes. **B)** EPM videos were analysed at a later time using EthoVision XT 13 software. The open (green) and closed (red) arms were delineated in the software, which tracked mice movements in the different areas and provided information regarding mice motility and time spent in each area, as well as the number of times a mouse crossed into one of the open arms.

2.8.2. Open Field (OF) paradigm

The OF arena consisted in a 60 x 60 cm box surrounded by 40 cm-high white opaque walls. All animals were placed individually in the same corner of the maze, as shown in Figure 2.19A, and left free to explore it for 10 minutes, prior to being returned to their home cage. The arena was cleaned with 20 % EtOH and fully dried between animals. Start recording before placing the animal and stop it 10 minutes from when you sit down having placed the animal in it. This was repeated for two days in a row; however, the second day was only treated as an habituation step for the following memory tasks and therefore mice performance during the second OF day will not be discussed in this thesis.

Videos were automatically assessed using EthoVision. As shown in Figure 2.19B, the arena was divided in a 5 x 5 squares grid, with the central 9 squares forming the “centre” area, while the surrounding 16 squares were indicated as “borders”. For all animals, EthoVision assessed the latency to the first entrance in the centre, the number of entries in the centre and the total time spent in that area, as well as the total distance travelled, the average speed and the percentage of time spent in movement (regardless of the position in the arena).

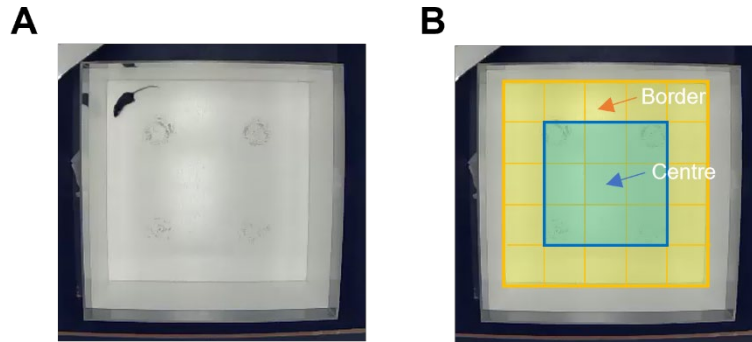


Figure 2.19 Open Field (OF) arena layout.

A 50 x 50 cm square arena, surrounded by opaque white walls (that precluded the mice from seeing the operator sitting in the room) was employed for this task. **A)** Mice were placed consistently in the same corner of the arena and left free to explore the arena for 10 minutes. This was repeated twice during two consecutive days of testing, to not only obtain information regarding strains locomotor and exploratory activity, but also to habituate them to the arena for the following tasks. **B)** OF videos were analysed using EhoVision XT 13 software. The arena was divided in a 5 x 5 grid and two areas (“border”, in yellow, and “centre”, in blue) were identified in the software. Mice movements around the arena were automatically tracked by the software and values regarding speed, distance moved and time spent in each area were extracted for downstream analysis.

2.8.3. Novel Object Recognition (NOR) paradigm

After being tested twice in the empty OF arena, mice were further habituated with one object (shown in Figure 2.20) on day 4 of the behavioural schedule. As before, mice were placed in the same corner of the maze and left free to explore the arena and interact with the object for 10 min each. Arena and object were cleaned with 20 % EtOH in between animals.

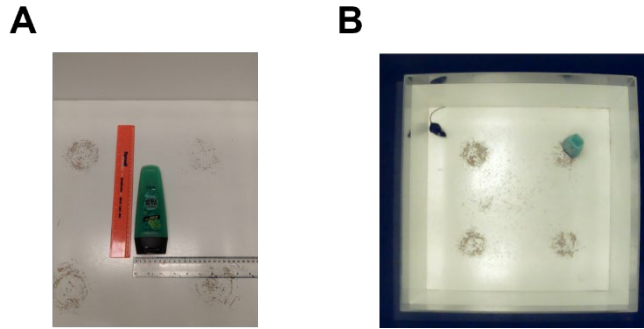


Figure 2.20 Visual representation of the additional habituation phase mice underwent before performing NOR task.

A) An object similar in size to those used for the following memory tasks was used to habituate the mice to the presence of foreign objects in the arena. B) Mice were placed in the same corner as before and left free to explore the object for 10 min before returning to their home cage until the next day.

On day 5 and 7 or 9 and 11, animals were tested with two sets of objects (as shown in Figure 2.21). Object were tested with untrained adult C57BL6/J mice prior to commencing of the experiments to ensure lack of preference for either object of each set. Objects were all of roughly similar size, high enough to prevent the animals from climbing them and sufficiently heavy to minimize the risk of an object falling due to an animal rearing and pushing on it.

As mentioned before, half of the cohort/sub-cohort was tested with the NOR paradigm on day 5 and 7, while the other half was tested with the OIP paradigm (which will not be shown in this thesis); the two groups were then tested again on day 9 and 11 with the appropriate remaining task. Objects were placed in two corners, along a diagonal line, and mice were individually transferred to the arena and positioned in the same corner as in the previous days, equally distanced to both objects. During the training phase, mice were left free to explore for 10 min two copies of the same objects, prior to being returned to their home cage. After a 10-min resting phase, mice were once again placed in the cage and tested for 10 min with a third copy of the same object used during the training phase (in order to further reduce olfactory cues, in combination with 20 % EtOH washings between animals) and a copy of a second object (Figure 2.21A).

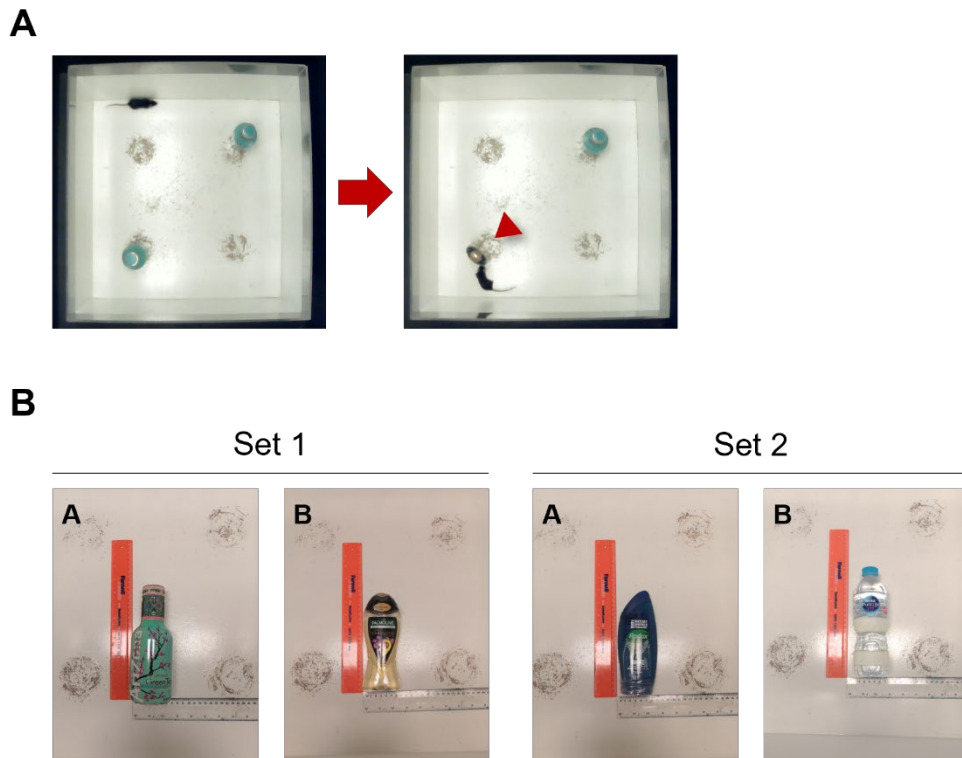


Figure 2.21 Representative images of the NOR assay set-up.

A) Mice were trained for 10 min with two identical copies of an object placed across a fixed diagonal, returned to their home cage for a 10-min rest phase and finally tested for 10 more minutes with a third copy of the familiar object, while a novel object was placed at the other side of the diagonal (red arrow). The diagonal was maintained constant, with mice being consistently placed in the same corner as the habituation phase, equally distant from both objects. **B)** Two sets of objects were employed during the NOR task. Each set comprised of 3 copies of object A and 3 of object B. An equal number of mice in each group was allocated either object A or B (for both repeats of the task) as novel object. The use of 3 copies of the same object ensured the task was not biased by olfactory cues which could help mice recognize the familiar object. Objects were all similar in size and tall enough to prevent animals from climbing on them. The time spent exploring each object during the test phase was manually quantified in blinded conditions.

Mice were allocated either object A or B (for both sets) as novelty object, taking care to maintain a balanced distribution across sexes and genotypes (so that approximately 50% of any group was tested with either object). The diagonal line along which objects were positioned was maintained constant throughout all testing sessions; however, during the test phase the novel object was allocated either to the

left or the right side, once again in a balanced way to compensate for any potential position bias.

Videos were recorded and were scored in a later occasion, to reduce interference during testing, using two stopwatches (one for each object; ThermoFisher Scientific); evaluation was performed in blinded conditions. Exploration was defined as the mouse's nose being pointed towards the object within 2 - 3 cm of the object, as well as the mouse rearing on the object, actively sweeping or sniffing. Animals that did not reach a minimum of 20 s total exploration time during the test phase were excluded from the analysis, due to potential confounding stress factors influencing mice behaviour (352). A percentage of exploration ($[\text{total exploration time} / \text{total test phase duration}] * 100$) and a discrimination index ($[\text{time spent exploring the novel object} - \text{time spent exploring the familiar object}] / \text{total exploration time}$) were calculated for each mouse.

2.8.4. Sucrose Preference (SP) paradigm

As mentioned above, at the age of approximately 54 weeks mice were isolated and transferred from medium to large polycarbonate cages with standard enrichment. Cage labels were then blinded and animals were allowed to habituate to the new environment for 24 hours. The next day, a second bottle of water was added to the cage and the mice were again allowed 24 hours to get accustomed to the change. The next morning both bottles were emptied, filled with either H₂O or a freshly made 2 % (w/v) sucrose solution (a commonly used concentration for this task (353)) and labelled accordingly. After being weighted, bottles were returned to the respective cages, randomly alternating position (left or right side of the cage) of the sucrose bottle (2.22).

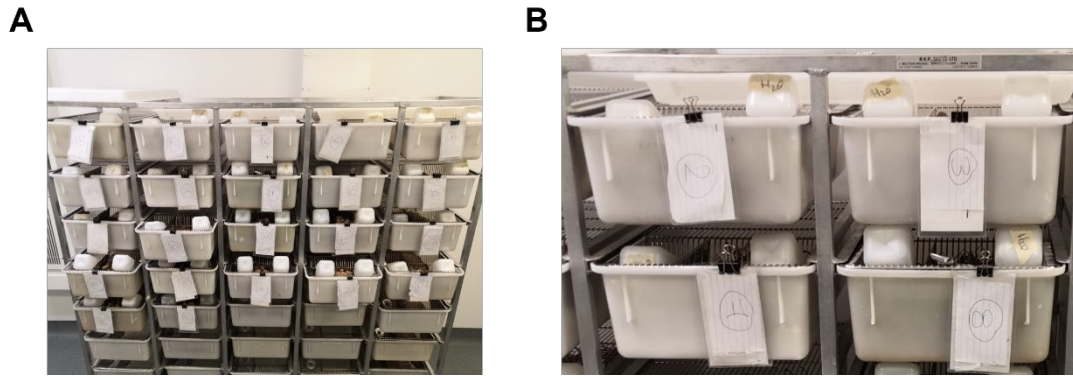


Figure 2.22 Sucrose Preference (SP) test set-up.

A) Example of cages set-up during the SP assay. **B)** A close-up from the previous image allows better visualization of the cage blinding, as well as of individual cages set-up. In particular, it is possible to appreciate the presence of two bottle per cage, one labelled with "H₂O", while the other contains freshly prepared 2 % sucrose solution. As it is possible to see, the water bottle positioning on either side of the cage is alternated across all animals, in order to account for any potential bias due to the position (e.g. bottles presented at different angles).

After 12 hours, bottle were weighted again and switched place to avoid any bias due to the position. Finally, after another 12 hours, bottles were weighted one last time, taking care to note any evident leak in the cage (which would lead the relative mouse to be excluded from the analysis). Mice were then returned to normal housing condition, i.e. provided with a single water bottle, and allowed to rest till the next day, before performing the nest scoring as discussed in the next session. A sucrose preference percentage ($[\text{volume of 2 \% sucrose consumed over 24 hours} / \text{total volume of liquid consumed over 24 hours}] * 100$) was calculated for each animal.

2.8.5. Nest Scoring

After being allowed to rest, mice were tested one last time to assess their ability to efficiently build a nest. At the end of the day (5-6 pm) any nesting material present in the cage was removed and replaced with two clean square of nestlets (approximately 8g total), consistently placed in the bottom left corner of the cage as shown in Figure 2.23A. Nests were scored the following day as close as possible to 1pm, in order to reduce variability across batches due to different length of testing.

Each cage was photographed for records, but nests were scored (still in blinded conditions) at the same time as image acquisition due to the difficulty of accurately assess depth of the nest site from the pictures. Nests were scored according to an established protocol (354). Briefly, if the material had not been manipulated at all (i.e. it had not been shredded or even moved from the initial position), the cage received a score of 0. If no nest site was obviously visible (with squares of nesting material simply moved around the cage and/or only partially shredded, with no clear central nest site) the cage received a score of 1. Finally, if a centralised nest site was visible, the nest was scored as if it was a square, with each side scored independently to then obtain an average value as shown in Figure 2.23B. If the walls were entirely flat, the nest/side was assigned a value of 2; if a slightly cupped shape was present, the nest/side scored a 3; if the wall appeared approximately half the height of a dome that would enclose the nest, it was assigned a 4 and, finally, in case of walls closer to the full height of a dome the score was a 5.



Figure 2.23 Representative images of the nest scoring set-up and scoring system.

A) Representative image of a random cage at the beginning of the test. The old nesting material was replaced by two nestlets squares (red arrow), but no other enrichment object was removed from the cage to avoid ulterior stress to the animal. B) In case of nest material manipulation and clear central nest site presence, nests were scored according to this visual reference chart. However, instead of scoring the nest as a single unit, it was treated as an imaginary square and each side assessed individually. The 4 values were then averaged to obtain the final nest score.

2.9. Statistics and analysis softwares

2.9.1. Cell assays

All the repetitions of the spreading assay, as well as the phagocytosis assay and the nuclei count for the Griess assay were performed using (Fiji is just ImageJ, version 1.52p).

2.9.2. qPCR data

Data was collected using QuantStudio™ Real-Time PCR software (version 1.7.1; Thermofisher Scientific). For each sample, 40-CT values were calculated as 40 (total number of cycles) minus the cycle threshold (number of cycles required for the fluorescent signal to exceed background level) for that sample. Similarly, 40-delta-CT (Δ CT) values were calculated as 40 minus the difference in cycle threshold between that of the target gene and the CT value of the endogenous control (*Ywhaz*). Relative quantification of fold change gene expression utilised the average Δ CT values of the biological replicates of the control group to create a 'Control Average', which was subtracted from the individual Δ CT to generate relative delta-delta CT ($\Delta\Delta$ CT), which was then converted to a log fold change ($2^{-(\Delta\Delta Ct)}$).

2.9.3. Flow Cytometry data

All flow cytometry files (for quantification of GFP expression in hABI3-overexpressing lines, as well as for DHR 123 analysis) were analysed using Flow Jo software (version 10.7.1; Beckton Dickinson).

2.9.4. Immunofluorescence and two-photon data

All histological analyses were performed on either Fiji Software or Imaris (Bitplane, Oxford Instruments, version 9.3.1) according to the protocols detailed in section 2.6. Similarly, two-photon videos were registered with MATLAB® (R2019 and following; MathWorks) and then processed with Fiji.

2.9.5. Behavioural paradigms data

Automated analysis of EPM and OF videos was performed using the EthoVision video-tracking system (v. XT 13; Noldus Information Technology Inc). Instead, NOR videos were manually scored in blinded conditions using two stopwatches.

2.9.6. Graphs and statistics

Statistical analyses were mostly performed using GraphPad Prism (GraphPad Software, version 8) and JASP (v0.16.3), or R (version 4.0.0).

All graphs were generated using GraphPad Prism. p -values of >0.05 were taken as non-significant (ns). p -values of ≤ 0.05 will be denoted with a single asterisk (*), p -values of ≤ 0.01 will be written as **, p -values of ≤ 0.001 by *** and p -value of ≤ 0.0001 as ****.

Chapter 3: Role of Abi3 on macrophages and microglia physiological activity

3.1. Introduction

Meticulous regulation of actin dynamics is essential to ensure correct execution of a multitude of cellular processes, including chemotaxis (277,355), phago- and endocytosis (356,357), as well as cell polarization, antigen presentation and other pro-inflammatory responses (262,264,323,358). It is therefore unsurprising that alterations of crucial regulators of the actin cytoskeleton can lead to immunodeficiencies such as the Wiskott-Aldrich syndrome and many more, as reviewed in (359). Changes in the rate of polymerisation/depolymerisation of actin filaments have also been associated to neurodegenerative diseases, including AD (360,361).

The identification of an AD risk variant (S209F) in ABI3, raises the question of how, exactly, this little-known member of the Abl-interactor family affects actin dynamics. As discussed in section 1.4, Abi3 is now accepted as a core microglia marker (293) and it is highly expressed in macrophages (291). It has been shown to form WAVE Regulatory Complex (WRC) distinct from that of Abi1, preventing WAVE2 phosphorylation and thus impacting cellular spreading (294,295). However, most of the studies currently available regarding the role of Abi3 on the actin cytoskeleton are based on non-physiological exogenous expression *in vitro* models (294,295,299,307,308,321).

For this reason, despite evidence supporting the decisive role of Abi3 in actin dynamics regulation, we are still lacking a deeper understanding of how exactly this factor modulates the WRC – and, consequently, the immune response – when expressed endogenously in macrophages. More is known about the role of Abi3 in microglia due to studies published during the writing of this thesis (302,303). Karahan *et al.* recently reported a significant reduction in microglia motility during an *in vitro* wound-healing assay, as well as a lower phagocytic activity, when Abi3 was knocked down, while *in vivo* data suggested a role of Abi3 in immune response regulation (302). However, further investigation is required to understand the mechanisms behind these observations.

Thus, the aim of this chapter was to investigate the effect of Abi3 alterations on macrophages. In order to do so, oestrogen-regulated Hoxb8 conditionally-immortalised bone marrow precursors (MØPs) and bone marrow derived macrophages (BMDMs) were obtained from Abi3-deficient and control mice, differentiated with the addition of M-CSF (20ng/ml) to model macrophages with “relevant” Abi3 expression *in vitro*. In the course of this chapter, cells were tested to

assess changes in their ability to spread on a fibronectin substrate following forced overexpression of human ABI3 or knockout of endogenous Abi3. Abi3-deficient BMDMs were also functionally challenged to evaluate Abi3 impact on phagocytic activity and release of inflammatory mediators, specifically ROS and NO.

3.2. Results

3.2.1. Overexpression of Abi3 impacts actin-mediated cell spreading in NIH 3T3 cell lines

As previously mentioned (see section 1.4), Sekino *et al.* reported a disruption of actin polymerisation following ABI3 overexpression (294). To do so, the authors transduced NIH 3T3 fibroblasts, a mouse embryonic fibroblast cell line expressing extremely low levels of endogenous Abi3 (294), with a recombinant retrovirus containing FLAG-tagged human ABI3 (hABI3).

At the commencement of this study, due to the identification of the rare S209F variant of ABI3, Dr R. Jones transduced NIH 3T3 cells with lentiviral vectors (kindly generated by Dr D. Fathalla) encoding either of the two known human variants of hABI3 (the common S209 and the rare F209) linked via a T2A-peptide to eGFP. A control cell line, transduced with a vector containing exclusively the T2A-eGFP construct (hereafter called “Empty Vector”), was generated at the same time.

These cells were then employed in an actin-mediated spreading assay, described in detail in section 2.4.1 of the Methods. Notably, the following assessment of hABI3’s effect on lamellipodia formation was not limited to the quantification of the number of cells showing membrane protrusions as shown by Sekino *et al.*, but was based on morphological analysis of the cells through Fiji software.

The experiment was repeated three times on the same set of cell lines, before switching to a different cellular model for reasons that will be discussed below. Figure 3.1 shows representative images (Figure 3.1A), as well as area and circularity quantification (Figure 3.1B-I), from the first repeat of the experiment.

The Fiji analysis showed that both variants displayed a significant reduction in cell area at 15 and 30 minutes compared to the control ($p \leq 0.0001$ for both groups at both time points, Figure 3.1B and D and Table 3.1, part I, replicate 1). At 15 minutes, the S209 variant resulted in smaller cells compared to the F209 variant ($p \leq 0.0001$, Figure 3.1B and Table 3.1, part I, replicate 1). It was interesting to note that at all the other time points the F209 variant showed the strongest effect on the NIH 3T3 cell spreading ability. Indeed, after 30 minutes of incubation the cells overexpressing the F209 variant were significantly smaller than both the common variant and the control ($p \leq 0.0001$ for both, Figure 3.1D and Table 3.1, part I,

replicate 1). At 2 hours, there was no significant difference in area values between the ABI3-S209 expressing cells and the control, while the ABI3-F209 expressing cells still showed a significant decrease compared to both the empty vector ($p \leq 0.0001$) and the S209 variant ($p \leq 0.001$, Figure 3.1F and Table 3.1, part II, replicate 1). The same was true after 4 hours, where only the rare variant appeared still significantly smaller than both the control ($p \leq 0.01$) and the S209 variant ($p \leq 0.0001$), as shown in Figure 3.1H and Table 3.1, part II, replicate 1.

When considering cell circularity, at 15 minutes it appeared to be significantly higher in the ABI3-S209 expressing group compared to the ABI3-F209 expressing sample ($p \leq 0.0001$, Figure 3.1C), with both overexpressing cell lines being significantly more circular than the empty vector control ($p \leq 0.0001$ for the common variant, $p \leq 0.01$ for the rare one, Figure 3.1C and Table 3.1, part I, replicate 1). After 30 minutes of incubation, the difference between the two variants became insignificant, but they both showed a less elongated morphology than the control ($p \leq 0.0001$ for both, Figure 3.1E and Table 3.1, part I, replicate 1). At the following time point, ABI3-S209 expressing cells were once again the least circular ones ($p \leq 0.001$ compared to the control and $p \leq 0.05$ compared to the rare variant), with the empty vector being the most elongated ($p \leq 0.01$ compared to ABI3-F209 expressing cells; Figure 3.1 G and Table 3.1, part II, replicate 1). Finally, at 4 hours the rare variant still showed a rounder morphology compared to the other two lines ($p \leq 0.001$ compared to the control and $p \leq 0.01$ compared to the S209 variant), although the S209 variant was still significantly less circular than the control ($p \leq 0.05$; Figure 3.1 I and Table 3.1, part II, replicate 1).

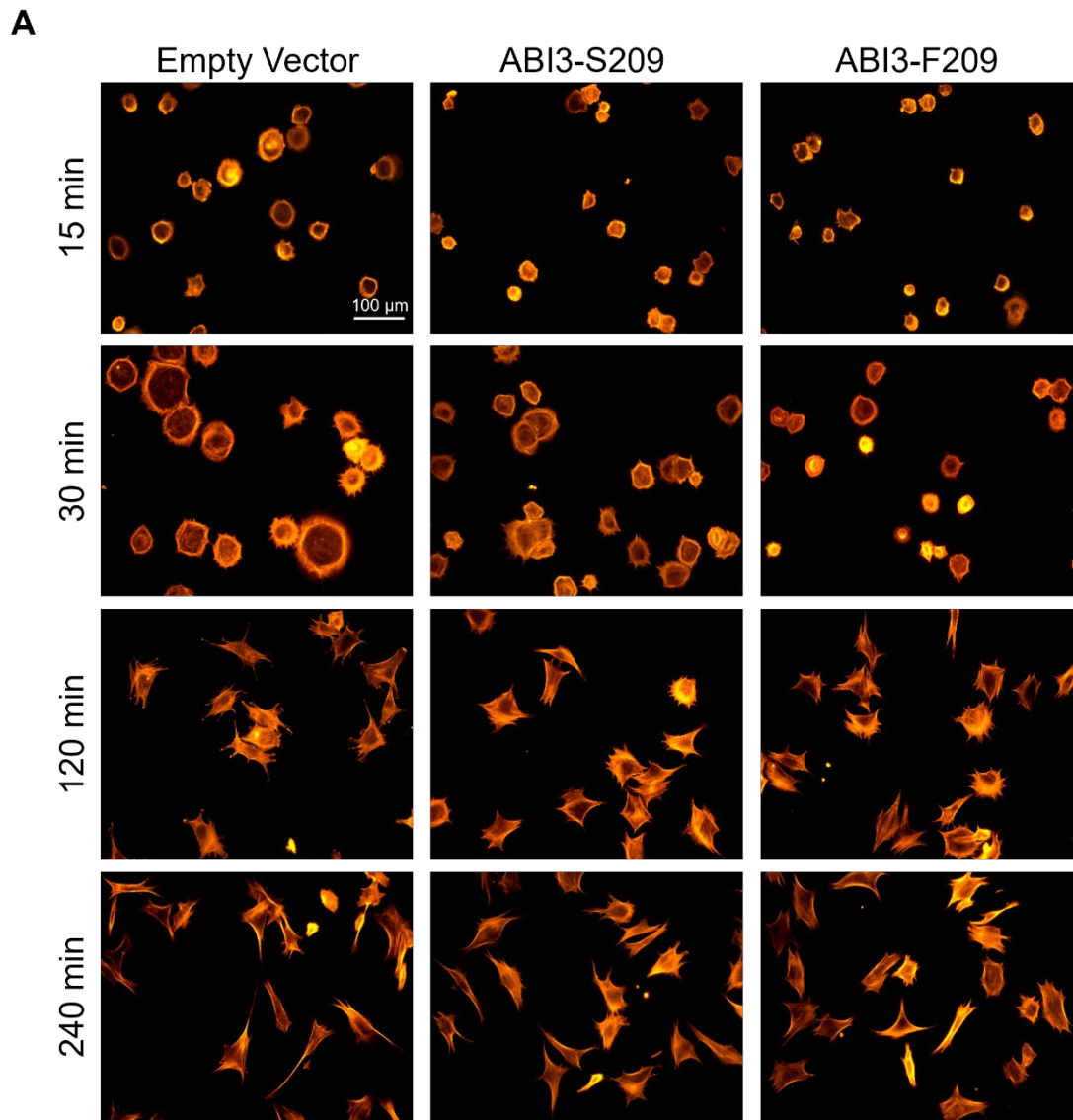


Figure 3.1, part I. Representative images of NIH 3T3 cells during the first of three repetitions of the actin-mediated spreading assay.

A) NIH 3T3 transduced with either an empty vector (which was identical to the other two, bar the ABI3 coding sequence), the common S209, or the rare F209 variant of ABI3, were stained using Phalloidin-AF555 (orange) to visualize actin cytoskeleton. Both overexpressing cell lines showed an impaired spreading capacity, with smaller and rounder cells compared to the empty vector control.

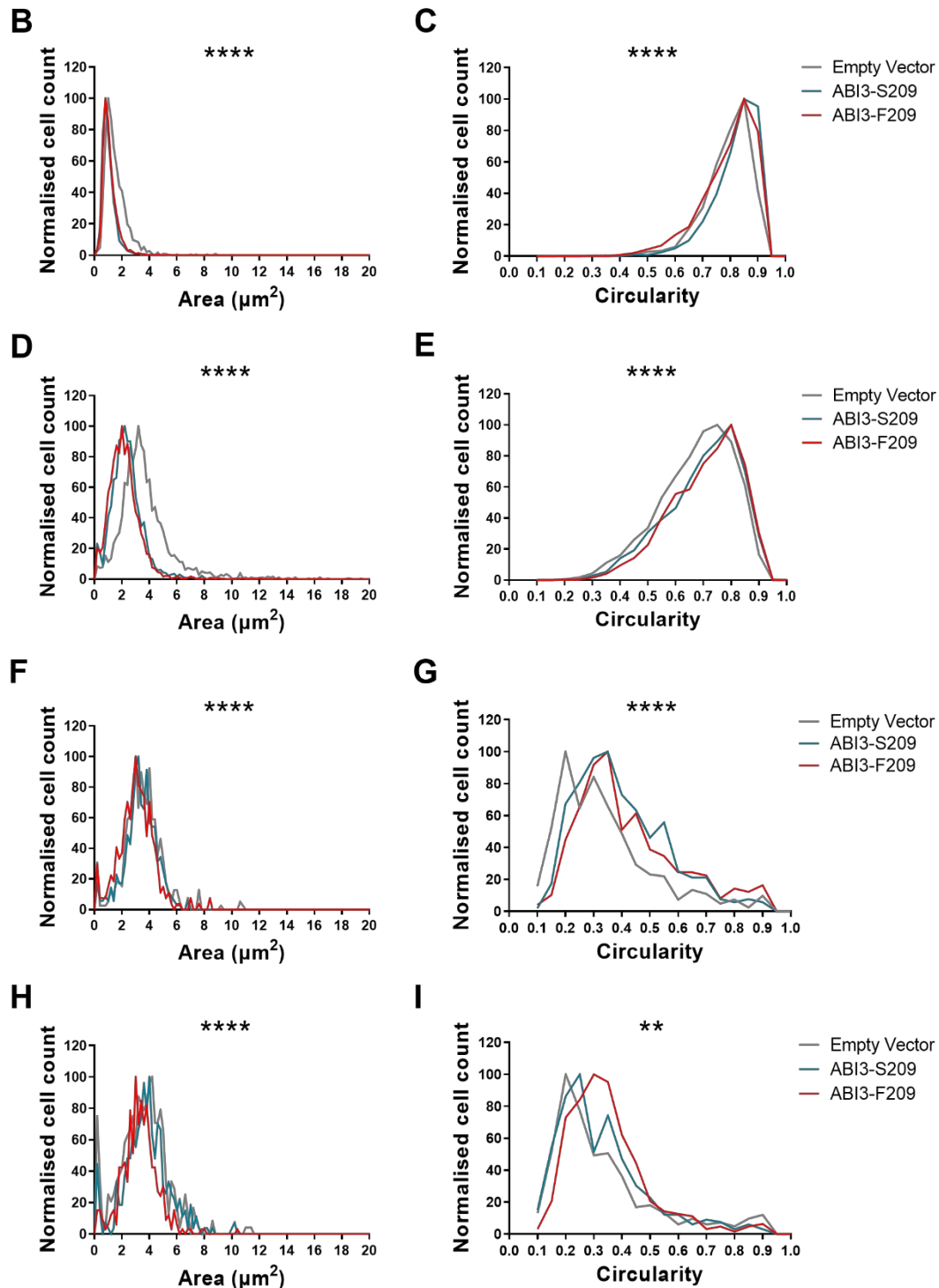


Figure 3.1, part II. Quantification of NIH 3T3 cell surface area and circularity following the first repetition of the spreading assay.

Area and circularity values obtained from the Fiji analysis are shown as normalized histograms of the frequency distribution of the samples. Grey line represents the empty vector control, while the blue line indicate the cells overexpressing the common S209 variant and the red line those transduced with the rare F209 variant. The results of the non-parametric ANOVA performed on each set of samples are reported on every graph. **B)** Graphical representation of the cell surface after 15 minutes, **D)** 30 minutes, **F)** 2 hours and

*H) 4 hours. C), E), G) and I) Evaluation of cell circularity at the same time points (C, 15 minutes; E, 30 minutes; G, 2 hours; I, 4 hours). Data were analysed via Kruskal-Wallis test to compare the medians, and wherever a significant difference was found, the individual p-values were calculated using Dunn's multiple comparison test. ** $p \leq 0.01$ and **** $p \leq 0.0001$. $n > 1400$ for the 15 and 30 minutes time points, whereas $n > 300$ for the 2 and 4 hours incubations.*

The second and third repetitions of the spreading assay, performed in a different lab with new equipment, were carried out with half the amount of NIH 3T3 cells, to increase the number of spatially separate cells available for the analysis, especially at the longer time points. The data shown in Figure 3.1 were consistent with previous observations of ABI3 inhibitory action on cell spreading and motility (294,299,305), and led to speculation about a possible hyper-functional nature of the rare F209 variant. However, a notable variability in the results was observed in the following repetitions, as shown in Table 3.1.

During the second repetition, the S209 variant resulted in a bigger cell size compared to both the empty vector and the rare variant after 15 minutes of incubation ($p \leq 0.0001$ compared to both the other groups), whereas cells expressing the F209 variant were significantly smaller than the control as well ($p \leq 0.0001$; Table 3.1, part I, replicate 2). After 30 minutes, the empty vector control was significantly bigger than the two overexpressing cell lines ($p \leq 0.01$ compared to the ABI3-S209 expressing cells, $p \leq 0.0001$ compared to the ABI3-F209 sample) and the F209 variant led to a greater reduction in cell area than the other variant ($p \leq 0.0001$; Table 3.1, part I, replicate 2). At both the longest time points, however, cells overexpressing the S209 variant resulted once again significantly bigger than the empty vector control ($p \leq 0.05$ for both at both time points), as well as than the ABI3-F209 expressing cells ($p \leq 0.0001$), which appeared to be the smallest ($p \leq 0.0001$ compare to empty vector at both time points, Table 3.1, part II, replicate 2).

A similar pattern was observed during the third repeat. The F209 variant proved to exert the strongest effect on cell size at all time points compared to both the empty vector control ($p \leq 0.0001$ for all) and the ABI3-S209 expressing cells ($p \leq 0.0001$ at 15, 30 and 240 minutes, $p \leq 0.05$ at 120 minutes; Table 3.1, replicate 3). Instead, no significant difference in cell size was noted at 15 and 30 minutes between the common variant and the empty vector (Table 3.1, part I, replicate 3), although the ABI3-S209 expressing fibroblasts resulted smaller than the control line at the longer

time points ($p \leq 0.001$ and $p \leq 0.01$ for 2 and 4 hours respectively Table 3.1, part II, replicate 3).

The variability between biological replicates was even more visible when analysing cell circularity. Indeed, at 15 minutes the empty vector control appeared the most circular in both repeats ($p \leq 0.0001$ compared to both variants in the second replicate, $p \leq 0.05$ compared to the S209 variant in the third), while the difference between the two variant wasn't significant in either experiment (Table 3.1, part I, replicate 2 and 3). After 30 minutes, in the second repetition the rare variant resulted the least circular ($p \leq 0.0001$ compared to both control and common variant) while the ABI3-S209 expressing cells were significantly more elongated than the empty vector ($p \leq 0.0001$; Table 3.1, part I, replicate 2). Instead, no significant difference in circularity was observed at the same time point during the next repetition (Table 3.1, part I, replicate 3). On the other hand, neither variant caused a significant impairment in cell elongation compared to the empty vector at 2 and 4 hours during the second repeat (Table 3.1, part II, replicate 2). However, at 2 hours the ABI3-S209 expressing cells resulted significantly less elongated than the ones overexpressing the F209 variant ($p \leq 0.05$), while at the last time point this trend appeared inverted ($p \leq 0.0001$; Table 3.1, part II, replicate 2). In the third experiment, instead, the empty vector control was the most elongated at both the longest time points ($p \leq 0.0001$ and $p \leq 0.001$ compared to ABI3-S209 and -F209 expressing cells respectively at 2 hours, $p \leq 0.0001$ for both variants at 4 hours; Table 3.1, part II, replicate 3), while in both cases ABI3-S209 overexpressing cells emerged as the most circular ($p \leq 0.001$ and $p \leq 0.0001$ compared to the rare variant at 120 and 240 minutes respectively; Table 3.1, part II, replicate 3).

A

A = B
 A > B
 A < B

		Area																	
		15 min									30 min								
Replicate		1			2			3			1			2			3		
Cell line	EV	ABI3-S209	ABI3-F209	EV	ABI3-S209	ABI3-F209	EV	ABI3-S209	ABI3-F209	EV	ABI3-S209	ABI3-F209	EV	ABI3-S209	ABI3-F209	EV	ABI3-S209	ABI3-F209	
Number of values	1445	2628	2250	669	908	927	802	610	426	2418	2519	2536	645	765	1022	1286	807	718	
Median	689.5	476.1	505.0	438.0	551.0	381.5	281.6	293.9	260.1	1719	1162	1059	616.0	556.0	363.2	435.8	432.3	370.4	
EV vs. ABI3-S209		****			****			ns			****			**			ns		
EV vs. ABI3-F209		****			****			****			****			****			****		
S209 vs. F209		****			****			****			****			****			****		

		Circularity																	
		15 min									30 min								
Replicate		1			2			3			1			2			3		
Cell line	EV	ABI3-S209	ABI3-F209	EV	ABI3-S209	ABI3-F209	EV	ABI3-S209	ABI3-F209	EV	ABI3-S209	ABI3-F209	EV	ABI3-S209	ABI3-F209	EV	ABI3-S209	ABI3-F209	
Number of values	1445	2628	2250	669	908	927	802	610	426	2418	2519	2536	645	765	1022	1286	807	718	
Median	0.809	0.837	0.815	0.817	0.594	0.608	0.802	0.788	0.792	0.695	0.721	0.729	0.688	0.611	0.735	0.620	0.602	0.619	
EV vs. ABI3-S209		****			****			*			****			****			ns		
EV vs. ABI3-F209		**			****			ns			****			****			ns		
S209 vs. F209		****			ns			ns			ns			****			ns		

Table 3.1part I. Detailed report of descriptive statistics and ANOVA results for the shortest time points of all three repetitions of the NIH 3T3 spreading assay.

The table shows the number of cells evaluated in each group, as well as the median of each sample. The summarised results of Dunn's multiple comparison test are reported for each pair of cell lines within the same experiment whenever the Kruskal-Wallis test was significant. To facilitate visualisation, asterisks are colour coded: for each pairwise comparison A vs. B, grey cells indicate no significant difference, blue cells indicate A > B and orange cells mean A < B. *p<0.05, **p<0.01, ***p<0.001 and ****p<0.0001.

B

Area																		
Replicate	120 min									240 min								
	1			2			3			1			2			3		
Cell line	EV	ABI3-S209	ABI3-F209	EV	ABI3-S209	ABI3-F209	EV	ABI3-S209	ABI3-F209	EV	ABI3-S209	ABI3-F209	EV	ABI3-S209	ABI3-F209	EV	ABI3-S209	ABI3-F209
Number of values	461	362	411	506	488	567	465	441	387	392	357	354	439	490	748	389	424	357
Median	1753	1729	1558	1356	1469	1084	1332	1157	1011	1876	1924	1696	1737	1940	1317	1829	1663	1409
EV vs. ABI3-S209	ns			*			***			ns			*			**		
EV vs. ABI3-F209	****			****			****			****			****			****		
S209 vs. F209	****			****			*			**			****			****		

Circularity																		
Replicate	120 min									240 min								
	1			2			3			1			2			3		
Cell line	EV	ABI3-S209	ABI3-F209	EV	ABI3-S209	ABI3-F209	EV	ABI3-S209	ABI3-F209	EV	ABI3-S209	ABI3-F209	EV	ABI3-S209	ABI3-F209	EV	ABI3-S209	ABI3-F209
Number of values	461	362	411	506	488	567	465	441	387	392	357	354	439	490	748	389	424	357
Median	0.297	0.362	0.330	0.324	0.315	0.352	0.293	0.455	0.357	0.258	0.284	0.325	0.213	0.241	0.205	0.191	0.269	0.229
EV vs. ABI3-S209	****			ns			****			*			ns			****		
EV vs. ABI3-F209	**			ns			***			****			ns			****		
S209 vs. F209	*			*			***			**			****			****		

Table 3.1, part II. Detailed report of descriptive statistics and ANOVA results for the longest time points of all three repetitions of the NIH 3T3 spreading assay.

Data analysed via Kruskal-Wallis test. To facilitate visualisation, asterisks are colour coded: for each pairwise comparison A vs. B, grey cells indicate no significant difference, blue cells indicate A > B and orange cells mean A < B. *p≤0.05, **p≤0.01, ***p≤0.001 and ****p≤0.0001.

The differing results observed during the first experiment could have been a result of different expression levels of the lentiviral construct in the various cell lines. To address this potential confounder, during the second and third repetition of the experiment the levels of the GFP reporter were assessed for each group. Figure 3.2A shows the gating strategy applied in the analysis of both repetitions, while Figure 3.2B reports the percentage of GFP⁺ single cells for each cell line. During both experiments, ABI3-S209 expressing cells showed the highest percentage of positive cells (93.7 % and 95.1 %, Figure 3.2B), while only 88.5 % of ABI3-F209 cells expressed GFP in the second experiment and 90.3 % in the third repeat (Figure 3.2B). At the same time, ABI3-F209 expressing cells displayed the highest Mean Fluorescence Intensity (MFI) among the three groups in both cases, while the fibroblasts expressing the common variant exhibited more variable expression (Figure 3.2C). This was confirmed when considering both the MFI and the percentage of GFP⁺ cells at the same time (as indicated by the “Fluorescence Index” in figure 3.2D). While the number of repetitions (n=2) prevented a statistical confirmation of these observed differences in expression, the difficulty in stably expressing ABI3 via lentiviral transduction could explain the variation observed among experimental repetitions, as discussed in section 3.3.

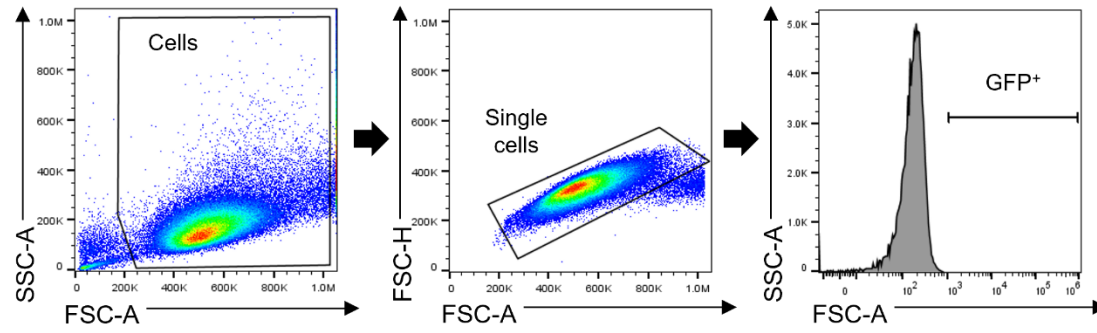
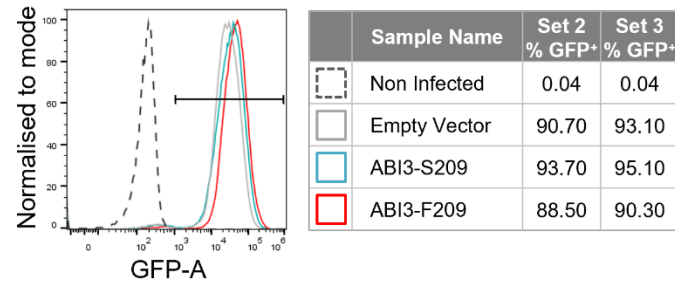
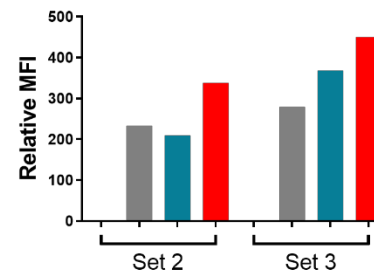
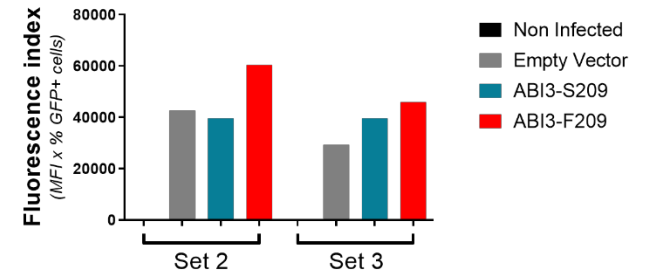
A**B****C****D**

Figure 3.2 Detection of GFP in NIH 3T3 cells transduced with a lentiviral construct containing either of the human ABI3 variants.

Grey represents the empty vector control, blue the ABI3-S209 overexpressing cells and red the ABI3-F209 expressing ones, while black indicates the non-infected control. **A)** Set of consecutive plots demonstrating the gating strategy to evaluate GFP expression in the overexpressing NIH 3T3 cells. A first gate was applied to exclude the majority of debris based on cell size and complexity. A second gate delimited the single cell population to avoid biases due to the analysis of doublets. Finally, a non-infected NIH 3T3 line was used to set up a gate to identify GFP⁺ cells based on signal intensity. **B)** Combined histograms of the GFP expression in the empty vector control, ABI3-S209 and -F209 overexpressing cells compared to a non-infected control during one of the repetitions, with a table detailing the percentage of GFP⁺ cells in each sample (referred to the single cell population). **C)** Graphical representation of the Mean Fluorescence Intensity (MFI) values, relative to the non-infected control, in the GFP⁺ population of both experimental sets. **D)** Evaluation of the fluorescence index (MFI X the percentage of single cells expressing GFP) calculated for each cell. Due to the lack biological triplicates, no statistical test could be performed. n=2.

3.2.2. Alterations in Abi3 levels cause defective spreading ability in Macrophages

While it may have been possible to sort all three cell lines again to obtain cells with comparable levels of expression of the lentiviral construct, it was decided to stop working with NIH 3T3 cells and start using more biologically relevant cells, where we could better control Abi3 expression. Dr R. Jones generated three independent pairs of conditionally immortalised MØP cell lines from the bone marrow of Abi3-WT and -KO mice as described in Methods section 2.3.5. She had previously confirmed the absence of Abi3 exons 5-7 at the genomic level in Abi3-deficient animals (Figure 3.3A) and in the first pair of cell lines she generated (Figure 3.3B) (329). She had also evaluated the impact of GM-CSF and M-CSF differentiation (in order to obtain dendritic cell-like or macrophage-like cells respectively) on Abi3 expression levels compared to MØP cells maintained indefinitely in culture with GM-CSF and β -Estradiol in the media (329). Consistently with the ImmGen microarray analysis of Abi3 expression in BMDMs and bone marrow-derived dendritic cells (291), she had reported a slightly higher (but not significant) Abi3 expression in the

M-CSF-differentiated samples compared to the GM-CSF ones analysed by qPCR (329). Considering the higher pertinence of macrophage-like cells in the study of *Abi3* in a microglial context and the known importance of Colony Stimulating Factor 1 receptor (CSF-1R) in macrophages and microglial biology (15,41), it was decided to use M-CSF in all the following experiments.

Once all three pairs of cell lines had been generated, Dr R. Jones confirmed *Abi3* knock-out at the mRNA level by qPCR. Figure 3.3 shows the 40-CT (Figure 3.3C), and relative gene expression (normalised to the average value of *Abi3*-WT controls, Figure 3.3E). The 40- Δ CT values were normalised by the expression level of the endogenous gene *Ywhaz* (Figure 3.3D). *Abi3* levels were barely detectable in both differentiated and undifferentiated samples derived from *Abi3*-KO mice, showing a significantly lower 40-CT ($p \leq 0.0001$ for both treated and untreated cells; Figure 3.3C) and 40- Δ CT ($p \leq 0.01$ in M \emptyset Ps and $p \leq 0.001$ in M-CSF differentiated cells; Figure 3.3D) values than their respective control. Congruently, *Abi3* expression was significantly lower in differentiated cells derived from *Abi3*-deficient mice compared to the differentiated control ($p \leq 0.0001$; Figure 3.3E). Notably, *Abi3*-WT cells showed significantly higher levels of *Abi3* after M-CSF treatment ($p \leq 0.0001$) as reported by Dr R. Jones in her thesis (329).

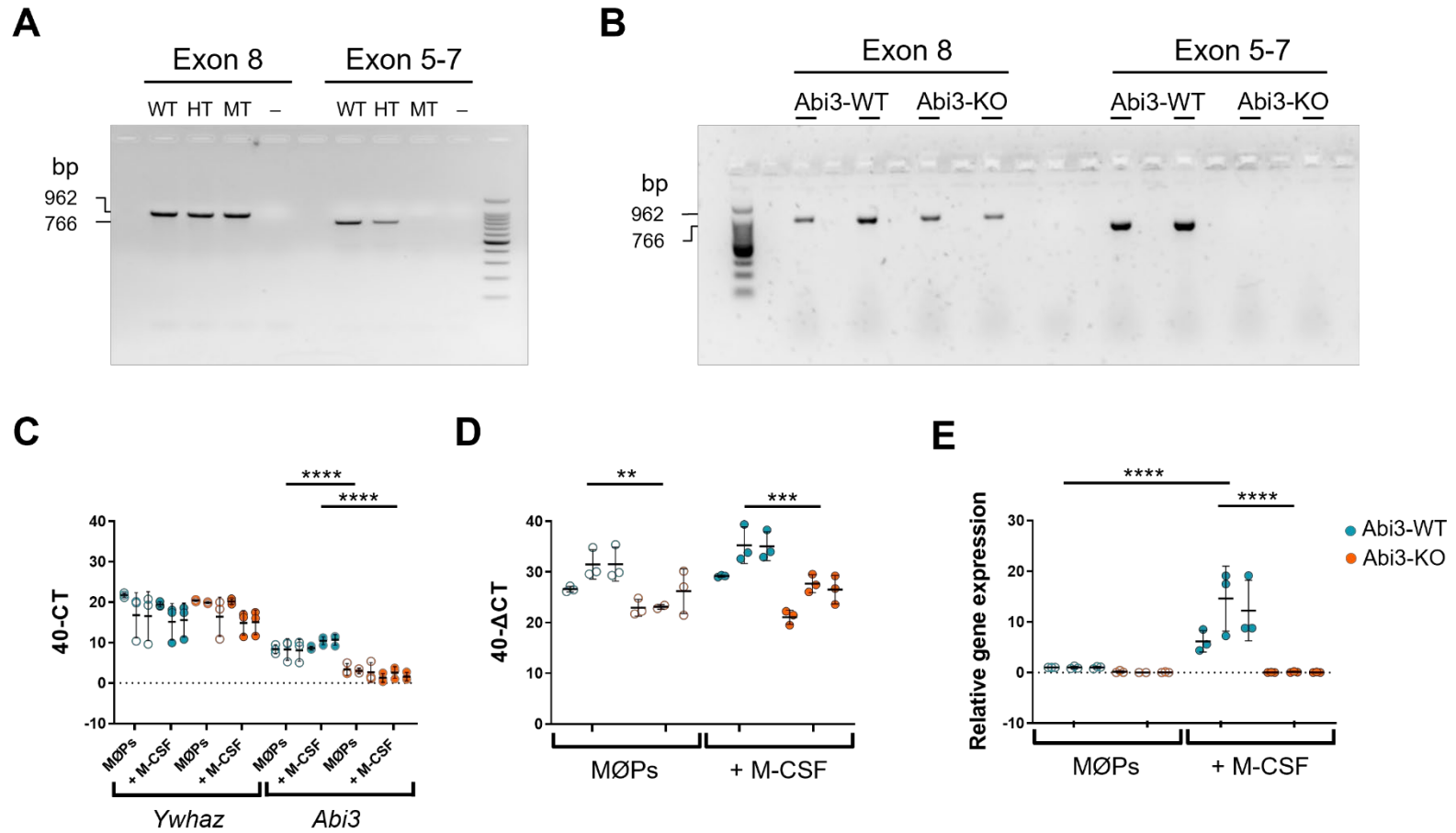


Figure 3.3. Confirmation of *Abi3* knock-out at genomic and transcriptional level in *Abi3*-KO mice and cell lines.

The raw data shown in this figure were kindly provided by Dr R. Jones, but were then analysed autonomously for the purpose of this thesis. Band size in PCR gels was estimated using a Promega 100bp Ladder. Blue represents *Abi3*-WT cells while orange indicates the -KO samples. Each dot represents the average of 3 technical replicates. Three different cell lines were tested for each genotype and each cell line was tested in 3 separate experiments. The horizontal black lines indicate the means, while the vertical bars reflect the standard deviation within each group. Cells were tested after being either maintained with GM-CSF and β -Estradiol (MØPs, represented by empty circles) or differentiated using M-CSF (filled circles). *Ywhaz* mRNA was used as endogenous housekeeping control. Whenever *Abi3* mRNA levels in *Abi3*-KO cells resulted in no signal despite high levels of *Ywhaz*, a CT of 40 was assigned to allow for statistical analysis. **A)** Confirmation of the knock-out of Exon 5-7 in genomic DNA extracted from *Abi3*-WT, -Het (HT) and -KO mice. **B)** Genomic PCR for *Abi3* Exons 5-7 and 8 on *Abi3*-WT and -KO MØPs. **C)** Graphical representation of the 40-CT values and **D)** of the 40- Δ CT values deriving from the qPCR analysis. **E)** Relative gene expression for *Abi3*, normalised to the average value of the *Abi3*-WT MØPs. Asterisks indicate p-values, where ** $p \leq 0.01$ *** $p \leq 0.001$ and **** $p \leq 0.0001$. Data analysed by One-Way ANOVA followed by Tukey's multiple comparison test. $n=3$.

Prior to the results of the NIH 3T3 spreading assay, Dr R. Jones had transduced the original *Abi3*-KO MØP cell line with the same *Abi3* over-expression and control lentiviral vectors used with the fibroblast line. For this reason, considering the variability in GFP reporter expression mentioned earlier in this chapter, a single experiment was performed on MØPs-derived macrophages (MØs) originated from these overexpressing cells, in order to assess whether MØs would react differently to *Abi3* alterations compared to fibroblasts.

Figure 3.4A shows the timeline of the differentiation protocol preceding the spreading assay performed on hABI3-overexpressing MØs, while Figure 3.4B shows representative images of the assay. At the first time point, Fiji analysis highlighted a reduction in surface area in both variants compared to the control, although this was only significant in the case of the ABI3-F209 expressing cells ($p \leq 0.001$) and no significant difference was noted between the two variants (Figure 3.4C and Table 3.2). As expected from the visual assessment, at 30 minutes the cells transduced with the empty vector resulted bigger than those expressing the rare variant ($p \leq 0.01$), but only slightly smaller than the ABI3-S209 expressing sample (data not significant, Figure 3.4E and Table 3.2). Similar to the NIH 3T3

experiments, the F209 variant appeared to lead to a greater reduction in cell size than the common one ($p \leq 0.0001$). At 2 hours, cells expressing the S209 variant resulted significantly bigger than the rare variant ($p \leq 0.0001$). However, they did not differ in size from the control cells, which were instead significantly bigger than the ABI3-F209 expressing group ($p \leq 0.0001$, Figure 3.4G and Table 3.2). Finally, after 4 hours both variants led to a decrease in cell size compared to the control ($p \leq 0.0001$ for both) while it was not possible to observe a notable difference between them (Figure 3.4I and Table 3.2).

With respect to cell solidity, a certain variability between time points was observed. After 15 minutes of incubation the empty vector led to the cells with the most solid morphology ($p \leq 0.0001$, compared to both variants), while no significant difference was seen between the variants. At 30 minutes a significant difference could be appreciated only between the two variants ($p \leq 0.05$; Figure 3.4F and Table 3.2). At 2 hours the frequency distribution of all three samples was extremely variable, leading to a complete lack of significant differences (Figure 3.4H and Table 3.2). Finally, at the last time point, both variants impaired cell spreading resulting in more solid cells compared to the control ($p \leq 0.05$ for the ABI3-S209 and $p \leq 0.0001$ for the ABI3-F209 expressing cells), with no significant effect between variants (Figure 3.4J and Table 3.2).

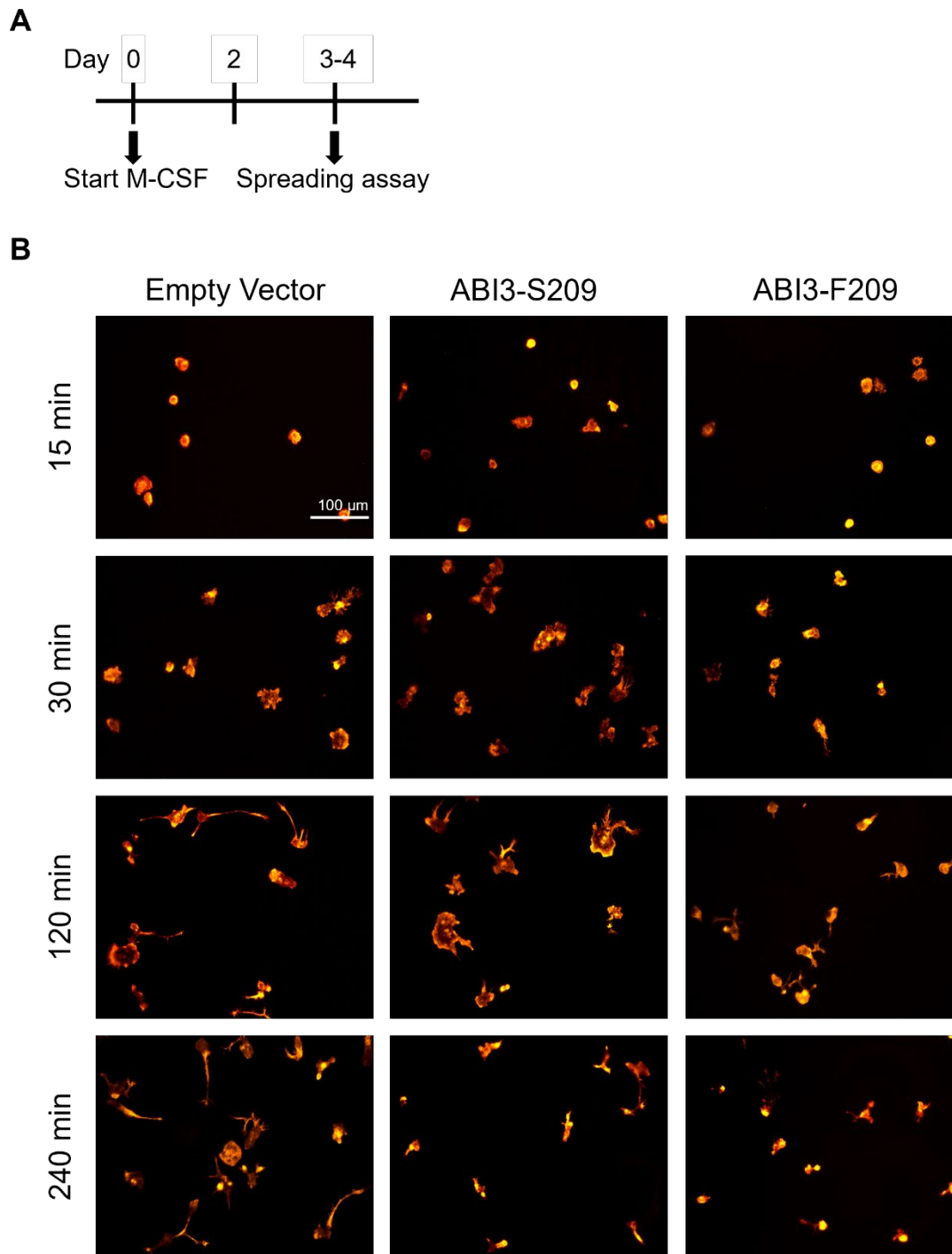


Figure 3.4, part I. Representative images from the single spreading assay experiment performed on Abi3-overexpressing M-CSF differentiated MØs.

A) Schematic representation of the M-CSF differentiation timeline used for all the experiments in this section employing MØPs-derived MØs. MØPs cells were supplemented with 20 ng/ml of M-CSF at day 0 and 2, before being tested on day 3 (or 4, in the case of subsequent experiments). For more details please see Methods sections 2.3.2 and 2.4.1. **B)** Representative images of all experimental groups at each of the chosen time-points, stained

with Phalloidin-AF555 (orange) to assess their actin cytoskeleton. Similarly to what had been observed in the fibroblast cell line, the over-expression of the F209 variant led to smaller and less ramified cells compared to the empty vector control. Morphological changes in the ABI3-S209 expressing group were visible but not as easily interpreted without the aid of the following Fiji analysis.

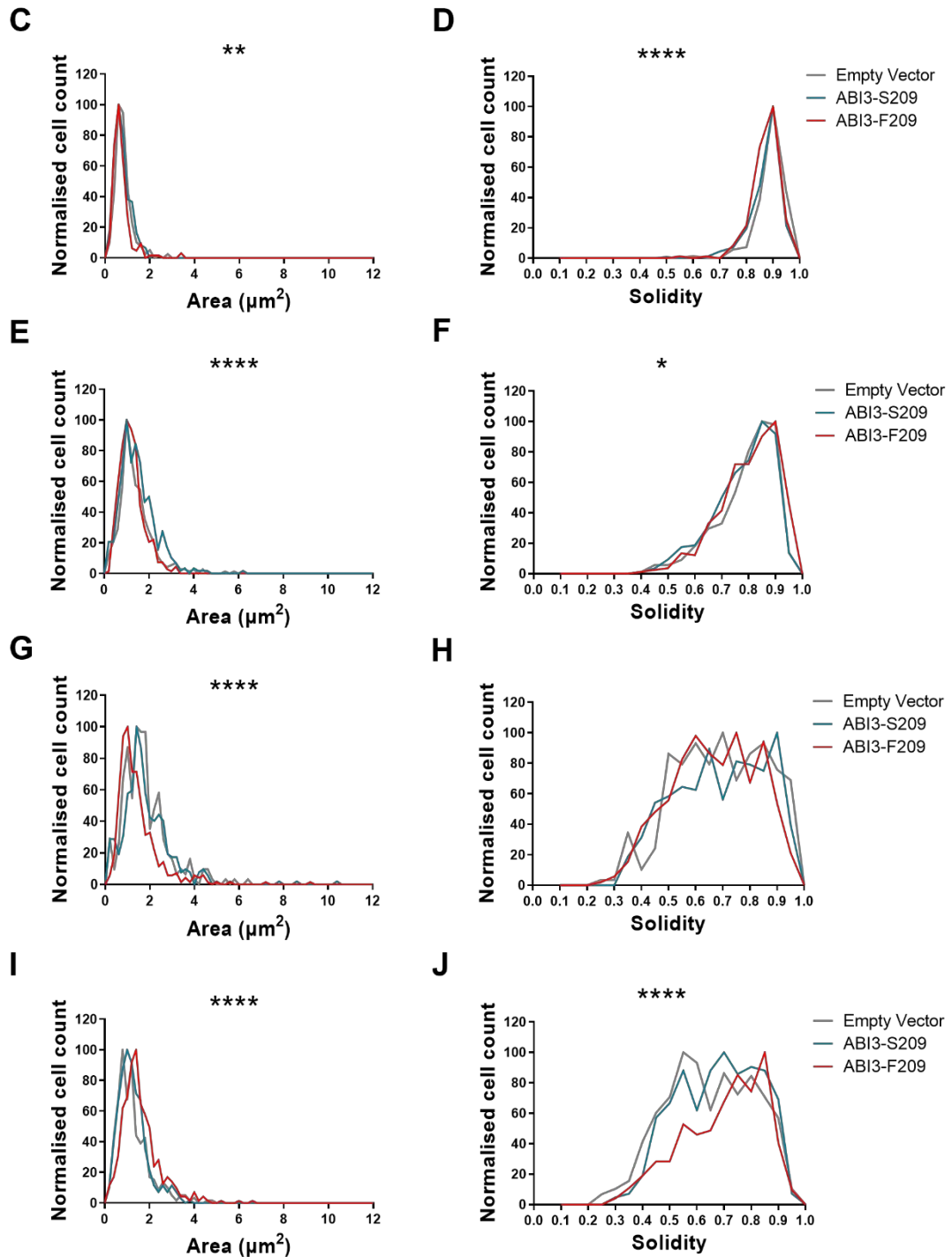


Figure 3.4, part II. Quantification of ABI3 overexpressing MØs cell surface area and solidity.

As before, area and solidity values obtained from the Fiji analysis are shown as normalized histograms of the frequency distribution of the samples. Grey line represents the empty vector control, while the blue line indicates the cells overexpressing the common S209 variant and the red line those transduced with the rare F209 variant. The results of any significant Kruskal-Wallis test are reported on the relative graph by means of asterisks. **C), E), G) and I)** Graphical representation of cell area over the four chosen time-points (C, 15 minutes; E, 30 minutes; G, 2 hours; I, 4 hours). **D), F), H) and J)** Evaluation of cell solidity at the same time points (D, 15 minutes; F, 30 minutes; H, 2 hours; J, 4 hours). Data were analysed via Kruskal-Wallis test to compare the medians, and wherever a significant difference was found, the individual p-values were calculated using Dunn's multiple comparison test. * $p \leq 0.05$, ** $p \leq 0.01$ and **** $p \leq 0.0001$. $n > 190$.

Area												
Time point	15 min			30 min			120 min			240 min		
Cell line	EV	ABI3-S209	ABI3-F209	EV	ABI3-S209	ABI3-F209	EV	ABI3-S209	ABI3-F209	EV	ABI3-S209	ABI3-F209
Number of values	271	228	192	394	411	400	263	389	441	488	350	455
Median	0.740	0.704	0.636	1.243	1.357	1.142	1.588	1.597	1.181	1.411	1.115	1.135
EV vs. ABI3-S209	ns			ns			ns			****		
EV vs. ABI3-F209	***			**			****			****		
S209 vs. F209	ns			****			****			ns		

Solidity												
Time point	15 min			30 min			120 min			240 min		
Cell line	EV	ABI3-S209	ABI3-F209	EV	ABI3-S209	ABI3-F209	EV	ABI3-S209	ABI3-F209	EV	ABI3-S209	ABI3-F209
Number of values	271	228	192	394	411	400	263	389	441	488	350	455
Median	0.902	0.891	0.880	0.816	0.807	0.823	0.695	0.703	0.669	0.643	0.681	0.726
EV vs. ABI3-S209	****			ns			ns			*		
EV vs. ABI3-F209	****			ns			ns			****		
S209 vs. F209	ns			*			ns			ns		

Table 3.2 Detailed report of descriptive statistics and ANOVA results for the spreading assay performed on Abi3-overexpressing MØs.

As before, the table shows the number of cells evaluated for each experimental group, noteworthy descriptive statistics and the summarised results of Dunn's multiple comparison test following a significant Kruskal-Wallis test result. To facilitate visualisation, asterisks are colour coded: for each pairwise comparison A vs. B, grey cells indicate no significant difference, blue cells indicate $A > B$ and orange cells mean $A < B$. * $p \leq 0.05$, ** $p \leq 0.01$, *** $p \leq 0.001$ and **** $p \leq 0.0001$.

Once again, the rare variant appeared to have a slightly stronger impact on actin dynamics than the common one. However, as in the previous case, this difference could have been due to a higher expression of the lentiviral construct in the ABI3-F209 overexpressing cells. Therefore, a small aliquot of M-CSF-differentiated cells utilised for the spreading assay was analysed by flow cytometry in order to quantify the GFP reporter expression. Unlike the NIH 3T3, the percentage of cells expressing GFP was extremely variable, going from a minimum of 76% in the ABI3-S209 expressing line to a maximum of 92.7% in the ABI3-F209 expressing line (Figure 3.5A). Moreover, the ABI3-F209 overexpressing cells seemed to be, once again, the ones with the highest MFI (Figure 3.5B) and highest overall expression when considering the Fluorescence Index (Figure 3.5C). Since these cells were not used any further experiment, the lack of triplicates made it impossible to evaluate the statistical significance of this observations, therefore this could have simply an aleatory event.

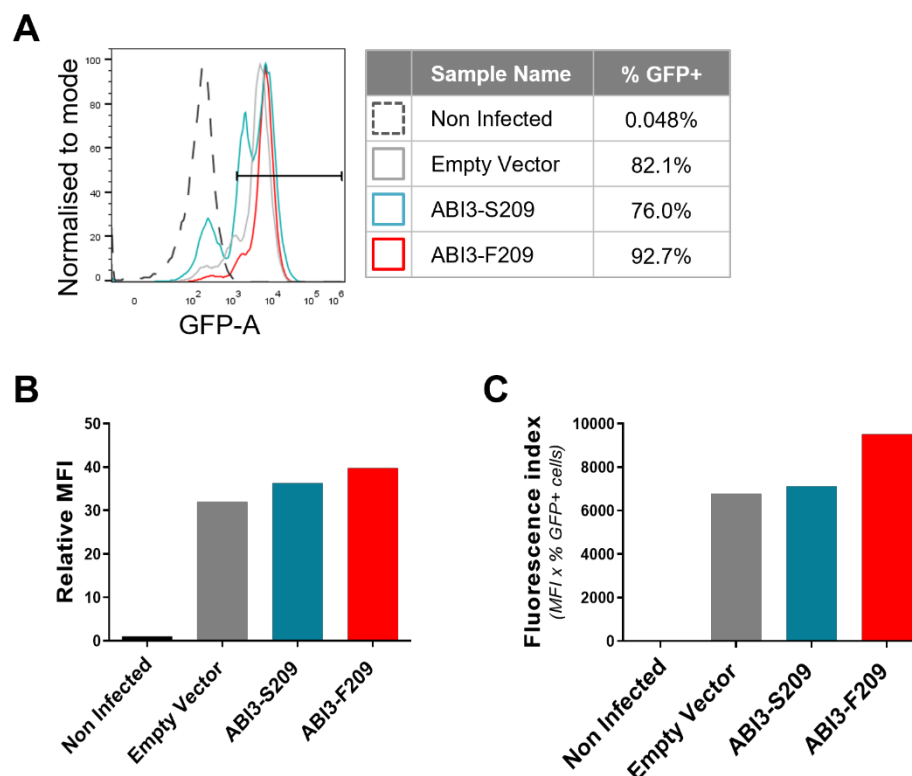


Figure 3.5 Detection of GFP in MØs derived from MØPs cells overexpressing either of the human ABI3 variants.

GFP expression in the transduced MØs was assessed by means of flow cytometry after applying a gating strategy similar to the one shown in Figure 3.3A. Grey represents the empty vector control, blue the ABI3-S209 overexpressing cells and red the ABI3-F209

overexpressing ones, while black indicates the non-infected control. **A)** Combined histograms of the GFP expression in the empty vector control, ABI3-S209 and -F209 overexpressing cells compared to a non-infected control. **B)** Graphical representation of the MFI values relative to the non-infected control, obtained after GFP⁺ population analysis. **C)** Evaluation of the fluorescence index, calculated as the product of MFI x percentage of GFP⁺ cells. n=1.

While the data obtained with this model supported the hypothesis of a hyperactivation of Abi3 in the presence of the F209 mutation, the variation in the lentiviral construct expression posed a great limitation to obtain clear data. The final aim of this chapter was to better elucidate the role of Abi3 at physiological levels, making the use of overexpressing cell lines not entirely biologically relevant. Furthermore, a mouse model harbouring the rare variant was being developed at the time of these experiments. Therefore, it was decided to focus on the Abi3-WT and -KO MØPs, while waiting for the Abi3^{F212} mice to be delivered and used to generate additional MØP cell lines.

Two repetitions of the spreading assay were performed on the original Abi3-WT and -KO MØs, indicated as “Cell line pair A” in Table 3.3. One last repetition was performed using the two newest pairs of cell lines, “B” and “C”. The first repetition of the experiment (including the longer time points, which are discussed below) was performed on the first pair of cell lines, after 3 days of differentiation, but sub-optimal cellular adhesion was observed at the shortest time points. The protocol for differentiation of these lines allows for 3-4 days in presence of M-CSF. Therefore for the remaining repetitions reported in Table 3.3 (including the second repetition of “pair A”, showed in Figure 3.6), the cells were left one day longer in M-CSF before testing, to improve their fitness and maturation and facilitate cell adhesion and therefore data interpretation at shorter time points.

Figure 3.6 shows images and results of the analysis performed on the second repetition of the original MØPs pair (“pair A”). These results are representative of all experiments (summarised below in Table 3.3). The following Fiji analysis and statistical evaluation showed a significant increase in cell area and solidity in Abi3-deficient cells compared to the -WT at all the time points ($p \leq 0.0001$, Figure 3.6B-H). The values of solidity at 4h were not significantly different (Figure 3.6I).

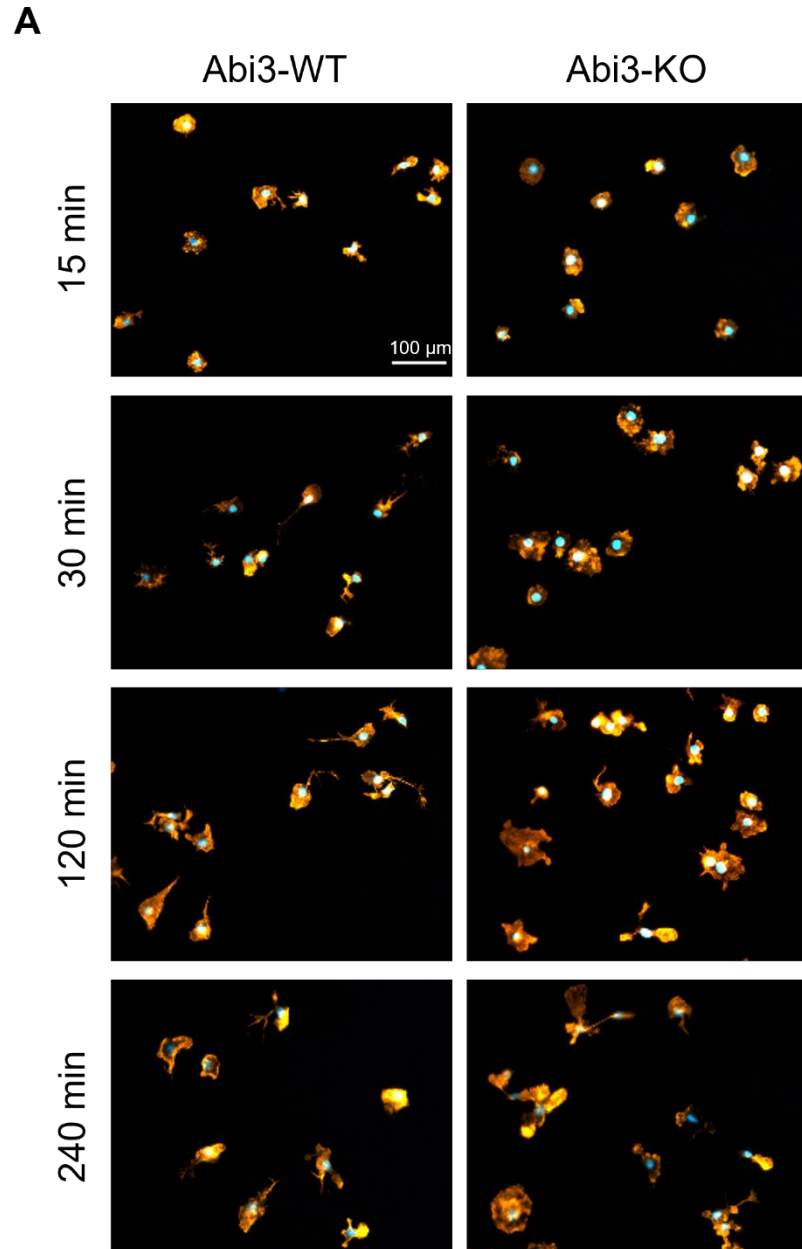


Figure 3.6, part I. Representative images from the second spreading assay experiments performed on M-CSF differentiated MØs derived from the original Abi3-WT and KO precursors cell lines.

A) Representative images of M-CSF differentiated Abi3-WT and -KO MØPs stained with Phalloidin-AF555 (orange) at different intervals after replating. DAPI (blue) was added to the staining protocol to visualise the cell nucleus and help distinguishing between small cells and debris. Even after the shortest incubation, Abi3-KO cells presented a visible increase in surface area and a concomitant reduction in ramifications compared to -WT cells.

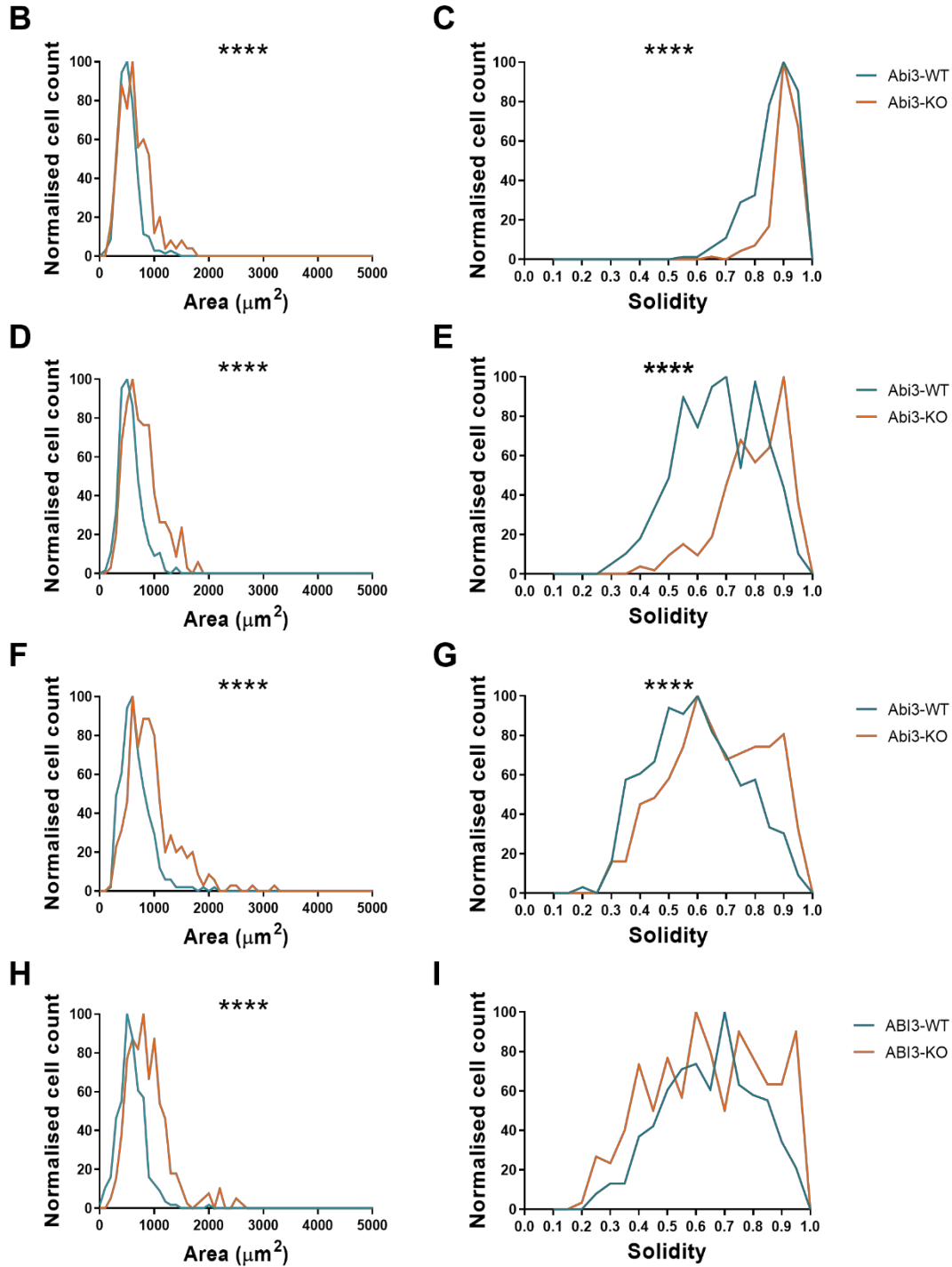


Figure 3.6, part II. Quantification of Abi3-WT and -KO MØs cell surface area and solidity following the second repetition of the spreading assay.

As before, area and solidity values obtained from the Fiji analysis are shown as normalized histograms of the frequency distribution of the samples. The blue line indicates cells derived from Abi3-WT mice, while the orange line those from Abi3-KO animals. The p-values resulting from the non-parametric t-test performed on each set of samples are shown in the graphs as asterisks. **B), D), F) and H)** Evaluation of cell area at increasing time points (respectively, 15 minutes, 30 minutes, 2 hours and 4 hours). **C), E), G) and I)** Quantification

*of cell solidity at the respective time points. Data were analysed via Mann-Whitney test. p-values are shown as asterisks, where **** $p \leq 0.0001$. $n > 140$.*

When considering all the repetitions of this assay, as shown in Table 3.3, it was possible to identify a clear trend, despite a small level of expected variability among biological replicates.

During the first repetition (after only 3 days of differentiation with M-CSF) no significant difference in area emerged at 15 or 30 minutes, however at the first time point Abi3-deficient cells already showed an impairment in the ability to form ramifications compared to the -WT ($p \leq 0.01$), which became more noticeable after 30 minutes ($p \leq 0.0001$; Table 3.3, part I, first “pair A”). At the longer time points the increase in Abi3-KO surface became significant ($p \leq 0.0001$ at both time points), with -WT cells resulting significantly more ramified at 2 hours ($p \leq 0.0001$; Table 3.3, part II, first “pair A”). At 4 hours the difference in solidity lost statistical significance.

During the final repetition, cell line pair “B” showed a significant increase in cell area in Abi3-KO cells already at the first time point ($p \leq 0.0001$; Table 3.3, part I, “pair B”), while no difference was observed in the other pair (Table 3.3, part I, “pair C”). Both pairs presented significantly higher solidity in the absence of Abi3 at this time point ($p \leq 0.0001$ for both; Table 3.3, part I). The phenotype manifested by Abi3-KO cells appeared to be consistent in all the following time points. Indeed, after 30 minutes both parameters were significantly different between genotypes ($p \leq 0.0001$ for the area of both sets; $p \leq 0.0001$ in the case of “pair B” solidity, $p \leq 0.05$ in “pair C”; Table 3.3, part I). While the area difference at 2 hours didn’t appear significant in “pair C”, the area of Abi3-KO cells in “pair B” as well the solidity values in both sets of cell lines resulted once again significantly different ($p \leq 0.0001$ for all; Table 3.3, part II). Finally, both parameters presented a $p \leq 0.0001$ between genotypes at the last time point (Table 3.3, part II).

A

Area																
Cell line pair	15 min								30 min							
	A		A		B		C		A		A		B		C	
Genotype	Abi3- WT	Abi3- KO	Abi3- WT	Abi3- KO	Abi3- WT	Abi3- KO	Abi3- WT	Abi3- KO	Abi3- WT	Abi3- KO	Abi3- WT	Abi3- KO	Abi3- WT	Abi3- KO	Abi3- WT	Abi3- KO
Number of values	221	287	286	140	613	517	449	552	385	402	291	227	595	538	454	429
Median	398.3	357.6	501.1	605.2	582.7	762.2	562.3	551.0	736.9	748.7	534.3	712.6	601.6	767.7	557.1	597.9
Mann-Whitney test	n.s.		****		****		n.s.		n.s.		****		****		****	

Solidity																
Cell line pair	15 min								30 min							
	A		A		B		C		A		A		B		C	
Genotype	Abi3- WT	Abi3- KO	Abi3- WT	Abi3- KO	Abi3- WT	Abi3- KO	Abi3- WT	Abi3- KO	Abi3- WT	Abi3- KO	Abi3- WT	Abi3- KO	Abi3- WT	Abi3- KO	Abi3- WT	Abi3- KO
Number of values	221	287	286	140	613	517	449	552	385	402	291	227	595	538	454	429
Median	0.862	0.877	0.881	0.913	0.884	0.900	0.854	0.889	0.707	0.826	0.674	0.810	0.732	0.781	0.764	0.772
Mann-Whitney test	**		****		****		****		****		****		****		*	

Table 3.3, part I. Detailed report of descriptive statistics and Mann-Whitney test results for the shortest time points of all repetitions of the spreading assay performed on Abi3-WT and -KO MØs.

To facilitate visualisation, asterisks are colour coded: for each pairwise comparison A vs. B, grey cells indicate no significant difference, blue cells indicate A > B and orange cells mean A < B. * $p \leq 0.05$, ** $p \leq 0.01$ and **** $p \leq 0.0001$.

B

Area																
Cell line pair	120 min								240 min							
	A		A		B		C		A		A		B		C	
Genotype	Abi3- WT	Abi3- KO	Abi3- WT	Abi3- KO	Abi3- WT	Abi3- KO	Abi3- WT	Abi3- KO	Abi3- WT	Abi3- KO	Abi3- WT	Abi3- KO	Abi3- WT	Abi3- KO	Abi3- WT	Abi3- KO
Number of values	432	422	272	261	392	392	324	359	430	442	270	289	392	279	345	260
Median	680.7	856.7	606.0	864.4	665.5	872.5	655.7	660.6	517.1	752.6	565.6	799.1	578.5	1021	565.0	684.7
Mann-Whitney test	****		****		****		n.s.		****		****		****		****	

Solidity																
Cell line pair	120 min								240 min							
	A		A		B		C		A		A		B		C	
Genotype	Abi3- WT	Abi3- KO	Abi3- WT	Abi3- KO	Abi3- WT	Abi3- KO	Abi3- WT	Abi3- KO	Abi3- WT	Abi3- KO	Abi3- WT	Abi3- KO	Abi3- WT	Abi3- KO	Abi3- WT	Abi3- KO
Number of values	432	422	272	261	392	392	324	359	430	442	270	289	392	279	345	260
Median	0.683	0.756	0.584	0.657	0.620	0.660	0.599	0.665	0.697	0.693	0.651	0.641	0.545	0.657	0.552	0.666
Mann-Whitney test	****		****		****		****		n.s.		n.s.		****		****	

Table 3.3, part II. Detailed report of descriptive statistics and Mann-Whitney test results for the 2- and 4-hour time points of all repetitions of the spreading assay performed on Abi3-WT and -KO MØs.

To facilitate visualisation, asterisks are colour coded: for each pairwise comparison A vs. B, grey cells indicate no significant difference, blue cells indicate $A > B$ and orange cells mean $A < B$. **** $p \leq 0.0001$.

In order to investigate whether the difference between the two genotypes was due to transient responses to substrate stimulation or it was maintained over time, a longer experiment (up to a week) was performed using pair “A” cells. Figure 3.7A shows representative images acquired at each chosen time-point. The surface area of Abi3-KO MØs was significantly increased compared to the -WT samples at all time points, with $p \leq 0.0001$ at 24, 48 and 72 hours (Figure 3.7B, D and F) and $p \leq 0.01$ at 1 week (Figure 3.7H). Similarly, the KO cell showed an increased solidity at 48 hours ($p \leq 0.0001$, Figure 3.7E), 72 hours ($p \leq 0.001$, Figure 3.7G) and 1 week ($p \leq 0.001$, Figure 3.7I). At 24 hours there was no significant difference in solidity between the two genotypes (Figure 3.7C). The detailed descriptive statistics are reported in Table 3.4.

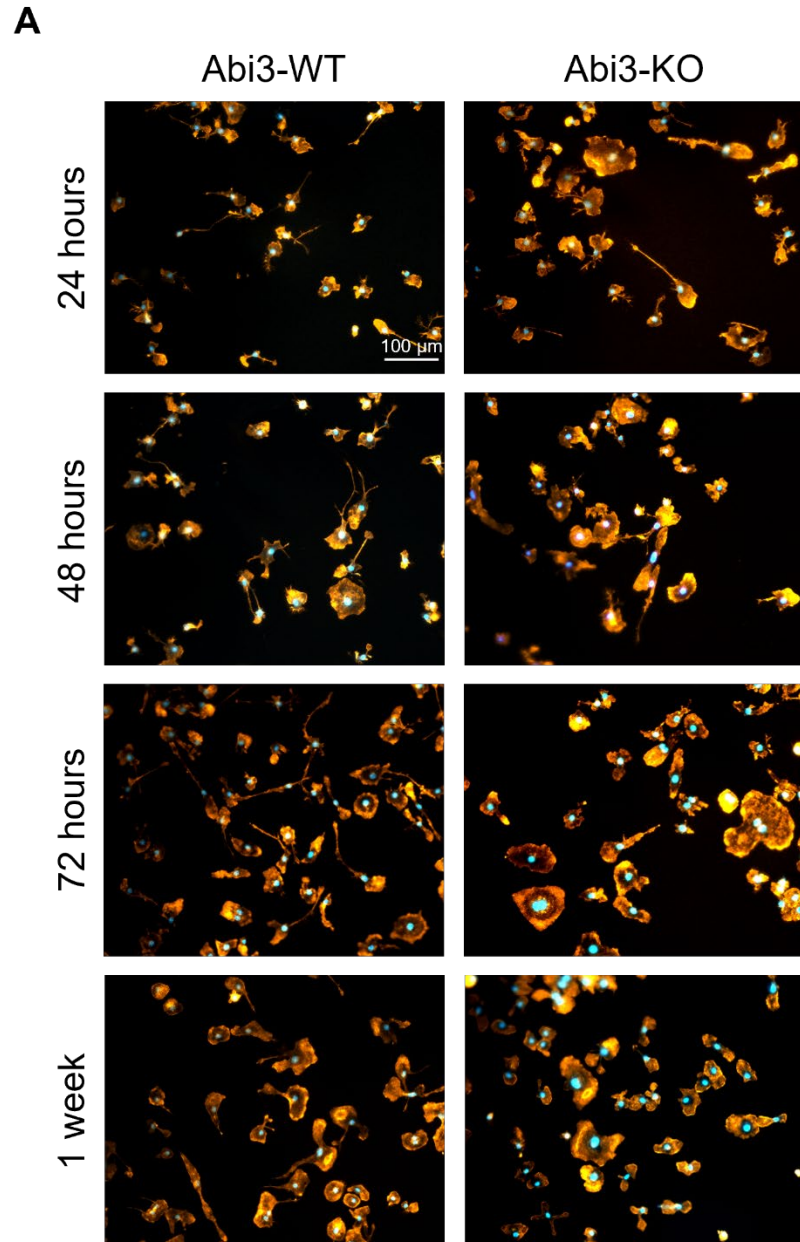


Figure 3.7, part I. Representative images from the single spreading assay experiment performed at longer time points on M-CSF differentiated MØs derived from Abi3-WT or KO precursors cell lines.

A) MØs were analysed after 24, 48 and 72 hours or 1 week after transfer to a new culture dish. As in the previous experiment, cells were stained with Phalloidin-AF555 (orange) and DAPI (blue). Even after longer incubations, it was possible to observe increased area and solidity in Abi3-KO cells compared to -WT cells.

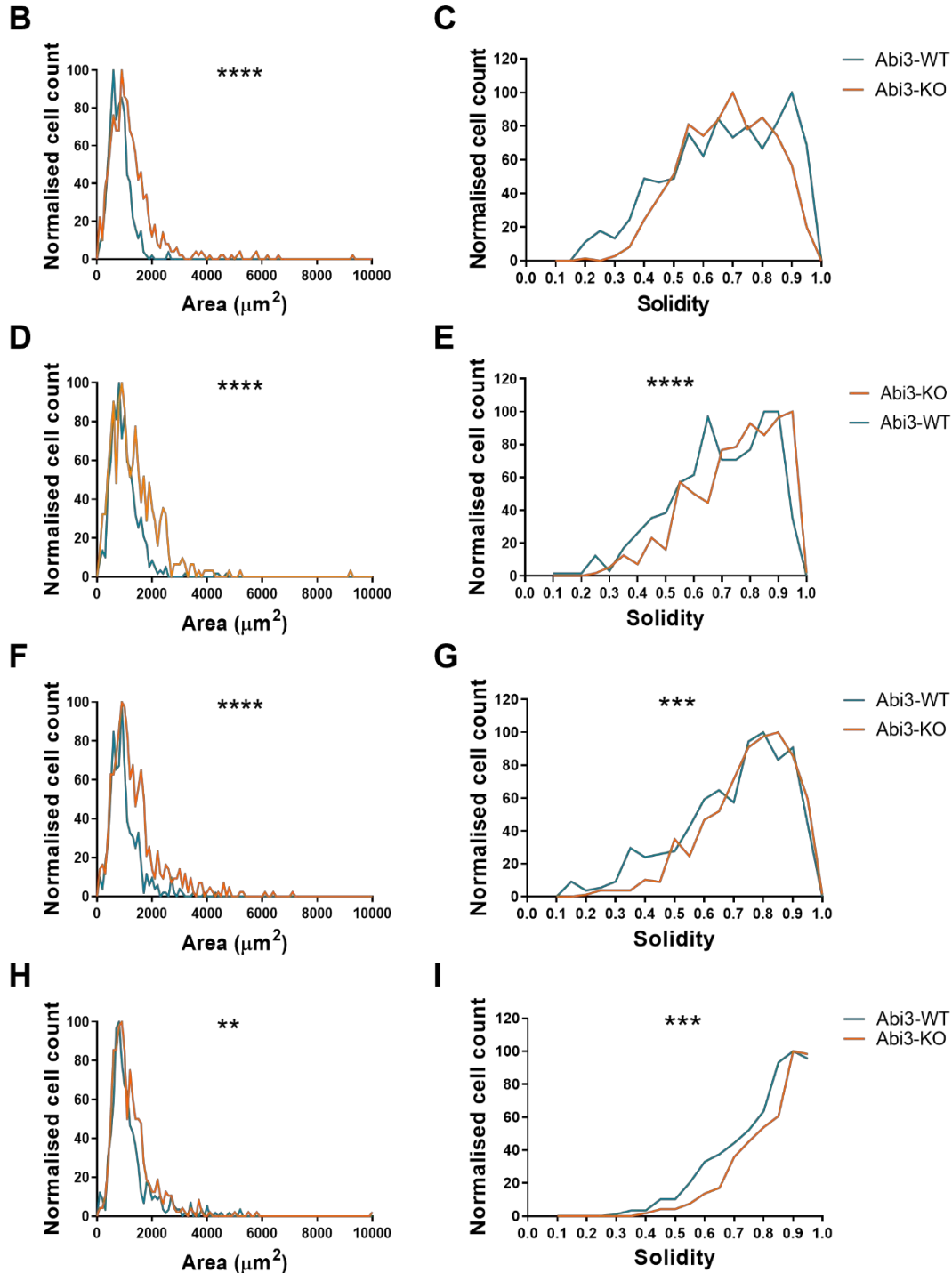


Figure 3.7, part II. Quantification of Abi3-WT and KO MØs cell surface area and solidity at longer time points.

Area and solidity values are shown as normalized histograms of the frequency distribution of the samples. The blue line indicates cells derived from the Abi3-WT mice, while the orange line those from the Abi3-KO animals. The p-values resulting from the non-parametric t-test performed on each set of samples are shown in the graphs as asterisks. **B), D), F) and H)** Graphical representation of cells surface after 24 (B), 48 (D), 72 hours (F) and 1 week (H). **C), E), G) and I)** Evaluation of cell solidity at the same time points. Data were analysed via

Mann-Whitney test. *p*-values are shown as asterisks, where ***p*≤0.01, ****p*≤0.001 and *****p*≤0.0001. *n*>380.

Area									
Time point	24 h		48 h		72 h		1 week		
Cell line	Abi3- WT	Abi3- KO	Abi3- WT	Abi3- KO	Abi3- WT	Abi3- KO	Abi3- WT	Abi3- KO	
Number of values	407	577	524	420	384	537	500	518	
Median	801.3	1051	897.9	1134	885.8	1128	948.1	1024	
Mann-Whitney test	****		****		****		**		

Solidity									
Time point	24 h		48 h		72 h		1 week		
Cell line	Abi3- WT	Abi3- KO	Abi3- WT	Abi3- KO	Abi3- WT	Abi3- KO	Abi3- WT	Abi3- KO	
Number of values	407	577	524	420	417	537	500	518	
Median	0.689	0.687	0.712	0.778	0.736	0.772	0.827	0.856	
Mann-Whitney test	ns		****		***		***		

Table 3.4 Detailed report of descriptive statistics and Mann-Whitney test results for each time point of the long-term spreading assay performed on Abi3-WT and -KO MØs.

To facilitate visualisation, asterisks are colour coded: for each pairwise comparison A vs. B, grey cells indicate no significant difference, blue cells indicate A > B and orange cells mean A < B. ***p*≤0.01, ****p*≤0.001 and *****p*≤0.0001.

All of these observations, taken together, confirmed a crucial role of Abi3 in actin dynamics and in the cellular ability to spread and form lamellipodia-like structures.

3.2.3. Abi3 ablation does not seem to impact the phagocytic activity of BMDMs

BMDMs were harvested from 6-week-old male APP^{NL-G-F} (henceforth referred to as App-KI) and App-KI Abi3-KO mice as described in Methods section 2.3.3. The strain had been crossed with Abi3-KO mice to obtain double-homozygous mice that were also employed for the experiments presented in Chapter 5. BMDM cells were

stimulated for 24 hours with 100 ng / ml LPS and 20 ng / ml IFN- γ . RNA was then extracted and Abi3 levels were quantified by qPCR (see Section 2.5).

Figure 3.8 shows the results of the 40-CT (Figure 3.8A), 40- Δ CT (normalised by the expression level of the endogenous gene *Ywhaz*; Figure 3.8B) and relative gene expression (normalised to the average value of unstimulated App-KI controls; Figure 3.8C) analysis following the qPCR.

As in the case of the M ϕ P cell lines, Abi3 was essentially undetectable in both treated and untreated samples derived from Abi3-deficient mice. A significant reduction of Abi3 levels in App-KI Abi3-KO cells was evident when looking at both the 40-CT ($p \leq 0.0001$; Figure 3.8A) and 40- Δ CT ($p \leq 0.001$; Figure 3.8B) values, regardless of the stimulation. While stimulated App-KI cells showed an apparent reduction in Abi3 relative expression compared to the unstimulated cells, this difference was not significant (Figure 3.8C), while treated and untreated Abi3-deficient cells expressed significantly less Abi3 compared to their respective control ($p \leq 0.001$ for unstimulated cells, $p \leq 0.05$ for stimulated ones; Figure 3.8C). Having confirmed the deficiency of Abi3 in the double-homozygous mice, these cells were then used for all the functional assays discussed in the next sections.

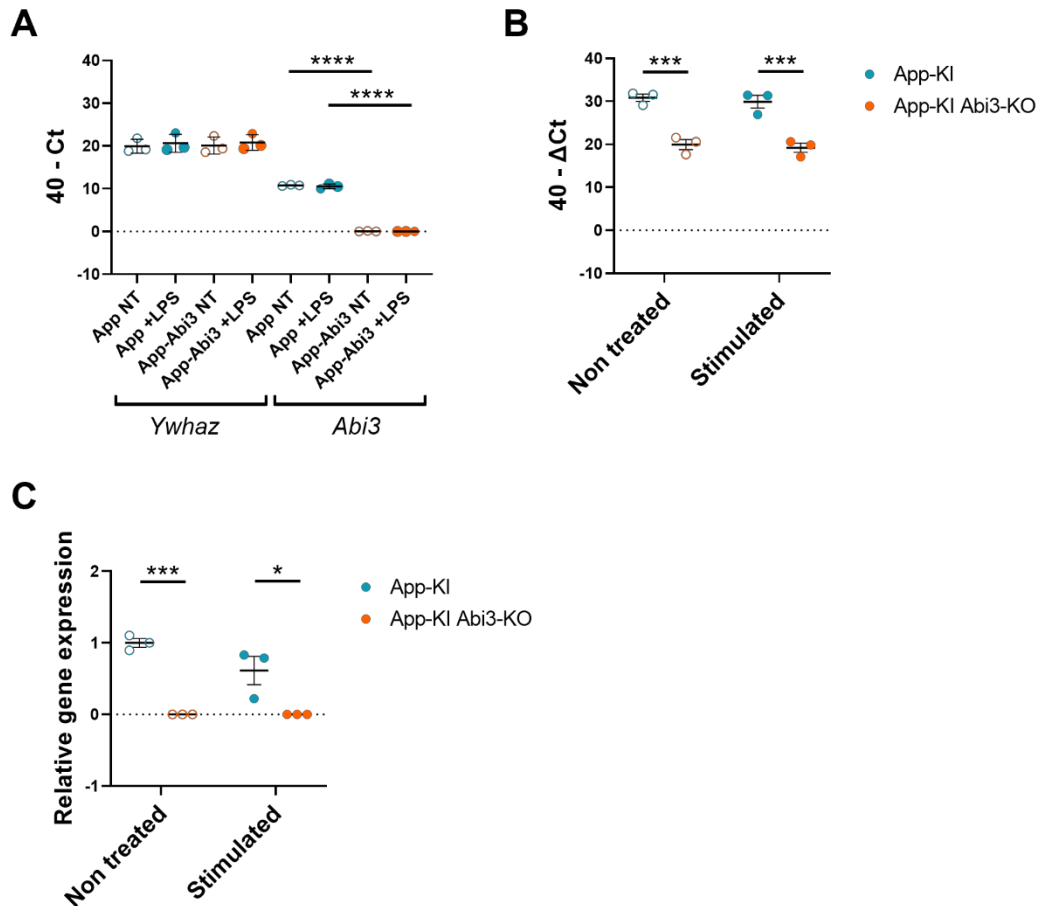


Figure 3.8 QPCR analysis of App-KI and App-KI Abi3-KO BMDMs to confirm Abi3 knock-out.

In all graphs, blue represents App-KI cells while orange indicates the App-KI Abi3-deficient samples. Each dot represents the average of 3 technical replicates. Three animals were tested for each genotype. The horizontal black lines indicate the means, while the vertical bars reflect the standard deviation within each group. Cells were tested after being stimulated for 24 hours with 100 ng / ml LPS and 20 ng / ml IFN- γ , in the presence of 2 % FBS and 10 ng / ml M-CSF (filled circles) and compared to unstimulated controls (maintained with 2 % FBS and 10 ng / ml M-CSF; empty circles). Ywhaz mRNA was used as endogenous housekeeping control. Whenever Abi3 mRNA levels in App-KI Abi3-KO cells resulted undetectable despite high levels of Ywhaz, a CT of 40 was assigned in order to be able to perform the following statistical analysis. **A)** Graphical representation of the 40-CT values and **B)** of the 40- Δ CT values deriving from the qPCR analysis. **C)** Quantification of the relative gene expression, normalised to the average value of the App-KI BMDMs. Asterisks indicate p-values, where * $p \leq 0.05$, *** $p \leq 0.001$ and **** $p \leq 0.0001$. Data analysed by One-Way ANOVA followed by Tukey's multiple comparison test. $n=3$.

As previously discussed (see section 1.1), macrophages and microglia rely on their actin cytoskeleton to execute their phagocytic activity (54,362). The phenotype manifested by Abi3-KO MØs during the spreading assay described earlier in this chapter underlined the importance of assessing the impact of Abi3 on phagocytosis.

App-KI and App-KI Abi3-KO BMDMs were differentiated for a week with addition of M-CSF and then tested using the Opera Phenix Plus High-Content Screening System (please see Methods section 2.4.2). For this assay, cells were stimulated using Zymosan (a cell wall preparation, rich in β -glucans, derived from *Saccharomyces cerevisiae*) conjugated to pHrodo™ Red, a pH-sensitive dye that increases in fluorescence as the pH of its microenvironment decreases (as per manufacturer's product description), such as in the case of phago-lysosomes. Cytochalasin D (CytoD), a fungal toxin able to inhibit actin polymerisation (363), was used as a negative control (148,264,364). Figure 3.9 shows representative pictures of selected time points of the assay.

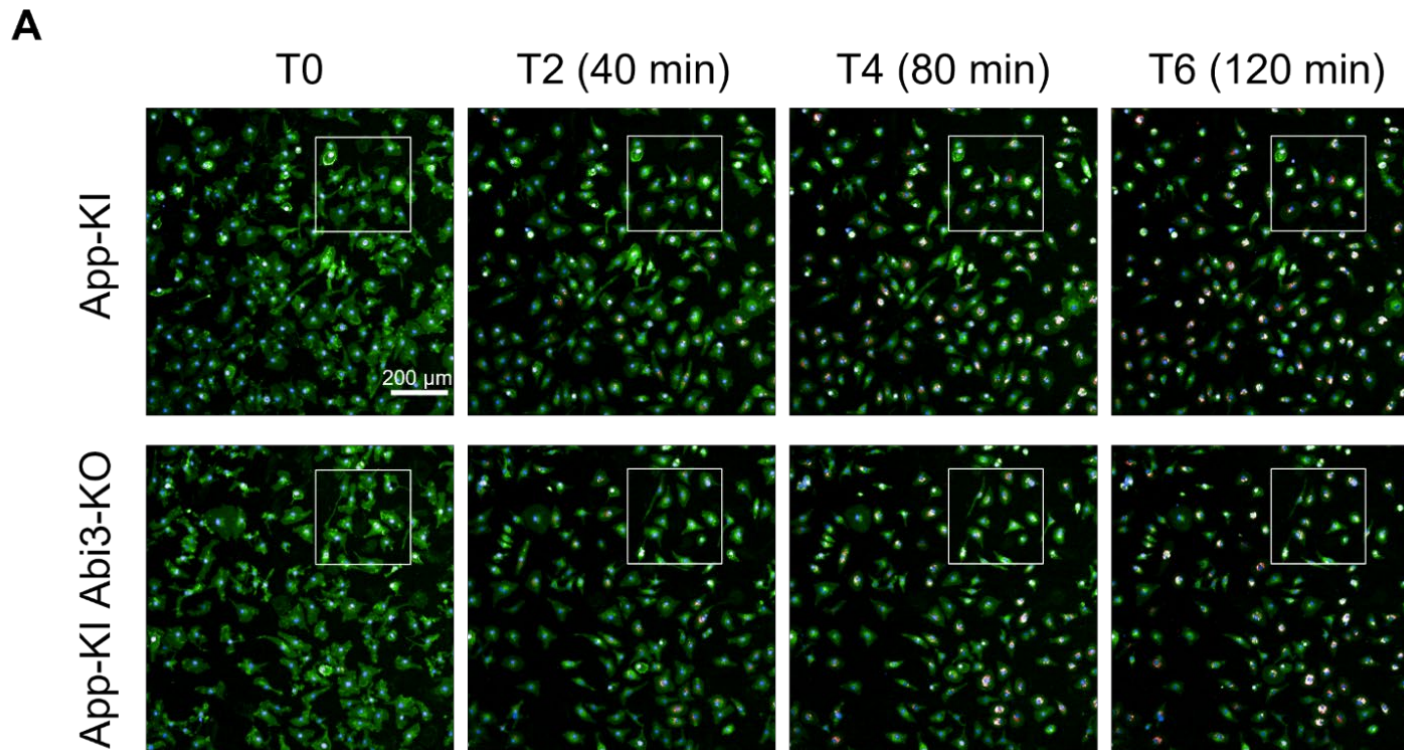


Figure 3.9, part I. Representative images from selected time points of a phagocytosis assay performed on BMDMs.

A) App-KI and App-KI Abi3-KO BMDMs were stained using a combination of CellMask™ Green (to visualize the plasma membrane, green) and Hoechst 33342 (to visualise the nuclei, blue) and challenged with pHrodo™ Red Zymosan (red). Images were acquired immediately before the addition of Zymosan (T-1, not shown) and immediately after (T0), and then again every 20 minutes for a total of 2 hours. Images show a representative field for each genotype across 4 of the 8 time points. White squares indicate a representative area chosen to be enlarged, as shown in Figure 3.9, part II.

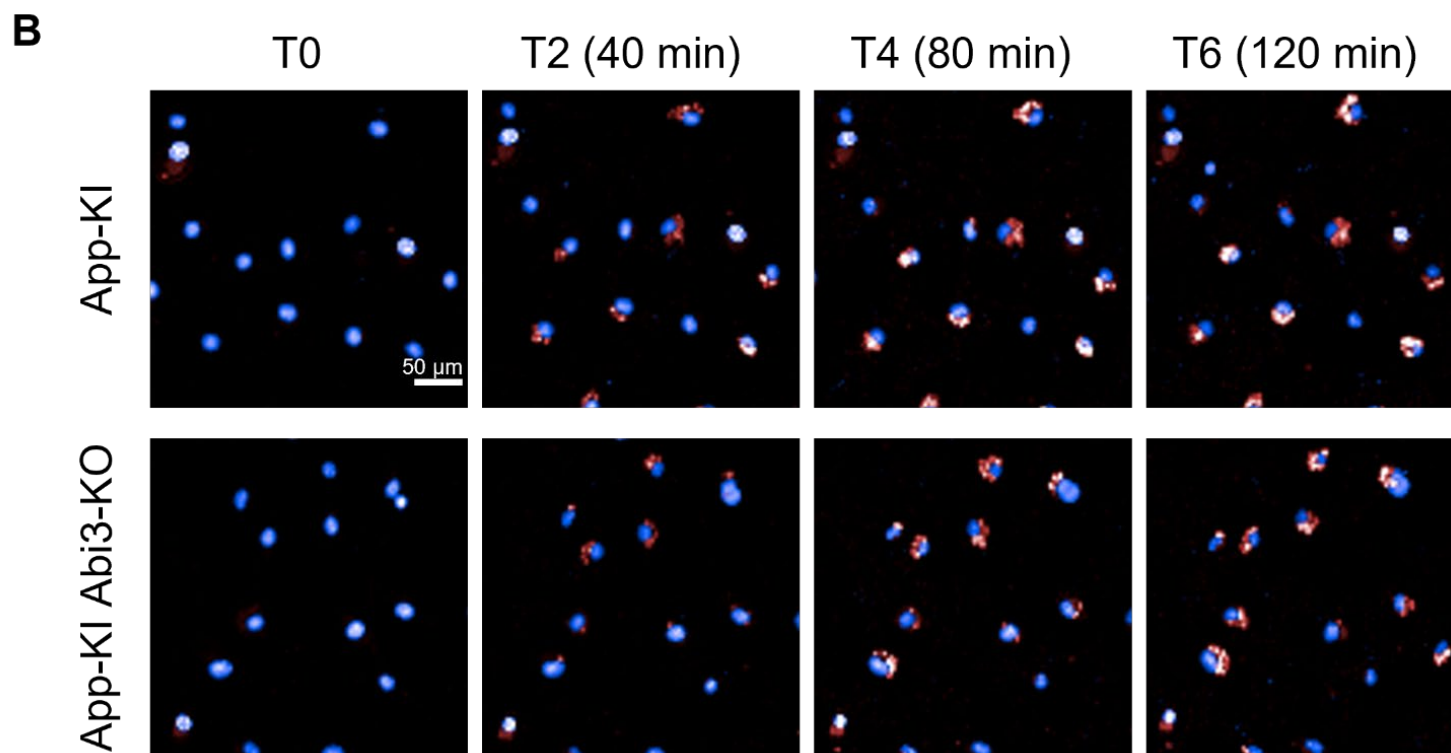


Figure 3.9, part II. Enlargements of the representative images shown in part I. B) For each image, the area identified by the white square was enlarged and it's here presented without CellMask™ Green channel to facilitate Zymosan visualisation.

Zymosan area and fluorescence intensity within the cells were quantified as described in Methods section 2.4.2. Figure 3.10A represents the percentage of CellMask™-positive area colocalised with Zymosan. This percentage was shown to increase with the passing of time ($p \leq 0.0001$ for the “Time point” effect; Figure 3.10A), while CytoD treatment appeared to significantly inhibit the uptake of Zymosan particles ($p \leq 0.0001$ for the “CytoD” main effect and $p = 0.0136$ for the two-way interaction between CytoD and Time point; Figure 3.10A) confirming the assay validity. However, genotype did not impact the percentage of colocalisation ($p = 0.6284$ for the “Genotype” main effect; Figure 3.10A) and no significant two- or three-way interaction including the Genotype factor was identified.

Similarly, pHrodo™ Red intensity increased over time ($p \leq 0.0001$ for the “Time point” main effect; Figure 3.10B) regardless of the genotype ($p = 0.6888$ for the “Genotype” main effect; Figure 3.10B). CytoD-treated samples displayed a reduced intensity throughout the assay ($p = 0.0036$ for the “CytoD” main effect and $p < 0.0001$ for interaction between CytoD and Time point; Figure 3.10B).

The combined effect of genotype and CytoD treatment was also not significant for both parameters analysed ($p = 0.9118$ and $p = 0.9084$; Figure 3.10A and B respectively), indicating that any pre-existing difference in actin cytoskeleton due to the lack of Abi3 has apparently no impact on cellular response to CytoD actin inhibition.

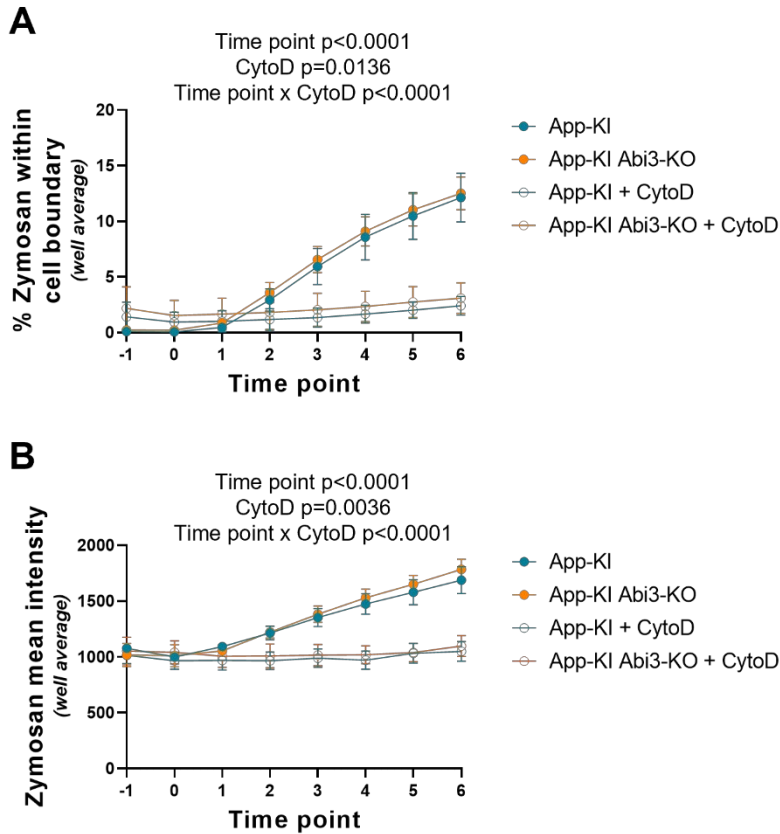


Figure 3.10 Quantification of pHrodo™ Red Zymosan area and mean intensity within App-KI and App-KI Abi3-KO BMDMs during a live-imaging phagocytosis assay.

Blue represents App-KI cells while orange indicates the App-KI Abi3-KO samples. Empty dots represent samples treated with CytoD, while filled dots indicate non-inhibited samples. All the values reported in these graphs were obtained by averaging the results of all the fields acquired for each well. Each dot represents the average of 3 biological replicates \pm SD. The p-value of any significant main effect or two- and three-way interaction identified by the statistical analysis is reported on each graph. **A)** Graphical representation of the percentage of cell surface and zymosan colocalization. **B)** Quantification of Zymosan fluorescence intensity. Data analysed by Three-Way ANOVA, $n=3$.

A source of concern was the high colocalisation percentage observed in both CytoD-treated groups at the beginning of the assay. This was, however, explained when assessing the relative images in more detail. Figure 3.11A shows the comparison between CytoD treated and untreated cells. The treatment caused a change in morphology in the cells, which appeared unable to spread correctly on the well surface. However, it also seemed to cause an increase in CellMask™ brightness around the nuclei. While bleed through from the green channel to the red in the untreated samples had been negligible, the brighter CellMask™ signal present

in the CytoD-treated wells caused fluorescence being visible in the red channel – and therefore being detected during the Fiji analysis – even before the addition of Zymosan to the plate, affecting multiple cells for each field of view (Figure 3.11B, T-1). However, this signal remained relatively consistent during the time course, with T6 images looking similar to the pre-treatment ones (Figure 3.11B) and visibly different from the time point-matched samples shown in Figure 3.9.

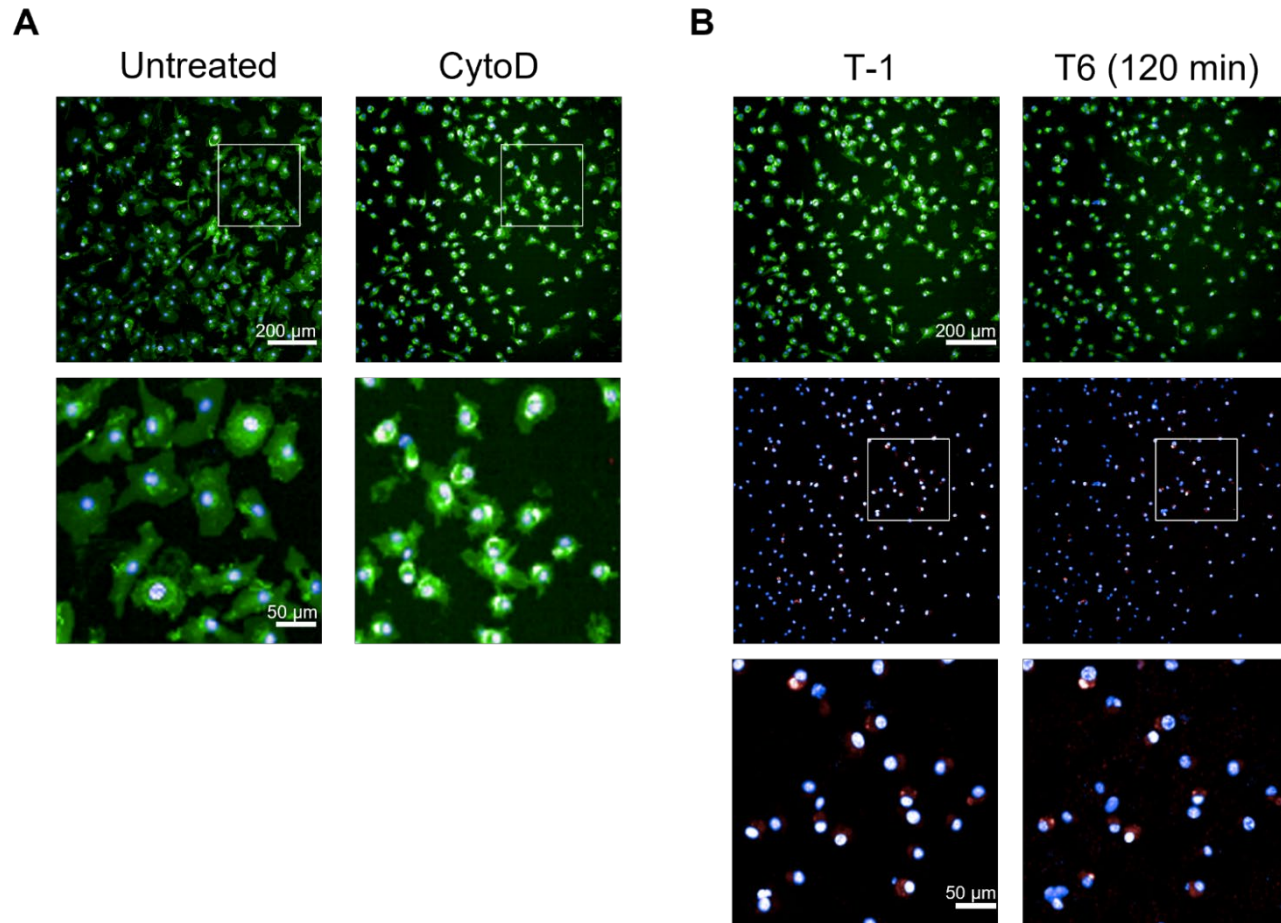


Figure 3.11. Representative images of App-KI cells with and without CytoD treatment.

Images were acquired with a 20x water-immersion objective on an Opera Phenix Plus High-Content Screening System. Green staining represents the plasma membrane (CellMaskTM Green), blue cell nuclei (Hoechst 33342) and red Zymosan (pHrodoTM Red Zymosan). The white squares drawn on some of the images indicate the areas that were chosen to be enlarged (as shown in the row immediately below) to ease cell visualisation. **A)** Representative images of morphological alterations caused by CytoD treatment. **B)** Comparison of Zymosan signal in CytoD-treated samples at the end of the assay and images acquired for the same cells before Zymosan addition (T-1).

3.2.4. The lack of Abi3 may cause alteration in ROS and NO production in BMDMs

Concurrent histological assessments performed on Abi3-WT and -KO brains, discussed more in detail in Chapter 4, evidenced a significant alteration in microglia morphology *in vivo* following Abi3 knock-out. Briefly, Abi3-KO mice presented less ramified microglia – consistent with the morphology manifested by Abi3-KO MØs in section 3.2.2 – reminiscent of activated cells.

An unbiased approach to clarify whether Abi3-KO microglia are indeed activated or simply dystrophic would be the employment of single-cell RNA sequencing. However, no consensus has been reached yet regarding an optimally balanced protocol to extract microglia without interfering with their activation state (more details regarding the challenges involved are presented in section 3.3). While this work was ongoing, it was decided to concurrently assess classical macrophage inflammation mediators to gain early insights into how MØs respond when a lack of Abi3 affects actin cytoskeleton reorganisation during immune challenges. Due to the role of oxidative stress in AD pathogenesis (365), the first preliminary analyses focused on ROS and NO production.

To stimulate ROS production, differentiated BMDMs were exposed to Zymosan particles and stained with Dihydrorhodamine 123 (DHR 123) as described in section 2.4.3 of the Methods. Figure 3.12A and B show the gating strategy employed in this assay. A ROS index – expressed as the product of DHR⁺ single cells percentage and MFI of the DHR⁺ cells – was calculated for each sample as shown in Figure 3.12C. Zymosan treatment successfully induced a significant increase in ROS production ($p \leq 0.0001$; Figure 3.12C). Interestingly, Abi3-deficient samples did seem to present an increase in ROS production. While the changes are fairly small in size, the difference in genotype appeared to have a significant impact on the ROS index ($p = 0.0088$; Figure 3.12C). No significant interaction was noted.

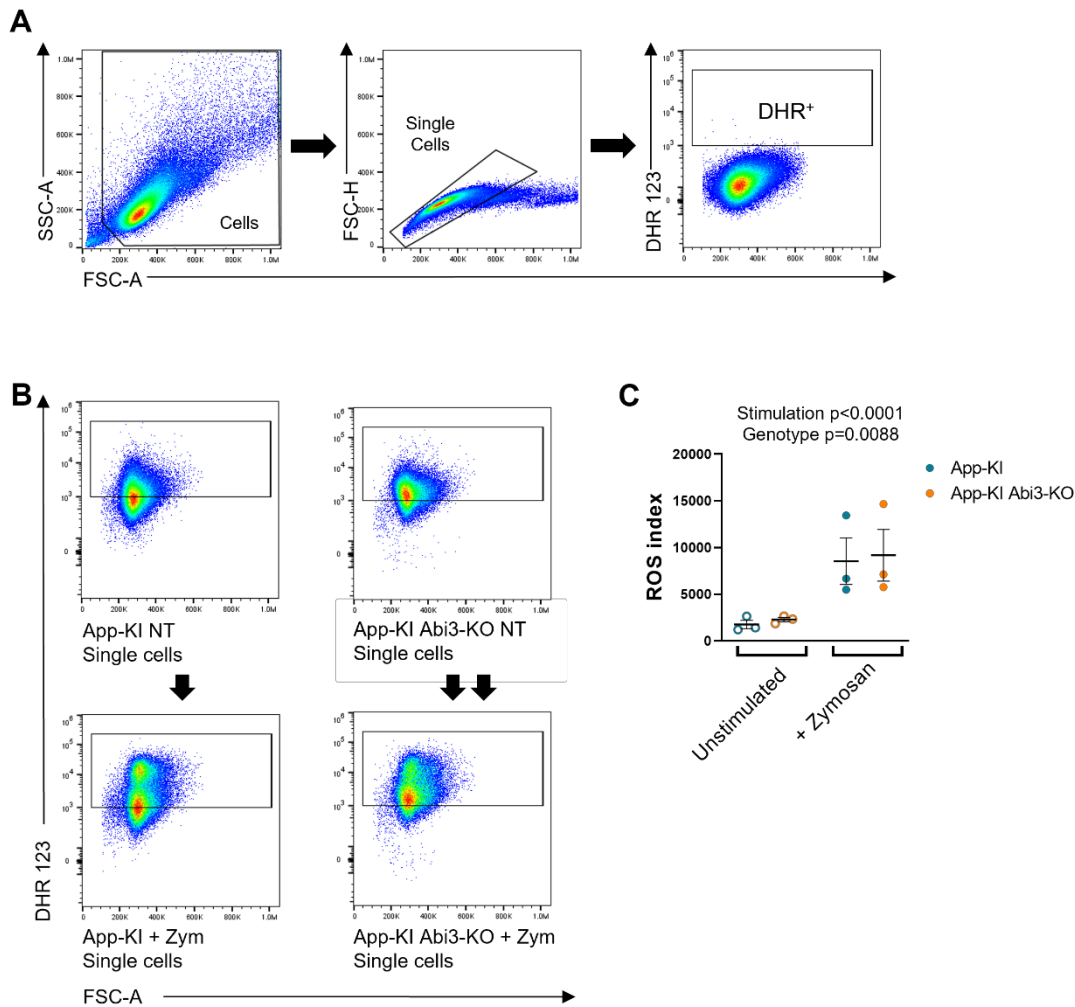


Figure 3.12 Assessing ROS production in App-KI and App-KI Abi3-KO BMDMs by flow cytometric analysis of DHR 123 staining.

App-KI samples are displayed as blue dots, while orange represents *App-KI Abi3-KO* cells; empty dots indicate unstimulated samples, whereas filled dots represent samples supplemented with Zymosan. Each dot depicts the average of three technical replicates assessed for each biological triplicate, while the black horizontal lines represent the mean of each experimental group \pm S.E.M. The *p*-value of any significant main effect or interaction identified by the statistical analysis is reported on the graph. **A)** Gating strategy used to quantify ROS production. Single cells and doublets were analysed separately after gating on the main cellular population to exclude debris. A DHR+ gate was then created based on an unstained control and the percentage of single cells falling into the gate, as well as their MFI, was calculated for each sample. **B)** Representative flow cytometry plots of DHR+ gate on BMDMs with (bottom row) and without (top row) Zymosan stimulation. **C)** Quantification of the ROS index in the single cells population. Data analysed via Two-way ANOVA. *n*=3.

In order to confirm whether the difference between genotypes was due to a higher ROS baseline in Abi3-deficient mice, a second gate was applied to the stimulated cells, based on App-KI controls, to identify a “DHR^{high}” population as shown in Figure 3.13A. Quantification of the ROS index in these cells, followed by a paired t-test, noted a lack of significant difference between stimulated App-KI and App-KI Abi3-KO cells ($p=0.4011$, Figure 3.34B). Overall, these results seem to suggest a higher baseline production of ROS in the absence of Abi3, not necessarily followed by an equally increased response following stimulation.

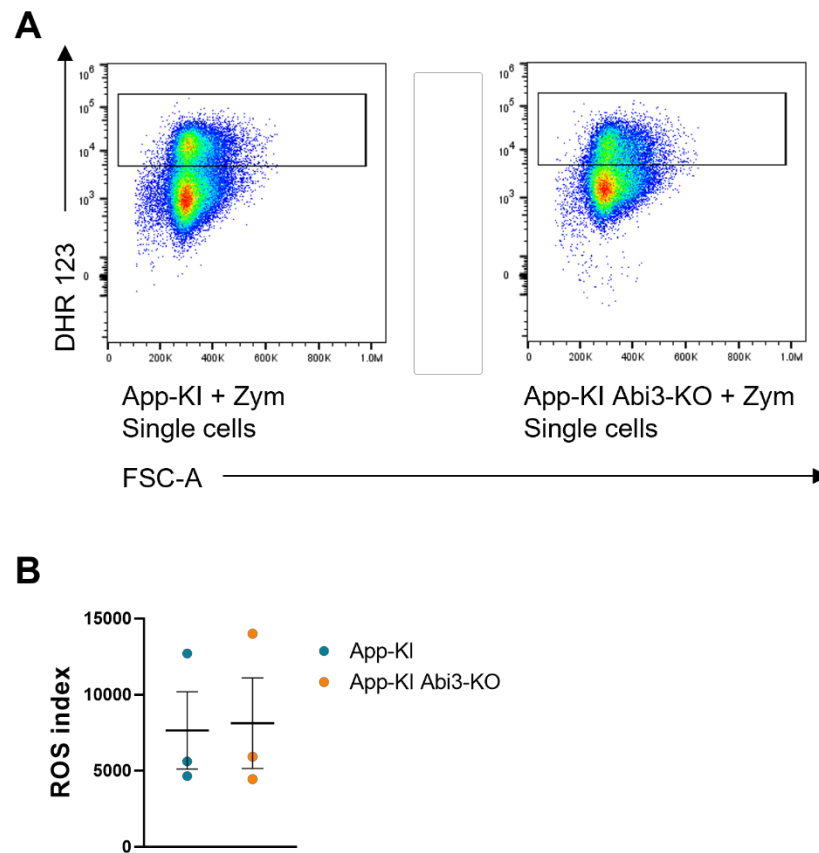


Figure 3.13 Alternative gating on stimulated BMDMs to focus on the DHR^{high} population.

As before, blue indicate App-KI samples, orange App-KI Abi3-KO cells. Each dot represents the average of 3 technical replicates for that given biological triplicate. The black horizontal lines represent the mean of each experimental group. Error bars indicate S.E.M. Only Zymosan-stimulated samples are displayed. **A)** Flow cytometry plots indicating a second, DHR^{high} gating strategy exclusively applied on stimulated single cells to better evaluate genotype-related differences after Zymosan stimulation. **B)** Graphical representation of the ROS index calculated for the DHR^{high} population. Data analysed via paired t-test. $n=3$

It has been previously shown that both CytoD and Jasplakinolide (an actin-stabilising drug (366)) cause significant inhibition in NO production in LPS-stimulated primary microglial (264). Given the clear impact of Abi3 ablation on actin reorganisation, differentiated BMDMs deriving from App-KI and App-KI Abi3-KO cells were stimulated with LPS and IFN- γ as per Methods section 2.4.4 in order to investigate whether a comparable effect was achieved following Abi3 ablation (Figure 3.15A). The supernatant of stimulated and unstimulated cells was then tested with the Griess reagent to quantify nitrite concentration as an indicator of NO secretion.

Due to the cell number-dependant nature of the assay, nuclei were quantified for each samples at the chosen time points (see section 2.4.4), as shown in Figure 3.14A. Cell counts resulted significantly impacted by the length of the stimulation ($p \leq 0.0001$; Figure 3.14A), with a dramatic reduction in cell number after 48 hours. A significant interaction was also identified between the stimulation and its length ($p \leq 0.0001$; Figure 3.14A). Genotype did not appear to influence cell numbers ($p = 0.0636$ for the “Genotype” main effect; Figure 3.14A) and no additional significant two- or three-way interactions were identified. Tukey’s post-hoc test identified a significant decrease in cell number for each experimental group after 48 hours compared to the respective 24 hours sample ($p \leq 0.0001$ for all except stimulated App-KI Abi3-KO, in which case $p \leq 0.001$; Figure 3.14A). However, while after 24 hours a significant decrease was observed in the stimulated App-KI samples compared to the genotype-matched unstimulated group ($p = 0.0097$; Figure 3.14A), such a difference was not observed in the 48-hour group.

Overall, the results of the ANOVA confirmed the necessity of considering the cell count when evaluating nitrite concentration. For this reason, Figure 3.14 displays nitrite concentration values pre- (Figure 3.14B) and post-normalisation (Figure 3.14C) by the average nuclei count of the respective sample.

When considering non-normalised data the stimulation protocol successfully stimulated a response in both genotypes ($p \leq 0.0001$ for the “Stimulation” main effect; Figure 3.14B). The length of the stimulation also caused a significant increase in nitrite concentration ($p \leq 0.0001$; Figure 3.14B), although this exclusively applied to the stimulated samples, while unstimulated samples failed to produce detectable levels of nitrites at either time point ($p \leq 0.0001$ for the “length of stimulation x stimulation” interaction; Figure 3.14B). Notably, the lack of Abi3 seemed to induce a small but overall significant increase in nitrite production following stimulation ($p = 0.0050$ for the “Genotype” main effect; Figure 3.14B), which as before only

applies to the stimulated samples ($p=0.0050$ for the “genotype x stimulation” two-way interaction; Figure 3.14B). No significant three-way interaction was detected.

However, once this data was normalised to the nuclei count, the difference related to Abi3 effect was lost. Indeed, genotype did not appear to be a significant source of variation ($p=0.0605$; Figure 3.14C), while stimulation and its length still significantly increased nitrites concentration ($p\leq 0.0001$ for both main effects and their two-way interaction; Figure 3.14C).

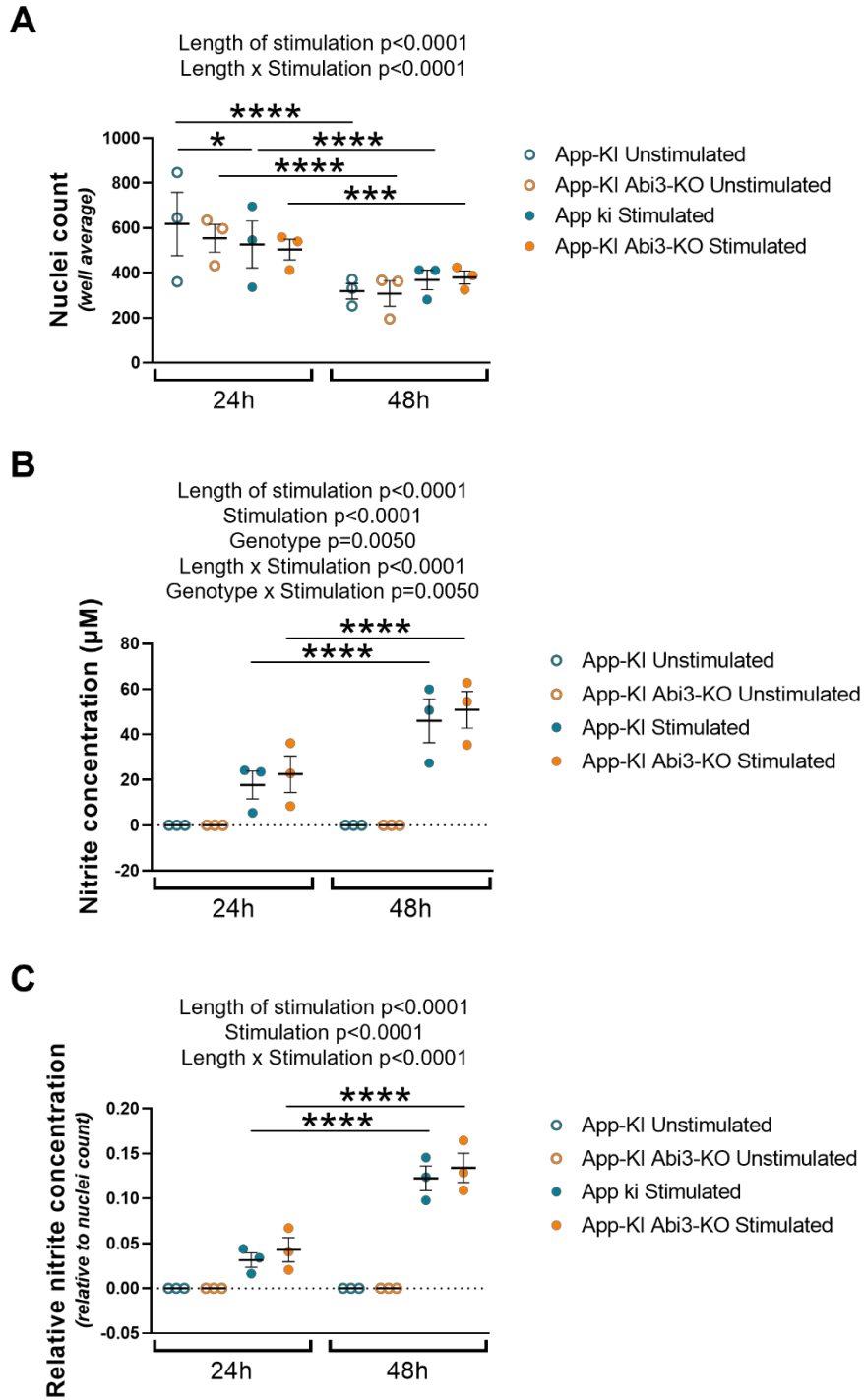


Figure 3.14 Evaluation of nitrite quantification with Griess reagent after LPS stimulation.

Blue dots represent App-KI cells, while orange ones indicate App-KI Abi3-KO samples. Unstimulated samples are depicted as empty dots, stimulated samples as filled dots. Due to their failure to produce detectable levels of nitrites, a value of 0 was assigned to each of them in order to perform the following statistical analysis. Each dot represents the average of 3 wells (technical replicates) for an individual biological triplicate. The black horizontal lines represent the mean of each experimental group. Error bars indicate S.E.M. The p-value of

any significant main effect or interaction identified by the statistical analysis is reported on the graph, while asterisks indicate the p-value obtained for pair-wise comparisons of interest following a post-hoc test. **A)** Graphical representation of the mean nuclei count, averaged among technical triplicates, for each sample. **B)** Quantification of nitrite concentration (expressed in μM), with and without stimulation, after 24 and 48 hours. **C)** Evaluation of nitrite concentration normalised for the average nuclei count in the respective well. Data analysed by Three-way ANOVA followed where appropriate by Tukey's multiple comparison test. $n=3$.

3.3. Discussion

This chapter starts delineating the role of Abi3 in actin dynamics in MØs, albeit more work is needed to fully clarify the mechanism through which Abi3 affects actin polymerisation.

The initial spreading assay experiments presented in sections 3.2.1 and 3.2.2 were performed on NIH 3T3 fibroblasts (as seen in (294)) and M-CSF differentiated MØP cell lines. These lines were transduced with a lentiviral vector encoding either the common or the rare human variant of ABI3 with the aim to start delineating the impact of the variant on actin dynamics. At a first glance, in all replicates of experiments performed on NIH 3T3 the rare variant seemed to exert the strongest effect on the cell's ability to correctly form membrane protrusions and assume the normal physiological elongated morphology, while the impact of the common variant appeared more variable (Figure 3.1 and Table 3.1). Notably, the fluctuations observed in ABI3-S209 cell area did not appear time-point related but rather due to variation between experimental replications. A similar observation was reported in lentivirus-transduced MØs, derived from conditionally-immortalised bone marrow precursors differentiated in M-CSF to obtain macrophage-like cells. As shown in Figure 3.4 and Table 3.2, a significant decrease in cell surface compared to the empty vector control was consistently visible only in the ABI3-F209 overexpressing line, while cell solidity was extremely variable throughout the assay for both overexpressing lines. Once again, the F209 variant appeared to cause more noticeable differences compared to the control than the overexpression of S209 variant.

Taken together, these observations initially suggested that the structural changes caused by the rare F209 coding variant could lead to an hyperactivation of ABI3.

However, the variability in expression levels of the different lentiviral constructs, as evidenced in Figure 3.2 and 3.5 by flow cytometry analysis of the GFP reporter signal, represented a major limitation of this approach. This appeared to be especially problematic given that in both NIH 3T3 and MØPs the biggest percentage of GFP⁺ cells, with the highest MFI, was observed in the ABI3-F209 overexpressing lines. It is also hard to predict the extent of the alterations caused by the transduction with a lentiviral vector, especially in macrophages.

For these reasons, the same assay was performed on three independent pairs of Abi3-WT and -KO MØs (section 3.2.2) in order to gain a better understanding of the role of Abi3 when physiologically expressed and avoid biases due to the use of lentiviral vectors. The lack of a specific anti-Abi3 antibody prevented a concurrent determination of what percentage of Abi3-WT cells expressed Abi3, and at what level, when interacting with the fibronectin substrate. Nevertheless, as shown in section 3.2.2, the knock-out of Abi3 caused a significant alteration in cell spreading, with Abi3-KO MØs consistently assuming a bigger and more solid morphology compared to the WT control, up to a week after replating (Figure 3.6-7 and Table 3.3-4).

To note, future repetitions of this assay should be analysed by employing a mixed model analysis. Indeed, this would allow to combine the various repetitions of the assay – instead of presenting them as individual replicates as in this thesis – while taking into account the intra-subject correlation, which would otherwise violate the assumption of independent observations and likely cause false positive (367).

As mentioned in section 1.4.2 of the Introduction, WAVE2 phosphorylation on its Tyr150 residue, which is mediated by c-Abl (286) and prevented by the presence of Abi3 in the complex instead of Abi1 (295), is crucial to WAVE2 translocation to the membrane. Abi3 deficiency has been shown to cause a significant impairment both *in vitro* and *in vivo* in macrophages and microglia ability to correctly form ramifications. A model has been proposed following these observations as shown in Figure 3.15. In the absence of the negative control exerted on the WRC by Abi3, the increased availability of activated Arp2/3 complex at the cell periphery stimulates a higher rate of lamellipodia structures formation, leading to rounder and bigger cells. However, the dysregulated increase in complexity of the branched actin network could result in reduced transition to parallel filaments and therefore in the inability of cross-linking proteins to form actin bundles, necessary for filopodia elongation. The forced overexpression of Abi3 would instead cause a reduction in the availability of activated Arp2/3, leading to fewer cells presenting lamellipodial structures (as seen

in NIH 3T3 by Sekino *et al.* (294) and in section 3.2.1-2). Notably, a recent work from Karahan *et al.* has reported a reduction in motility following siRNA-mediated knockdown of Abi3 in HMC3 microglia (302), which supports the hypothesis of a stiffer actin cytoskeleton in Abi3-deficient cells.

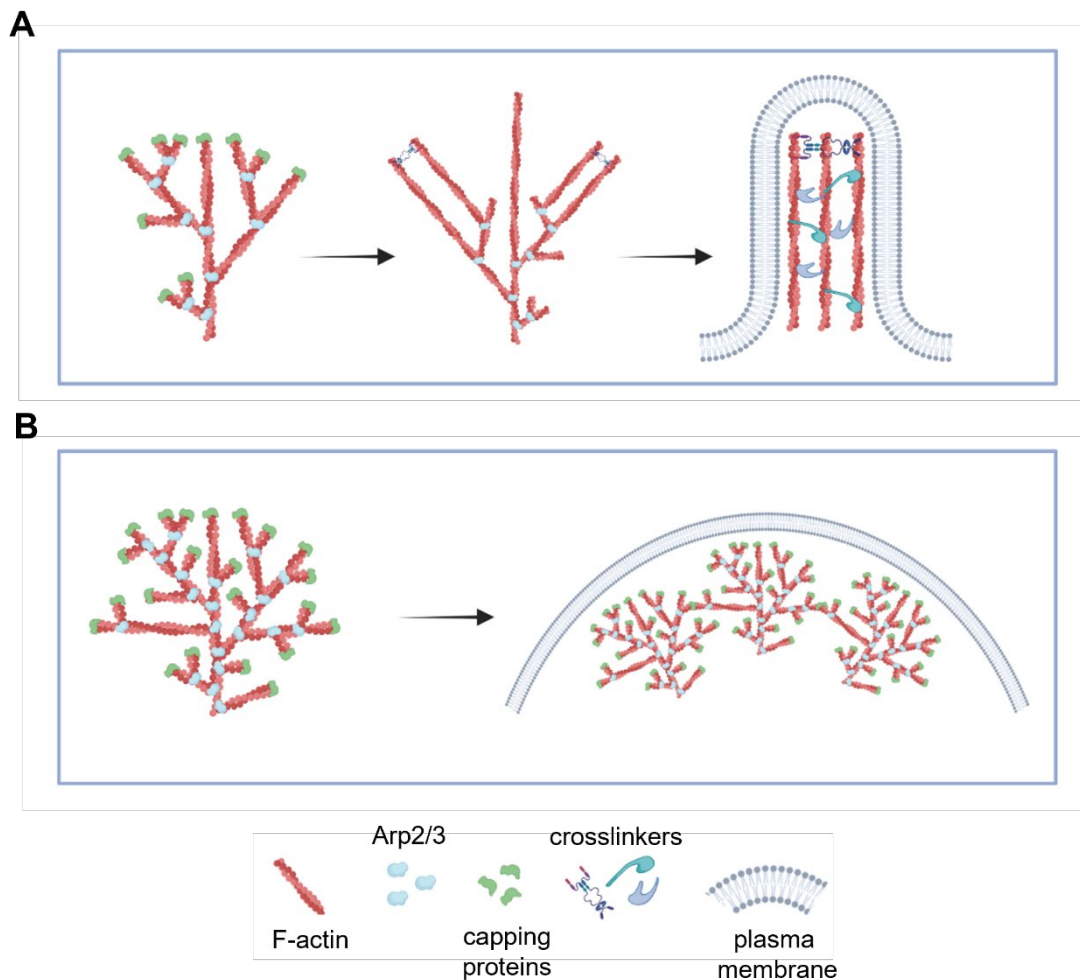


Figure 3.15. Schematic representation of the proposed model for Abi3 action on actin cytoskeleton.

A) Normally, Abi3 allows the phosphorylation of WAVE2, which is therefore able to migrate to the cellular edge, interact with the Arp2/3 complex and activate it. This in turn leads to de novo actin nucleation and the consequent formation of a branched actin network. The presence of Abi3 in the WRC ensures a controlled availability of activated Arp2/3, so that following the displacement of capping proteins, actin filaments are free to extend. The progressive shift to parallel filaments allows crosslinkers to organise the adjacent filaments into filopodia structures. B) In Abi3-deficient cells, one of the crucial steps of Arp2/3 regulation is lost due to the exclusive presence of the pro-activation Abi1-WRC. The increase in active Arp2/3 complex could lead to a higher branching complexity in the filament network which forms lamellipodia. However, this may limit filament elongation and reduce the likelihood of actin filaments assuming a parallel conformation, therefore leading to bigger

cells with reduced number of ramifications. For a detailed explanation of actin mechanics see (368).

Immunostaining of unstimulated and stimulated MØs to highlight localisation and interaction of WAVE2 and Arp2/3 as well as Abi1 and, once a specific antibody is available, Abi3, would provide a first validation of the suggested model. However, a live imaging approach on these MØs would undoubtedly help to clarify differences in primary and secondary responses to external stimuli (such as change in substrate or M-CSF stimulation). The employment of cells deriving from the recently acquired Abi3^{F212} mice will allow bypassing the limitations presented by ABI3-F209 overexpressing lines and shed light on the effective impact of the rare variant on actin dynamics.

Filopodia are essential for macrophage phagocytic activity (356) and the proposed model raised the question of how the absence of Abi3 would have affected this process. This was therefore investigated in section 3.2.4 by employing a live imaging approach on Abi3-deficient BMDMs stimulated with pHrodo Zymosan. Previous work from Dr R. Jones on Abi3-KO pMØs, analysed through an Amnis Imagestream MkII[®] imaging cytometer, had highlighted a reduction in phagocytic activity in a subset of the Abi3-deficient pMØs (F4/80⁺Tim4^{low}) (329). It was hoped that following phagocytosis dynamics over 2 hours of stimulation, via a live imaging approach (with no need to detach and hold cells in suspension), would have allowed to detect more subtle differences related to internalisation kinetics. However, no significant difference was detected following Abi3 ablation. This could be partially explained considering that the Arp2/3 complex has been shown to mostly impact C3-dependent phagocytosis rather than the FcR pathway (322), as discussed in section 1.1.3.1 of the Introduction, so C3b opsonisation of the bait should be included in future experiments. Recent observation of a significantly reduced phagocytic activity in Abi3-knocked-down BV2 cells (302), do however suggest that the higher stiffness of the actin cytoskeleton – or possibly the reduced availability of G-actin monomers following increase rate of polymerisation – in the absence of Abi3 may affect phagocytosis regardless of the phagocytic pathway assessed so further investigation is required to clarify this aspect.

Phagocytosis of Zymosan particles by MØs is initiated after β -glucan recognition mainly by the transmembrane receptor Dectin-1 (369,370). This in turn leads to the activation of downstream antimicrobial pathways including production of (ROS) in a subpopulation of MØs by the NADPH phagocyte oxidase complex present on the

phagosomal membrane (371). The assembly of this complex depends on Rac1, which is essential for cytosolic p67^{phox} interaction with the catalytic subunit Nox2 (372) as well as for Arp2/3 complex activation via WRC (373). Despite Rac1 involvement in both ROS production and actin polymerisation, the two are entirely separate downstream effects of Rac1 activation (374). Kustermans *et al.* reported an association between actin and ROS production mediated by NF-κB, possibly through the activation of the p47^{phox} subunit of the NADPH oxidase in human monocytes (358). However, the exact role of actin dynamics in NF-κB-dependent ROS production is still uncertain. For this reason, and due to the significance of ROS secretion and oxidative stress in pathological contexts such as in AD (365), ROS levels were assessed in BMDMs with and without Zymosan stimulation. Preliminary data shown in the first part of section 3.2.4 suggest a potential involvement of Abi3 and actin regulation in ROS production at a baseline level, while the impact on the respiratory burst that follows phagocytosis of Zymosan particles was minimal. Both genotypes displayed an increase in DHR 123 oxidation in similar proportions of their population and no significant increase in ROS index was detected in the DHR^{high} Abi3-deficient cells (Figure 3.13). In case of future repetitions of this assay, the standardised protocol could be adapted in order to include pHrodo (or other fluorescently-labelled) Zymosan to identify potential alterations in Zymosan uptake. Additional reporters could also be employed, such as MitoSOXTM Red, which is selectively oxidized by superoxide but not by other ROS or reactive nitrogen species RNS. Moreover, catalase abundance and activity should be assessed as well, in order to confirm whether the in DHR 123 signal is related to ROS production and not to alterations in H₂O₂ clearance.

While little is known about the interaction between actin cytoskeleton and ROS production, the influence of actin dynamics in NO production had been previously described by Eswarappa *et al.*, who revealed a significant decrease in NO secretion in LPS-stimulated pMØs after CytoD or Latrunculin B (another actin polymerisation inhibitor (375)) treatment (323). Similar findings were reported by Uhlemann *et al.*, who observed a significant inhibition in NO production following drug-driven alterations in the actin cytoskeleton of LPS-activated primary microglial (264). For this reason, BMDMs were stimulated with LPS and IFN-γ and NO release in the supernatant was assessed at two different time point. A significant increase in nitrites concentration was initially observed in Abi3-deficient cells (Figure 3.14). However, once this data was normalised by the average nuclei count, the genotype effect appeared not to significantly impact NO production (Figure 3.14). Multiple

factors could have impacted nitrite quantification. First of all, despite plating identical cell numbers when preparing for the assay, it is possible there was some variation, minimised by the use of technical triplicates. It was also noted that, especially following a 48-hour stimulation (when cell death is more evident), the cellular layer was particularly sensitive to pipetting. Indeed, this is the reason why a nuclei count was chosen for normalisation over other approaches, such as total protein quantification. During the set-up phase, it had been seen that complete removal of media before addition of RIPA buffer was causing major portion of the cellular layer to detach and be lost with the discarded media, obviously impacting the final protein quantification. Instead, the addition of Hoechst 33342 followed by immediate imaging did not require complete media removal, providing a more gentle way to quantify cell content. While this approach could have caused dead cells not in suspension to be included in the count, the observed average nuclei count showed a significant reduction in cell number after 48 hours (Figure 3.14) that matched brightfield observations of the cells performed before the assay, providing confidence in this approach. All samples were visually assessed before the assay was performed and were imaged in an automated fashion using a set of locations ranging across the well surface and chosen a priori (as shown in Methods section 2.4.4) to reduce bias. Thus, while it is possible that a particular well presented an increased/reduced number of cells in some area of the well due to issues during re-seeding, this is unlikely to have affected multiple wells across all repetitions. In the future, this concern could be addressed through the use of a temperature controlled CO₂ chamber to allow imaging of the whole well surface. Another confounding factor is the potentially diverse rate of cell death among genotypes in response to stimulation and serum reduction. The presence of an increased number of dead cells in a specific sample could indeed provide additional stimulation to the cells in that well, causing difficulties in the interpretation of the results. This could be assessed performing a MTT assay on stimulated and unstimulated cells.

Overall, section 3.2.4 hinted at a potential involvement of Abi3-dependent actin dynamics in the release of inflammatory mediators following *in vitro* challenging of MØs. These observations will have to be repeated with a more appropriate experimental set-up and cellular model, such as primary microglia and/or iPSC-derived microglia. Further experiments are required to clarify whether any observed difference is a direct consequence of Abi3 ablation or a secondary event.

A considerable concern for any *in vitro* functional assay aimed to identify cellular processes impacted by Abi3 ablation is the current lack of a specific antibody to

evaluate the level and heterogeneity of Abi3 expression at protein level in WT cells in any specific challenge. We previously assessed β -Galactosidase expression by IHC and/or flow cytometry in Abi3-KO pM \emptyset s, M \emptyset Ps and BMDMs (329). Only a small portion of resting pM \emptyset s expressed this reporter indicating the Abi3 KO gene was being transcribed, approximately 30 % as seen by β -galactosidase staining, ~15 % when assessed by flow cytometry. The LacZ reporter was instead almost undetectable in M \emptyset Ps and BMDMs, possibly due to a disruption of regulatory elements necessary for LacZ β -Galactosidase expression as well as culturing conditions, making it an unreliable tool for Abi3 detection.

Another major limitation to the work presented in this chapter – and to future experiments – was the scarce availability of truly representative cellular models for the *in vitro* study of Abi3 in macrophages. Initially, the use of conditionally-immortalised M \emptyset progenitors not only ensured elevated numbers of cells readily available for experiments regardless of potential issues related to mice breeding, but it also allowed an effective application of the “Reduction” principle of the 3Rs. Hoxb8-immortalised progenitors had been previously reportedly maintained in culture for prolonged period and still presented normal karyotype as well as stable ability to commit to a macrophage-like phenotype (376). Moreover, M-CSF differentiated M \emptyset Ps had been shown to recapitulate M \emptyset s morphology and surface markers (333). Despite this, all three pairs of M \emptyset P cell lines derived from Abi3-WT and -KO eventually presented an abnormal expansion of smaller cells resistant to M-CSF-induced differentiation (not shown). This phenomenon appeared to be independent from the number of passages, with even early generations displaying this second population. When visually evaluated, these cells appeared apoptotic. The progressive increase in number shown by this second group of cells, concurrent with the reduction of the healthy population, would support the hypothesis of M \emptyset Ps becoming apoptotic. Further work would be required to clarify the cause of these observations.

Due to the problematic issues with the immortalisation of M \emptyset s precursors, it was decided to switch to the use of primary BMDMs. These cells expressed Abi3 at comparable levels to differentiated M \emptyset Ps and were preferred to primary microglia because of their more reliable culture protocol. In theory, the use of BMDMs would have ensured a faster availability of differentiated cells to complete this chapter. Unfortunately as this time there were issue with the breeding of the mouse colonies, resulting in the inability to run biological replicates in parallel in the assays shown in sections 3.2.3-4. Bone marrow can be easily stored while waiting for more tissue to

be collected, in order to synchronously culture Abi3-KO cells and their controls. Despite mice being maintained in ventilated scintainers to reduce the risk of infection, this approach is potentially flawed due to the possibility of differences due to exposure of the mice to different microenvironmental conditions or unidentified technical variation during cell extraction. The reduced sample availability, as well as the inability to co-house animals of the two strains before bone marrow harvest – stemming from unforeseeable breeding difficulties experienced during this period of study – placed a caveat over the interpretation of the described observations.

Therefore, before any further *in vitro* study, a better cellular model should be identified. MØPs and BMDMs were initially chosen due to availability of established protocols for their culturing. However, Abi3 expression in bone marrow is just a fraction of the one detected in microglia and appears to be approximately half of Abi3 levels in pMØs (Figure 3.16) (291). The use of microglial cells would therefore provide more confidence in any observation related to Abi3 deficiency. However, microglia – as macrophages in general – are extremely dependent on their microenvironment (377) and recapitulating their physiological phenotype *in vitro* is therefore particularly challenging. A number of microglia cell lines are available, however they have been reported to lack expression of adult microglial signature genes (114) as well as to respond less than primary microglia to LPS stimulation (320) with many potential implications for *in vitro* functional assays. On the other hand, the use of primary culture poses just as many challenges. The physiological gene expression profile of freshly isolated microglia is disrupted within few hours of cells being isolation from brain tissue, leading to dedifferentiation, while serum exposure has been shown to artificially increase cell proliferation and phagocytic activity in culture (90). The use of mixed glial culture (90) as well as the addition of TGF- β (90,114), cholesterol and CSF-1/IL-34 (90) has been shown to help partially retaining appropriate expression of microglial signature genes. While these findings have increased the reliability of primary microglial culture, a greater understanding of the profound differences exhibited between mouse and human microglia (89,378,379) challenges the validity of the current murine models from the clinical translation perspective. For this reason, future work on primary microglia should be complemented through the use of human iPSC-derived microglia whilst attempting to recapitulate brain microenvironment, perhaps through the use of cerebral organoids (380).

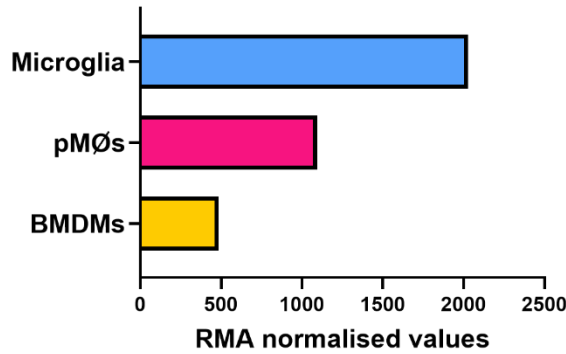


Figure 3.16 *Abi3* expression in primary murine microglia compared to pMØs and BMDMs as shown by Micro-array.

Immgen Micro-array Gene Skyline database (291), showing *Abi3* expression values normalised by Robust Multichip Average (RMA), clearly highlights the difference between microglia and other macrophage populations. Notably, *Abi3* expression in pMØs is doubled compared to BMDMs.

3.4. Conclusion and future work

In conclusion, this chapter support the hypothesis of a major role of *Abi3* in actin dynamics and leads to speculations on the potential impact on the activation status of macrophages. Previous reports of *Abi3* involvement in the WRC functionality have been mostly based on the ectopic expression of *ABI3* in *in vitro* cellular models (299,306,308). Instead, this work provides evidence of *Abi3* importance while expressed at physiological levels in relevant cell types such as macrophages.

As previously discussed, a first vital step in order to continue investigating *Abi3* role *in vitro* is the identification of a better cellular model. *Abi3*^{F212} mice, carrying the murine equivalent of the rare F209 variant identified in AD patients (192) could help clarifying the impact of said variant without the need for forced expression through viral vectors, which can result in unknown alterations on macrophage physiology. Moreover, human iPSCs could be engineered to not express *Abi3*, or to instead express either the human or mouse rare variant. These lines could be then differentiated into microglia-like cells and seeded into cerebral organoids to mimic the brain environment, in order to clarify the effect of *Abi3* ablation or mutation on human microglia. Any results obtained from morphological and functional analyses,

or RNA sequencing experiments, could be then compared to those obtained from freshly extracted microglia.

These cells could be then functionally challenged based on pathways identified by the sequencing analysis. Examples of potential approaches include live chemotaxis assays and evaluation of both phagocytic and endocytic ability using pHrodo labelled compounds (e.g. not just apoptotic cells, Zymosan and Dextran, but also AD-relevant stimuli such as A β -oligomers and synaptoneuroosomes, with and without C3b opsonisation) through the Opera Phenix Plus High-Content Screening System; use of Agilent Seahorse Analyser for metabolic measurements and calcium dynamics assessment with a FLIPR[®] Penta High-Throughput Cellular Screening System; evaluation of inflammatory response by means of BioLegend's LEGENDplex[™] immunoassay kit as well as characterisation of multiple activation markers through multicolour flow cytometry. Recent availability of CellMask[™] Actin Tracking Stain (which allows F-actin staining in live cells for up to 24 hours) will allow a better understanding of actin reorganisation during different challenges.

Some of these results could be compared to those obtained from primary microglia extracted from mice crossed with the APP^{NL-G-F} model of AD. For instance, freshly isolated microglia could be fixed, stained for internalised β -amyloid and analysed by flow cytometry in order to evaluate the rate of A β -plaques phagocytosis *in vivo*. The application of a laser injury protocol on anaesthetised Cx3cr1-GFP mice crossed with relevant strains (already employed in two-photon experiments such as those discussed in section 4.2.3 of this thesis) would instead provide an *in vivo* perspective on Abi3-KO and Abi3^{212F} microglia chemotactic ability.

An anti-Abi3 antibody is currently being produced in-house. Should this attempt be successful – or should a specific, commercial antibody become available in the meantime – assessment of the co-localisation between Abi3 and members of the WRC such as Arp2/3 or Wave2, as well as a protein-interaction screen via immunoprecipitation, in unchallenged and stimulated cells during different type of assays would help shedding light on the mechanisms behind Abi3 action on the actin cytoskeleton.

Finally, it is important to consider the suggested role of Abi3 on cell cycle – due to its connection to the PI3K/AKT pathway (296,300) – and senescence (305,306). These observations suggest the necessity to further clarify the impact of both mutation and knock-out of Abi3 on cell proliferation, death and senescence. Cell death could be

assessed using anti-cleaved Caspase3 antibody or an Annexin-V fluorescent detection kit to identify cells which have activated apoptotic pathways. A (3-(4,5-dimethylthiazol-2-yl)-2,5-diphenyltetrazolium bromide) tetrazolium (MTT) assay would instead allow detection of metabolically active cells. Additional *in-vivo* studies, e.g. intraperitoneal injection of EdU, would help overcoming the limitations associated to the use of cell lines.

**Chapter 4: How does Abi3
influence microglia
physiological activity?**

4.1. Introduction

Microglial heavily rely on their ability to quickly expand and retract their processes to perform their homeostatic functions as well as to promptly respond to potentially detrimental exogenous stimuli (as discussed in details in Introduction section 1.2.3). As such, the phenotype manifested by Abi3-KO MØs reported in the previous chapter led to several implications for microglia functionality.

For instance, the reduction in MØs ramifications, if similarly manifested in Abi3-deficient microglia *in vivo*, could have impacted their ability to migrate towards and phagocyte dying cells, pathogens or other aggregates (such as A β deposits in AD brains). Moreover, the potential involvement of Abi3 in the regulation of baseline ROS levels in macrophages, emerged in section 3.2.4, together with evidences of NO production alterations following actin cytoskeleton manipulation of MØs and microglia (264,323), led to speculations regarding the activation state of naïve Abi3-KO microglia *in vivo*.

In the brain, Abi3 is primarily expressed in microglia (292,293), as discussed in section 1.4. However, Ibanez et al. have recently reported putative expression of Abi3 in neuronal cells (303), and previous work by Bae et al. highlighted a potential role of Abi3 in dendritic spine morphogenesis (308). At the same time, astrocytes rely on microglia for both their maturation (influenced by microglia-secreted factors including IL-6 and leukaemia inhibitory factor (LIF) (124)) and their response to changes in the brain environment, such as in the case of traumatic brain injury or other pathological states of the CNS (381,382). In turn, activated astrocytes play a crucial role in neuronal survival as well as acting as mediators for microglia activation (130). Therefore, regardless of the levels of Abi3 expression in other glial or neuronal cells, any alteration in microglia functionality following Abi3 depletion could have severe repercussion on the CNS health.

A deeper understanding of the physiological role of Abi3 in microglia within the healthy brain is therefore essential. Abi3 had been previously suggested to play a crucial role in the regulation of WAVE2-dependent actin polymerisation (295,299). However, at the commencing of this work no observation on the role of this factor *in vivo* had been published yet using a model in which Abi3 was expressed at physiological levels.

Thus, the aim of this chapter was to clarify the extent of the impact of complete Abi3 ablation on microglial morphology and functionality in the brain of young (8- to

10-week-old) Abi3-KO mice. This was achieved through the employment of a combination of histological techniques and *in vivo* imaging approaches. Moreover, given the extremely interconnected nature of microglia and astrocytes in the brain, astrogliosis was also evaluated in the hippocampus of the same animals by immunofluorescence.

4.2. Results

4.2.1. Basic characterisation of microglia in young Abi3-KO mice brain

The impact of Abi3 ablation on microglia was assessed in young (8-9 week-old) mice through immunostaining for Iba1, a commonly used marker for microglia (383). Considering the prominent role of the Prefrontal Cortex (PFC) and the hippocampus in memory formation and retention (384,385), and their involvement in Alzheimer's disease (386,387), the following analyses were performed on sections comprising these regions (for more details, please refer to Methods section 2.6.2).

Young male and female mice were analysed for both genotypes in order to take into account the impact of sexual dimorphism on microglia morphology and distribution (152). Images were analysed as described in Methods section 2.6.4.

Figure 4.1A shows representative images of the Iba1 staining on the PFC (Figure 4.1A, top row) and the hippocampus (Figure 4.1A, bottom row) of Abi3-WT and -KO mice. Following quantification of microglia number, a significant difference between genotypes emerged from the cell count analysis in both the PFC ($p=0.0001$; Figure 4.1B) and the hippocampus ($p\leq 0.0001$; Figure 4.1C), with Abi3-KO mice showing an increase in cell density. Male and female mice of the same genotype showed no obvious differences ($p=0.9857$ in the PFC and 0.5003 in the Hippocampus; Figure 4.1B and C respectively). Consistent with the increase in cell number and the reduction in the arborisations, Abi3-KO cells resulted significantly closer to each other ($p\leq 0.0001$ in both brain regions; Figure 4.1D and E). Nevertheless, as it was already possible to appreciate by simple visual assessment, the percentage of image area covered by Iba1⁺ pixels were found to be significantly lower in the Abi3-KO samples ($p\leq 0.0001$ in both the PFC and the hippocampus; Figure 4.1F and G respectively) regardless of the sex ($p=0.8983$ and $p=0.5643$ for the two areas respectively; Figure 4.1F and G).

Taken together, these observations demonstrated that the differences in Iba1⁺ staining between the samples were indeed due to alteration of microglia morphology in the Abi3-KO mice and not to a simple reduction in cell number.

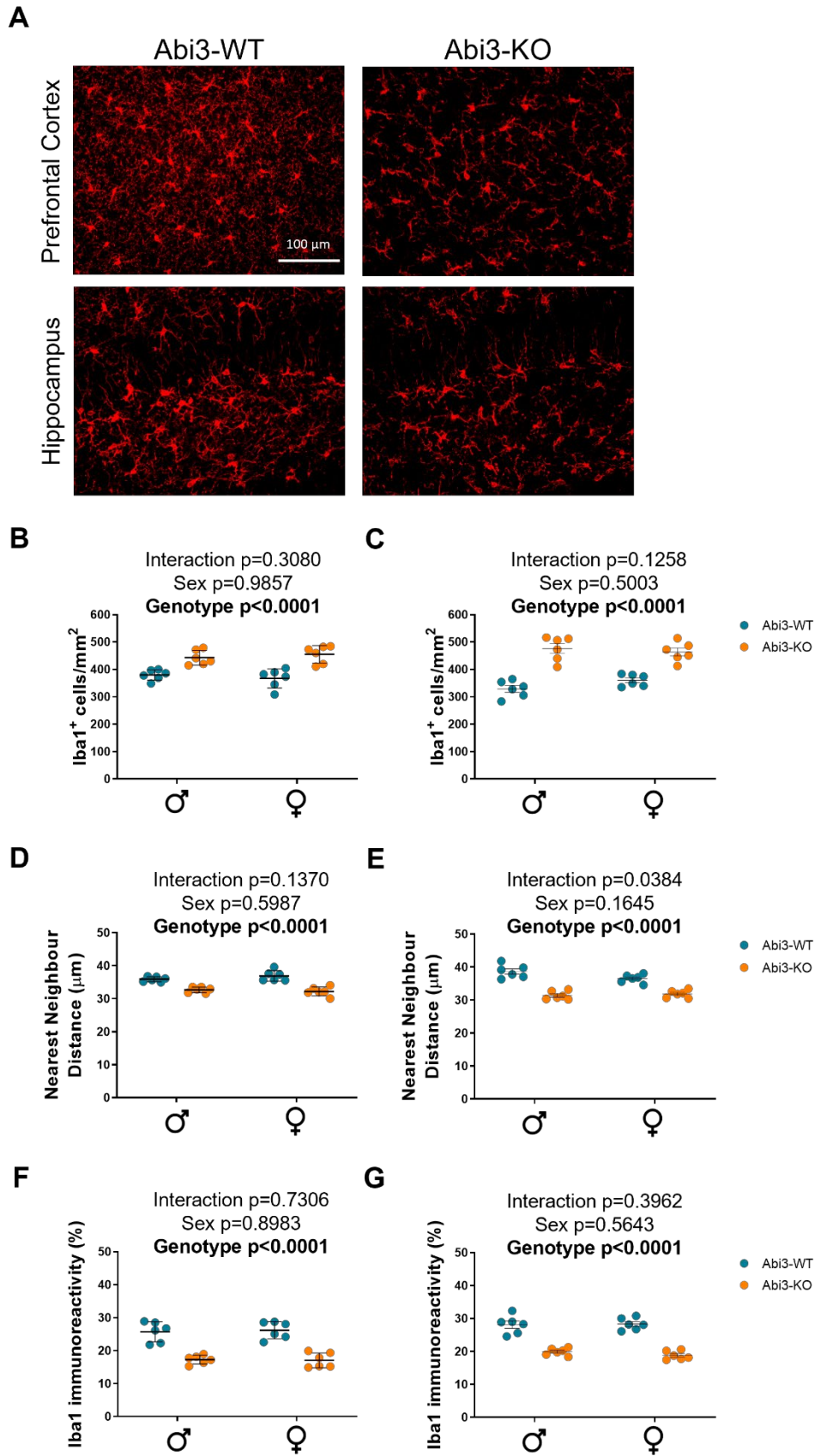


Figure 4.1 Representative images and quantification of the Iba1 staining for microglia in Abi3-WT and -KO mice brain sections.

Each datapoint on the graphs represents the average value obtained through Fiji analysis from all the pictures acquired for one section. The blue dots indicate Abi3-WT mice, while the orange dots those from the Abi3-KO animals. The black horizontal lines represent the mean of each experimental group. Error bars indicate S.E.M. The p-values resulting from the Two-way ANOVA are reported on each graph. A) Representative pictures of the Iba1 staining (red) performed on the PFC and the hippocampus (in these images, specifically in the DG) of Abi3-WT and -KO mice. The alteration in microglia morphology following Abi3 ablation was striking, with Abi3-KO cells showing an important reduction in their processes. In particular, these cells seemed to lack the thinner processes, although a more in-depth analysis was required to confirm this observation. B) and C) Quantification of microglia density in the PFC (B) and the hippocampus (C) of Abi3-WT and -KO mice. D) and E) Quantification of Nearest Neighbour Distance in Abi3-WT and -KO mice (in the PFC, D, and hippocampus, E). F) and G) Evaluation of Iba1 immunoreactivity in the same PFC (F) and hippocampus (G) slides. Data were analysed via Two-way ANOVA test. n=6.

These *ex-vivo* analyses performed on brain samples from naïve Abi3-WT and –KO mice confirmed the previous observations on the MØ cultures discussed in Chapter 3. In order to properly assess the impact of Abi3, a further in-depth 3D morphological analysis of these samples was therefore warranted.

4.2.2. In-depth morphological characterisation of individual Abi3-KO microglia

One of the biggest limitations of the Fiji analysis performed in the previous section – as well as of similar 2D analyses – is the oversimplification of microglia structure. This can in turn lead to an underestimation of morphological changes due to pathological conditions or, as in this case, to genetic modifications. A growing set of software and computational approaches have been recently developed to address this issue (388–390). However, one of the most widely used tools is Imaris software (143,391–394). Its “Filament Tracer” module allows both automated and manual tracing of single microglia cells from 3D z-stacks, as described in section 2.6.4.4 of the Methods. Figure 4.2 demonstrates the higher resolution allowed a better appreciation of the structural differences between Abi3-WT and -KO microglia.

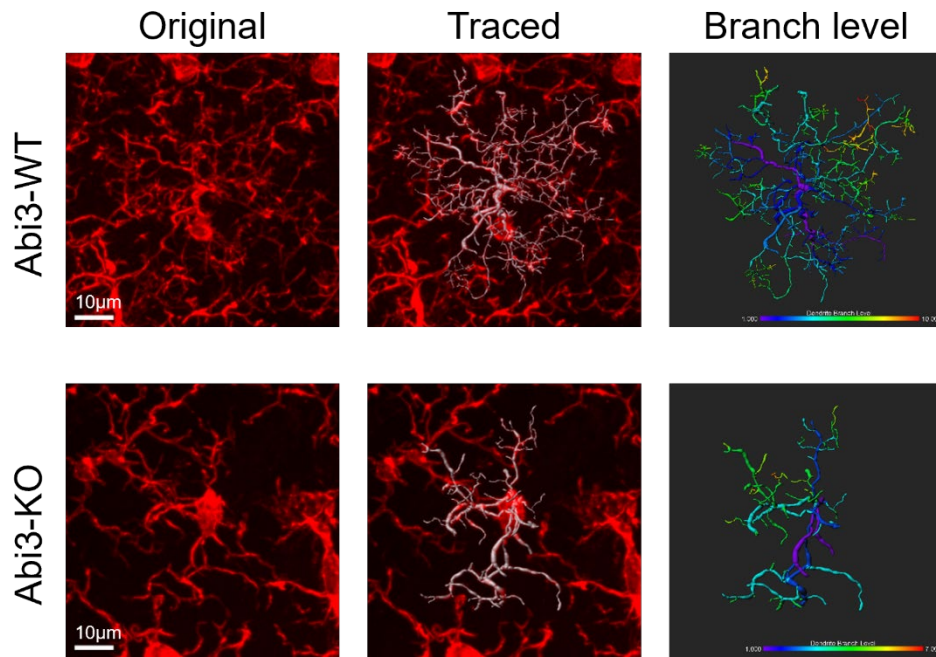


Figure 4.2 Representative images of single microglia obtained from Abi3-WT and -KO mice brain sections, stained with Iba1 antibody and traced using Imaris software.

Each individual cell, stained with an anti-Iba1 antibody (first column, red) was manually 3D traced (middle column, white) on Imaris. The third column presents an example of the same tracing colour-coded based on branch level to highlight the dramatic difference in arborisation complexity between genotypes. Images are representative of 60 microglia per genotype analysed in this way.

Consistent with previous considerations, the lack of Abi3 lead to a significant increase in average segment length ($p \leq 0.0001$, Figure 4.3A). While this observation could seem antithetic, but are explained by considering the reduction in ramification complexity shown by Abi3-KO microglia, which extends the distance between two consecutive branch points (or between a branch point and a terminal point). Abi3-WT microglial ramifications were also characterised by significantly smaller mean diameter compared to Abi3-KO cells ($p \leq 0.0001$, Figure 4.3B). In line with these findings, Abi3-WT cells were richer in segments with smaller area (Figure 4.3C) and volume (Figure 4.3D), with $p \leq 0.0001$ for males and females in both datasets. Notably, no significant difference was observed between animals of different sexes within each genotype group (Table 4.1).

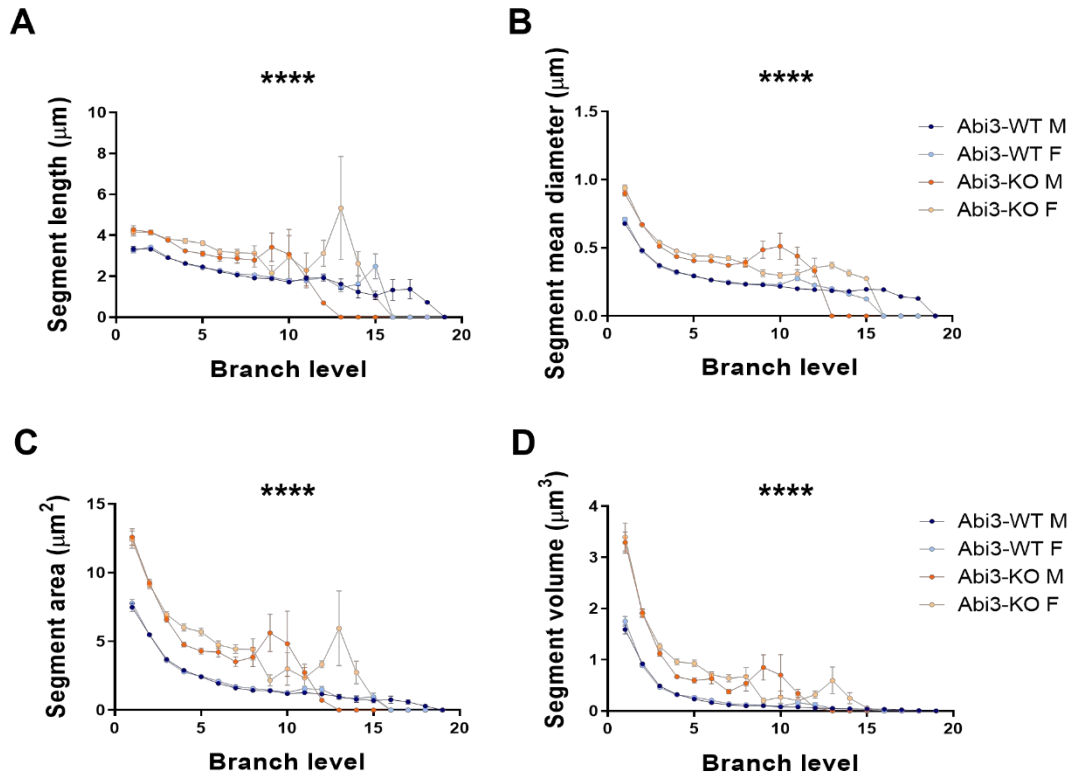


Figure 4.3 Quantification of ramification length, mean diameter, area and volume of Abi3-WT and -KO microglia.

Each point in the line graphs represents the average value for all the segments of one experimental group at that specific branch level \pm S.E.M.. Blue and light-blue lines represent male (“M”) and female (“F”) Abi3-WT mice respectively, while the red (males) and orange (females) lines indicate Abi3-KO animals. Evaluation of **A)** ramification length, **B)** diameter, **C)** surface and **D)** volume for Abi3-WT and -KO microglial ramifications. Data were analysed via linear mixed model analysis; the *p*-value for the genotype effect obtained from the regression model is reported on each graph by means of asterisks, where *****p* ≤ 0.0001. *n* > 9000 segments from 30 cells/group.

	Segment length		Segment mean diameter		Segment area		Segment volume	
	t value	p value	t value	p value	t value	p value	t value	p value
Sex	1.214	0.238	0.448	0.658	0.785	0.441	0.675	0.507
Genotype	8.251	3.12e ⁻⁰⁸	5.991	6.01e ⁻⁰⁶	7.527	2.09e ⁻⁰⁷	6.974	6.83e ⁻⁰⁷

Table 4.1 Summary table of the *t*- and *p*-values calculated for the genotype and sex effects for segment-related data generated by Imaris analysis.

The reported *t*- and *p*-values represent the effect size and statistical significance, respectively, for the fixed effects. While branch level was included as a fixed effect in the regression model, it was only used as a grouping factor and therefore the relative *t*- and *p*-

values are not shown in this table. A positive t-value corresponds to a higher mean of the outcome variable in Abi3-KO mice as compared to Abi3-WT. Overall values for the whole cell – including number of branching points, full branch level, cell area and cell volume – were calculated for all 120 cells analysed.

Figure 4.4A shows the total number of branching points for Abi3-WT and –KO microglia, an indication of the complexity of the ramification apparatus of a cell. Both males and females Abi3-WT cells presented a significantly higher number of branching points compared to Abi3-KO ones ($p \leq 0.0001$). Strikingly, the average value for Abi3-WT cells resulted 5.5x (for males) and 4.3x (for females) higher than Abi3-KO mice of the same sex. However, no significant difference was observed between males and females of the same genotype ($p = 0.727$, Table 4.2).

The Full Branching Level value is another indicator of complexity: the higher the value, the higher the number of consecutive branching points (and therefore, indirectly, ramifications). Again, Abi3-WT cells scored significantly higher than those from Abi3-KO animals ($p \leq 0.0001$, Figure 4.4B). As in the previous case, sex did not appear to influence the complexity of the arborisations system ($p = 0.358$, Table 4.2).

While Abi3-KO mice showed a higher percentage of thicker and longer processes, the considerable difference in branch number meant microglia showed a significant reduction in cell surface in the absence of Abi3. Indeed, males and females Abi3-WT cells presented a greater area ($p \leq 0.0001$, Figure 4.4C) than Abi3-KO cells. The difference between genotyping resulted less striking when evaluating the total cell volume, possibly due to the small contribution of the thin processes (in which Abi3-WT cells are rich) to the overall volume. Nevertheless, in the presence of Abi3 cells resulted significantly bigger than those from Abi3-KO mice ($p \leq 0.05$, Figure 4.4D), with no difference between sexes ($p = 0.8865$, Table 4.2).

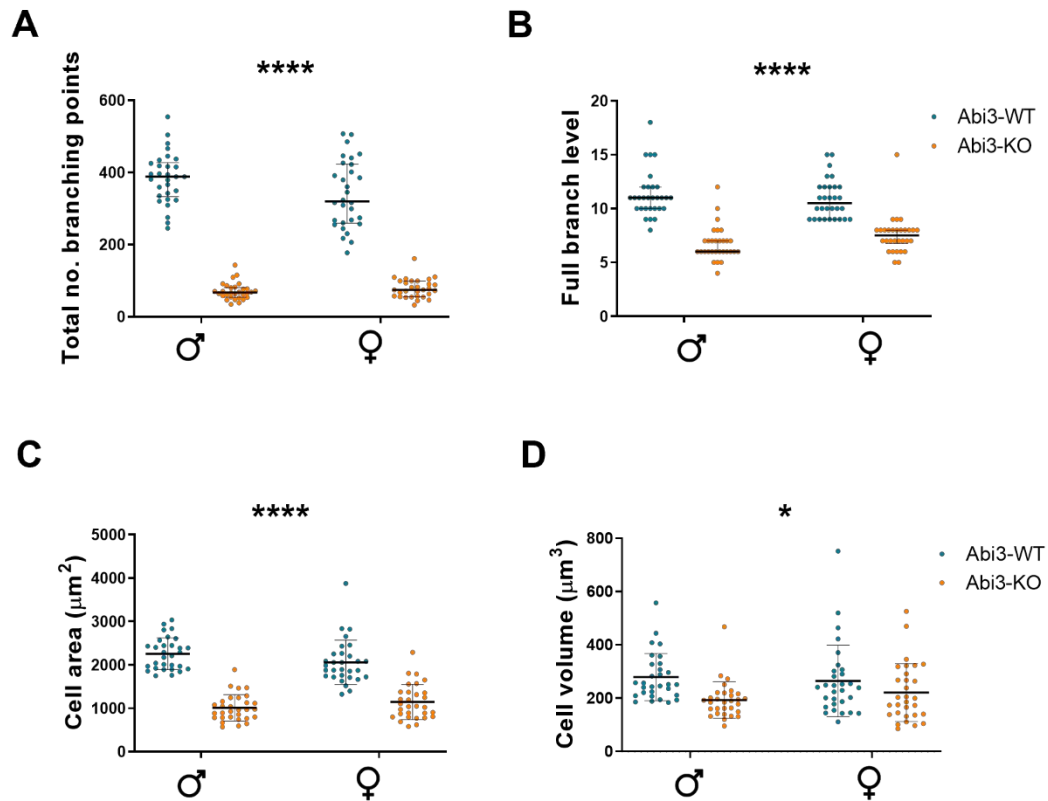


Figure 4.4 Evaluation of complexity of the ramification apparatus and overall cell size.

Each datapoint on the graphs represents the value of a single cell. The blue dots indicate Abi3-WT mice, while the orange ones the Abi3-KO animals. In the first two graphs, the black horizontal lines represent the median of each experimental group \pm interquartile range, while in the other two they indicate mean \pm S.D. Quantification of **A)** the number of branching points, **B)** overall Branching Level value (an index of ramifications complexity), **C)** cell surface and **D)** cellular volume. Data were analysed via a linear mixed model, with sex and genotype used as fixed effects; p-values for the genotype effect are shown as asterisks on the graph, where * $p \leq 0.05$ and **** $p \leq 0.0001$. $n=30$ for each group.

	Total no. branching points		Full branch level		Cell area		Cell volume	
	t value	p value	t value	p value	t value	p value	t value	p value
Sex	-0.354	0.727	0.94	0.358	0.03	0.977	-0.144	0.8865
Genotype	-23.727	$<2e^{-16}$	-10.98	$3.65e^{-10}$	-12.53	$3.29e^{-11}$	-2.657	0.0147

Table 4.2 Summary table of the t- and p-values calculated for the genotype and sex effects for the whole-cell parameters analysed.

A positive t-value corresponds to a higher mean of the outcome variable in Abi3-KO mice as compared to Abi3-WT, while a negative t-value represents a lower mean in Abi3-KO animals.

While the number of branching points and the full branching level are useful indicators of cell complexity, the easiest way to visualise a potential difference in the amount of microglia ramifications is by means of a Sholl profile, as described in the Methods (section 4.5.6, Figure 4.11).

Figure 4.5A shows the results of the Sholl analysis. The Sholl profiles showed a marked difference between Abi3-WT and -KO cells. Indeed, Abi3-WT mice showed a greater amount of ramifications already at 3 μm from the cell body ($p \leq 0.01$, Figure 4.5A). This difference became even more striking between 6 μm and 36 μm ($p \leq 0.0001$ at all points, Figure 4.5A). At further radius level, 39-69 μm , the difference progressively reduces, albeit Abi3-WT cells still presented an increased number of intersections. Sex did not appear to exert a strong effect on the phenotype, with only two radii being significantly influenced by it (21 μm , $p = 0.0259$, and 36 μm , $p = 0.0242$, Table 4.3). All of these observations led to a significant decrease in the Area Under the Curve (A.U.C.) of Abi3-KO samples of both sexes, as shown in Figure 4.5B ($p \leq 0.0001$ for genotype, $p = 0.526$ for sex, Table 4.3).

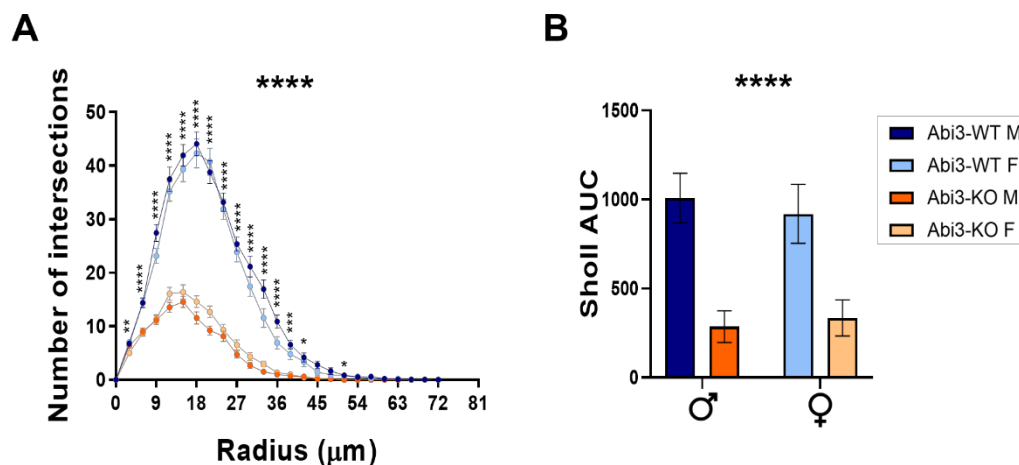


Figure 4.5 Sholl analysis of Abi3-WT and -KO microglial cells.

The blue and light-blue lines/bars indicate Abi3-WT mice, while the orange and red ones refer to Abi3-KO animals. The p -value for the overall genotype effect is reported on top of each graph by means of asterisks, while the individual p -values for the genotype effect on each radius are reported on the corresponding point on the Sholl profile. **A)** Average number of intersections for each experimental group, plotted against the radius of the sphere as mean \pm S.E.M. **B)** A.U.C. of the Sholl profile of each group each, showed as bars representing the average of all the cells in the group \pm SD. Data analysed via linear mixed model, with the

*p-values for the genotype effect reported by means of asterisks, where * $p \leq 0.05$, ** $p \leq 0.01$, *** $p \leq 0.001$ and **** $p \leq 0.001$. $n=30$ for each group.*

	Sholl intersections		Sholl A.U.C.	
	t value	p value	t value	p value
Sex	-0.521	0.602	0.636	0.526
Genotype	-23.383	$<2e^{-16}$	-25.171	$<2e^{-16}$

Table 4.3 Summary table of the t- and p-values calculated for the Sholl intersections and the Sholl Area Under the Curve values.

The radius of each shell was included in the regression model as a fixed effect, but it was only used as a grouping factor and is therefore not reported in the table above.

Taken together, all the parameters assessed in this section confirmed the visual observations previously discussed. Indeed, Abi3 ablation resulted in a severe impairment of microglia arborisations. Abi3-KO cells resulted provided of thicker and longer processes, while almost entirely lacking thin and short processes branching off the primary and secondary ramifications. Moreover, Abi3-KO cells showed a reduced complexity of their ramification apparatus, with significantly fewer ramifications compared to Abi3-WT cells, in particular, closer to the soma. That in turn caused a significant reduction in cell surface, only partially compensated by the greater ramification volume.

4.2.3. Evaluation of microglia dynamics *in vivo* through two-photon imaging on Abi3-KO mice

Histological analyses are a useful tool to gather basic information about microglia morphology and distribution within the brain. However, they only provide a snapshot of the extent of microglia scavenging activity. Even in their homeostatic state, the microglial cytoskeleton constantly remodels itself in order to efficiently scan brain parenchyma, with processes extending and retracting at a speed of about 1.47 $\mu\text{m}/\text{min}$ (47).

To better evaluate microglia dynamics and assess the real impact of Abi3 ablation on their actin cytoskeleton remodelling, awake mice were imaged using a two-photon microscope (see section 2.7). Two-photon technology uses near infrared light (wavelengths >700 nm) to excite the chosen fluorophore, therefore reducing the risk of tissue damage due to phototoxicity and thus allowing repeated and prolonged acquisition of *in-vivo* data (395) up to ~500 μm deep within the tissue (395).

Three females and two males (all 10 week-old), who underwent a craniotomy and a single awake *in vivo* imaging session as described in section 2.7, were analysed for each genotype (Appendix 3, Video A and B). Figure 4.6A shows representative images of Abi3-WT and -KO cells at different steps of the analysis. As it was apparent from the visual observation, the lack of Abi3 severely impaired the ability of microglia to extend ramifications to scan the surrounding parenchyma. Indeed, only $51.88\% \pm 7.49\%$ (for males; mean \pm SD) and $53.32\% \pm 3.77\%$ (for females mean \pm SD) of the total area is covered by microglia processes in Abi3-KO animals, while the percentage is significantly higher in Abi3-WT animals ($p=0.005$, Genotype effect of Two-way ANOVA) with $75.41\% \pm 1.80\%$ and $73.07\% \pm 4.35\%$ (mean \pm SD). No difference was observed between animals of the same genotype, but different sex ($p=0.7908$, Figure 4.6B).

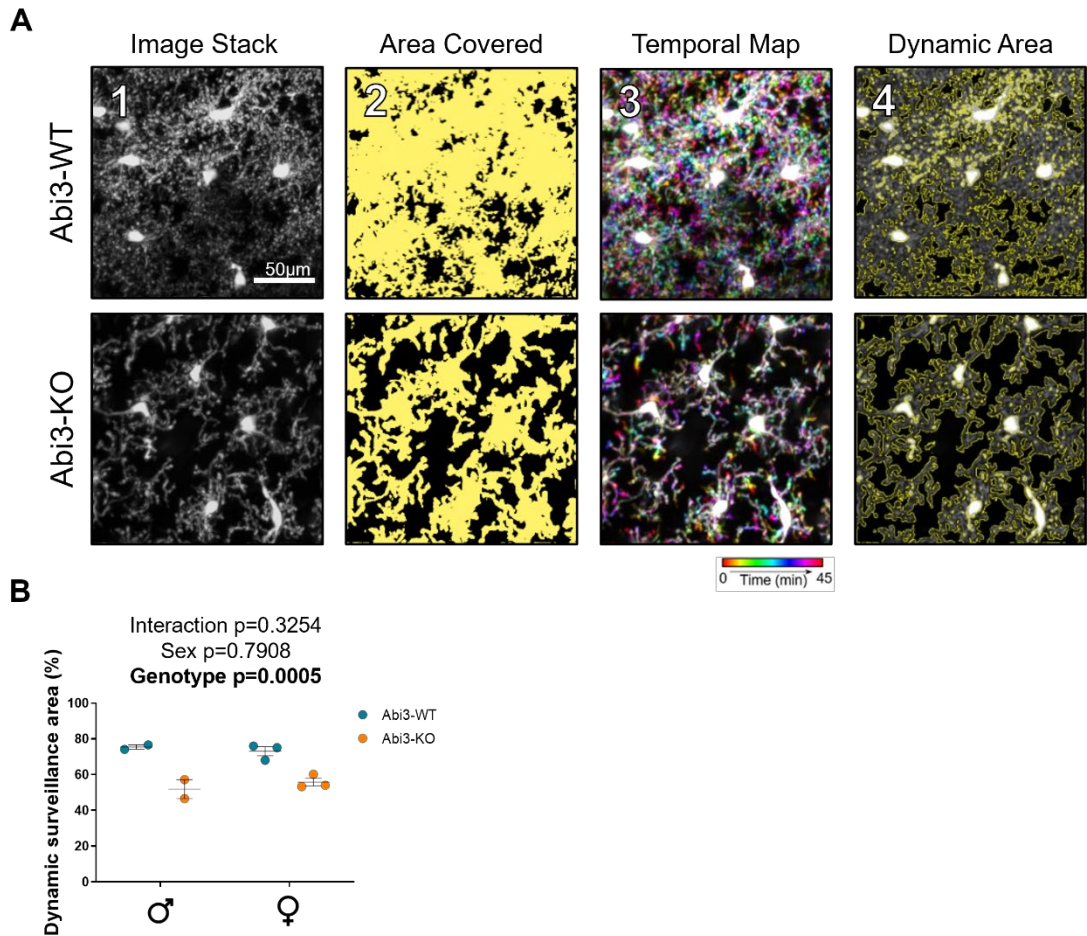


Figure 4.6 Quantification of microglia surveillance activity through two-photon imaging.

Each datapoint on the graphs represents an individual mouse. *Abi3*-WT mice are indicated by blue dots, *Abi3*-KO animals by the orange ones. The black horizontal lines represent the mean of each experimental group \pm S.E.M. The results of a Two-way ANOVA are reported on each graph. **A)** Representative images of *Abi3*-WT and -KO mice flattened time-stacks. The difference between genotypes appeared obvious when looking at the orthogonal projection originated from the 4D files (1), but it was even more striking once a threshold was applied to create binary images and select the area (in yellow) covered by microglia soma and processes (2). The temporal map showed in (3) allowed visualization of the extreme remodelling of *Abi3*-WT cells during the span of the 45-minutes acquisition. As it emerged from the videos, while a certain degree of actin cytoskeleton rearrangement was present even in *Abi3*-KO cells, it was remarkably reduced compared to the *Abi3*-WT cells. Finally, applying the dynamic area ROI (in yellow) to the orthogonal projection of the time stack proved the accuracy of the analysis. **B)** Quantification of the percentage of dynamic surveillance area (obtained from a 45-minute long acquisition of a single field of view for each mouse) in *Abi3*-WT and -KO mice. Data were analysed via Two-way Anova test. Males $n=$, Females $n=3$ for each genotype.

While this preliminary analysis did not quantify process retraction/expansion, it clearly confirmed that morphological changes discussed in sections 4.2.1 and 4.2.2 are impacting microglia surveillance activity, despite the increased cell number observed in Abi3-KO mice.

4.2.4. Histological evaluation of phagocytosis and astrocytosis in young Abi3-KO mice brain

As previously mentioned, the overall morphological phenotype presented by Abi3-KO microglia resembled the one characterising activated microglia. Indeed, upon stimulation microglia quickly assume amoeboid morphology by withdrawing their ramifications and presenting short and thick processes and a bigger cell body instead (110). One of the most commonly used macrophage lineage markers, in particular as an histological marker of microglia phagocytosis, is Cluster of Differentiation 68 (CD68) (396). CD68 is a lysosomal marker upregulated in phagocytically-active microglia and, notably, seemingly increased in the brain of AD patients (397). For this reason, we investigated CD68 levels in the brain of young animals in the absence of Abi3 as described in section 4.5.5.

Figure 4.7A shows representative images of the Iba1 and CD68 co-staining in the hippocampus of Abi3-WT and -KO mice. Quantification of co-localisation surface (described in Methods section 2.6.4.3) identified a significant difference between genotypes. Indeed, Abi3-KO mice showed significantly more CD68 signal colocalising with Iba1⁺ pixels in both the PFC and the hippocampus ($p \leq 0.0001$ in both brain regions; Figure 4.7B-C). Once again, no significant difference was observed between animals of the same strain but different sexes ($p = 0.3375$ in the PFC and $p = 0.9813$ in the hippocampus; Figure 4.7B-C).

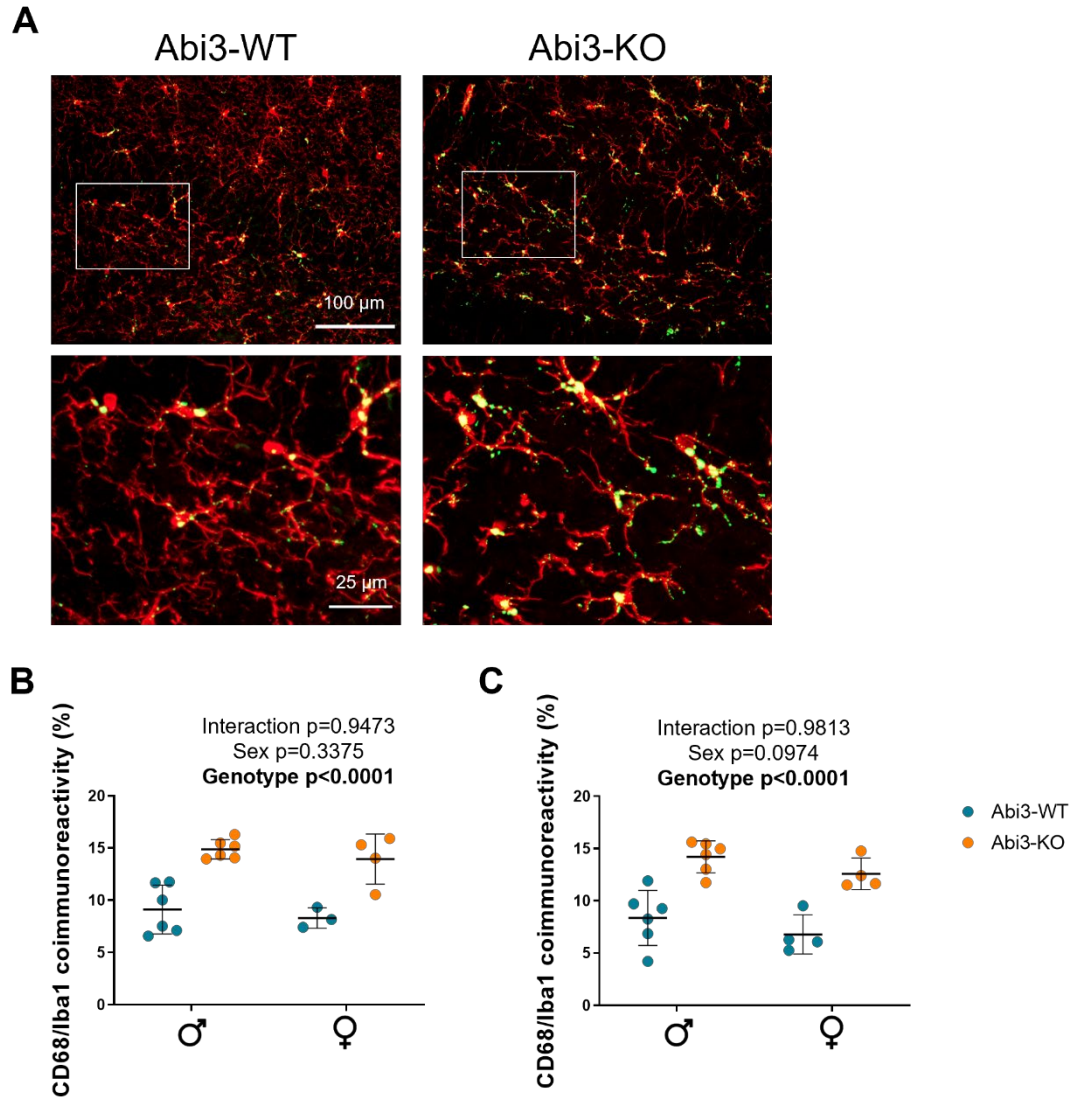


Figure 4.7 Representative images and quantification of the Iba1-CD68 co-staining in Abi3-WT and -KO mice.

Each datapoint on the graphs represents the average value obtained from all the pictures analysed for one animal. The blue and orange dots indicate Abi3-WT and Abi3-KO animals, respectively, while the black horizontal lines represent the mean of each experimental group \pm S.E.M. The p -values resulting from the Two-way ANOVA are reported on each graph. **A)** Representative pictures of the Iba1 (red) and CD68 (green) staining performed on the hippocampus of 8-week-old Abi3-WT and -KO mice. The bottom row represents an enlargement of the area highlighted in the image above with a white square. Abi3-KO mice appeared to present a severe increase in CD68 signal within Iba1⁺ microglial cells. **B)** and **C)** Quantification of CD68 and Iba1 positive pixels in the PFC (B) and the hippocampus (C) of Abi3-WT and -KO mice. Data were analysed via Two-way ANOVA test. $n=6$ for males; $n=3-4$ for females.

While further analyses were required to fully clarify the activation state of microglial cells in Abi3-KO animals, the increase in CD68 presented by these cells, together with the altered morphology and impairment in homeostatic movements, supported the possibility that Abi3 knock-out microglia could be activated and affect the brain environment even in the absence of further pathological conditions. Given the extremely interconnected nature of the microglia-astrocytes populations, any shift in microglia homeostatic balance towards an activated state could indeed result in increased production of pro-inflammatory cytokines, NO, TGF- α and VEGF-B, which would indirectly impact astrocytic phenotype (398).

Thus, the expression of Glial Fibrillary Acidic Protein (GFAP), a classical astrocytic marker, was assessed within the hippocampus of young Abi3-KO and control mice (as per Methods section 2.6.4.2). Representative images are presented in Figure 4.8A. Quantification of astrocytic number with Fiji confirmed that Abi3-KO mice had increased astrocyte density compared to Abi3-WT controls ($p=0.0013$; Figure 4.8B). Despite the higher number of cells, no significant difference was evident in the levels of GFAP immunoreactivity ($p=0.2660$, Genotype effect of Two-way ANOVA; Fig. 4.8C), suggesting a potential alteration of astrocytic morphology following the loss of Abi3. As with microglia, sex did not seem to influence the astrocytic population ($p=0.8683$ and 0.8380 for cell number and GFAP immunoreactivity, respectively; Figure 4.8B-C).

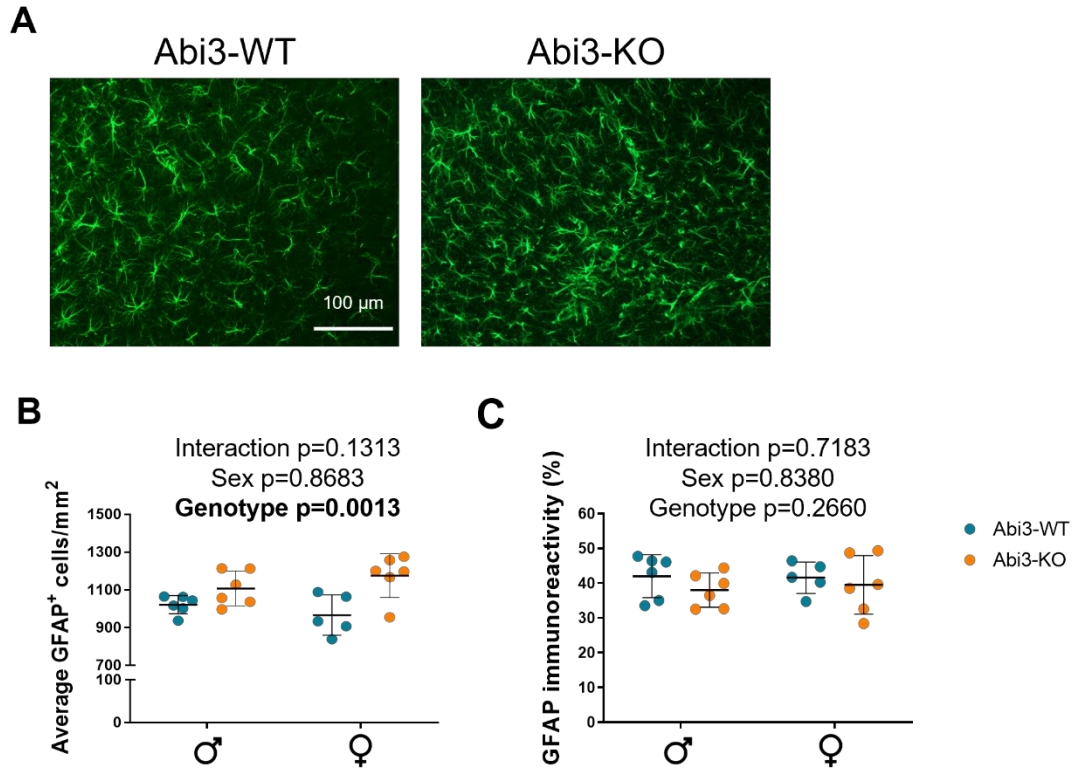


Figure 4.8 Representative images of GFAP⁺ astrocytes in the hippocampus of Abi3-WT and -KO mice.

Each datapoint on the graphs represents the average value obtained from all the pictures analysed for one section. The blue dots indicate Abi3-WT mice, while the orange ones Abi3-KO animals. The black horizontal lines represent the mean of each experimental group \pm S.E.M. The p-values resulting from the Two-way ANOVA are reported on each graph. Note the scale has been truncated for clear visualization in B. **A)** Representative images of GFAP (green) staining performed on hippocampal sections of 8-week-old Abi3-WT and -KO mice. A notable increase in the number of GFAP⁺ astrocytes was observed within the hippocampus of Abi3-KO mice, with cells looking not only closer to each other but also smaller than in Abi3-WT animals. Interestingly, Abi3-KO mice also presented multiple sites of astrocytes aggregation. **B)** and **C)** Quantification of GFAP⁺ cells number (B) and area covered by GFAP⁺ pixels (C) in Abi3-WT and -KO mice. Data were analysed via Two-way ANOVA test. $n=6$ /group, except Abi3-WT females ($n=5$).

4.3. Discussion

The data presented in this chapter, while still far from fully revealing Abi3 role in microglia, support findings presented in Chapter 3. Abi3-KO macrophage-like cells, tested *in vitro* by means of a spreading assay, showed a drastic reduction in filopodia formation. In this chapter, a reduction in small-calibre ramifications was instead observed in Abi3-deficient microglia cells within the brain of 8-week-old mice (Figure 4.1 and 4.2). As shown in section 4.2.1., the reduction in ramification complexity in Abi3-KO mice appeared striking even before proceeding to the successive morphological assessment. However, manual quantification of cell number highlighted a significant (but less obvious from the initial visual assessment) increment in microglia density in the absence of Abi3 in both the PFC and the hippocampus (Figure 4.1).

Notably, these observations were only partially confirmed by Ibanez and colleagues in their recent publication based on the same knock-out model (303). Indeed, the authors reported a decrease in Iba1 immunoreactivity within both the cortex and the hippocampus of 3-month-old mice following heterozygous deletion of Abi3, but no significant difference was observed between Abi3-WT and -KO animals (303). This could be at least in part explained by differences in tissue processing (since Ibanez and colleagues utilised paraffin-embedded tissue fixed in 10 % formalin) as well as by the use of entirely different reagents and softwares for the following analysis. Moreover, the authors did not assess cell count, which makes it hard to understand whether the reduction in Iba1 immunoreactivity is due to the same morphological differences reported in this chapter or to technical divergences.

In order to fully understand the nature of the morphological alterations observed in this initial analysis, the same samples were re-imaged using a higher magnification to capture the entirety of their processes. These images, that further emphasized the differences between genotypes (as shown in Figure 4.2), were then employed for a more in-depth morphological assessment using Imaris software. The 3D reconstruction of the ramification was performed on a total of 120 individual cells from 12 animals (3 for each sex and genotype). This analysis confirmed that Abi3-KO microglia are provided of thicker ramifications, characterised by significantly fewer branching points (and therefore reduced complexity of their Sholl profile) compared to control cells (see section 4.2.2).

Interestingly, both the basic 2D characterisation and the in-depth morphological assessment did not highlight any potential influence of sexual dimorphism on

microglia phenotype of the mice studied. Indeed, only the number of Sholl intersections at two specific radii (21 and 36 μm from the origin) presented a significant difference between sexes. This is surprising due to the multiple sources of evidence supporting a severe impact of sexual hormones (in particular of the peak of testosterone release that precede birth in male rodents (399)) on microglia transcriptomic profile and morphology from the earliest stage of development in rodent brains, as discussed in details in section 1.2.4. For instance, previous reports described the presence of a higher number of microglia in specific regions of the brain (including cortex and hippocampus) of 13-week-old males (155), as well as increased process surface and volume, coupled with a higher number of ramifications and intersections, in the CA3 of the hippocampus of 8-week-old mice of the same sex (391).

Inconsistency in background strains of the mice across studies, as well as technical discrepancies in tissue processing and imaging approaches (including the availability of high resolution imaging equipment), could most likely explain the aforementioned differences in observations. However, an additional source of confusion could be ascribable to the choice between fully- or semi-automated analysis of histological data. For instance, the major drawback of Imaris is the incredibly high time demand of this approach: the Filament Tracer module was originally developed to analyse neurons and, while it can be adapted for microglia analysis, it requires considerably more human intervention and manual editing of the traced filaments. Fully automated tracing is possible, and with careful consideration of the creation parameters during the set-up phase, it can be a useful tool for a fast and acceptably accurate assessment of microglia morphology. However, an unsupervised approach is likely to generate substantial artefacts which, if not manually corrected, could drastically alter the interpretation of the results. Similarly, new softwares have been developed in the past years for fully-automated count and basic characterisation of microglia in either 2D or 3D environments. However, whenever any of these approach was tested on the datasets showed in this thesis, substandard evaluation of critical parameters was noted, due in part to the dramatic differences between Abi3 deficient mice and their controls. Examples of this included, but were not limited to, the incorporation of surrounding ramifications (parallel to the loss of most of the smaller calibre processes and merging of close ramification, with obvious implications on the final process volume) in Abi3-WT cells on Imaris, incorrect segmentation of highly ramified cells and erroneous combination of excessively close Abi3-KO cells.

Moreover, as amply discussed before, microglia are extremely sensitive to environmental factors, which could result in an additional confounding factor across published works. For the scope of this thesis, age- and sex-matched mice of the two genotypes were cohoused from weaning (21-26 days of age) to exclude any artefact caused by potential exposure to different microbiomes and consequent microgliosis. The increase in microglial density within Abi3-KO brains could therefore be explained by taking into consideration the known (albeit still not fully understood) phenomenon of lateral inhibition in microglia tiling during development and CNS repopulation (41). Presenting shorter and sparser ramifications, Abi3-deficient microglia could try to compensate for their reduced arborisation apparatus by increasing in number, in an attempt to efficiently monitor the brain parenchyma.

In order to investigate whether Abi3-KO microglial numbers successfully compensated for the likely functional disruption caused by their dystrophic morphology, histological analyses were supported by *in vivo* two-photon data (shown in section 4.2.3). In the absence of Abi3, over the course of the 45-min long acquisition microglia resulted unable to survey an amount of tissue comparable to that of Abi3-WT cells. This further supported the notion of a crucial role of Abi3 in microglial actin dynamics, crucial for the rapid remodelling of microglia ramifications. Further investigation is warranted to clarify whether Abi3-KO processes extend at a slower rate or do not contract/extend at all due to impaired actin recycling. However, even if Abi3 deficient cells were able to monitor the entire territory given a longer time interval, such a severe surveillance impairment would inevitably cause extremely detrimental effects on the brain microenvironment.

There were initial concerns regarding the appropriateness of using Iba-1 as a microglial marker for morphological analyses involving alterations in the actin cytoskeleton due to its ability to bind and cross-link F-actin (42), which could have led to biases in the downstream evaluation. However, two-photon microscopy images confirmed Abi3-KO phenotype, suggesting the observed morphological changes were not simply an artefact related to the immunostaining protocol or antibody choice.

Alternatively to the homotypic tiling hypothesis, Abi3-KO phenotype could be explained by the potentially activated nature of these cells. Coherently with this theory, the CD68/Iba1 immunostaining analysis presented in section 4.2.4 (Figure 4.7) showed a significant increase of CD68 – a marker of microglia activation and phagocytic activity (397) – within Abi3-deficient microglia cells. As in the case of

microglia quantification, sex seemingly did not impact CD68 expression. Sequencing data, as well as chemokines quantification recently published on this same model seemed to support the hypothesis of a more activated state of Abi3-KO cells (302,303). In particular, among the differentially expressed genes detected by Karahan and colleagues were genes involved in phagocytosis and antigen presentation, such as several Fcγ receptors, ApoE, CD74 and Plc-γ2 (302). This finding would support the hypothesis of an increased phagocytic activity in Abi3-KO mice reported in section 4.2.4. The same work also highlighted an increase in genes involved in the complement pathway and immune response genes – such as Cq1a, IL-3 and TLR7 – and reported significantly higher levels of pro-inflammatory cytokines including CXCL10 and CCL3 (302). Notably, C1q has been recognised as an essential mediator of astrocytes activation (402) and is involved in synapse tagging (69), while CXCL10 and CCL3 have been shown to negatively impact LTP and synaptic function (403,404). However, the use of animals crossed with the 5XFAD model in the work by Karahan and colleagues posed a caveat to the interpretation of their results, since the observed increase in inflammation markers could be a secondary ramification of the higher amyloid plaques burden that the authors described in the Abi3-KO mice, and not the primary cause of the increased neuroinflammation (302). Ibanez and colleagues instead highlighted the expression, in 3-month-old Abi3-KO mice, of genes associated with amyloid deposition in AD, despite the absence of Aβ (303). Additional single cell RNA sequencing experiments would be required to complement Ibanez *et al.* finding, generated through a bulk sequencing approach. However, a putative increase in activation levels in young, healthy animals, as well as enhanced phagocytosis leads to speculations regarding the presence of a potentially severe synaptic impairment due to excessive synaptic pruning and/or LTP impairment caused by a highly pro-inflammatory brain environment.

Young Abi3-KO animals also presented increased number of astrocytes across their entire hippocampus compared to -WT controls, not accompanied by a parallel increase in GFAP immunoreactivity (section 4.2.4, Figure 4.8). The identification of potential astrogliosis in Abi3-deficient mice was in line with recent observations from Ibanez *et al.* (303). Indeed, the authors reported that 3-month-old Abi3-KO mice presented significantly increased astrogliosis that persisted at 6 months of age (303). To note, as in the case of microglia, Ibanez and colleagues used quantification of GFAP immunoreactivity as means to assess astrogliosis, with no parallel cell count. As shown in Figure 4.8, no significant genotype effect was

observed in this thesis in the case of area % covered by GFAP⁺ pixels, despite a significant increase in astrocytes number. The average hippocampal percentages shown by Ibanez et al. also appear considerably lower than the one reported in this manuscript (approximately 8-12 % in (303) compared to 35-45 % in Figure 4.8). Besides the different analytical approaches discussed before, another potential source of dissimilarity, related to the workflow for GFAP immunoreactivity quantification employed in this thesis, was initially considered. The elevated brightness of the astrocytes cell bodies compared to their ramifications could have indeed biased the thresholding step and caused a partial loss of ramifications in an attempt to avoid excessively expanding the threshold and artefactually selecting non-positive pixels surrounding the cell bodies. This issue would have been inevitably accentuated in the Abi3-KO brains due to the increased number of astrocytes, with bodies closer to each other. However, successive analysis of adult animals, which will be described in the next chapter, did reveal a similar pattern, with no obvious difference in GFAP immunoreactivity despite the increased cell number between Abi3-WT and -KO, while the average values appeared more elevated in animals crossed with the App-KI model. These findings therefore supported the hypothesis of a parallel alteration of astrocytes number and morphology (as well as, potentially, activation state) in Abi3-KO mice. Even more interestingly, multiple fields across different Abi3-deficient samples presented agglomerates of astrocytes, to some extent reminiscent of astrocytic scars.

Considering the role of microglia-secreted factors in astrocytes recruitment and scar formation (124,126,398), the data reported in section 4.2.4 confirms the importance of further assessing other brain cell type in the Abi3-KO model, regardless of their physiological expression of Abi3. This is particularly relevant in the case of pathological states such as AD, where a positive feedback instated by activated (or less functional) microglia could rapidly worsen the neuroinflammation and lead to premature exacerbation of the pathological condition.

4.4. Conclusion and future work

In conclusion, this chapter supports the hypothesis of a major impact of Abi3 on glia cells *in vivo*. The basic characterisation of microglia and astrocyte cells in young

Abi3-WT and -KO animals provides an interesting basis for further histological and molecular evaluation of these mice.

First, to evaluate whether Abi3-KO microglia morphological changes reflect a more activated state of these cells, Reactive Oxygen Species (ROS) production could be assessed by means of Dihydroethidium staining on brain sections. Moreover, brain extracts could be used to evaluate inflammatory cytokines levels in these mice via BioLegend's LEGENDplex™ bead-based immunoassays or a 31-plex Bio-Plex Pro Mouse Chemokine Panel (Bio-Rad) similar to that recently used by Karahan and colleagues (302). Nitric Oxide (NO) production could instead be assessed through Griess Reaction. Even more appropriate would be the employment of single cell sequencing technologies to analyse the transcriptomic profile of both microglia and astrocytes of animals lacking Abi3 in order to identify more subtle alterations. The recently published datasets from Karahan *et al.* (302) and Ibanez *et al.* (303) provided extremely useful insights regarding the impact of Abi3 ablation on gene expression. However, Karahan and colleagues focused their assessments on mice crossed with the 5XFAD model of AD (302), while Ibanez and colleagues employed a bulk transcriptomic approach, therefore warranting further investigation of the consequences of Abi3 depletion in young naïve animals. The parallel analysis of Abi3^{F212} animals would ensure an even deeper understanding of Abi3 functions and of its role in AD pathology.

The use of a two-photon microscope for *in vivo* imaging of Abi3-KO mice will provide the best supporting evidence for any *in-vitro* or *ex-vivo* functional, molecular and morphological observation, allowing the visualisation of microglia in the most physiological environment possible. However, higher resolution images to the ones currently available are required to fully characterise the extent of Abi3 impact on microglial ramification dynamics. To provide such increased resolution and allow 4D analysis of process movement via Imaris, GFP reporter mice crossed with Abi3-WT and -KO animals could be imaged under anaesthesia, to reduce blurriness due to animal movements. However, whilst this approach is undoubtedly less challenging than awake imaging, multiple evidences highlighted the importance of neuronal control on microglia surveillance activity (405,406). When such control is lost, it is possible to observe an increase in microglia process extension, which therefore could lead to a biased interpretation of two-photon data (406). At the same time, employing anaesthetised animals would allow the study of microglial migration and debris clearance *in vivo* following laser injury. This, in turn, would help overcoming all the limitations presented by microglial cell culture discussed in section 3.3.

Microglial phagocytic activity is highly dependent on the actin cytoskeleton (264) and crucial not only for debris or pathogens removal in homeostatic conditions, but also for processes such as synaptic pruning (84,407). Alterations in microglial phagocytosis, such as those highlighted in section 4.2.4, could therefore affect synapses in Abi3-KO mice. For this reason, Synaptophysin and PSD95 (commonly used pre- and post-synaptic markers) levels should be evaluated by means of histological and Western Blot analyses on brain tissue derived from Abi3-WT and -KO mice of different ages. A parallel in-depth 3D spine tracing, using the DiOlistic labelling approach (in which beads coated with Dialkylcarbocyanine are being “shot” with a gene gun directly on to brain tissue *in vitro* (408)) could help further clarify the impact of Abi3 on the neuronal compartment. Interestingly, preliminary results of Western Blot analyses on 52 week-old mice, as well as the DiOlistic analyses on age-matched mice, highlighted a dramatic decrease in Synaptophysin levels, as well as a significant reduction in spine density in Abi3-KO animals (data not shown). These observations, if confirmed, should encourage further investigation of classical complement proteins such as C1q and C3 which, in homeostatic conditions, are expressed at synaptic level and mediate tightly regulated synaptic pruning by activating microglia complement receptors (68).

Finally, microglia have also been implicated in synaptic plasticity, in particular in the modulation of long-term potentiation and depression (LTP/LTD) (409,410), which in turn affect synaptic transmission. LTP and LTD are especially noteworthy in the context of pathologies that impair cognition and memory, such as Alzheimer’s Disease, due to their role in shaping hippocampal neuronal circuits connected with learning and information retention (411). Microglial production of pro-inflammatory cytokines, such as IL-1 β and TNF- α , has been reported to negatively affect LTP in models of depression (412) while ROS secretion triggers LTD (409). Microglia are also responsible for the secretion of BDNF (413), which regulates the expression levels of Vesicular Glutamate Transporter 1 (VGLut1), thus indirectly affecting glutamatergic synaptic function and synaptic plasticity (414). More recently, Karahan *et al.* demonstrated a reduction in LTP following Abi3 ablation in 6-month-old mice crossed with the 5XFAD model of AD (302). This evidence, together with microglial phenotype in Abi3-KO animals, highlight the importance of a more in-depth analysis of synaptic plasticity. This could be achieved either via basic histological and immunoblotting analyses of markers such as VGLut1 and pro-/mature-BDNF, or by electrophysiological extracellular field recordings in an acute hippocampal slice preparations. These experiments could be coupled to two-photon calcium imaging in

awake mice injected with GCaMP6-encoding recombinant Adeno-Associated Virus vectors (415) in order to study neuronal activity.

**Chapter 5: What is the effect of Abi3
on the development of Alzheimer's
disease-like pathology?**

5.1. Introduction

Early response to A β accumulation involves the secretion of elevated levels of IL-1 β by reactive microglia (222), which in turn commences an activation cascade that involves astrocytes and eventually leads to the severe neuroinflammation observed in AD (374). Despite early observations of microglia contribution to AD pathogenesis (163,216,217), however, the body of literature focused on this topic has only recently started to expand, following the identification of risk variants in TREM2 (58,59) which were later connected to an impairment in microglial migration towards A β -plaques (325).

It is now generally accepted that, parallel to disease progression, microglia gradually transition to a disease-associated phenotype, characterised by an initial proliferation step, followed by upregulation of genes related to phagocytosis and inflammation (251). However, the full extent of microglia involvement has not yet been established, with numerous contrasting pieces of evidence on the beneficial/detrimental nature of microglia activity in AD emerging in the past decade (as discussed in detail in section 1.2.3). For instance, Lee and colleagues found that *in vivo* insertion of extra copies of human TREM2 in two mouse models of AD led to an amelioration of the disease progression (324), in agreement with earlier reports by Wang *et al.* of an increased amyloid burden in Trem2-deficient mice (325). Conversely, Krasemann *et al.* demonstrated that suppression of APOE following Trem2 knock-out restored homeostatic microglial phenotype (188).

It is apparent that further answers need to be sought before a clear picture can be delineated, in order to efficiently employ microglia for therapeutical purposes. However, it is also evident that an appropriate microglial response to A β deposition is a determining factor for the fate of brain homeostasis. Therefore, a marked alteration of microglial morphology and functionality, such as the one manifested by Abi3-KO mice, could greatly impact disease progression in AD, in particular if associated to a parallel increase in astrogliosis. It was firstly hypothesized that Abi3-KO dystrophic microglia would fail to effectively recognise A β deposits and migrate towards them, causing an increase in amyloid burden in the brain. Alternatively, the marked microgliosis and astrogliosis presented by Abi3-deficient animals could origin a severe neuroinflammation, thus worsening AD pathogenesis. However, it was also possible to speculate that the presence of “primed” microglia, with an increased phagocytic activity (based on the increased expression of CD68 discussed in section 4.2.4), could lead to a more efficient immune response to the

early deposition of A β and therefore delay the onset of the disease or ameliorate its development.

This chapter was therefore aimed to assess the impact of complete Abi3 ablation on aging and AD pathogenesis. In order to do so, Abi3-KO animals were crossed to APP^{NL-G-F} mice (260) – hereafter addressed as App-KI – to generate App-KI Abi3-KO mice. Mice of both sexes, with and without AD-like pathology, were aged to 16 weeks and used to evaluate micro- and astrogliosis and A β deposition by means of histological analyses. Mice were also tested with a number of well-established behavioural paradigms to assess the impact of Abi3 knock-out on locomotor activity, anxiety levels, memory retention and stress-induced anhedonia.

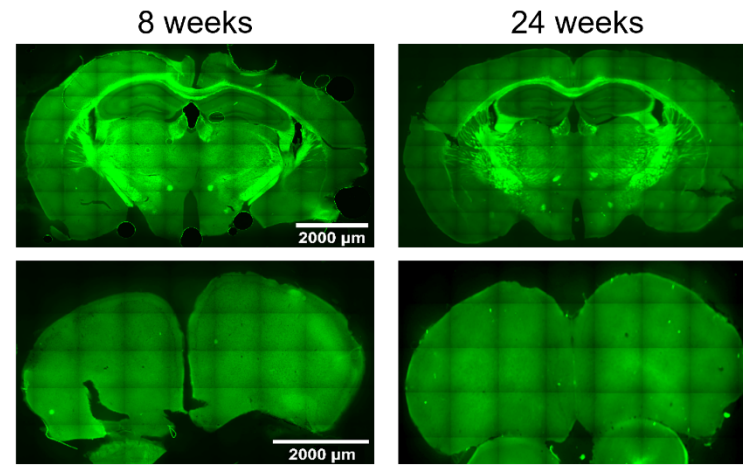
5.2. Results

5.2.1. Basic characterisation of adult Abi3-KO mice crossed with the App^{NL-G-F} AD model

Upon generation of the APP^{NL-G-F} strain, Saito and colleagues reported deposition of A β in homozygous mice from the age of 2 months of age (260). The first step, before commencing any further investigation on the role of Abi3 in AD, was to confirm this observation and visually assess the presence and severity of β -amyloidosis in App-KI mice at different time points. This was achieved by staining brain section with Thioflavin-S (Th-S), a commonly used dye that emits green fluorescence after binding β -sheets structures (416).

As shown in Figure 5.1, Abi3-WT mice presented a complete lack of amyloid deposits both at young age (8 weeks) and at a later stage (24 weeks). Instead, App-KI mice showed a progressive increase in the number of A β deposits, starting from 8 weeks of age, as previously reported (260), although very few plaques were visible – mostly in the cortex – at this age. At 24 weeks, both areas of interest presented amyloid deposition, however this appeared more severe in the PFC than within the hippocampus. Based on this visual assessment, it was decided to focus histological analyses for this thesis on 16-week-old mice (highlighted in red in Figure 5.1), as discussed in section 5.3.

Abi3-WT



App-KI

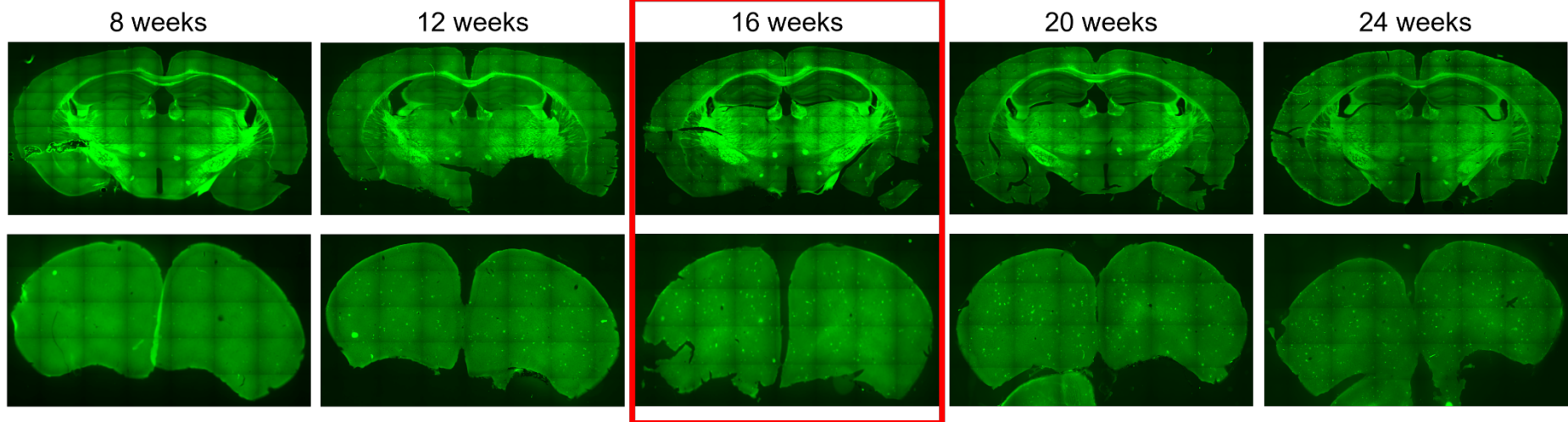


Figure 5.1 Representative images of Thioflavin-S (Th-S) staining for Amyloid β (A β) plaques in Abi3-WT and App-KI mice brain sections.

8 Abi3-WT App-WT mice (2 animals of each sex at 8 and 24 weeks of age) and 30 Abi3-WT App-KI mice (3 animals per each sex at 8, 12, 16, 20 and 24 weeks of age) were stained with Th-S (green) and imaged using an EVOS™ FL Auto 2 Imaging System with a 20x objective. One section per mouse for each selected region – hippocampus (top row of each pair) and PFC (bottom row of each pair) – was used in this experiment. Th-S was (green) used to visualise plaque burden in the brain. Based on this visual evaluation, the 16-weeks time-point (marked in red) was chosen to conduct further analyses. Tissue from 8- and 24-week-old animals was also collected for experiments outside the scope of this thesis.

Following these observations, males and females mice of all four genotypes (Abi3-WT, Abi3-KO, App-KI, App-KI Abi3-KO) were appropriately cohoused since weaning and aged to 16 weeks. Tissue was then collected and processed as described in section 2.6 in order to evaluate microglial distribution and morphology in the PFC and the hippocampus.

Figure 5.2A shows representative images of both the PFC (top row) and the hippocampus (bottom row) of each strain stained with an anti-Iba1 antibody to visualise microglia. Consistently with the observations described in the previous chapter, the absence of Abi3 appeared to overall significantly impact microglia density in both areas of interest ($p < 0.0001$ for both PFC and hippocampus; Figure 5.2B and C respectively). Similarly, animals crossed with the AD model showed a significant increase in cell number compared to healthy mice ($p < 0.0001$ in the PFC and $p = 0.0478$ in the hippocampus for the “presence of mutant App” effect; Figure 5.2B and C). No significant two- or three-way interactions were identified by the Three-way ANOVA and, as in the case of young mice, sex did not appear to impact microglia density (Figure 5.2B and C).

The microgliosis presented by Abi3-deficient mice was associated to a significant reduction in the distance between neighbouring cells in both the PFC and the hippocampus ($p = 0.0002$ and $p < 0.0001$ respectively for the simple main effect “absence of Abi3”; Figure 5.2D and E respectively). A significant impact was also identified by the Three-way ANOVA for the presence of mutant App ($p < 0.0001$ in the PFC, $p = 0.0052$ in the hippocampus; Figure 5.2D and E). As before, the ANOVA did not identify significant interactions on main effect of sex on the NND (Figure 5.2D and E).

Finally, when assessing the percentage of tissue covered by Iba1⁺ microglia, the Three-way ANOVA identified a significant contribution of Abi3 ablation to the phenotype ($p < 0.0001$ for both the PFC and the hippocampus; Figure 5.2F and G). The impact of the presence of mutant App did not appear significant in either region (Figure 5.2F and G), while sex significantly altered Iba1 immunoreactivity in the PFC ($p = 0.0273$; Figure 5.2F) but not in the hippocampus. However, a significant two-way interaction between sex and the absence of Abi3 was identified in both regions ($p = 0.0016$ in the PFC, $p = 0.0018$ in the hippocampus; Figure 5.2F and G respectively), as well as an interaction between sex and mutant App in the hippocampus alone ($p = 0.0400$; Figure 5.2G). Coherently, the subsequent Šidák's multiple comparisons test highlighted a significant difference between Abi3-WT and -KO mice ($p < 0.0001$; Figure 5.2 F) as well as between App-KI and App-KI Abi3-KO ($p < 0.0001$; Figure 5.2 F) in the PFC of male animals only. Similarly, in the hippocampus, only males animals showed a significant decrease in Iba1 immunoreactivity following Abi3 deletion compared to their respective Abi3-sufficient controls ($p = 0.0001$ for Abi3-WT and -KO mice, $p < 0.0001$ for App-KI and double-transgenic animals; Figure 5.2G). However, in this case, a difference was also noted between Abi3-KO mice of both sexes, with females presenting a significantly higher percentage of tissue covered in microglia ($p = 0.0094$; Figure 5.2G).

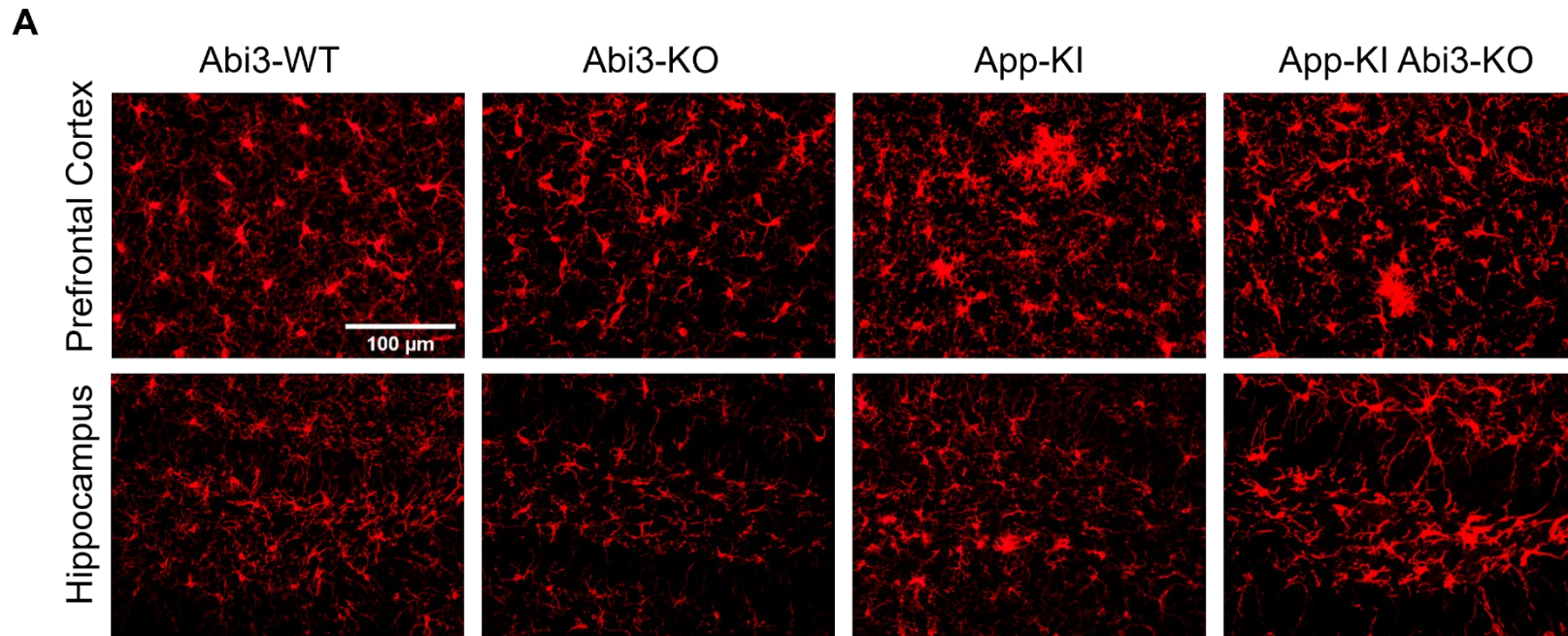


Figure 5.2, part I. Representative images of a microglial immunostaining in 16-week-old Abi3-WT, Abi3-KO, App-KI and App-KI Abi3-KO mice.

A) Representative images of the Iba1 (red) staining performed on the PFC and the hippocampus of males and females animals of all four strains under evaluation in this manuscript. Mice were co-housed from weaning to avoid artefactual microglial activation due to the exposure to different microbiomes. The lack of Abi3 caused a drastic reduction in microglial processes both in healthy mice and in the presence of mutated App. A small increase in cell density was visible in Abi3-KO and App-KI Abi3-KO animals compared to Abi3-WT and App-KI mice respectively, as well as in both the mutant App strains compared to the healthy controls. Moreover, mice crossed to the AD model showed multiple clusters of microglia (more frequent in the PFC), presumably around A β deposits.

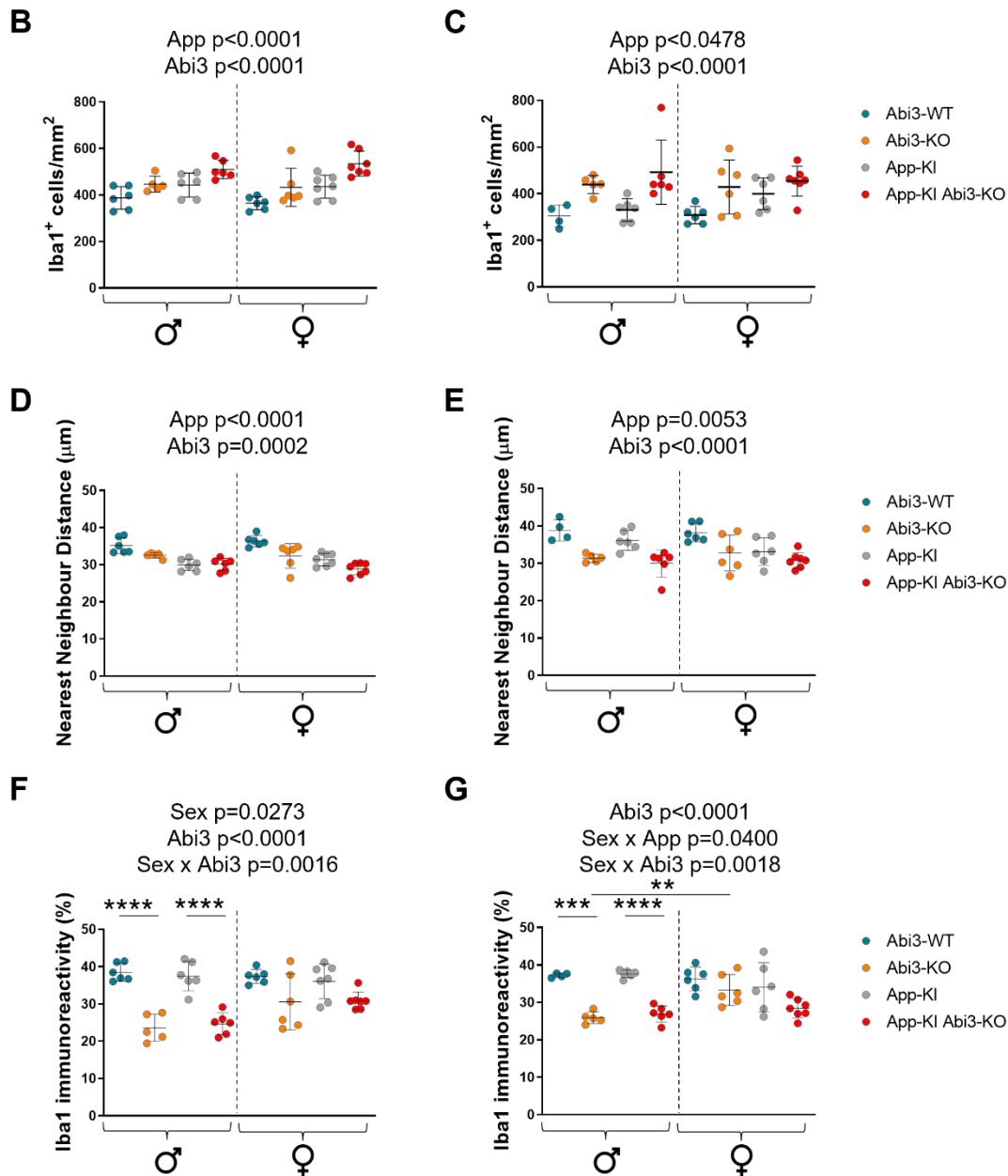


Figure 5.2, part II. Quantification of Iba1 immunostaining in 16-week-old Abi3-WT, Abi3-KO, App-KI and App-KI Abi3-KO mice.

Each datapoint on the graphs represents the average value from one sample. Abi3-WT mice are represented by light blue dots, Abi3-KO mice by oranges one, while the grey dots indicate App-KI animals and, finally, the red dots App-KI Abi3-KO mice. The black horizontal lines represent the mean of each experimental group, while the vertical ones indicate the Standard Error. The p -values resulting from the Three-way ANOVA are reported on each graph. The p -values of any significant pairwise comparison generated through the Šidák's multiple comparisons test are reported on the graphs by means of asterisks for any significant two- or three-way interaction identified. **B) and C)** Quantification of microglia

number in the PFC (B) and Hippocampus (C). **D**) and **E**) Evaluation of the NND in the PFC and Hippocampus (in the PFC and hippocampus respectively). **F**) and **G**) Quantification of the surface covered by Iba1⁺ pixels in the PFC (F) and Hippocampus (G). Data were analysed via Three-Way ANOVA followed by Šidák's Multiple Comparisons Test. For males and females respectively: n=6 Abi3-WT, n=5 and 6 for Abi3-KO, n=6 and 7 for App-KI and App-KI Abi3-KO. **p≤0.01, ***p≤0.001, ****p≤0.0001.

Given that Abi3 impact on microglial morphology and distribution was confirmed in 16-week-old mice regardless of their AD status, these same samples were stained with an anti-GFAP antibody (as per Methods section 2.6.4.2) to evaluate whether the observation of astrogliosis in healthy young mice, discussed in the previous chapter, was reflected in adult animals as well. Representative images are shown in Figure 5.3A.

The quantification of GFAP⁺ cells through Fiji highlighted an increase in cell density (Figure 5.3B). Indeed, the Three-way ANOVA detected a significant increase in astrogliosis due to either the deletion of Abi3 (p=0.0162; Figure 5.3B) or the presence of mutated App (p=0.0433; Figure 5.3B). The statistical analysis also highlighted a significant two-way interaction between App and Abi3 (p=0.0045; Figure 5.3B) and a significant three-way interaction (p=0.0182; Figure 5.3B). Accordingly, the subsequent post-hoc showed that female Abi3-WT mice had a markedly lower number of astrocytes compared to both Abi3-KO (p=0.0001; Figure 5.3B) and App-KI (p=0.0071; Figure 5.3B) females, while no significant pairwise comparison was identified in males.

Interestingly, the increased astrogliosis presented by Abi3-KO females was not reflected by a similar increase in GFAP immunoreactivity (p=0.9996; Figure 5.3C), similar to what had been observed in section 4.2.4 on young animals. Indeed, the absence of Abi3 only seemed to impact GFAP immunoreactivity in case of interaction with sex (p=0.0471; Figure 5.3C). Instead, the impact of the presence of mutated App resulted significant following the Three-way ANOVA (p<0.0001; Figure 5.3C).

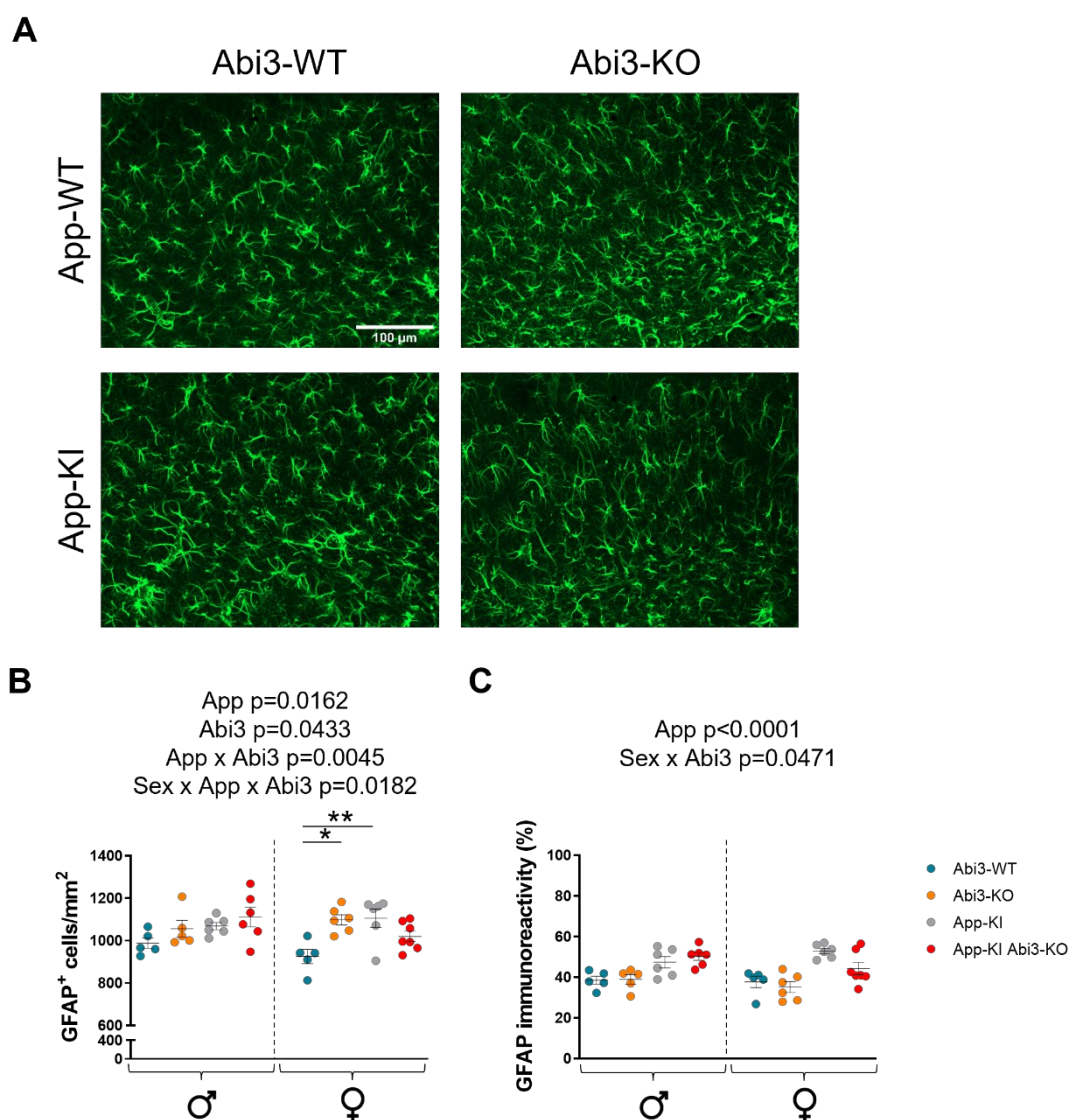


Figure 5.3 Representative images of GFAP⁺ astrocytes, and relative quantification, in the hippocampus of 16-week-old mice.

The average value for each animal is represented by an individual dot. The blue dots indicate Abi3-WT mice, the orange ones Abi3-KO animals, the grey dots App-KI mice and the red App-KI Abi3-KO mice. The black horizontal lines represent the mean of each experimental group \pm S.E.M. The p-values resulting from the Three-way ANOVA are reported on each graph. The p-values of any significant pairwise comparison generated through the Šidák's multiple comparisons test are reported on the graphs by means of asterisks for any significant two- or three-way interaction identified. Note the scale has been truncated for clear visualization in B. **A)** Hippocampal sections of 16-week-old Abi3-WT and -KO mice, as well as of Abi3-deficient animals crossed with the App-KI line – were stained with an anti-GFAP (green) antibody to visualize astrocytes. Abi3-KO mice presented a similar phenotype to the one observed in young mice, with visibly more cells and areas of particularly high astrocytic density. An increase in cell number was also visible in both App-KI and App-KI Abi3-KO samples, with some visible clusters of reactive astrocytes. No

obvious difference was visible between *Abi3*-deficient mice with and without AD background. Notably, *Abi3*-WT mice presented a slightly less organised distribution across the hippocampus, as well as few cells resembling reactive astrocytes. **B)** Quantification of GFAP⁺ cell density and **C)** graphical representation of the area covered by GFAP⁺ pixels. Data were analysed via Three-Way ANOVA followed by Šidák's Multiple Comparisons Test. For males and females respectively: *n*=5 *Abi3*-WT, *n*=5 and 6 *Abi3*-KO, *n*=6 *App*-KI, and *n*=6 and 7 *App*-KI *Abi3*-KO. **p*≤0.05, ***p*≤0.01.

5.2.2. Amyloid burden and peri-plaque microgliosis assessment on adult *Abi3*-KO *App*-KI mice

The phenotype described in the adult *Abi3*-deficient mice crossed with the *App*-KI model encouraged further investigation of the impact of the observed changes in microglia on β -amyloid deposition. To achieve this, additional brain sections from the same mice assessed in the previous section were stained with a 6E10 antibody, specific for residues 1-16 of A β (350). Each entire PFC or hippocampal region was then imaged and analysed as described in section 2.6.4.5. Due to the complete lack of plaques observed in *Abi3*-WT and -KO mice, only *App*-KI and *App*-KI *Abi3*-KO sections were examined. Figure 5.4A shows representative images of PFC sections from *App*-KI and *App*-KI *Abi3*-KO mice.

For each sample, three parameters were evaluated: number of plaques per mm², average plaque area and percentage of tissue covered by plaques. Following statistical evaluation, no significant difference was observed between *Abi3*-deficient mice and the controls ("genotype" main effect: *p*=0.0910 for number of plaques/mm², Figure 5.4B; *p*=0.8169 for average plaque area, Figure 5.4C; *p*=0.1635 for percentage of area covered by plaques, Figure 5.4D). Sex did not affect amyloid deposition either, and no significant interaction was identified (Figure 5.4B-D).

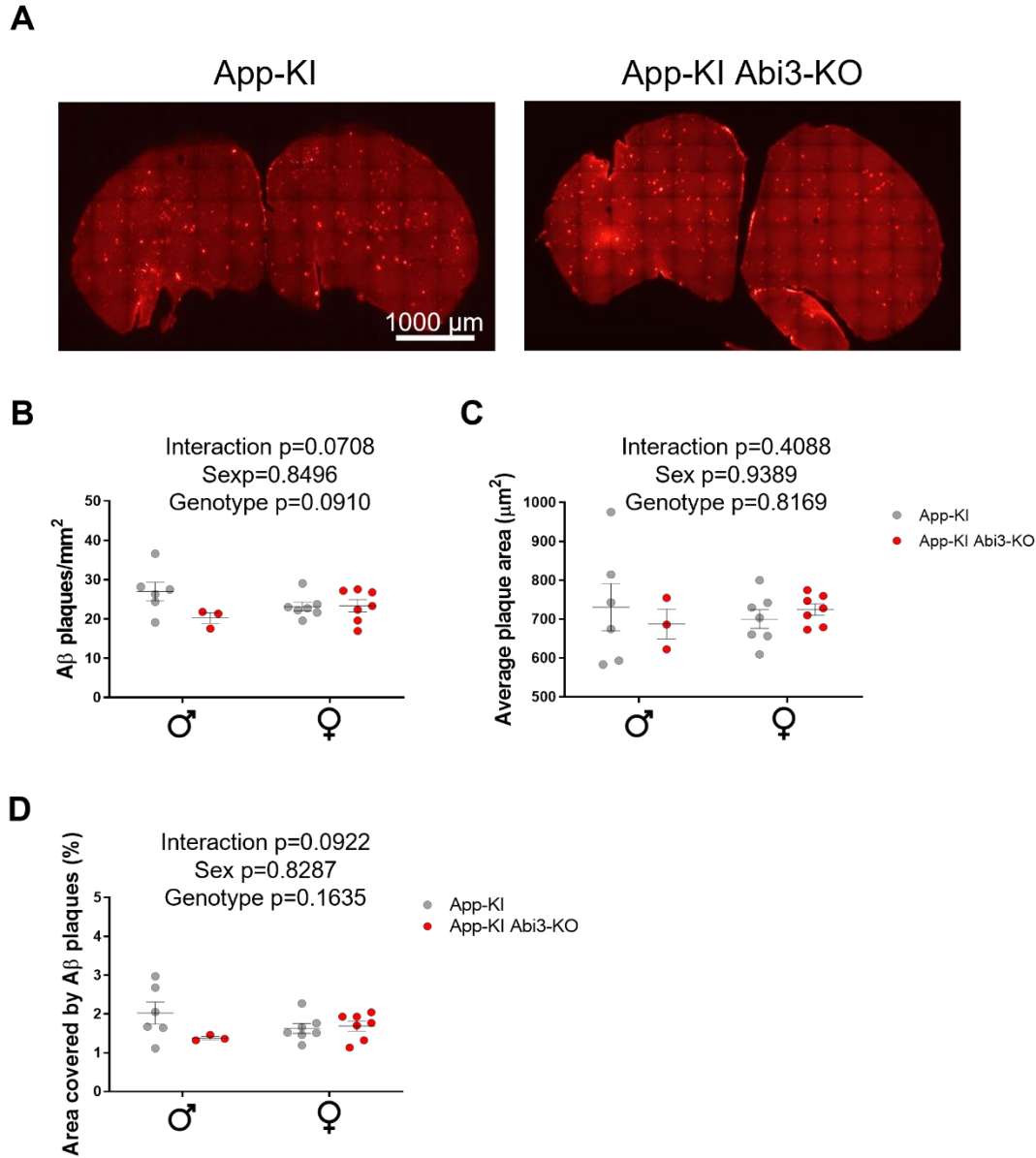


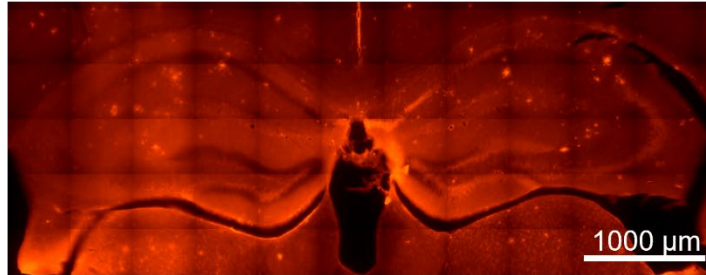
Figure 5.4 Representative images of A β plaques stained with a 6E10 antibody and relative quantification in the PFC of 16-week-old App-KI and App-KI Abi3-KO mice.

Each datapoint on the graphs represents the value obtained through Fiji analysis for each section (B and D) or the average value for all the analysed plaques in each section (C). The grey dots indicate App-KI animals and the red dots represent App-KI Abi3-KO mice. The black horizontal lines represent the mean of each experimental group, while the vertical ones indicate the S.E.M. The results of the Two-way ANOVA are reported on each graph. **A)** Representative images of the 6E10 staining (red) performed on the PFC of male and female animals. An elevated number of A β deposits was visible in mice of both sexes in the presence of mutated App. Abi3 ablation did not seem to influence plaque burden. **B)** Quantification of plaque density, **C)** average plaque area and **D)** percentage of cortical surface covered by plaques. Data analysed via Two-Way ANOVA. For males and females respectively: n=6 and 7 for App-KI, and n=3 and 7 App-KI Abi3-KO.

The same analysis was then performed on hippocampal sections. Figure 5.5A shows representative images of the hippocampus of App-KI and double-transgenic mice, stained with the same 6E10 antibody. As shown in Figure 5.5B-D, the “genotype” effect resulted significant for all the parameters evaluated ($p=0.0005$ for number of plaques/mm², Figure 5.5B; $p=0.0053$ for average plaque area, Figure 5.5C; $p=0.0009$ for percentage of area covered by plaques, Figure 5.5D). The impact of sex, as well as that of the interaction between sex and genotype, was not significant in all cases (Figure 5.5B-D).

A

App-KI



App-KI Abi3-KO

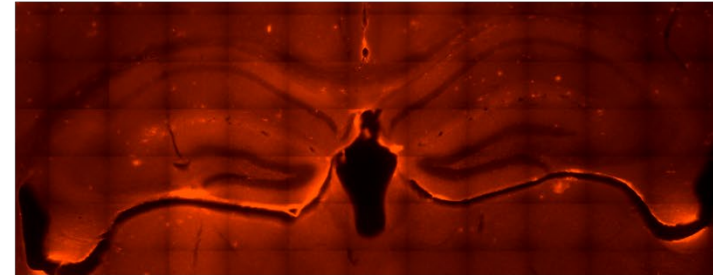
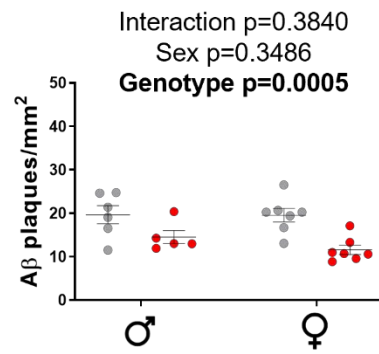
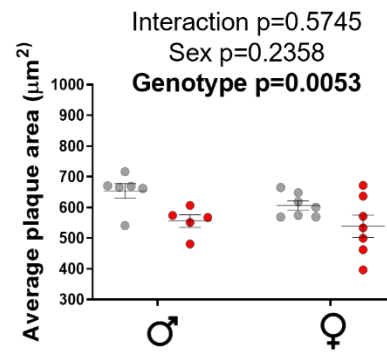
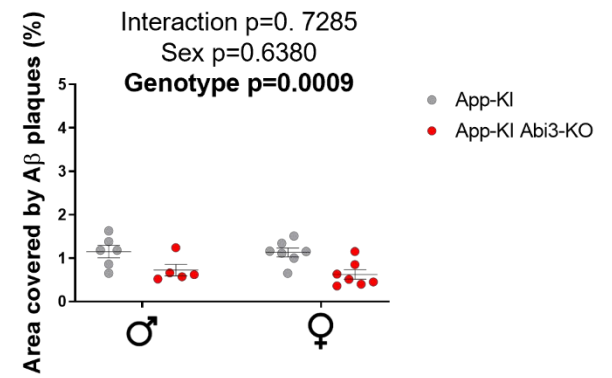
**B****C****D**

Figure 5.5 Representative images and relative quantification of the 6E10 staining performed on hippocampal sections of adult Abi3-deficient mice and App-KI controls.

*Each dot in the graphs represents the value obtained through Fiji analysis for each section (B and D) or the average value for all the analysed plaques in each section (C). App-KI mice are represented by grey dots, while red dots indicate App-KI Abi3-KO mice. The black horizontal lines represent the mean of each experimental group \pm S.E.M. The results of the Two-way ANOVA are reported on each graph. **A)** Visual assessment of the 6E10 staining (red) identified a marked reduction in amyloid plaques in App-KI Abi3-KO mice compared to their App-KI controls. No visible difference between sexes was described. **B)** Evaluation of the number of plaques/mm². **C)** Quantification of the average plaque area. **D)** Graphical representation of the resulting percentage of tissue covered by plaques. Data analysed via Two-Way ANOVA. For males and females respectively: n=6 and 7 for App-KI, and n=5 and 7 App-KI Abi3-KO.*

Taken together, these findings warranted further investigation of the mechanisms behind Abi3 impact on AD. The reduced surveillance activity shown by Abi3-KO microglia, discussed in section 4.2.3, had led to the hypothesis of a reduced recognition of – and consequent migration towards – A β plaques. In light of the reduction in amyloid burden in the absence of Abi3, a more in-depth analysis of peri-plaques microgliosis was performed as described in Methods section 2.6.4.6. Due to the low number of plaques visible in the hippocampus, PFC sections were employed for this analysis.

Figure 5.6 shows representative images of the 6E10 and Iba1 staining of a single plaque (Figure 5.6A) and the following 3D rendering and automated quantification (Figure 5.6B). Figure 5.6C-D details the peri-plaque microglial count for each individual plaque within 15 μ m (Figure 5.6C) or 30 μ m (Figure 5.6D) from the plaque. Due to the high variability in plaque size, cell counts were grouped based on the plaque volume (<20,000 μ m³, 20,000-30,000 μ m³, >30,000 μ m³).

Despite the previously described elevated microgliosis in App-KI Abi3-KO mice, particularly evident in the PFC of double-transgenic females compared to sex-matched App-KI mice (Figure 5.2), no significant difference emerged from the analysis of individual plaques (Figure 5.6C-D).

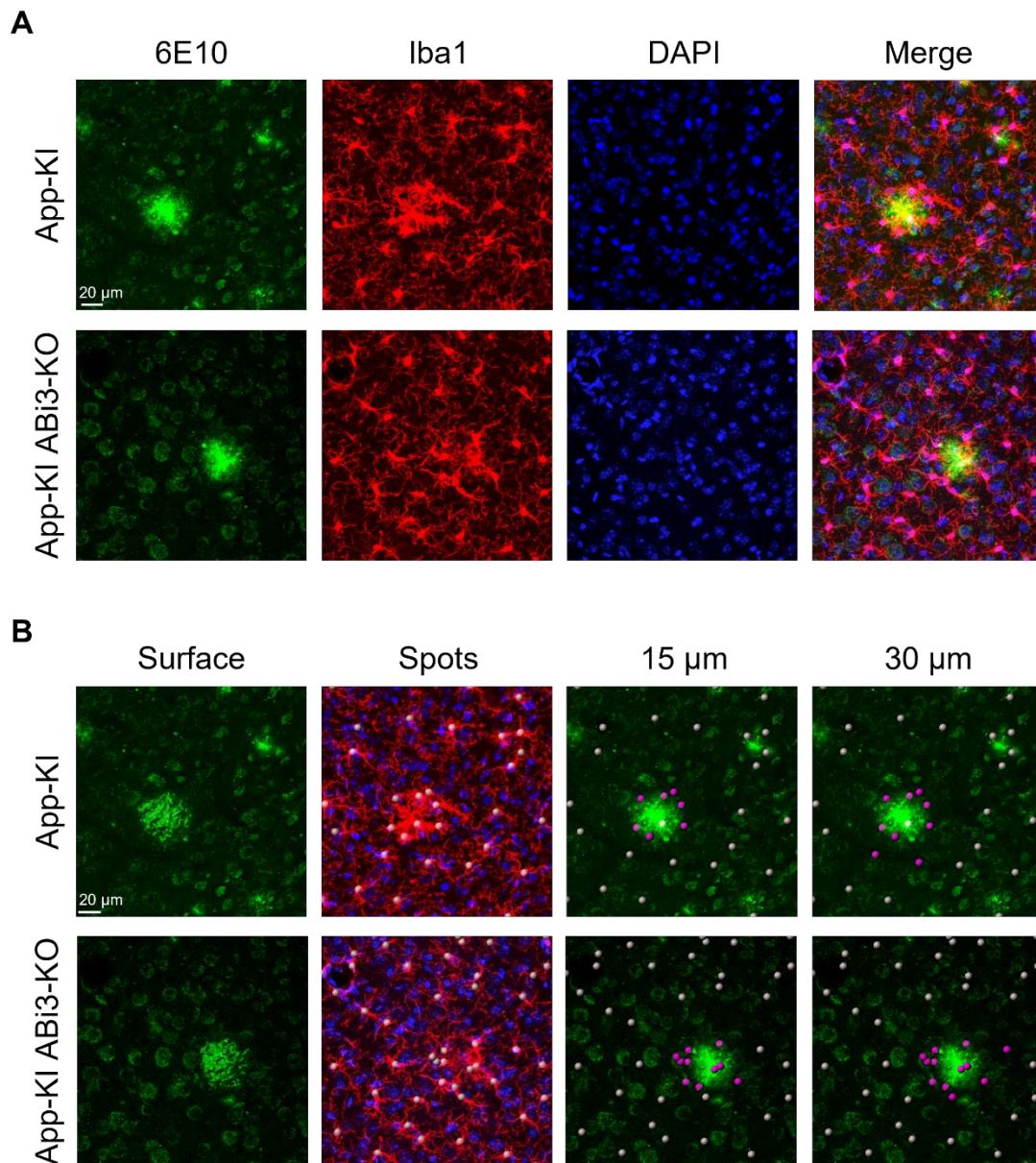


Figure 5.6, part I. Representative images of individual plaques analysis.

A) Representative images of 6E10 (green), Iba1 (red) and DAPI (blue) staining of individual plaques in App-KI (top row) and Abi3-KI Abi3-KO mice (bottom row). Peri-plaque microgliosis was visible even in the absence of Abi3, although it was apparently not accompanied by the same extent of morphological changes associated with amyloid recognition (namely, soma enlargement and parallel swelling of ramifications) presented by App-KI cells, although further analyses will be required to validate this observation. **B)** Imaris “Surface” creation module allowed the 3D rendering of individual plaques (first column), while the “Spots” module was employed to automatically count microglia (second column). The number of cells within pre-selected distances from each plaque (specifically, 15 and 30 μm) was then automatically quantified and the spots included in the radius of interest were highlighted in pink (third and fourth columns).

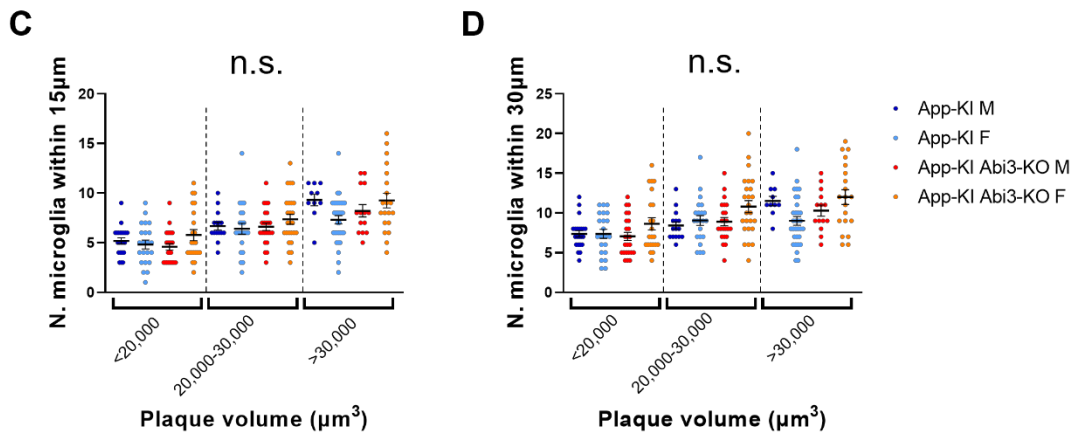


Figure 5.6, part II. Quantification of peri-plaque microgliosis.

Each dot in the graphs represents the peri-plaque microglia count for one single A β plaque. App-KI mice are represented by dark or light blue dots (for males and females respectively), while red and orange dots indicate male and female App-KI Abi3-KO mice. The black horizontal lines represent the mean of each experimental group \pm S.E.M. Plaques are divided according to their volume in three groups: small plaques with a volume of less than 20,000 μm^3 , medium plaques (20,000 to 30,000 μm^3) and large plaques, bigger than 30,000 μm^3 . **C)** Quantification of the number of microglia comprised with a radius of 15 μm or **D)** 30 μm from each plaque. Data were analysed via linear mixed model analysis. $n=47$ plaques for App-KI males, $n=76$ for App-KI females, $n= 61$ for App-KI Abi3-KO males and $n=67$ for App-KI Abi3-KO females.

5.2.3. Evaluation of Abi3 impact on adult mice behaviour

The presence of variable amyloid burden in different brain regions of App-KI Abi3-KO mice compared to App-KI animals led to speculations about the impact of such phenotype on mice behaviour. As discussed in section 1.2.4, memory deficits in the App-KI strain have been described starting at 9 months of age (417), while locomotor and anxiety changes have been shown to appear as early as 6 months of age (261,417).

Mice of both sexes, with and without amyloid pathology, were therefore aged to 40 weeks and challenged with a sequence of well-accepted behavioural paradigms including Elevated Plus Maze (EPM) to measure anxiety, Open Field (OF) task to assess locomotor activity as well as anxiety-like behaviours, and Novel Object Recognition (NOR) to evaluate recognition memory. For more details regarding

these paradigms and the protocol employed in this thesis please see Methods section 2.8.

Mice were first challenged with the EPM paradigm in order to avoid any bias in anxiety measurements due to repeated testing. Figure 5.7 shows representative heatmaps images generated by EthoVision software based on 10-minute-long recordings.

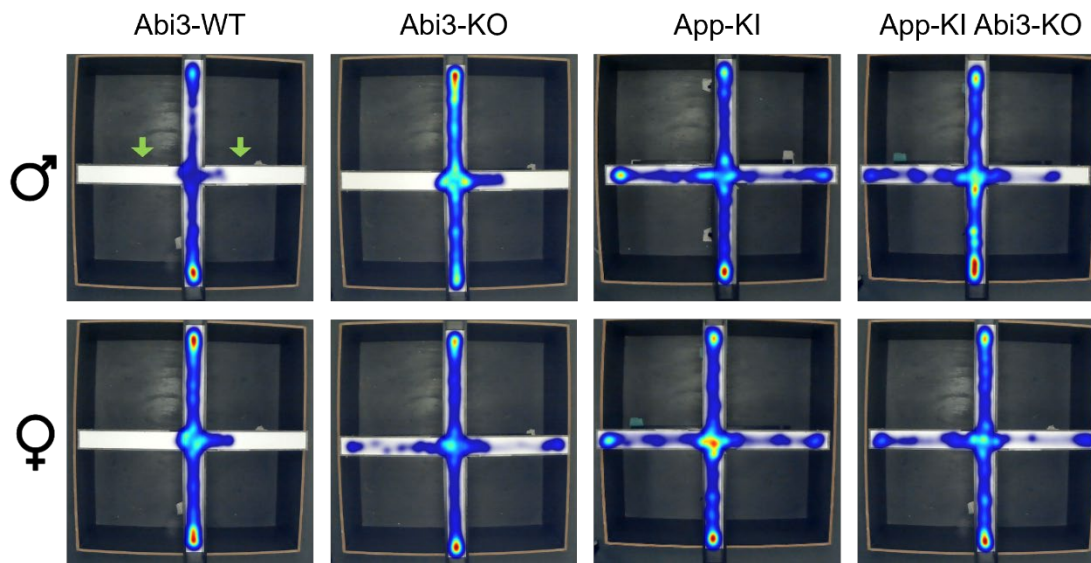


Figure 5.7 Representative images of the heatmaps automatically generated by EthoVision for every individual mouse.

Mice movements were tracked for 10 minutes and heatmaps were computed based on the time spent in each location along the track. Mice of either sex bearing AD-related mutations spent noticeably more time in the open arms (indicated by green arrows in the top left map) compared to healthy animals, indicating reduced anxiety levels. It was also possible to notice an increased anxiolytic behaviour in Abi3-KO mice compared to Abi3-WT controls in the same sex group – although this was particularly evident in females – while no obvious difference was identifiable at this time between App-KI and double-transgenic mice.

Automatic tracking of mice movement across the arena through EthoVision allowed quantification of latency to the first entrance in the open arms (Figure 5.8A), total number (Figure 5.8B) and percentage (Figure 5.8C) of entries in the open arms and total time spent in the open arms (Figure 5.8D).

For the latency to the first entry, the Three-way ANOVA identified a single significant main effect (“presence of mutant App”, $p=0.0215$; Figure 5.8A) and a single two-way interaction between App and Abi3 ($p=0.0279$; Figure 5.8A). Indeed, healthy Abi3-KO

males appeared more prone to enter the open arms after a short latency phase compared to sex-matched App-KI, while the opposite was true for App-KI and double-transgenic males; a less marked difference was visible in the female group. The subsequent post-hoc identified a significant reduction in latency only in App-KI males compared to sex-matched Abi3-WT controls ($p=0.0242$; Figure 5.8A). No significant pairwise comparison was observed in the females or between Abi3-KO mice with and without AD-like pathology.

The total number of entries in the open arms showed a significant impact of sex ($p=0.0089$; Figure 5.8B) and App ($p=0.0015$; Figure 5.8B), but no significant two- or three-way interactions. Coherently with the visual observation of the heatmaps, App-KI lines, as well as females, appeared to entry more often in the open arms (Figure 5.8B).

When the entries in the open arms were expressed as a percentage of total entries in any type of arm (to take into consideration potential differences in locomotor activity) sex did not appear to have a significant impact on this parameter ($p=0.1137$). Instead, the presence of mutant App still caused a significant increase in the open arms preference ($p=0.0001$; Figure 5.8C).

Finally, the presence of mutant App was found to be the only statistically significant main effect to impact the total time spent in open arms ($p<0.0001$; Figure 5.8D), while no impact of Abi3 or sex (or any two- or three-way interaction) was noted.

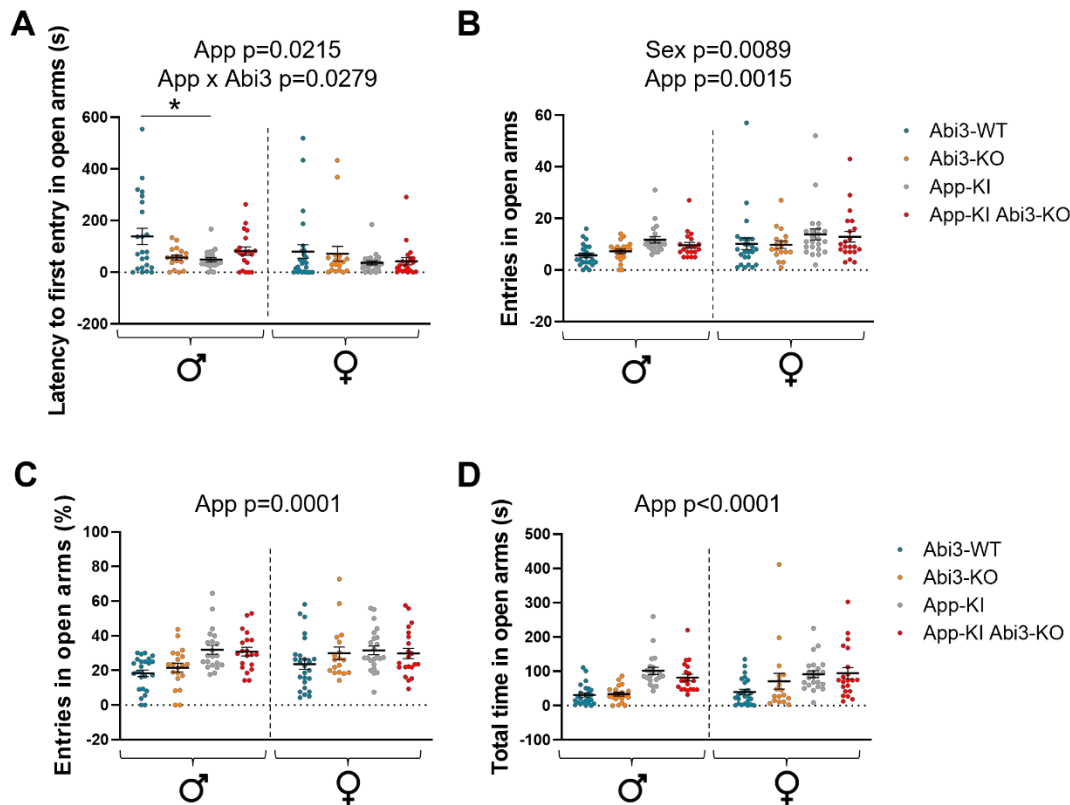


Figure 5.8 Graphical representation of selected parameters to assess anxiety-like behaviours during the EPM task.

Each dot represents one individual animal. Abi3-WT and -KO mice are indicated by light blue and orange dots respectively, while App-KI mice are represented by grey dots and double-transgenic animals by red ones. The black horizontal lines represent the mean of each experimental group \pm S.E.M. The p-values resulting from the Three-way ANOVA are reported on each graph. The p-values of any significant pairwise comparison generated through the Šidák's multiple comparisons test are reported on the graphs by means of asterisks for any significant two- or three-way interaction identified. **A)** Graphical representation of the time interval occurred before the first entry in the open arms. **B)** Quantification of the total number of entries in the open arms and **C)** the total number of entries in the open arms normalised by the total number of crossings into any kind of arm. **D)** Evaluation of the total time spent in the open arms. Data were analysed via Three-Way ANOVA followed by Šidák's multiple comparisons test. For males and females respectively: $n=25$ for Abi3-WT, $n=20$ and 18 for Abi3-KO, $n=21$ and 23 for App-KI, $n=20$ and 21 for App-KI Abi3-KO. * $p \leq 0.05$, ** $p \leq 0.01$, *** $p \leq 0.001$.

During the testing sessions, an increased locomotor activity was noted in the App-KI line, particularly in females, while in the EPM arena. For this reason, mice movements were further assessed to validate this observation. EthoVision provided quantification of time spent in movement (Figure 5.9A-B), as well as the distance

travelled (Figure 5.9C-D) and mean velocity (Figure 5.9E-F), in either the open or closed arms.

The presence of mutant App significantly impacted the percentage of time spent in movement in the open arms ($p=0.0001$; Figure 5.9A), with App-KI and double-transgenic mice spending less time moving while in this area. No significant main effect or two-way interaction was noted when considering the percentage of movement in the closed arms instead (Figure 5.9B), although a significant three-way interaction between sex, App and Abi3 was reported ($p=0.0078$; Figure 5.9B). However, no significant pairwise comparison was identified by the Šidák's multiple comparison test.

The initial observation of reduced movement in the open arms in the App-KI strains apparently clashed with the visual observations reported during the task. This was clarified when considering the distance travelled by App-KI mice and their mean velocity. In the open arms, the presence of mutant App caused a significant increase in both parameters ($p<0.0001$ for both; Figure 5.9C and E). A significant two-way interaction between App and Abi3 was also noted in both cases ($p=0.0135$ for distance travelled, $p=0.0009$ for mean velocity; Figure 5.9C and E). The subsequent post-hoc test identified a significant increase in distance travelled in App-KI mice of both sexes compared to their respective Abi3-WT controls ($p<0.0001$ for both; Figure 5.9C). Similarly, App-KI mice resulted significantly faster than their sex-matched controls ($p=0.0153$ for males, $p<0.0001$ for females; Figure 5.9E). This was not the case for Abi3-KO and double-transgenic mice, with no significant difference due to the presence of amyloid pathology was reported (Figure 5.9C and E).

The presence of mutant App also affected both distance and velocity in the closed arms ($p=0.0164$ and $p=0.0267$ respectively; Figure 5.9D and F). A significant interaction between sex and App was identified for the distance travelled ($p=0.0484$; 5.9D). Sex also appeared to significantly impact the mean velocity ($p=0.0012$; 5.9F). Interestingly, a three-way interaction between sex, App and Abi3 was also highlighted in both cases ($p=0.0193$ and $p=0.0071$ for distance and velocity respectively; 5.9D and F). The following post-hoc test showed that in the male group, App-KI Abi3-KO animals travelled significantly less in the closed arms than Abi3-KO mice ($p=0.0228$; Figure 5.9D), while no significant pairwise comparison was observed in the female group. The mean velocity resulted instead significantly different between double-transgenic mice of the two sexes ($p=0.0142$; Figure 5.9F), with females moving significantly faster than males. No parallel alteration was observed in the App-KI or non-AD lines.

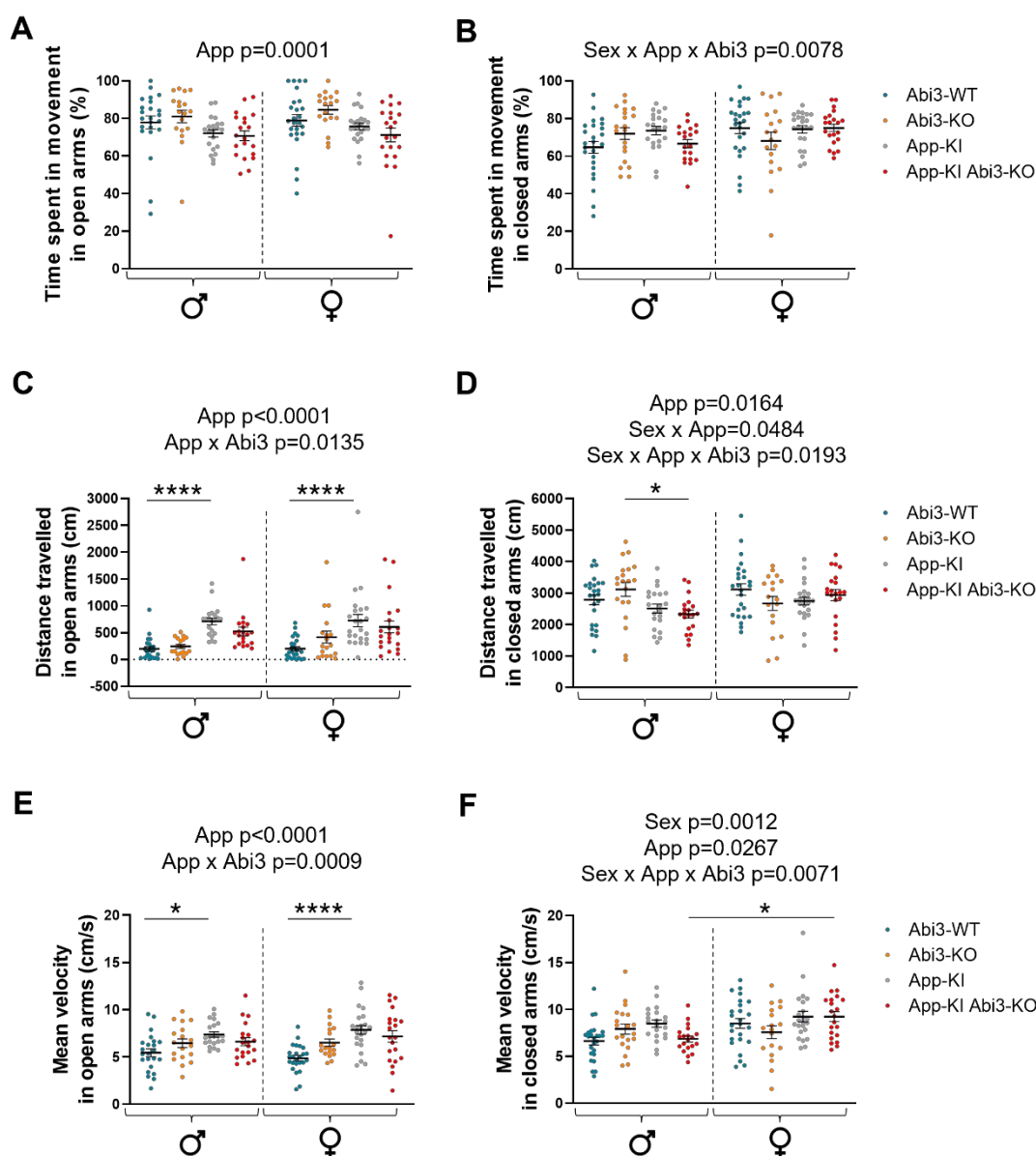


Figure 5.9 Quantification of locomotor activity in the EPM arena.

Each dot represents the percentage of time spent moving, the total distance travelled or the mean velocity value relative to a single mouse. Light blue dots represent Abi3-WT mice, orange dots Abi3-KO animals, grey dots App-KI mice and red dots App-KI Abi3-KO mice. The black horizontal lines represent the mean of each experimental group \pm S.E.M. The p -values resulting from the Three-way ANOVA are reported on each graph. The p -values of any significant pairwise comparison generated through the Šidák's multiple comparisons test are reported on the graphs by means of asterisks for any significant two- or three-way interaction identified. **A)** and **B)** Graphical representation of the percentage of time spent in movement in either the open (A) or closed arms (B). **C)** and **D)** Evaluation of the distance travelled (expressed in cm) in the open (C) or closed (D) arms of the maze. **E)** and **F)** Quantification of the mean velocity of the animals while moving in the open arms (E) or in the

closed ones (F). Data were analysed via Three-Way ANOVA followed by Šidák's multiple comparisons test. For males and females respectively: $n=25$ for Abi3-WT, $n=20$ and 18 for Abi3-KO, $n=21$ and 23 for App-KI, $n=20$ and 21 for App-KI Abi3-KO. $*p\leq 0.05$, $****p\leq 0.0001$.

Overall, these observations confirmed previous reports of anxiolytic behaviour in the App-KI strain (380,381) and suggested potential alterations in the locomotor activity of Abi3-deficient animals. To further assess the impact of Abi3 on AD-dependant behavioural changes, mice were tested with in the OF arena. Figure 5.10 shows representative heatmaps from 10-minute-long recordings for animals of all groups.

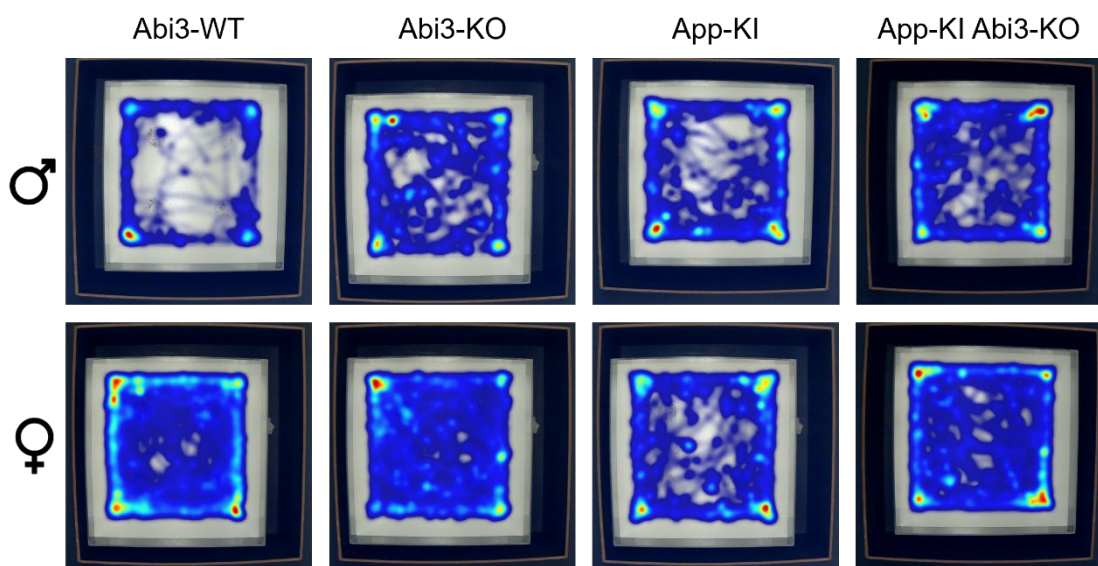


Figure 5.10 Representative heatmaps from the OF task.

Animals were left free to explore and empty arena for 10 min and their movements were then tracked with EthoVision, that generated heatmaps for each animal based on their respective movements track and time spent in each position. A first obvious difference was observed between male and female Abi3-WT or -KO mice, with females exploring the arena remarkably more than males of the same strain. A similar observation was reported in App-KI Abi3-KO mice, while no evident sex-dependant alteration appeared in the App-KI line. A second source of difference, particularly evident in healthy males, was the absence of Abi3, which appeared to cause an increase in arena exploration. Finally, male App-KI appeared more prone to explore the OF arena than healthy controls, while the opposite appeared to be true in the case of females.

The analysis was firstly focused on anxiolytic-like behaviours, which were assessed by evaluating mice exploration of the centre of the arena. As in the case of the EPM

task, EthoVision provided quantification of latency to the first entry in the centre (Figure 5.11A), as well as the number of entries in the centre (Figure 5.11B) and the total time spent there (Figure 5.11C).

The statistical evaluation of the latency to the first entry highlighted only one significant simple main effect, namely the absence of Abi3 ($p=0.0307$; Figure 5.11A), which caused an overall decrease in the latency. No significant two- or three-way interactions were identified (Table 5.6).

Coherently with the visual observation of the heatmaps, the Three-way ANOVA identified a significant impact of sex on the total number of entries in the centre ($p<0.0001$; Figure 5.11B) as well as an effect of mutant App ($p=0.0031$; Figure 5.11B) and a significant interaction between sex and App ($p=0.0010$; Figure 5.11B). Indeed, female Abi3-WT and -KO entered the centre significantly more times than males of the respective strain ($p<0.0001$ for Abi3-WT, $p=0.0002$ for Abi3-KO; Figure 5.11B). Moreover, Abi3-KO females also showed an increased preference for the centre compared to sex-matched double-transgenic mice ($p=0.0024$, Figure 5.11B). No evident difference was visible among genotypes in the male group or between male and females mice of the App strains.

Finally, consistently with the previous observations, the Three-way ANOVA identified a significant impact of sex ($p=0.0002$; Figure 5.11C) and absence of Abi3 ($p=0.0123$; Figure 5.11C) as well as a significant interaction between sex and App ($p=0.0003$; Figure 5.11C) on the total time spent in the centre. Indeed, healthy female Abi3-WT and -KO mice spent more time in the centre compared to males of the same strain ($p<0.0001$ for Abi3-WT, $p=0.0323$ for Abi3-KO mice; Figure 5.11C) while no parallel difference was observed in the case of mice bearing mutant App.

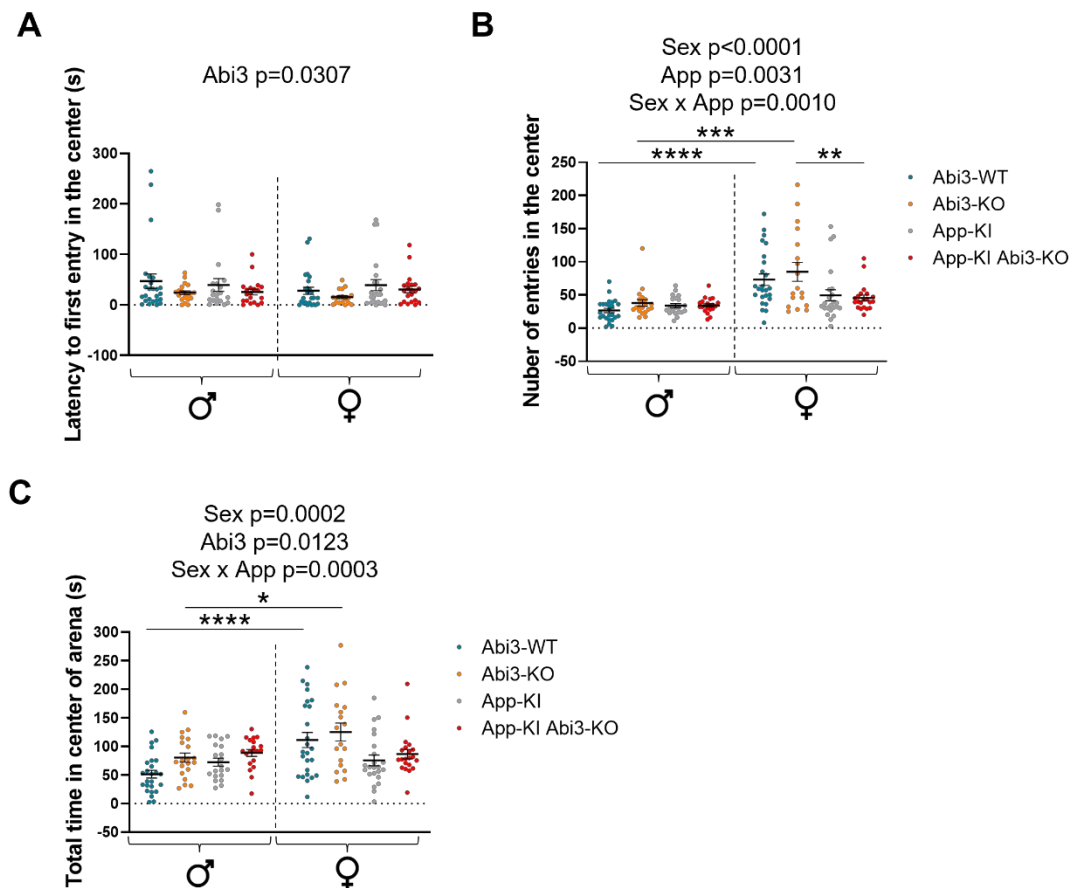


Figure 5.11 Quantification of anxiety-like behaviour in the OF arena.

Each dot represents a single mouse. Abi3-WT and -KO mice are indicated by light blue and orange dots respectively, while App-KI mice are represented by grey dots and double-transgenic animals by red ones. The black horizontal lines represent the mean of each experimental group \pm S.E.M. The p-values resulting from the Three-way ANOVA are reported on each graph. The p-values of any significant pairwise comparison generated through the Šidák's multiple comparisons test are reported on the graphs by means of asterisks for any significant two- or three-way interaction identified. **A)** Graphical representation of the latency to the first entrance of each mouse in the centre of the arena. **B)** Evaluation of the number of entries in the centre. **C)** Quantification of the total time spent in the centre of the arena (expressed in seconds). Data were analysed via Three-Way ANOVA followed by Šidák's multiple comparisons test. A single App-KI male was excluded from the analysis due to a technical issue with the camera. For males and females respectively: n=25 for Abi3-WT, n=20 and 18 for Abi3-KO, n=20 and 23 for App-KI, n=20 and 21 for App-KI Abi3-KO. *p \leq 0.05, **p \leq 0.01, ***p \leq 0.001, ****p \leq 0.0001.

The subsequent examination of locomotor activity through a Three-way ANOVA confirmed once again a significant overall impact of sex (p<0.0001; Figure 5.12A) on the percentage of time spent in movement across the whole arena.

Similar to what was observed during the EPM task, sex appeared to markedly influence the mean velocity of the mice ($p < 0.0001$; Figure 5.12B), with females moving generally faster than males. The presence of mutant App also impacted mice velocity ($p = 0.0408$; Figure 5.12B). A two-way interaction between sex and App was also identified ($p = 0.0103$; Figure 5.12B), with females mice bearing the App mutation moving overall more slowly than healthy mice, while no obvious difference was visible in the male group. The following post-hoc test identified no significant pairwise comparisons (Figure 5.12B).

In agreement with these findings, female mice travelled significantly more across the arena than males ($p < 0.0001$ for the “sex” main effect; Figure 5.12C). A single significant two-way interaction between sex and App was identified as well ($p = 0.0229$; Figure 5.12C), with healthy female mice moving for longer distances than the AD counterparts. Šidák’s test no significant pairwise comparisons.

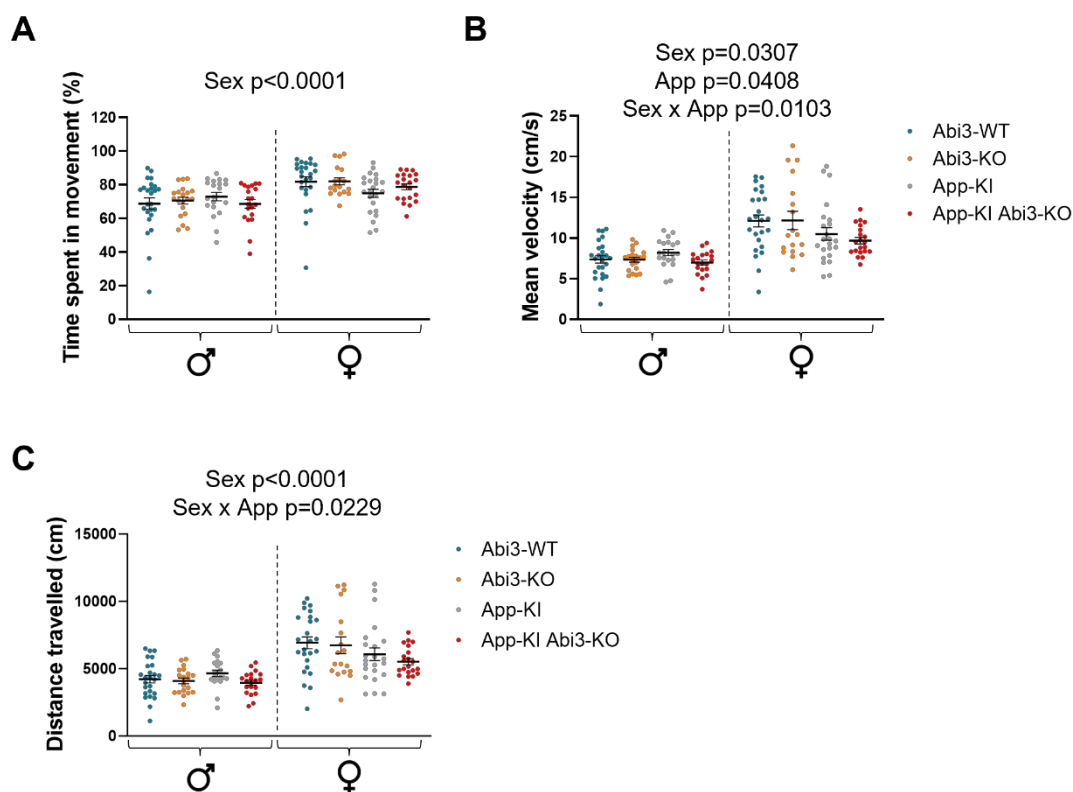


Figure 5.12 Graphical representation of locomotor activity quantified in the OF arena.

Each datapoint on the graphs represents one animal. Abi3-WT mice are indicated by light blue dots, Abi3-KO mice by oranges ones, while the grey dots indicate App-KI animals and, finally, the red dots App-KI Abi3-KO mice. The black horizontal lines represent the mean of each experimental group, while the vertical ones indicate the Standard Error. The p-values

resulting from the Three-way ANOVA are reported on each graph. The *p*-values of any significant pairwise comparison generated through the Šidák's multiple comparisons test are reported on the graphs by means of asterisks for any significant two- or three-way interaction identified. **A)** Quantification of the percentage of time spent moving during the OF task. **B)** Evaluation of mice velocity (in cm/s). **C)** Graphical representation of the total distance travelled by mice during the task, expressed in cm. Data were analysed via Three-Way ANOVA followed by Šidák's multiple comparisons test. A single App-KI male was excluded from the analysis due to a technical issue with the camera. For males and females respectively: *n*=25 for Abi3-WT, *n*=20 and 18 for Abi3-KO, *n*=20 and 23 for App-KI, *n*=20 and 21 for App-KI Abi3-KO. **p*≤0.05, ***p*≤0.01, *****p*≤0.0001.

The results of the EPM and OF tasks hinted to a potential impact of Abi3 ablation on anxiety-like behaviour and locomotor activity regardless of the presence of AD-like pathology. In order to investigate any repercussion on the cognitive domain, mice were tested twice to assess recognition memory through the NOR paradigm as described in section 2.8.3.

The total exploration time was initially assessed on the full dataset, without exclusion of animals due to low exploration. The following Three-way ANOVA reported a significant increase in total exploration time in the presence of mutant App for both datasets (*p*=0.0071 for the first repeat and *p*=0.0035 for the second, data not shown). However, after removing animals based on the pre-determined exclusion criteria, the difference became less noticeable. Indeed, the increase in total exploration time in animals bearing App mutation did not result significant for the first NOR repeat (*p*=0.0728; Figure 5.13A). In the case of the second repeat, instead, the presence of mutant App still caused a significant overall increase in exploration (*p*=0.0459; Figure 5.13B). This was coherent with the extremely different number of animals for each strain that did not meet the minimum inclusion criteria: for instance, only 5 App-KI and 5 App-KI Abi3-KO mice had to be excluded from the first NOR dataset, compared to 11 Abi3-WT and 11 Abi3-KO animals.

The discrimination index for each of the repeats of the NOR task was then evaluated by a Three-way ANOVA. In the first repeat, a significant reduction in the average discrimination index value was observed in animals crossed with the AD model (*p*=0.0020; Figure 5.13C). No additional significant main effect or two- or three-way interaction was identified.

During the second repeat of the assay, App-KI samples presented once again a lower discrimination index. However, in this case no significant main effect due to

the presence of mutant App was identified ($p=0.6637$; Figure 5.13D). Instead, a significant two-way interaction between App and Abi3 was detected ($p=0.0260$; Figure 5.13D) and indeed, Abi3-KO mice appeared to recognize the novel object as much (in the case of males) or even less (for females) than mice bearing mutant App. Female Abi3-KO mice presented a particularly low discrimination index (0.05 ± 0.28 , mean \pm SD; Figure 5.13D), despite no significant pairwise comparisons being identified by the subsequent Šidák's multiple comparisons test.

Unfortunately, an explanation for this last observation was offered by the analysis of the discrimination index where the use of object A or B as novelty was used as a grouping factor instead of sex. No significant impact of the object was identified during the first repeat of the assay ($p=0.9298$; Figure 5.13E). However, during the second repeat a clear preference for object B was noticeable in every strain, and it was then confirmed through a Three-way ANOVA test ("object" main effect: $p=0.0003$; Figure 5.13F). When analysing this more in detail, Abi3-KO females showed the lowest discrimination index for object A (-0.06 ± 0.18 , mean \pm SD), which accounted for the results presented in Figure 5.13D. For further discussion please see section 5.3.

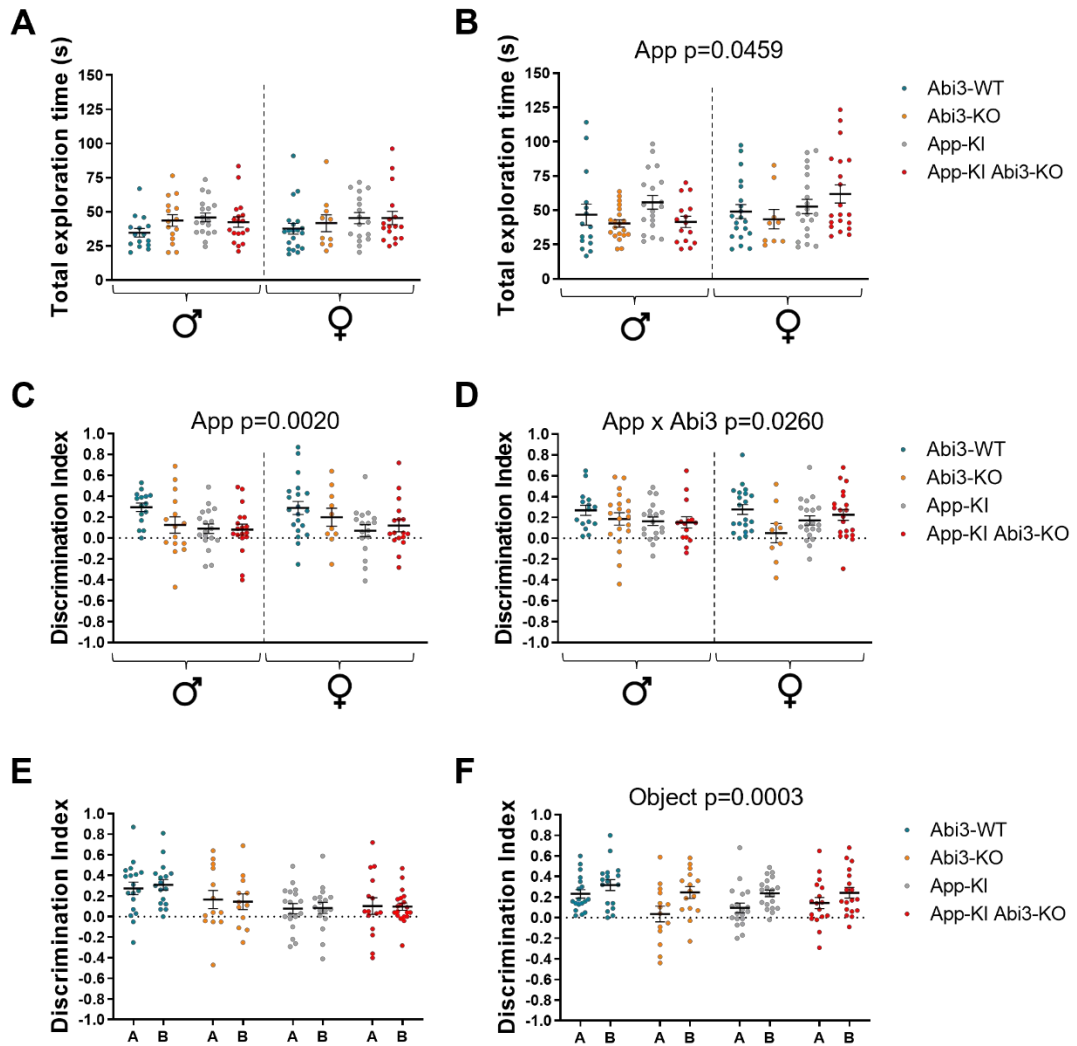


Figure 5.13 Graphical representation of the NOR task results.

Light blue dots represent *Abi3*-WT animals, while *Abi3*-KO mice are indicated by orange dots, *App*-KI by grey dots and *App*-KI *Abi3*-KO by red dots. Each datapoint on the graphs represents one animal; the mean of each experimental group is indicated by a black horizontal line, \pm S.E.M. The *p*-values resulting from the Three-way ANOVA are reported on each graph. The *p*-values of any significant pairwise comparison generated through the Šidák's multiple comparisons test are reported on the graphs by means of asterisks for any significant two- or three-way interaction identified. **A)** and **B)** Quantification of the total time spent exploring either of the objects (in seconds) for either the first (A) or second (B) set of objects. **C)** and **D)** Evaluation of the discrimination index for the first (C) or second (D) set of objects. **E)** and **F)** Assessment of the discrimination index for object A or B for each genotype regardless of the sex. A total of 11 *Abi3*-WT (7 males, 4 females), 11 *Abi3*-KO (5 males, 6 females), 5 *App*-KI (1 male, 4 females) and 5 *App*-KI *Abi3*-KO (2 males, 3 females) animals were excluded from the analysis due to not reaching the minimum threshold (20 s) for total object exploration during the first NOR task. Similarly, a total of 10 *Abi3*-WT (7 males, 3 females), 4 *Abi3*-KO (1 male, 3 females), 3 *App*-KI (1 male, 2 females) and 3 *App*-

KI *Abi3*-KO (all males) animals were excluded for the second NOR task. Data were analysed via Three-Way ANOVA followed by Šidák's multiple comparisons test. For the first repetition of the NOR (A and B), for males and females respectively: $n=15$ and 20 for *Abi3*-WT, $n=15$ and 10 for *Abi3*-KO, $n=18$ and 17 for *App*-KI and *App*-KI *Abi3*-KO. For the second repetition (C and D), for males and females respectively: $n=15$ and 20 for *Abi3*-WT, $n=15$ and 9 for *Abi3*-KO, $n=19$ and 20 for *App*-KI, $n=15$ and 20 for *App*-KI *Abi3*-KO. $*p \leq 0.05$.

Anxiety-like behaviours, as well as locomotor activity and memory impairment have been fairly extensively evaluated in *App*-KI mice (417,418,420). Less is known, instead, about depression-like behaviour in this strain. For this reason, stress- and depression-induced anhedonia was assessed in blinded conditions in 54-week-old mice by means of a sucrose preference test carried on for 24 hours as described in section 2.8.4.

Neither sex or loss of *Abi3* appeared to significantly impact the innate preference for sucrose according to the results of the Three-way ANOVA ($p=0.6129$ and $p=0.1829$ respectively; Table 5.9). The presence of mutant *App*, instead, appeared to cause a significant increase in sucrose consumption in both sexes ($p=0.0042$; Figure 5.14 and Table 5.9). A two-way interaction between *App* and *Abi3* was also noted ($p=0.0370$; Figure 5.14 and Table 5.9), with double-transgenic of both sexes mice showing a markedly reduced preference for the sweetened solution compared to *App*-KI mice. However, when these observations were further investigated with a Šidák's multiple comparisons test, no significant pair-wise comparison was identified.

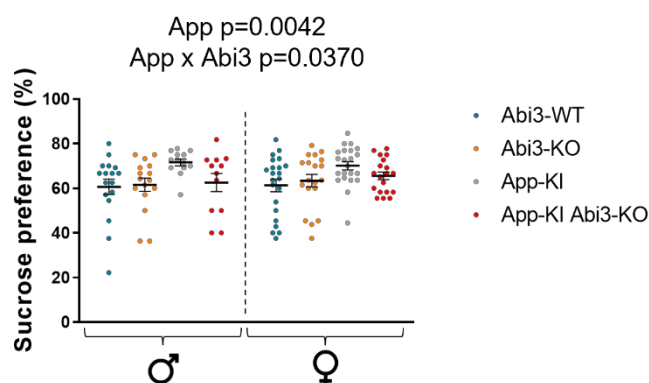


Figure 5.14 Graphical representation of the percentage of sucrose preference after 24 hours.

Abi3-WT mice are represented by light blue dots, Abi3-KO mice by oranges one, while the grey dots indicate App-KI animals and, finally, the red dots represent App-KI Abi3-KO mice. Each datapoint on the graphs represents one animal; the mean of each experimental group is indicated by a black horizontal line, \pm S.E.M. The p-values resulting from the Three-way ANOVA are reported on each graph. Data were analysed via Three-Way ANOVA followed by Šidák's multiple comparisons test. A single Abi-KO female was excluded from the analysis due to a leakage in the cage overnight. For males and females respectively: n=17 and 22 for Abi3-WT, n=16 and 19 for Abi3-KO, n=13 and 22 for App-KI, n=12 and 19 for App-KI Abi3-KO.

Another spontaneous behaviour of small rodents typically affected by AD is their ability to build appropriately-shaped nests (421). For this reason, at the very end of the behavioural experiments, single-caged mice were provided fresh nesting material and left free to interact with it for approximately 20 hours prior to scoring (for more details, please see section 2.8.5 of the Methods). Figure 5.15 show a schematic representation of the scoring system and parallel images of actual nests.



Figure 5.15 Schematic description and representative images of nest scoring assessment.

A) In case of no manipulation of nesting material, a 0 score was assigned, while barely manipulated material was assigned a 1. If a clear nest site was identified, each side of an imaginary square comprising the nest was scored individually, to then average the four values. A flat nest was scored as a 2 and slightly cupped walls were scored as a 3, while higher walls were assigned either 4 (less than half-dome) or 5 (more than half-dome) points. **B)** Representative images of nests with increasing score. In case of cupped walls (3-5), red arrows point to areas with the relative score. Due to difficulties of accurately scoring nests from images, the score was assigned contextually to the image acquisition.

The average score for each animal is indicated in Figure 5.16. The Three-way ANOVA test identified a significant impact of both sex and presence of mutant App on the average score ($p < 0.0001$ for both main effects; Figure 5.16), while the absence of Abi3 alone did not appear to play a crucial role on this specific behaviour ($p = 0.4418$). However, a significant two-way interaction between App and Abi3 was highlighted ($p = 0.0003$; ; Figure 5.16). The successive post-hoc test reported a significant decrease in the average nest score in App-KI mice compared to Abi3-WT controls for both sexes ($p < 0.0001$ for both; Figure 5.16). Male Abi3-KO mice also performed worse than their sex-matched controls ($p = 0.0379$), while the difference between females of the same strain was not significant. Interestingly, females mice scored overall markedly worse than the males.

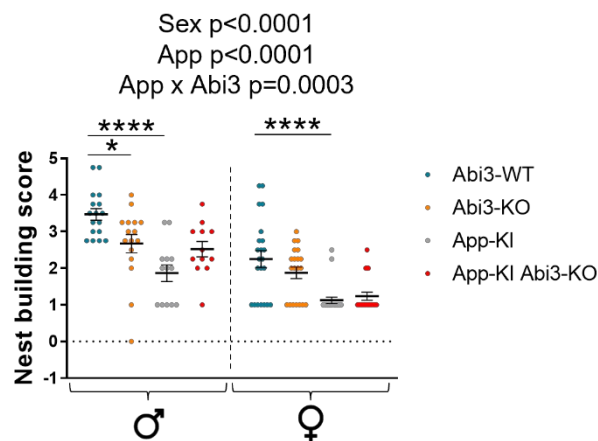


Figure 5.16 Quantification of nest building score for male and female mice of all the strains of interest in this thesis.

Light blue and orange dots represents Abi3-WT and -KO mice respectively, while grey dots indicate App-KI mice and red dots App-KI Abi3-KO animals. All the values reported in this graphs were obtained by averaging the score of all 4 sides of the nest for any given animal; each dot indicate one animal. The black horizontal lines represent the mean of each experimental group \pm S.E.M. The p-values resulting from the Three-way ANOVA are reported on each graph. The p-values of any significant pairwise comparison generated through the Šidák's multiple comparisons test are reported on the graphs by means of asterisks for any significant two- or three-way interaction identified. Data were analysed via Three-Way ANOVA followed by Šidák's Multiple Comparisons Test. For males and females respectively: $n = 17$ and 22 for Abi3-WT, $n = 16$ and 20 for Abi3-KO, $n = 13$ and 22 for App-KI, $n = 12$ and 19 for App-KI Abi3-KO. * $p \leq 0.05$, **** $p \leq 0.0001$.

5.3. Discussion

In the previous chapters, *Abi3* deficiency was shown to affect actin dynamics *in vitro* and cause severe morphological changes in microglia of young animals *in vivo*. Here, the repercussions of these changes were assessed in the aged and pathological brain context with a combination of histological and behavioural approaches.

In the first result section of this chapter, microglia distribution was assessed in *Abi3*-deficient mice and controls, as well as in mice crossed with an *App* knock-in model of AD, specifically the APP^{NL-G-F} mice, firstly described by Saito and colleagues (260). Following a preliminary visual evaluation of amyloid burden in *App*-KI mice (Figure 5.1), to identify one or more timepoints for the successive histological analysis, animals were aged to 16 weeks prior to tissue collection. Following an *Iba1* staining to visualise microglia, it appeared evident that the dystrophic microglial phenotype described in Chapter 4 was maintained with age regardless of sex and *App* mutation. Despite slight differences between cortical and hippocampal region, the overall trend showed an increase in microglia number and concurrent decrease in NND values within animals lacking *Abi3*, as well as visible microgliosis in both strains carrying the mutant *App* gene (Figure 5.2). Coherently with the visually appreciable morphological alterations in *Abi3*-deficient mice, *Abi3* ablation caused a decrease in *Iba1* immunoreactivity, corresponding to the reduction in microglial processes. Previous reports from Masuda and colleagues showed a significant increase in microgliosis in *App*-KI mice compared to WT controls at 12 months of age (384), while Saito *et al.* had previously reported enhanced microgliosis in 9-month-old *App*-KI mice compared to the APP^{NL-F} model (260). Here we show that clear clusters of activated microglia are visible in both the cortex and in the hippocampus of mice bearing mutant *App*, leading to a significant increase in microgliosis already at the age of 16 weeks.

As in the case of young, healthy animals, the observations described above provide contrasting evidence on *Abi3* impact on microgliosis compared to the recent publication by Ibanez and colleagues based on the same *Abi3*-KO model (303). The authors described an initial significant decrease in *Iba1* immunoreactivity in the hippocampus of 3-month-old heterozygous (Het) animals compared to *Abi3*-WT controls, followed by a significant increase in microglia-covered area in these same mice at the age of 6 months. No significant difference was observed between *Abi3*-WT and -KO mice. Conversely, *Abi3*-KO animals crossed with the *TgCRND8*

strain showed a significant increase in Iba1 immunoreactivity compared to Abi3-Het mice, but not Abi3-WT, in the cortex of 3-month old mice. No difference was observed in 6-month-old mice (303). Likewise, Karahan *et al.* reported no difference in Iba1 levels in 8-month-old Abi3-KO mice compared to Abi3-WT controls, crossed with the 5XFAD model, as assessed by western blot (302)

Similar discrepancies were observed in astrogliosis levels reported in section 5.2.1 compared to Ibanez *et al.* (303). In this thesis, a significant increase was observed in astrocytes number within the hippocampus of 16-week-old animals lacking Abi3, which was not followed by a parallel increase in GFAP immunoreactivity (Figure 5.3), suggesting potential alterations in astrocyte morphology. In agreement with data presented in section 4.2.4, adult Abi3-KO mice showed multiple areas extremely enriched in astrocytes, characterised by the loss of the typical tiled organisation of these cells. Moreover, App-KI mice presented a clear astrogliosis (indicated by a higher cell count as well as GFAP immunoreactivity) compared to Abi3-WT mice. Ibanez and colleagues, while overall agreeing on the increased astrocytic burden caused by the absence of Abi3, reported a significant increase in GFAP immunoreactivity in the hippocampus of healthy 3- and 6-month-old Abi3-KO animals compared to Abi3-WT controls (303). Instead, in 6-month-old mice crossed with the TgCRND8, the authors described comparable GFAP levels between Abi3-WT and -KO mice (303).

The phenotype observed in young Abi3-KO (Chapter 4) had led to speculations regarding a potential impairment of amyloid recognition and microglial migration towards A β deposits in these mice. However, the visual observation of microglial clustering in App-KI Abi3-KO animals suggested that microglia chemotaxis was not entirely suppressed in these mice, even in the presence of dystrophic ramifications and reduced tissue surveillance. To further investigate the impact of the previous findings on amyloid deposition in mice crossed with the App-KI strain, PFC and hippocampal sections were stained using a 6E10 antibody specific for residues 1-16 of A β (350). Interestingly, Abi3-KO mice bearing the mutant App gene did not show obvious alterations in A β deposition within their PFC (Figure 5.4), however a significant reduction in A β deposition was observed in the hippocampus of both male and female double-transgenic mice compared to App-KI controls (Figure 5.5). This could be related to the difference in overall plaque number between the two areas, since the hippocampus presented a slightly lower number of microglia/mm², consistent with previous observation of faster accumulation of A β 42 in the cortex (260,423). It is possible that the higher number of plaques observed in the PFC

exceeded microglial ability to effectively clear A β , leading to no appreciable difference. Instead, the amyloid burden in the hippocampus could have been still sufficiently low to enable the identification of an enhanced clearance in Abi3-KO brains. To clarify this, evaluation of additional time points should be performed to assess whether the protective effect of Abi3 ablation extends to older mice and whether, in the presence of lower amyloid burden in young mice, a reduction is visible in the PFC as well as the hippocampus. It is also possible that, despite no obvious phenotypic difference between PFC and hippocampus in these mice, spatial heterogeneity affecting microglial functionality (148) (discussed more in detail in section 1.1.5.1) could account for at least some of the discrepancies. No impact of sexual dimorphism on amyloid deposition was noted, despite previous reports of increased amyloid deposition in females across multiple mice models of AD (424). Masuda and colleagues, however, reported increased amyloidosis and neuroinflammation in females at the age of 18 months in App-KI mice (422), so it is possible the lack of an obvious effect of sexual dimorphism in this chapter could be due simply to the early time point considered.

In order to understand whether the phenotype observed in the hippocampus was connected to a more efficient translocation of microglia to amyloid plaques, higher resolution images of individual plaques were obtained to quantify plaque-associated microgliosis. Due to the significant decrease in both plaque number and size observed in the hippocampus, the identification of enough plaques with comparable size in this region proved to be extremely complicated. For this reason, despite the higher relevance of hippocampal sections, it was chosen to proceed with PFC samples instead. In spite of their apparent dystrophic phenotype, Abi3-KO cells could have been favoured by their sheer number and close proximity. The assessment of microglia count around plaques, however, did not detect any significant difference between genotypes regardless of plaque size (Figure 5.6). Notably, a potential reduction in morphological changes in plaque-associated Abi3-KO microglia compared to App-KI controls was visible, with Abi3-deficient cells not obviously assuming a fully amoeboid morphology, which could be explained by the higher stiffness of the actin cytoskeleton in these cells. Further investigation is warranted to confirm this observation and understand its potential implications.

A potential source of bias in this thesis is the use of a single marker for amyloidosis assessment. The choice to use a 6E10 antibody was dictated by the fact that Th-S staining, while extremely cheap and fast to perform, is particularly photosensitive and the fluorescent signal tends to dim quickly. Th-S also shows elevated

background signal and the quality of the staining is batch-dependent due to the need for freshly-made solution, making the immune-labelling with 6E10 preferable for more reliable results in the case of large experimental groups that would require multiple imaging sessions. However, recent work from Clayton and colleagues showed that the use of a 82E1 antibody – which recognises the same residues as the 6E10 – did not allow detection of changes in amyloid burden following microglial depletion, whereas a significant increase in the number of diffuse plaques was observed upon utilisation of a 4G8 antibody, specific for residues 17-24 (350). Therefore, further investigation of Abi3 impact on amyloid deposition should include additional markers to account for both diffuse and compact deposits and better characterise changes in plaque morphology and number. Moreover, spatial transcriptomic approaches could lead to the identification of differences in gene expression in microglia localised around amyloid plaques and provide unbiased insights on Abi3-dependant changes associated to its apparently protective role in the hippocampus.

Coherently with the description of reduced A β deposition in the absence of Abi3 in App-KI mice, Ibanez and colleagues reported a significant amelioration of amyloid burden in Abi3-KO mice crossed with the TgCRND8 model (303). In stark contrast, Karahan and colleagues showed a significant reduction in microglial localisation around plaques in Abi3-deficient mice accompanied by a severe increase in amyloid burden in the cortex of both male and female mice (302). It is worth noting that the amount of microglial cell bodies and processes visible in their samples is remarkably lower than what was observed in Figure 5.6 and that the authors appeared to employ quantification of Iba1 area as a measure of microglia density. However, it has been shown in this thesis that these two parameters do not correlate in Abi3-deficient mice due to the morphological changes in Abi3-KO cells. Moreover, a 2D approach could potentially introduce bias due to the lack of information along the z-axis, which could cause underestimation of plaque size as well as incorrect inclusion of microglia cells that appear close to the plaque but are, in fact, further away along the z-axis. Thus, while the divergent results between this thesis and Karahan's paper could be ascribed to the use of a different mouse models of AD, it is likely that the chosen method for histological analysis could account for at least part of the discrepancies.

An accurate comparison between the results reported in this thesis and published work (302,303) is impossible due to previously discussed technical discrepancies, as well as different time points and, most importantly, different models employed for

the study of AD. However, the results reported in these new studies support the need for further investigation of Abi3 role in mice crossed with the APP^{NL-G-F} strain, to provide a better understanding of the (still uncharacterised) alterations caused by Abi3 depletion on disease progression in this particular model. For this reason, tissue has been collected for histological and molecular biology analyses at additional time points (namely, 8, 24 and 52-54 weeks of age) for future experiments aimed to evaluate the impact of Abi3 knock-out on early and late stages of the disease.

Interestingly, it has been shown that plaque burden does not necessarily correlate with other pathological hallmarks such as neuronal loss or behavioural changes and memory impairment (237,425,426). Spangenberg et al. have shown that the ablation of microglia in adult 5XFAD mice, following CSFR1 inhibition, lead to no difference in β amyloid deposition. However, the authors reported a reduction in neuroinflammation and concomitant increase in mushroom spine number, reduction in neuronal loss and overall amelioration of the impairment (237). Prior to this work, Couch and colleagues had reported a similar mismatch between severity of brain amyloidosis and performance of the mice in behavioural tasks using inbred and out-crossed double-transgenic mice (426). More recently, Arboleda-Velasquez *et al.* reported the identification of an AD patient bearing the APOE3 Christchurch mutation (R136S), which showed only mild cognitive impairment despite the severe accumulation of A β (426). Remarkably, most of the therapeutic anti-A β antibodies been developed in the last decade have been abandoned or failed the clinical trial due to lack of efficacy in slowing cognitive decay (427). Taken together, these observations support the idea that, while amyloid deposition certainly plays a role in AD pathogenesis, it does not necessarily correlate with cognitive decline.

For this reason, section 5.2.3 focused on the assessment of emotional and cognitive changes ascribable to the ablation of Abi3 in 40-week-old mice, summarised in Figure 5.17.

Same as control
 Lower than control
 Higher than control

Behavioural tasks	Parameter evaluated	Presence of mutant App				Absence of Abi3		Sex
		Abi3-WT vs App-KI		Abi3-KO vs App-KI Abi3-KO		Abi3-WT vs Abi3-KO	App-KI vs App-KI Abi3-KO	Males vs Females
Elevated Plus Maze	Anxiety	Blue		Blue		Grey	Grey	Grey
	Locomotor activity	Yellow		Yellow		Yellow	Blue	Grey
Open Field	Anxiety	♂ Yellow	♀ Blue	♂ Grey	♀ Yellow	Blue	Blue	Blue
	Locomotor activity	♂ Grey	♀ Blue	♂ Grey	♀ Yellow	Grey	Grey	Yellow
Novel Object Recognition	Recognition memory	Blue		Blue		Grey	Grey	Grey
Sucrose preference	Sucrose preference	Yellow		Grey		Grey	Blue	Grey
Nesting	Nest building ability	Blue		Blue		Blue	Yellow	Blue

Figure 5.17. Summary table of the behavioural tasks performed on 40-week-old mice.

For each parameter, the overall influence of App mutations, Abi3 ablation and Sex has been reported with the use of different colours. Grey cells show no difference between the two groups considered; blue cells indicate a lower overall score compared to the control strain (for instance, App-KI mice showed reduced anxiety during the Elevated Plus Maze task compared to Abi3-WT mice, as shown by the blue cell in the top left corner); yellow cells indicate a higher score compared to the control strain (e.g. App-KI mice showed increased locomotor activity in the Elevated Plus Maze task compared to Abi3-WT mice, as indicated by the first yellow cell from the left in the second row).

Anxiety and locomotor activity were assessed first, through the Elevated Plus Maze (EPM) and the Open Field (OF) paradigms, as shown in Figures 5.7-12. Overall, the EPM confirmed the presence of an anxiolytic behaviour in App-KI mice (418,428) which spent significantly more time exploring the open arms compared to Abi3-WT controls (Figure 5.7-8). App-KI mice were found to spend significantly less time moving in the open arms despite moving faster and for longer distances than healthy controls (Figure 5.9). During the testing sessions, it was noted that, indeed,

these mice were more prone to explore the surrounding environment, while Abi3-WT mice – males in particular – spent more time grooming in the safety of the closed arms. However, future evaluation of head-dipping, elongation and vertical activity, as well as grooming, defecation and urination will be required to clarify if this is the correct interpretation of these findings. While Abi3 ablation did not appear to impact anxiety-like behaviour in this particular task, it did cause an overall significant increase in the distance travelled and mean velocity in healthy Abi3-KO mice of both sexes compared to sex matched Abi3-WT controls (Figure 5.9). This was not true in mice crossed with the App-KI line, where instead a slight reduction was visible in Abi3-deficient animals.

In the OF arena, Abi3 knock-out was found to deeply impact mice performance. Specifically, Abi3-deficient mice started to explore the centre of the arena earlier and spent overall more time in that area compared to sex-matched Abi3-WT or App-KI mice, with females being particularly disinhibited (Figure 5.10-11). Females of all strains also spent significantly more time moving and were remarkably faster than their male counterpart (Figure 5.12). The presence of mutant App, in combination with sexual dimorphism, led to more complex alterations of both arena exploration and locomotor activity. For instance, female App-KI Abi3-KO mice entered in the central area fewer times than sex-matched Abi3-KO mice (Figure 5.11), and a similar – albeit not significant – difference was observed between App-KI and Abi3-WT females. Overall, healthy females appeared to be more prone to abandon the safety of the borders than females bearing App mutations. This result appears to conflict with the anxiolytic behaviour demonstrated by App-KI mice during the EPM. Previous studies performed on the same AD model reported variable outcomes when animals were tested with the OF paradigm at 6 months of age, with the App-KI mice spending more time in the centre of the maze according to a study by Latif-Hernandez *et al.* (429), or showing no difference in centre exploration compared to control mice according to Whyte *et al.* (430). Pervolaraki *et al.* reported the same incongruity observed in this thesis when testing 8-month-old mice with both the EPM and OF (428). Moreover, a similar dichotomy was observed in other AD models, such as the Tg2576 mice (431). Further investigation is required to fully understand the underlying causes of such overt contradiction. Pervolaraki and colleagues also highlighted age-dependent differences in locomotor activity, with 6-month-old App-KI mice travelling a greater distance than controls (429,430), while at 8 and 10 months no significant difference had been reported (428,429). This is consistent with the behaviour of male animals in this thesis, while females App-KI

mice showed a decreased locomotor activity compared to sex-matched controls (Figure 5.12).

Animals were further tested for recognition memory, which has been shown to be impaired in the App-KI model starting from the age of 9 months (417). The hippocampus and the Perirhinal Cortex (PRh) have been found to play two distinct roles in recognition memory: short term exploration (for example under 10 second per object) lead to the formation of weak memories with the involvement of the PRh, while longer exploration depends on the CA1 region of the hippocampus (432). While the PRh has not been included in the analysis of amyloid deposition in this thesis, the reduction in hippocampal burden observed in 16-weeks-old mice (if still present in older mice, which will have to be confirmed) could have led to an increased memory retention in double-transgenic mice compared to the App-KI controls. However, during the first repetition of the NOR, the presence of mutant App was found to significantly reduce the ability of the mice to discriminate between novel and familiar object, while Abi3 did not appear to have an effect on memory retention (Figure 5.13). Similarly, App-KI mice seemed to perform worse than Abi3-WT in the second day of testing, but in this instance healthy Abi3-KO, in particular females, scored extremely low as well despite no obvious differences in the total exploration time. This led to further investigation to exclude the possibility that an unexpected object-induced bias was the source of this observation. Indeed, this was found to be the case, since mice of all strains, but it particular Abi3-KO females were shown to significantly prefer object B (Figure 5.13). Each pair of objects had been tested prior to the commencing of the experiment, using 10 young C57BL/6J males to assess the presence of innate preference. Mice had been left free to explore each pair of objects for 10 minutes without prior training. Any object with an average discrimination index over 0.05 or below -0.05 had been excluded from the following experiments (see Appendix 3). A potential reason behind this could be the difference in age and background strain. Indeed, mice in this thesis were bred on a C57BL/6NJ background, which has been found to carry the rd8 mutation in the Crb1 gene, which can cause retina degeneration in an autosomal recessive pattern (433). Mice with obvious eye issues were not included in the analysis and, since Abi3-WT mice showed a significantly higher discrimination index than App-KI animals, even if present the mutation clearly did not severely impair their vision. However, it is possible that this somehow caused a different response to the objects compared to when tested with young C57BL/6J mice. Another possibility is a difference in anxiety levels due to sex and aging. A significant increase in anxiety levels in female mice

following aging has been previously reported (434), so it is possible that using young, male mice to assess innate preference did not recapitulate stress-induced repulsion towards a specific object observed in adult mice. Either way, due to this bias the second repetition of the NOR cannot be taken into account for the evaluation of Abi3 impact on recognition memory.

Finally, mice were assessed through a sucrose preference task, followed by a nest scoring test, in order to evaluate stress-induced anhedonia and organisation skills. A big limitation to the sucrose preference assay was the lack of specialised equipment. As shown in Methods section 2.8.4, the test was conducted in large cages provided with two standard bottles, one for either liquid. This implies that no control over leakage was possible other than exclusion of mice in case of obvious leak in the case as evidenced by a wet patch on the bedding material. However, to reduce the impact of the bottle position, bottles were swapped after 12 hours and bedding was checked for leaks at this stage as well as at the end of the test. Despite the limitations, App-KI mice showed a significantly increase in preference for the sucrose solution compared to Abi3-WT mice over a 24-hour period (Figure 5.14), which would be coherent with their anxiolytic behaviour. However a significant interaction was found between App and Abi3, and indeed the sucrose preference score for double-transgenic mice of both sexes appeared comparable to that of non-App mice.

Similarly, the absence of Abi3 appeared to impact the overall ability of mice to efficiently build nests. While males scored better than females overall, Abi3-KO males showed a significant reduction in average nest score compared to Abi3-WT controls (Figure 5.16). App-KI mice presented an even further reduction in nest quality, especially in the female group. Interestingly, as in the case of the sucrose preference, a significant interaction between App and Abi3 was identified by the Three-way ANOVA. Coherently, male double-transgenic mice showed an increase average compared to sex-matched App-KI mice (Figure 5.16). The prefrontal cortex has been attributed a role in supporting executive functions such as planning (435), which is necessary for efficient nest building (436). Therefore, it is not surprising that this behaviour is impaired in multiple models of AD (421), including the App-KI mice (420). However, the results observed in Abi3-KO mice could suggest the presence of an insult to the PFC in this group regardless of pathological conditions. Further investigation is needed to understand whether this is the case, and – if so – whether it is ascribable to increased neuroinflammation or synaptic impairment.

A great limitation for the interpretation of most of the data presented in this chapter, however, is the use of a basic Šidák's multiple comparisons test following the Three-way ANOVA. Due to software-related restrictions, this post-hoc test performed an elevated number of unrequired pairwise comparisons for each dataset, leading to a considerable loss in power. This in turn complicated the interpretation of the Three-way ANOVA results, especially in the presence of significant two- and three-way interactions. A better approach would be the use of a more complex mixed model analysis in R (which would allow more flexibility in the design of the subsequent multiple comparisons compared to GraphPad). This would not only provide a clearer understanding of the data, but – if performed on datasets including younger and older mice – would also allow a more informative analysis of Abi3 impact across all the various time points, potentially highlighting genotype-dependent differences that are not explicit when simply considering a single time point.

5.4. Conclusion and future work

In conclusion, this chapter provided further evidence of a severe contribution of Abi3 to microglia morphology and distribution, as well as to astrogliosis. It was also shown that, despite morphological and functional changes in microglia, App-KI Abi3-KO mice presented a still unidentified compensatory mechanism that prevented a worsening of β amyloidosis in the PFC and even appeared to reduce amyloid deposition in the hippocampus. Finally, Abi3 ablation was shown to impact the emotional domain in healthy mice, leading to alterations in anxiety-like behaviour and in step-to step-planning, while no evident effect was noted when considering cognitive ability. Further analyses are needed to fully disclose the nature of this mechanism and correctly assess the impact of Abi3 ablation on AD.

Firstly, additional histological analyses are needed to support the findings discussed in this chapter. Young (8-week-old) App-KI and double-transgenic mice need to be analysed to exclude an impact of Abi3 on the earlier stages of the disease. Other than gliosis characterisation, these analyses should include markers of inflammation and phagocytosis (e.g. CD68, C1q and DHE staining to evaluate ROS production). It would also be interesting to perform an immunostaining for A β oligomers, in order to identify potential Abi3-dependant changes in the deposition of this toxic species prior to clear identification of A β plaques and gliosis. Likewise, 24- and 52-week-old mice should be assessed to gain a better comprehension of disease progression in

these mice. Histological analyses should also include a more in-depth characterisation of plaque number and morphology through the use of multiple immunofluorescence approaches (for instance, a combined use of 6E10 and 4G8 antibody as well as Th-S).

Evaluation of soluble and insoluble levels of A β 40 and A β 42 in mice of different ages would provide increased confidence in the histological results. Additional molecular analyses, including the assessment of inflammation markers such as NO, ROS and pro- or anti-inflammatory cytokines would not only help clarifying whether Abi3-deficient mice presented a potentially detrimental increase in neuroinflammation, but would also allow a better comparison of the results of this study to those published by others using the same Abi3-KO model crossed with different AD models.

Given the observed difference in plaque burden in the hippocampus, histological analyses of pre- and post-synaptic markers (i.e. Synaptophysin, PSD95 and VGlut1), coupled with electrophysiological recordings in an acute hippocampal slice preparations and/or two-photon calcium imaging, could help clarify if and how Abi3 depletion impacts synapse plasticity. This in turn would provide additional insights for the interpretation of behavioural results.

Behavioural paradigms at 50 weeks of age will be soon completed. Once all tests have been scored (together with the repetition of Object In Place performed at 40 weeks but excluded from this thesis due to time constraints), it would be possible to employ a more complex mixed model analysis to evaluate Abi3 impact on mice behaviour taking into account both time points at the same time to provide additional power. This will hopefully help with the interpretation of Abi3 deficiency impact on anxiety-like behaviour.

An additional indication of the mechanisms at the base of the phenotype observed in App-KI Abi3-KO mice could be provided by two-photon imaging of App-KI and double-transgenic mice crossed with a Cx3cr1-eGFP reporter strain as in Chapter 4. These mice could be used for basic characterisation of microglia motility either distally or in close proximity to plaques (which would be identifiable with no need for additional stainings due to visible microglia aggregation). Notably, commercially available compounds such as methoxy-X04 allow *in vivo* fluorescent labelling of amyloid plaques (437,438). This would in theory enable in-depth analysis of live microglial interaction with A β deposits, possibly leading to the identification of migration or phagocytosis alterations. Pilot tests were performed to assess the

viability of this approach due to the overlap in fluorescence spectra of methoxy-X04 and GFP. Unfortunately, despite previous reports of such combined use (399), it appeared impossible to distinguish between methoxy-X04 staining and microglial clusters (data not shown), however other approaches could be attempted, including the use of luminescent conjugated oligothiophenes (439)

Finally, as discussed in the previous chapters, single cell sequencing approaches such as the iCell8 technology, would help obtaining a broader view of eventual transcription alterations in animals lacking *Abi3*. The analysis of a combination of healthy and AD-modelling mice, would allow an unbiased assessment of *Abi3* impact on neuroinflammation and overall microglial and astrocytic transcriptomic profile, regardless of a pathological setting. At the same time, if *App-KI* and double-transgenic mice of different ages were analysed in a consistent way, it would be possible to clarify the time course of *Abi3*-dependant changes in the pathological context of AD.

Chapter 6: General discussion

6.1. Introduction

Until very recently, little was known about ABI3. Most of the publications preceding this thesis were based on forced over-expression of ABI3 in non-physiological *in vitro* models, including cancer cells and cultured hippocampal neurons (294,295,299,307,308,321). These studies provided initial insights on ABI3 impact on cell motility (299) and actin polymerisation through its association to the WAVE2 Regulatory Complex (294,295), as well as on potential mechanisms involved in Abi3 regulation by the PI3K/AKT pathway (300). However, despite high levels of Abi3 in macrophages (291) and its identification as a core microglia marker (293) the role of Abi3 in microglia, and more broadly MØs, had not been explored.

The interest in Abi3 was sparked by the identification of a rare coding variant (rs616338) associated to an increased risk of developing LOAD (192). Two following meta-analyses provided additional evidences for this association (440,441). The identified SNP results in a missense mutation leading to a serine-to-phenylalanine non-conservative amino-acidic change in position 209 (S209F) in ABI3. This has been recently suggested to cause an impairment of ABI3 phosphorylation, which in turn could result in functional inactivation of ABI3 (303).

The restricted expression of ABI3 in microglia within the brain (293), as well as the inclusion of ABI3 in an AD risk associated 56-gene interaction network enriched in immune-response genes (192), led to the hypothesis that the S209F variant increased AD risk by impairing microglial functionality. However, due to the chronic lack of information regarding ABI3 involvement in microglial homeostatic functions it was possible to only speculate about potential repercussions of ABI3 mutation on cell migration, endocytosis and phagocytosis based to its involvement in the WRC regulation. Hence, the broad objective of this thesis was to elucidate the role of Abi3 in macrophages and microglia, employing a combination of biologically relevant *in vitro* models and *in vivo* approaches.

The work in this thesis was performed on newly developed Abi3-KO mice, which at the commencing of this study had not been characterised. This model provided interesting insights regarding Abi3's role when expressed at physiological levels compared to Abi3-WT controls. It is worth noting, however, that while this thesis referred to the Abi3-KO mice as a single knock-out, transcriptomic data from two extremely recent studies – published during the completion of this thesis – reported a concurrent marked reduction in expression of G protein subunit gamma transducin 2 (Gngt2), due to its close proximity to Abi3 on Chromosome 17 (302,303). Very

little is known about this gene, other than its role in the phototransduction cascade and early expression in embryonic photoreceptors (302). Expression levels of *Gngt2* in humans reported a consistent high expression of its mRNA in cells from the eye tissue (Figure 6.1A). However, a work from 2015 highlighted increased expression of *Gngt2* in classically activated MØs (M1) (442). A more recent sequencing project reported its enrichment in M1 kidney macrophages of aged mice compared to cells from younger animals (which are instead enriched in alternatively activated MØs, M2, signature genes), but not in aged brain myeloid cells (443). Multiple human macrophage subtypes present elevated levels of *Gngt2* mRNA, while they appear remarkably low in microglia (Figure 6.1A). Expression levels of *Gngt2* as measured in mouse microglia by Micro-array for *Aif1* (the gene encoding *Iba1*) and *Abi3* are presented in Figure 6.2B. Taken together, these observations highlight the need for the generation of a better *Abi3*-KO model, in order to exclude any bias in data interpretation due to still uncharacterised functions of *Gngt2* in microglia and macrophages.

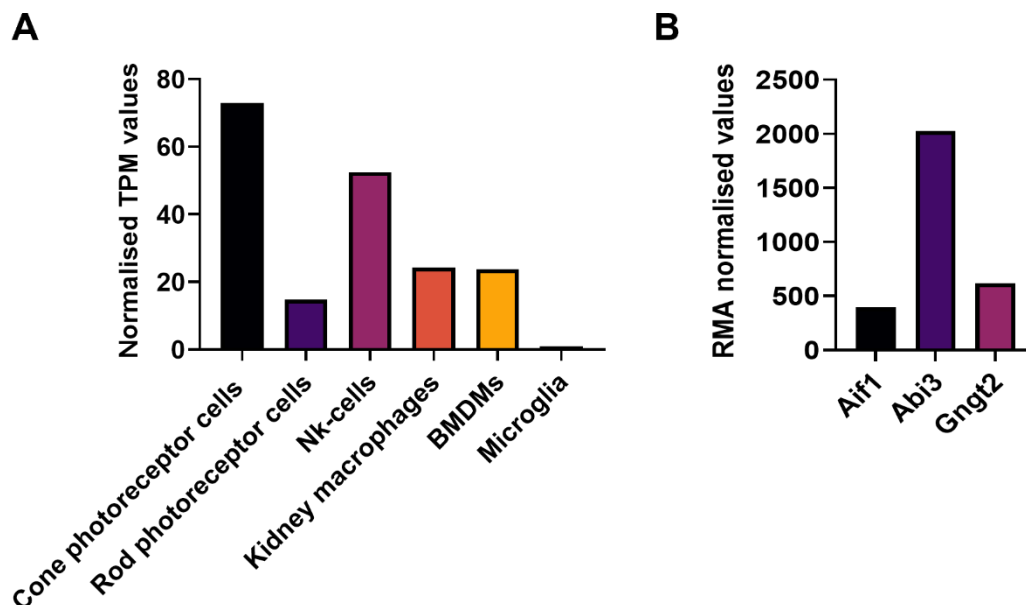


Figure 6.1 Graphical representation of *Gngt2* expression in human and mouse.

A) *Gngt2* expression across different cell types as shown by ScRNAseq data from *The Human Protein Atlas* (405). Values expressed as transcript per million (TPM) normalised by Trimmed mean of M values. **B)** *Aif1* (*Iba1*), *Abi3* and *Gngt2* expression in primary murine microglia as shown by Micro-array. Data obtained from *Immgen Micro-array Gene Skyline database* (257). Values normalised by Robust Multichip Average (RMA).

6.2. Main findings

In the course of the following sections, the main findings from each of the results chapters will be briefly recapitulated and presented with respect to the current body of literature in the field.

6.2.1. *In vitro* assessment of Abi3 impact on macrophage functionality

The first aim of this thesis was to elucidate the role of Abi3 in MØ function. For this reason, conditionally-immortalised MØP cell lines were derived from the bone marrow of Abi3-WT and -KO mice, prior to switching to the use of BMDMs (originated from App-KI and App-KI Abi3-KO strains). NIH 3T3 cell lines, overexpressing either the common or the rare human variant of ABI3, were generated together with similarly manipulated MØP cell lines to provide an initial mean of comparison with previously published studies (specifically, work by Sekino and colleagues employing hABI3-overexpressing NIH 3T3 (294)).

In sections 3.2.1 and 3.2.2, both fibroblast and MØ overexpressing cell lines were tested by means of an actin-dependant spreading assay. Initial evaluation of these experiments apparently hinted to the possibility of an hyper-functionality of ABI3 in the presence of the F209 coding variant. Indeed, in all replicates of the assay, ABI3-F209 overexpressing cells showed the most severe impairment in their ability to spread on the fibronectin-coated surface and assume a correct morphology. However, during the second and third repeat of the assay performed on the NIH 3T3 cells, inconsistent results were noted when comparing the ABI3-S209 overexpressing cells to the empty vector control. Similarly, in the single repeat performed on MØP cell lines, a very marginal impact of the common variant was reported. Due to conflicting results with the literature (260), the GFP reporter was analysed in all the cell lines by flow cytometry. This allowed the detection of extremely variable levels of expression of the lentiviral constructs in both cell types. Notably, in both cases cells overexpressing the F209 variant presented the highest levels of GFP.

Due to the inability to reliably interpret any result obtained with these cells, it was decided to abandon the overexpressing model and instead focus on the more

relevant Abi3-WT and -KO comparison. Thus, three pairs of MØP cell lines were tested with the same assay, providing particularly interesting insights on Abi3 role in cell spreading. Abi3-KO cells were shown to consistently assume an extremely solid morphology, characterised by a parallel increase in cell area. A certain degree of ramification was visible, but it was significantly reduced compared to Abi3-WT cells. This led to the proposal of a model to explain Abi3 action in MØs (explained in detail in section 3.3), according to which the genetic ablation of Abi3 would cause an uncontrolled increase in actin filament branching at the edge of the cells due to increase availability of the Arp2/3 complex. This would in turn prevent the transition towards parallel actin filaments, which represents a necessary step for the formation of filopodia. The opposite would instead be true in case of Abi3 overexpression, with reduced branching of the actin filaments (and therefore reduced lamellipodia formation), which is consistent with observation of increased filopodial structures in Arp2/3 knock-out cells (322)

This model would not only explain the results described by Sekino and colleagues (260), but also present critical implications with regards to several essential MØs functions. For instance, given the essential role of lamellipodia formation at the leading cell for cell movement (288) the absence of Abi3 would be expected to favour cell migration. Previous reports from Ichigotani *et al.* seem to confirm this (299) model. Indeed they observed reduced migration of cancer cells following ABI3 transfection which would be expected to lead to reduced lamellipodia formation. In agreement with this hypothesis, both Abi3 knock down in the BV2 microglial cell line and Abi3 ablation in primary microglia (derived by the same Abi3-KO model employed in this thesis) reportedly caused a significant increase in cell migration (318). Conversely, knockdown of ABI3 in the HMC3 microglial cell line was recently described to reduce cell motility in a scratch-wound assay (302). This observation could be due to potential biases associated to the use of microglial cell lines (445). However, Kim and colleagues recently demonstrated that reduction in WAVE2 expression (which could, at least in part, mimic the phenotype of Abi3 overexpression) caused a decrease in the F/G-actin ratio (446). If the opposite was true in the absence of Abi3, due to monomers of G-actin being “trapped” in the highly ramified actin network of lamellipodia, the reduction in cell migration described by Karahan and colleagues (302) could represent a genuine phenotype dictated by an alteration in protrusion and retraction cycles of lamellipodial structures. Further *in vitro* assays, such as a live-imaging chemotaxis assay, ideally corroborated by *in vivo* two-photon imaging, would help clarify this point.

Another process expected to be affected in MØs by the total ablation of Abi3 was phagocytosis, which relies on filopodia to capture and internalise any recognised target such as A β or pathogen particles (356). The WAVE2 complex has been implicated in phagocytosis (446) and, consistently with model proposed in this thesis, Dr R. Jones had previously described a reduction in phagocytic activity in a subset of the Abi3-deficient pMØs (F4/80⁺Tim4^{low}) (329). Indeed, the decrease in filopodial structures that would be formed in the absence of Abi3 could impair the recognition of the chosen bait (such as the Zymosan used in these experiments). In agreement with this observation, Karahan and colleagues very recently reported a significantly impairment of phagocytosis in Abi3-knocked-down BV2 cells (302). This is particularly interesting given that the same authors reported an enrichment in phagocytosis-related genes in Abi3-KO mice (302). However, when BMDMs were challenged with pHrodo Zymosan (section 3.2.3), the following evaluation of phagocytic activity of Abi3-deficient cells over the course of 2 hours did not highlight any visible difference compared to their controls.

Similarly, subsequent assessment of ROS levels in BMDMs stimulated with Zymosan (which is known to activate antimicrobial pathways following phagocytosis (371)) did not highlight any major impact of Abi3 on ROS production. However, it was interesting to see that unstimulated Abi3-deficient cells appeared to have a higher baseline compared to controls. Likewise, a marginal impact of Abi3 on NO secretion was observed at the end of section 3.2.4, when BMDMs were stimulated with LPS and IFN- γ . A significant increase in NO production in Abi3-KO cells following stimulation was not observed, but multiple confounding factors (including the chosen method of normalisation and potential differences in cell death rate between genotypes) complicated the interpretations of this result, thus requiring further evaluation to clarify the effective impact of Abi3 on inflammatory response.

Two main limitations were identified in this chapter. Firstly, multiple commercially-available anti Abi3-antibodies were tested by western blot against Abi3-KO samples, but none proved to be specific for Abi3. An attempt to produce one in-house led to similar results, and the LacZ reporter expression, examined by Dr R. Jones before the commencing of this work, was considered unreliable (329). Thus, it was impossible to assess Abi3 protein expression in Abi3-WT cells during any of the assay, which would have provided a better understand of the dynamics of Abi3 action during different challenges such as fibronectin coating or phagocytosis induction.

A second and more meaningful limitation was represented by the lack of a reliable *in vitro* model for the study of Abi3. As discussed more in detail in section 3.3, all three pairs of MØP cell lines showed a considerable decrease in viability within a short time frame from their generation. When that model was abandoned, parallel issues with mice breeding led to the use of primary BMDMs. This choice was dictated by the possibility of storing samples and synchronously starting Abi3-deficient and control cell culture even in case of litters weaned at different times, which would have not been possible in case of pMØs and primary microglia. However, Abi3 expression in BMDMs is remarkably lower than in microglia (291), preventing a clear interpretation of the results presented in this chapter. Ideally, despite technical challenges future experiments should be performed on human iPSC-derived microglia-like cells. This would represent a major improvement compared to primary murine microglia cultures for multiple reasons. Firstly, the use of iPSCs would greatly reduce the number of animals included in the study. These cells would also allow the evaluation of molecular mechanisms underlying AD in glial cells derived from patients or healthy donors, while the combined use of genome editing tools would enable the insertion of relevant mutations or knock-out of genes of interest. The use of cerebral organoids (380,447) or chimeras (448,449) would allow overcoming the marked alterations in gene expression that affect iPSC-derived, as much as primary, microglia (89,90).

6.2.2. *In vivo* evaluation of Abi3 role in the healthy brain

6.2.2.1. *Loss of Abi3 causes alterations in microglia number and distribution and severely impact microglial morphology and functionality*

A first, extremely interesting finding in Chapter 4 was the observation of a significant increase in microglial density in both the Prefrontal Cortex (PFC) and the hippocampus in Abi3-KO animals. This increase was accompanied by a concurrent reduction in nearest neighbour distance, possibly in an attempt to compensate for the reduced territory covered by each cell. Indeed, in addition to alterations in microglia count, a second noteworthy observation reported in this chapter was the

striking morphological changes presented by Abi3-deficient microglia. The presence of a dystrophic phenotype, which was already noticeable through visual assessment, was confirmed by a significant reduction in Iba1 immunoreactivity. Further in-depth analysis through 3D tracing of microglial processes of individual cells (presented in section 4.2.2) revealed an increase in process calibre parallel to a severe reduction of the arborisation apparatus in Abi3-KO animals, leading to overall significantly smaller microglial cells. To date, these findings represent the first and only evidence of Abi3-KO microglia dystrophic morphology and should be taken into consideration for future studies employing this model. Quantification of Iba1 immunoreactivity is a commonly used method to rapidly evaluate microgliosis. However, here it was shown that, in the case of Abi3-KO animals, increased microglial count is not matched by an equal rise in area covered by Iba1⁺ pixels. Therefore, evaluation of Iba1 immunoreactivity, unsupported by additional quantification approaches such as in (303) could lead to a severe underestimation of microgliosis and therefore bias downstream results interpretation and pose a caveat to otherwise extremely informative comparisons between pathological models.

The observed dystrophic phenotype warranted further investigation of the repercussion on microglial functionality. For this reason, *in vivo* two-photon imaging was employed to evaluate tissue surveillance in awake Abi3-WT and -KO mice crossed with a Cx3cr1-GFP reporter strain. As shown in section 4.2.3, despite the increase in cell number and proximity in Abi3-deficient mice, large portions of the parenchyma remained unsurveyed in the time studied. Relatively few process dynamics were observed in Abi3-deficient animals compared to controls (Appendix 4, Video A and B). In homeostatic conditions, microglial processes extend and contract at an average rate of approximately 1.47 $\mu\text{M}/\text{minute}$ (47,48). However, a very recent study has identified previously uncharacterised filopodial structures that have been shown to extend and retract at an even higher speed (7.68 ± 0.35 and $8.61 \pm 0.49 \mu\text{m}/\text{min}$, respectively) from the tip of the main processes (450). These actin-dependant structures were shown to considerably increase microglial surface and to move in random directions, constantly scanning the brain parenchyma for cues (450). As such, the differences in surveillance activity between Abi3-WT and -KO mice could be even more dramatic than they firstly appeared. Thus, further evaluation of process dynamics and microglial migration towards stimuli should be encouraged, although higher resolution than the current available one would be required for a better characterisation of the Abi3-KO model.

While *in vitro* assessment of phagocytosis had not highlighted any difference between Abi3-WT and -KO cells, the severely dystrophic microglial phenotype observed *in vivo* warranted further investigation of the phagocytic activity of these cells. An initial histological evaluation of CD68 levels (often used as a marker of phagocytic activity in microglia (397)) was performed on naïve Abi3-WT and -KO mice and, surprisingly, a conspicuous increase in CD68 was observed in both male and female mice lacking Abi3. Given the role of microglial phagocytosis in removal of dying neuronal progenitors during development (71) as well as in hippocampal neurogenesis in the early post-natal stage (72) and synapse refinement (84), the increased CD68 expression in unchallenged Abi3-KO animals led to speculation regarding potential alterations in synaptic plasticity in these animals, which would be worthy of further investigation.

6.2.2.2. *Abi3* knock-out leads to increased astrocytic burden in young healthy mice

Another intriguing finding, given the restricted expression of Abi3 in microglia, was the identification of a significant increase in astrocytic burden in the hippocampus of naïve Abi3-KO mice of both sexes, presented in section 4.2.4. Even more interesting was the apparent lack of a parallel raise in GFAP immunoreactivity, which suggested the presence of still uncharacterised alterations in the morphology of Abi3-deficient astrocytes.

Ibanez and colleagues recently confirmed the observation of noticeable astrogliosis in young and adult Abi3-KO mice, which the authors reportedly observed prior to microgliosis (303). This last finding could be due to a bias in microgliosis assessment, as discussed above. However, it would be interesting to further investigate astrocytes throughout various developmental stages together with microglia to better understand the dynamics of the astrogliosis onset.

Given the higher number, and the reportedly activated nature (303) of microglia in young Abi3-KO mice, the increase in astrocytic burden could be due to a raise in microglial secretion of factors such as C1qa, IL1- α and TNF- α , which have been shown to be sufficient to cause a shift in astrocytes towards the reactive A1 phenotype (451). In turn, reactive astrocytes have been shown to participate to neuroinflammation through the release of phosphatidylcholines with very-long-chain fatty acid acyl chains and long-chain saturated free fatty acids, extremely toxic to neurons and oligodendrocytes (451). Astrocytes have also been shown to be crucial

for a correct synaptic refinement in the developing and the adult brain, they regulate BBB function and provide metabolic support to other brain cells (130). Therefore, a dysregulation in their homeostatic functions could subject Abi3-KO mice to several detrimental effects, including enhanced neuroinflammation and alterations in synaptic plasticity.

6.2.3. Investigation of Abi3 impact on AD

6.2.3.1. Loss of Abi3 increases gliosis in adult mice

A first aim of the third and last result chapter was the evaluation of gliosis in adult mice crossed with the App-KI model. Despite lack of a glaring impact of sexual dimorphism in young mice, histological analyses were conducted on 16-week-old animals of both sexes due to previous reports of a more severe neuroinflammation in App-KI females (422). A first observation reported in section 5.2.1 was the presence of a significant increase in microglial number in App-KI mice compared to Abi3-WT controls. However, as before no overt difference was noted between male and female mice, even in the App-KI line, although this could be due to the relatively young age compared to the mice analysed by Masuda and colleagues (422). A second finding was that the phenotype manifested by young mice following the ablation of Abi3 was confirmed in adult animals regardless of the presence of AD-like pathology. Abi3-KO mice showed the same morphological alterations described in sections 4.2.1-2 as well as increased microglial density. Interestingly, double transgenic animals presented an even higher cell count than App-KI mice leading to speculations about the implication of such extensive microgliosis.

One of the first potential consequences considered was the likely parallel deterioration of astrogliosis, which was therefore evaluated in the same mice. In agreement with the current literature (452), Abi3-WT mice did not show any obvious increase in average value of astrocytes/mm² (988.23 ± 54.82 in males, 925.90 ± 75.47 in females; mean ± SD) compared to younger animals (1021.45 ± 48.13 males, 966.31 ± 106.60 in females; mean ± SD). A sustained astrogliosis was observed in Abi3-KO mice compared to Abi3-WT in animals of either sex, and an increase in astrocytic burden was also noted in App-KI mice

compared to Abi3-WT controls, particularly in females. Instead, while double transgenic males presented a number of astrocytes comparable to that of App-KI mice, an unexpected reduction was noted in App-KI Abi3-KO females. As reviewed in detail by Chowen and Garcia-Segura (453), the current body of literature provide multiple examples of sexually-dimorphic responses to aging and pathological insults in astrocytes. The reduction in App-KI Abi3-KO cell count was not significant compared to neither App-KI nor Abi3-KO mice (nor to double transgenic males), but if confirmed in later time points it could represent an additional example of divergent response to neurodegeneration. It is also worth noting that GFAP upregulation does not necessarily correspond to increased overall cell number, and should instead be interpreted as an increase in reactive astrocytes (452). Therefore, to explore the observed difference any further, additional astrocytic markers such as S100 β should be employed. Single cell sequencing of astrocytes from mice of both sexes would also provide insights about any noteworthy alteration in response to amyloidosis and Abi3 ablation.

A slight loss of the typical astrocytic tiled organisation was noted in Abi3-WT mice compared to younger animals, and few bigger cells – resembling reactive astrocytes – were observed as well. This would be in line with reports of a transition to a moderately reactive phenotype with age (452). However, previous reports of changes in astrocytic morphology and domain overlap are focused on comparisons between much older mice (for instance, Grosche *et al.* compared 5- and 21-month-old mice (454) while Rodriguez and colleagues analysed changes in morphology in 3- and 24-month-old mice (455)). The changes described in Abi3-WT cells could thus represent the beginning of more extensive age-related alterations. It would be therefore interesting to compare the current dataset to older mice to confirm the progression and the extent of these changes. As seen in young animals, Abi3-KO mice did not show an increase in GFAP immunoreactivity, despite the stark increase in territory overlap. App-KI and double transgenic mice also presented an altered distribution of cells across the hippocampus and areas enriched in reactive astrocytes.

Neither Karahan *et al.* (302) or Ibanez *et al.* (303) described an increase in microgliosis comparable to the one observed in this thesis (regardless of age or AD-model of choice). Karahan *et al.* did not assess astrogliosis in the 5XFAD model (268), while Ibanez and colleagues reported an increased astrocytic burden in healthy animals but not in mice crossed with their TgCRND8 AD model (302). As discussed before, these disparities could be due to a combination of different

analysis approaches and pathological model employed for the study, placing a caveat over the interpretation of published gliosis results in comparison to this thesis.

6.2.3.2. *Abi3* ablation differently impacts amyloid burden in PFC and hippocampus without affecting microglia recruitment around plaques

A second aim of this chapter was the evaluation of whether genetic ablation of *Abi3* affected amyloid deposition. In section 5.2.2 the PFC and hippocampus of 16-week-old App-KI and App-KI *Abi3*-KO mice were therefore assessed using the 6E10 antibody to evaluate the overall plaque burden in these regions.

It has been shown that adult microglial cells present an increasingly pro-inflammatory profile(116,142,146,456), similarly to what is observed in astrocytes (452,457). While mice analysed in Chapter 5 are still fairly young, the severe gliosis described in the absence of *Abi3*, in combination with potential age-dependant changes (albeit still at early stages) and amyloid deposition, is likely to lead to an extremely neuroinflammatory brain microenvironment. This hypothesis is now supported by Karahan's description of a significant upregulation of complement system and immune response genes in 8-month-old *Abi3*-KO males crossed with the 5XFAD model, concurrent of increase in secretion of multiple pro-inflammatory cytokines (302). Likewise, Ibanez *et al.* recently described upregulation of DAM and A1 signature genes in bulk transcriptomic of *Abi3*-deficient mice crossed with the TgCRND8 model (303). However, pro-inflammatory mediators such as IL-1, TNF- α and IFN- γ have been shown to alter the synthesis and metabolism of App (458–460). Thus, the likely increase in neuroinflammation in the brain of *Abi3*-KO mice, in combination to their dystrophic microglial phenotype, led to speculations about potential worsening of amyloid deposition in these mice.

When the App-KI model was first published, Saito *et al.* described an consistently enhanced amyloid deposition in the cortex from 4 to 9 months of age (422). In agreement with this report, the PFC of App-KI mice of both sex appeared visually much more affected than the hippocampus. However, an extremely exciting finding was the unexpected observation of a glaring amelioration of amyloid burden in the hippocampus of double transgenic mice, later confirmed by plaques quantification. Interestingly, this was not replicated in the PFC. No evident difference from the

App-KI strain was visible in this area. It was also noted that females did not appear to present an exacerbated amyloidosis, which had been previously described in the App-KI strain (422), potentially due to the younger age of the animals analysed in this thesis. Notably, recent finding by Ibanez *et al.* corroborated the observations reported in this thesis. Indeed, the authors described a significant decrease in amyloid burden in their TgCRND8 model in the absence of Abi3 (303). Conversely, Abi3-KO mice crossed with the 5XFAD model showed a drastic exacerbation of amyloid pathology (302)

During the basic characterisation of microgliosis in adult mice described in the previous section, numerous microglial clusters of variable size were observed across the whole PFC section as well as in the hippocampus of both App-KI and App-KI Abi3-KO mice. In the second part of section 5.2.2. plaque-associated microgliosis was further investigated to clarify the actual impact of Abi3 ablation on microglial recruitment. Previous studies on TREM2-KO mice crossed with the 5XFAD model showed that reduced microglia translocation to plaques leads to a severe increase in amyloid burden (325,326). Interestingly, Satoh and colleagues reported elevated ABI3 protein expression in microglia closely associated to amyloid plaques in human brain tissue samples (311), which reinforced the idea of a crucial role of Abi3 in peri-plaque microgliosis. Two-photon observations described in the previous chapter had led to the hypothesis of a reduced ability of Abi3-KO cells to detect A β and efficiently migrate towards the plaques, with a consequent increase in amyloid burden. Indeed, supporting evidence to this theory was recently published in the 5XFAD model (302). It was therefore, perhaps, surprising to see that Abi3-deficient cells surrounded amyloid plaques in equal number to App-KI control. This could be explained as a consequence of increased proximity of microglia lacking Abi3, which would require them to migrate for shorter distances in order to reach the plaques. Wang and colleagues reported a contribution of resident microglia proliferation to plaque-associated microgliosis (326), so in the future it could be worth exploring this possibility as well, for instance through a Ki67 staining of brain sections as in the aforementioned work. It would also be interesting to examine phagocytosis of A β , either through histological approaches or via two-photon imaging. A previous study based on overexpression of human TREM2 in 5XFAD mice reported that the observed increase of this marker in peri-plaque microglia correlated to an amelioration of the overall amyloidosis (302). Network analysis performed in 5XFAD mice also highlighted an enrichment in phagocytosis genes after Abi3 ablation (302). Hence, if confirmed in adult App-KI Abi3-KO mice, the

increased CD68 immunoreactivity presented by young Abi3-KO mice could relate to an increased amyloid clearance in double transgenic animals, which in turn would explain the reduced plaque burden observed in the hippocampus.

6.2.3.3. Genetic ablation of Abi3 appear to cause emotional, but not cognitive, changes in adult mice

In 2015, Dagher *et al.* employed a selective CSF-1R/c-kit inhibitor to cause microglial ablation in 3xTg-AD mice. While the treatment did not cause major changes in amyloid deposition, the authors reported improved spatial recognition (461). Likewise, Spangenberg and colleagues demonstrated an amelioration of neuronal and synaptic spine loss – with a consequent improvement in contextual memory – in 5XFAD mice, which they ascribed to the considerably reduced neuroinflammation in these mice following CSF-1R inhibition (237). These studies suggested microglial involvement in synaptic dysfunction leading to the cognitive alterations observed in AD models. Coherently, *in vitro* studies showed that microglial-secreted soluble factors (such as TNF- α , NO and IL-6) can induce synaptic loss (462,463). The same factors were later identified as responsible for microglial-dependant induction of A1 phenotype in astrocytes (451). Moreover, complement molecules such as C1q and C3, upregulated in mouse models of AD (464), have been involved in microglia-mediated synaptic pruning and their genetic ablation resulted in a reduction in synaptic loss and amelioration of cognitive deficits in AD regardless of the amyloid burden (465,466). Interestingly, genes involved in the complement system have been recently shown to be upregulated following Abi3 depletion in the 5XFAD mice (302). Taken together, these observations supported the hypothesis of a potential impairment of synaptic functionality in Abi3-deficient mice due to the augmented gliosis described in these mice.

Indeed, Karahan and colleagues reported reduced LTP in 6-month-old Abi3-KO mice crossed with the 5XFAD strain (302). Ibanez *et al.* described instead a significant increase in Synaptophysin protein levels in 3-month-old Abi3-KO mice crossed to the TgCRND8 model. A similar (not significant) trend was observed in the case of PSD95, while vGlut1 showed a significant reduction, which suggested a potentially dysfunctional glutamatergic signalling in these mice (303). In-depth analysis of dendritic spines, currently being conducted by another member of our group, detected a significant reduction in overall spine density in 6- and 12-month-old Abi3-KO mice, due to the decreased number of thin spines in these

animals. Given that thin spines are particularly dynamic and involved in memory formation during synaptic plasticity process (467), the reduction in their number could lead to critical alterations in mice behaviour. Preliminary results on 52-week-old mice also hinted to a potential reduction in Synaptophysin levels in Abi3-KO mice compared to Abi3-WT controls (data not shown). While these observations represent still very preliminary work and require further validation, they would support the hypothesis of an impairment in synaptic plasticity due to the absence of Abi3, regardless of additional pathological stimuli. This suggests the need for further assessment of synaptic engulfment and remodelling by Abi3-KO microglia. The use of conditional Abi3-KO mice should be considered in order to exclude any impact of Abi3 ablation in neurons (which have been recently suggested to express Abi3 (303)), especially in light of previous reports of Abi3 impact on synapse formation and morphology in cultured hippocampal neurons (308).

The impact of Abi3 absence on the emotional and cognitive domain of adult mice was described in section 5.2.3. Mice were initially meant to be tested at 6, 9 and potentially 12 months of age, in order to evaluate progressive changes due to aging and amyloid deposition. However, due to unforeseeable circumstances, the testing schedule had to be adjusted and mice were therefore tested at the age of 40 and 50 weeks of age. For the scope of this thesis, only the first time point was evaluated.

The first paradigm, the Elevated Plus Maze, was aimed to evaluate mice anxiety-like behaviours. This was motivated by the presence of non-cognitive neuropsychiatric alterations (such as marked increase, or decrease, of anxiety levels), in a majority of AD patients, which is recapitulated by multiple mouse models of AD presenting A β accumulation in the brain (418). A first observation was that this task confirmed the anxiolytic phenotype previously reported in App-KI mice (418,428), that spent more time exploring the open arms of the arena. A second, more interesting finding, was the identification of altered locomotor activity in the absence of Abi3. While Abi3-deficient mice explored the open arms in equal amount as their respective Abi3-WT or App-KI controls, they showed an interesting dichotomy when considering distance travelled and mean velocity. Healthy Abi3-KO mice were shown to move faster and for longer distances than Abi3-WT animals. Instead, double transgenic mice presented a slight decrease in activity compared to the App-KI strain. However, the increased locomotor activity in Abi3-KO mice was not associated to an overt increase in open arms exploration. Abi3-KO males manifested a reduced latency to the first entry in the open arms compared to sex-matched controls, while Abi3-KO females appeared to spend more time in the open

arms compared to Abi3-WT mice of the same sex, but no significant difference was noted. This is particularly interesting in light of previous observations of an influence of elevated levels of gliosis – due for instance to traumatic brain injury or local overexpression of IL1 β – on the induction of an anxiolytic behaviour in mice (468,469), which suggested Abi3-deficient mice could have manifested a similar phenotype.

To further evaluate both anxiety levels and locomotor activity, mice were also tested in an Open Field arena. During this task, Abi3-deficient mice showed a striking reduction in thigmotaxis, spending more time in the centre of the arena compared to sex-matched Abi3-WT or App-KI mice. App-KI mice instead presented a reduced preference for the centre and showed a reduced locomotor activity, as previously reported (428,430), despite a slight increase (not significant) in mean velocity and distance travelled in females. Another interesting observation was that the increase in thigmotaxis due to mutations in App appeared to affect mice regardless of Abi3 depletion, so that for instance, double transgenic females were seen entering the centre significantly fewer times than sex-matched Abi3-KO mice. A particularly obvious sex-dependant difference was also observed in this task, with females presenting a marked increase in locomotor activity. The impact on sexual dimorphism on behaviour is however particularly difficult to dissect, due to a great number of studies focusing solely on male animals to avoid any additional variability caused by discrepancies in the estrus stage across females (470). Even studies that include both males and females, such as the one by Pervolaraki *et al.* (428), mostly employ females to study social behaviour. Thus, the data reported in this thesis represent, to the best of my knowledge, one of the first reports of increased locomotion in female wild-type mice in the OF paradigm, while it confirms an extremely moderate impact of sex on the behaviour of App-KI mice (422).

A previous study from Mehla and colleagues reported an impairment in recognition memory in the App-KI model at the age of 9 months (417). This would be consistent with histological observation of severe gliosis and plaque deposition, with parallel loss of synaptic markers, in the brain of these mice (260). Indeed, the presence of reactive gliosis and A β deposition has been shown to be a key requirement for the development of cognitive deficits in the App-KI model (261). In agreement with these findings, App-KI mice in this thesis were seen to present a reduced discrimination index compared to Abi3-WT animals regardless of sex. No obvious differences were instead observed between App-KI and App-KI Abi3-KO mice. While 16-week-old mice presented a lighter amyloid burden in their hippocampus, mice of comparable

age to those tested in this assay have not been characterised in this thesis, preventing speculations regarding potential association between behavioural performance and amyloid/gliosis phenotype. An exciting finding was that, at first glance, Abi3-KO animals appeared to perform worse than sex-matched Abi3-WT controls, despite no significant main effect or interaction between Abi3 and App was found during the first repeat of the assay. This would have been in line with findings of reduced synaptic plasticity in these mice already at 6 months of age. The interpretation of Abi3 impact was however limited by an unexpected innate preference for one of the objects during the second repetition of the test, which although present in all the strains, was particularly evident in Abi3-KO females, preventing any further interpretation of this data. Moreover, multiple mice – particularly in the non-AD strains – had to be excluded from the statistical analysis of both repeats due to not reaching the minimum 20-second exploration threshold in the testing phase, suggesting an increased stress-induced repulsion towards the testing objects that had not emerged during their initial pilot assessment. The Abi3-KO line was particularly affected by this phenomenon, leaving only 10 females to be evaluated. For this reason, it is possible that an increase in sample size (for the first repeat of the assay, at least), coupled with a more powerful statistical approach as discussed in section 5.3, would help clarifying whether the visible reduction in Abi3-KO mice recognition memory is indeed meaningful and worth of further exploration. An intriguing explanation, should the recognition deficit be confirmed, could be the contribution of deficits in attentional control. This executive function has been long associated to PFC control in collaboration with areas of the parietal cortex (471). Therefore, alterations in synaptic functionality in these areas, due to increased gliosis and neuroinflammatory stimuli in the absence of Abi3, may cause a decrease in spontaneous object recognition regardless of alterations in networks associated with memory retention (namely, hippocampus and the perirhinal cortex (432)). However, given the absence of observed differences in microgliosis between PFC and hippocampus, any recognition memory deficit could also be due to a combined alterations of the aforementioned pathways.

In addition to anxiety, AD patients often present symptoms of depression and lack of planning ability (328). For this reason, in the last part of section 5.2.3 mice were tested with two final behavioural paradigms – the sucrose preference test and the nest building scoring – in order to assess whether Abi3 ablation led to meaningful alterations. Unexpectedly, App-KI mice manifested a marked preference towards sucrose solution, thus showing reduced anhedonia, while App-KI Abi3-KO animals

showed comparable to healthy mice. This could be however explained taking into account the increased anxiolytic behaviour manifested by App-KI mice, since sucrose preference is known to be reduced in the presence of stress factors (353). A more interestingly observation was the striking impairment in nest building shown by Abi3-KO mice compared to sex-matched Abi3-WT controls, in particular in males. App-KI Abi3-KO males, instead, scored markedly better than App-KI mice of the same sex. Finally, as recently reported (420), the quality of the nest built by App-KI was extremely poor. Since planning abilities have been ascribed to the control of the PFC (435), these findings support the hypothesis of a deficit in executive functions in healthy Abi3-KO mice as discussed before. Further work is necessary to fully understand the complex interaction between App, Abi3 and sex at the base of the apparent amelioration in double transgenic mice.

6.3. Conclusions

The work in this thesis provide novel insights regarding the role of Abi3 in both homeostatic and pathological brain environments. This is the first report of major alterations in microglia morphology, which should be carefully considered in future studies on the Abi3-KO model in order to ensure correct interpretation of microgliosis observations. This thesis also provides evidence supporting a severe and sustained micro- and astrogliosis in the brain of Abi3-deficient animals starting from a young age, which could lead to important repercussion on neuroinflammation and synaptic plasticity. Additionally, this is the first report of Abi3-dependant alterations in amyloid burden in the APP^{NL-G-F} mouse model of AD, as well as in the emotional domain of Abi3-KO animals. Taken together, the findings presented in this thesis support the hypothesis of a crucial role of Abi3 in the maintenance of brain homeostasis and highlight the necessity for further investigation of Abi3 impact in AD in light of future therapeutical applications.

6.4. Future work

While the results of this study provided novel insights of the role of Abi3 both in healthy animals and in a mouse model of AD, there is ample room for further research on the topic.

First of all, scRNAseq of microglia and astrocytes derived from young, naïve mice of both sexes would provide a sorely needed understanding of the homeostatic role of Abi3 in the absence of confounding pathological stimuli. The addition of Abi3^{F212} mice in the same experiment would allow an unbiased comparison between Abi3-deficient and mutant mice. This could in turn support the hypothesis of an hypofunctional Abi3 in the presence of the S209F variant, and clarify how closely (if at all) Abi3^{F212} mice resemble Abi3-KO animals. Likewise, a parallel experiment on adult mice crossed with the App-KI model would contribute to the current understanding on the impact of Abi3 on AD in the still uncharacterised App-KI Abi3-KO. These findings could be then compared to the recently published results of a similar experiment performed on Abi3-KO mice crossed with the 5XFAD strain (268) to gain a broader understanding on how manipulation of Abi3 levels affects pathology progression on different disease models. Performing a pseudotime analysis on these samples would also allow to discriminate cells based on their position along the pseudotime axis and thus clarify disease progression, as previously reported in (472).

The design of future *in vitro* experiments should be guided by the bioinformatic analysis of the scRNAseq datasets. As discussed before, more appropriate cellular models should be sought before commencing any additional *in vitro* work. Of particular interest would be the use of iPSCs-derived microglia, which could be engineered to either express the F212 variant or no Abi3 at all and then seeded in brain organoids prior to testing, to reduce as much as possible bias due to culturing conditions (380). These cells could also be employed for the generation of human-to-mouse chimeras (448). This approach, while technically challenging, currently represents the best alternative to assess human microglial response to pathological stimuli.

The chosen *in vitro* model(s) could then be used to functionally validate any noteworthy finding of the scRNASeq. Likely experiments, based on this thesis as well as published information on the Abi3-KO model (302,303), would include assessment of chemotaxis and phagocytic activity as well as evaluation of proliferation and inflammatory responses. Wherever possible, live imaging

approaches should be preferred to detect subtle alterations that may be overlooked in end-point assays. A characterisation of WAVE2 and Arp2/3 localisation should also be included to confirm the model proposed in section 3.3 to explain the phenotype observed in the absence of Abi3.

Alterations in microglial motility could be also assessed *in vivo* via two-photon microscopy through a laser injury model, which would provide additional information regarding the ability of Abi3-deficient cells to efficiently detect CNS insults and migrate towards the site of injury. This would in turn complement not just *in vitro* assays, but also the histological analyses of plaque-associated microgliosis.

Histological characterisation of Abi3-KO mice is far from being completed. Additional gliosis assessment in young (8-week-old) and old (24-week-old) mice crossed with the App-KI model is required to fully understand the impact of Abi3 loss on reactive gliosis in this particular model of AD. It would also be interesting to evaluate CD68 and DAM signature markers (including *Clec7a/Dectin-1* and *P2ry12*) in adult mice both in plaque-associated microglia and in the healthy brain, in particular following the identification of a DAM signature in Abi3-KO mice (302,303). The combined use of Th-S and 4G8, in addition to already available 6E10 data, would provide increased confidence in the quantification of amyloid burden (350), while the use of an antibody specific for A β oligomers such as the A11 would permit examination of potential differences between genotypes closer to the onset of the disease. A more detailed characterisation of amyloid plaques morphology should also be performed, similar to what has been previously reported in 5XFAD mice crossed with Trem2-KO mice (326). These experiments should be supported by molecular evaluation of amyloid burden and cytokine secretion through ELISAs or commercially available pre-defined panels, which would also allow a potentially interesting comparison between App-KI mice and the 5XFAD (302) or the TgCRND8 (303) models. Spatial transcriptomic approaches would be extremely useful to distinguish discrepancies in gene expression between peri-plaque and distal microglia in Abi3-deficient mice and clarify the mechanisms behind the reduced amyloid burden presented by double transgenic animals.

Both recent publications employing Abi3-KO mice reported alterations of synaptic functionality in this model (302,303), as discussed before. These observations, in addition to the marked increase in gliosis and alteration of Abi3-KO mice behaviour described in this thesis, strongly encourage further evaluation of synaptic plasticity. Healthy animals of different ages should be assessed in parallel to sex-matched App-KI or double transgenic mice to fully evaluate the repercussions of Abi3

ablation. This could be done by employing a combination of histological (including DiOlistic labelling for in-dept spine morphological assessment), electrophysiology approaches and two-photon calcium imaging.

Finally, the use of a conditional knock-out model would allow to dissect the impact of *Abi3* when deleted exclusively in microglia and clarify the cell-type specificity of any change observed in *Abi3*-KO mice. Particular care should be taking with the design of the knock-out, in order to avoid causing a parallel ablation of *Gngt2* to provide full confidence in the model.

Bibliography

1. Hugh Perry V. A revised view of the central nervous system microenvironment and major histocompatibility complex class II antigen presentation. *Journal of Neuroimmunology*. 1998;90(2):113–21.
2. Prinz M, Jung S, Priller J. Microglia Biology: One Century of Evolving Concepts. *Cell*. 2019;179(2):292–311.
3. Rio-hortega P Del. The Microglia. *Lancet*. 1939;
4. Ginhoux F, Lim S, Hoeffel G, Low D, Huber T. Origin and differentiation of microglia. *Frontiers in Cellular Neuroscience*. 2013;7(MAR):1–14.
5. Hao C, Richardson A, Fedoroff S. Macrophage-like cells originate from neuroepithelium in culture: Characterization and properties of the macrophage-like cells. *International Journal of Developmental Neuroscience*. 1991;9(1):1–14.
6. De Groot CJA, Huppes W, Sminia T, Kraal G, Dijkstra CD. Determination of the origin and nature of brain macrophages and microglial cells in mouse central nervous system, using non-radioactive in situ hybridization and immunoperoxidase techniques. *Glia*. 1992;6(4):301–9.
7. Matsumoto Y, Fujiwara M. Absence of donor-type major histocompatibility complex class I antigen-bearing microglia in the rat central nervous system of radiation bone marrow chimeras. *Journal of Neuroimmunology*. 1987;17(1):71–82.
8. Murabe Y, Sano Y. Morphological studies on neuroglia - VI. Postnatal development of microglial cells. *Cell and Tissue Research*. 1982;225(3):469–85.
9. Murabe Y, Sano Y. Morphological studies on neuroglia - VII. Distribution of “brain macrophages” in brains of neonatal and adult rats, as determined by means of immunohistochemistry. *Cell and Tissue Research*. 1983;229(1):85–95.
10. Perry VH, Hume DA, Gordon S. Immunohistochemical localization of macrophages and microglia in the adult and developing mouse brain. *Neuroscience*. 1985;15(2):313–26.

11. Akiyama H, McGeer PL. Brain microglia constitutively express β -2 integrins. *Journal of Neuroimmunology*. 1990;30(1):81–93.
12. McKercher SR, Torbett BE, Anderson KL, Henkel GW, Vestal DJ, Baribault H, et al. Targeted disruption of the PU.1 gene results in multiple hematopoietic abnormalities. *EMBO Journal*. 1996;15(20):5647–58.
13. Walton MR, Gibbons H, MacGibbon GA, Sirimanne E, Saura J, Gluckman PD, et al. PU.1 expression in microglia. *Journal of Neuroimmunology*. 2000;104(2):109–15.
14. Beers DR, Henkel JS, Xiao Q, Zhao W, Wang J, Yen AA, et al. Wild-type microglia extend survival in PU.1 knockout mice with familial amyotrophic lateral sclerosis. *Proc Natl Acad Sci U S A*. 2006;103(43):16021–6.
15. Ginhoux F, Greter M, Leboeuf M, Nandi S, See P, Gokhan S, et al. Fate mapping analysis reveals that adult microglia derive from primitive macrophages. *Science (1979)*. 2010;330(6005):841–5.
16. Palis J, Robertson S, Kennedy M, Wall C, Keller G. Development of erythroid and myeloid progenitors in the yolk sac and embryo proper of the mouse. *Development*. 1999;126(22):5073–84.
17. Orkin SH, Zon LI. Hematopoiesis: An Evolving Paradigm for Stem Cell Biology. *Cell*. 2008;132(4):631–44.
18. Kierdorf K, Prinz M. Factors regulating microglia activation. *Frontiers in Cellular Neuroscience*. 2013 Apr 23;7:44.
19. Schulz C, Gomez Perdiguero E, Chorro L, Szabo-Rogers H, Cagnard N, Kierdorf K, et al. A lineage of myeloid cells independent of Myb and hematopoietic stem cells. *Science*. 2012 Apr;336(6077):86–90.
20. De S, Deren D Van, Peden E, Hockin M, Boulet A, Titen S, et al. Two distinct ontogenies confer heterogeneity to mouse brain microglia. *Development (Cambridge)*. 2019;146(3).
21. Kierdorf K, Erny D, Goldmann T, Sander V, Schulz C, Perdiguero EG, et al. Microglia emerge from erythromyeloid precursors via Pu.1- and Irf8-dependent pathways. *Nature Neuroscience*. 2013;16(3):273–80.
22. Gomez Perdiguero E, Klapproth K, Schulz C, Busch K, Azzoni E, Crozet L, et al. Tissue-resident macrophages originate from yolk-sac-derived erythromyeloid progenitors. *Nature*. 2015;518(7540):547–51.

23. Matcovitch-Natan O, Winter DR, Giladi A, Vargas Aguilar S, Spinrad A, Sarrazin S, et al. Microglia development follows a stepwise program to regulate brain homeostasis. *Science* (1979). 2016;353(6301):aad8670.
24. Datta M, Staszewski O, Raschi E, Frosch M, Hagemeyer N, Tay TL, et al. Histone Deacetylases 1 and 2 Regulate Microglia Function during Development, Homeostasis, and Neurodegeneration in a Context-Dependent Manner. *Immunity*. 2018;48(3):514-529.e6.
25. Hoeffel G, Chen J, Lavin Y, Low D, Almeida FF, See P, et al. C-Myb+ Erythro-Myeloid Progenitor-Derived Fetal Monocytes Give Rise to Adult Tissue-Resident Macrophages. *Immunity* [Internet]. 2015;42(4):665–78. Available from: <http://dx.doi.org/10.1016/j.immuni.2015.03.011>
26. Ajami B, Bennett JL, Krieger C, Tetzlaff W, Rossi FMV v. Local self-renewal can sustain CNS microglia maintenance and function throughout adult life. *Nat Neurosci*. 2007 Dec;10(12):1538–43.
27. Mildner A, Schmidt H, Nitsche M, Merkler D, Hanisch UK, Mack M, et al. Microglia in the adult brain arise from Ly-6ChiCCR2+ monocytes only under defined host conditions. *Nat Neurosci*. 2007 Dec;10(12):1544–53.
28. Priller J, Flugel A, Wehner T, Boentert M, Haas CA, Prinz M, et al. Targeting gene-modified hematopoietic cells to the central nervous system: Use of green fluorescent protein uncovers microglial engraftment. *Nature Medicine*. 2001 Dec;7(12):1356–61.
29. Utz SG, See P, Mildener W, Thion MS, Silvin A, Lutz M, et al. Early Fate Defines Microglia and Non-parenchymal Brain Macrophage Development. *Cell*. 2020;181(3):557-573.e18.
30. Hashimoto D, Chow A, Noizat C, Teo P, Beasley MB, Leboeuf M, et al. Tissue-resident macrophages self-maintain locally throughout adult life with minimal contribution from circulating monocytes. *Immunity*. 2013 Apr;38(4):792–804.
31. Bruttger J, Karram K, Wörtge S, Regen T, Marini F, Hoppmann N, et al. Genetic Cell Ablation Reveals Clusters of Local Self-Renewing Microglia in the Mammalian Central Nervous System. *Immunity*. 2015;43(1):92–106.
32. Huang Y, Xu Z, Xiong S, Sun F, Qin G, Hu G, et al. Repopulated microglia are solely derived from the proliferation of residual microglia after acute depletion. *Nature Neuroscience*. 2018;21(4):530–40.

33. Lawson LJ, Perry VH, Gordon S. Turnover of resident microglia in the normal adult mouse brain. *Neuroscience*. 1992;48(2):405–15.
34. Fügen P, Hefendehl JK, Veeraraghavalu K, Wendeln AC, Schlosser C, Obermüller U, et al. Microglia turnover with aging and in an Alzheimer's model via long-term in vivo single-cell imaging. *Nature Neuroscience*. 2017;20(10).
35. Askew K, Li K, Olmos-Alonso A, Garcia-Moreno F, Liang Y, Richardson P, et al. Coupled Proliferation and Apoptosis Maintain the Rapid Turnover of Microglia in the Adult Brain. *Cell Reports*. 2017;18(2):391–405.
36. Réu P, Khosravi A, Bernard S, Mold JE, Salehpour M, Alkass K, et al. The Lifespan and Turnover of Microglia in the Human Brain. *Cell Reports*. 2017;20(4):779–84.
37. Tay TL, Mai D, Dautzenberg J, Fernandez-Klett F, Lin G, Sagar, et al. A new fate mapping system reveals context-dependent random or clonal expansion of microglia. *Nat Neurosci*. 2017 Jun;20(6):793–803.
38. Zhan L, Krabbe G, Du F, Jones I, Reichert MC, Telpoukhovskaia M, et al. Proximal recolonization by self-renewing microglia re-establishes microglial homeostasis in the adult mouse brain. Vol. 17, *PLoS Biology*. 2019. 1–35 p.
39. Eyo UB, Mo M, Yi MH, Murugan M, Liu J, Yarlagadda R, et al. P2Y12R-Dependent Translocation Mechanisms Gate the Changing Microglial Landscape. *Cell Reports*. 2018;23(4):959–66.
40. Israël A. The IKK complex, a central regulator of NF-kappaB activation. *Cold Spring Harb Perspect Biol*. 2010;2(3):1–14.
41. Elmore MRPP, Najafi AR, Koike MA, Dagher NN, Spangenberg EE, Rice RA, et al. Colony-stimulating factor 1 receptor signaling is necessary for microglia viability, unmasking a microglia progenitor cell in the adult brain. *Neuron*. 2014;82(2):380–97.
42. Greter M, Lelios I, Pelczar P, Hoeffel G, Price J, Leboeuf M, et al. Stroma-Derived Interleukin-34 Controls the Development and Maintenance of Langerhans Cells and the Maintenance of Microglia. *Immunity*. 2009;130(29):9492–9.

43. Mendes MS, Le L, Atlas J, Brehm Z, Ladron-De-guevara A, Matei E, et al. The role of p2y12 in the kinetics of microglial self-renewal and maturation in the adult visual cortex in vivo. *Elife*. 2021;10:1–28.
44. Harley SBR, Willis EF, Shaikh SN, Blackmore DG, Sah P, Ruitenberg MJ, et al. Selective ablation of BDNF from microglia reveals novel roles in self-renewal and hippocampal neurogenesis. *Journal of Neuroscience*. 2021;41(19):4172–86.
45. Mendes MS, Majewska AK. An overview of microglia ontogeny and maturation in the homeostatic and pathological brain. *European Journal of Neuroscience*. 2021;53(11):3525–47.
46. Li Q, Barres BA. Microglia and macrophages in brain homeostasis and disease. *Nature Reviews Immunology* [Internet]. 2018;18(4):225–42. Available from: <http://dx.doi.org/10.1038/nri.2017.125>
47. Nimmerjahn A, Kirchhoff F, Helmchen F. Resting microglial cells are highly dynamic surveillants of brain parenchyma in vivo. *Science* (1979). 2005 May 27;308(5726):1314–8.
48. Davalos D, Grutzendler J, Yang G, Kim J v., Zuo Y, Jung S, et al. ATP mediates rapid microglial response to local brain injury in vivo. *Nature Neuroscience*. 2005;8(6):752–8.
49. Madry C, Kyrargyri V, Arancibia-Cárcamo IL, Jolivet R, Kohsaka S, Bryan RM, et al. Microglial Ramification, Surveillance, and Interleukin-1 β Release Are Regulated by the Two-Pore Domain K⁺ Channel THIK-1. *Neuron*. 2018 Mar 27;97(2):299-312.e6.
50. Kettenmann H, Kirchhoff F, Verkhratsky A. Microglia: New Roles for the Synaptic Stripper. *Neuron*. 2013;77(1):10–8.
51. Dudvarski Stankovic N, Teodorczyk M, Ploen R, Zipp F, Schmidt MHH. Microglia–blood vessel interactions: a double-edged sword in brain pathologies. *Acta Neuropathologica*. 2016;131(3):347–63.
52. Ousman SS, Kubes P. Immune surveillance in the central nervous system. *Nature Neuroscience*. 2012;15(8):1096–101.
53. Hefendehl JK, Neher JJ, Sühs RB, Kohsaka S, Skodras A, Jucker M. Homeostatic and injury-induced microglia behavior in the aging brain. *Aging Cell*. 2014;13(1):60–9.

54. Freeman SA, Grinstein S. Phagocytosis: Receptors, signal integration, and the cytoskeleton. *Immunological Reviews*. 2014;262(1):193–215.
55. Lemke G. Biology of the TAM receptors. *Cold Spring Harbor Perspectives in Biology*. 2013;5(11):1–17.
56. Fourgeaud L, Través PG, Tufail Y, Leal-bailey H, Erin D, Burrola PG, et al. TAM receptors regulate multiple features of microglial physiology. *Nature*. 2016;532(7598):240–4.
57. Li Q, Cheng Z, Zhou L, Darmanis S, Neff NF, Okamoto J, et al. Developmental Heterogeneity of Microglia and Brain Myeloid Cells Revealed by Deep Single-Cell RNA Sequencing. *Neuron* [Internet]. 2019;101(2):207–223.e10. Available from: <https://doi.org/10.1016/j.neuron.2018.12.006>
58. Guerreiro R, Ph D, Wojtas A, Bras J, Carrasquillo M, Rogaeva E, et al. TREM2 variants in Alzheimer’s Disease. *New England Journal of Medicine*. 2013;368(2):117–27.
59. Jonsson T, Stefansson H, Steinberg S, Jonsdottir I, Jonsson P v., Snaedal J, et al. Variant of TREM2 associated with the risk of AD. *New England Journal of Medicine*. 2013;368(2):107–16.
60. Takahashi K, Rochford CDP, Neumann H. Clearance of apoptotic neurons without inflammation by microglial triggering receptor expressed on myeloid cells-2. *Journal of Experimental Medicine*. 2005;201(4):647–57.
61. Hsieh CL, Koike M, Spusta SC, Niemi EC, Yenari M, Nakamura MC, et al. A role for TREM2 ligands in the phagocytosis of apoptotic neuronal cells by microglia. *Journal of Neurochemistry*. 2009;109(4):1144–56.
62. di Gioia M, Zanoni I. Toll-like receptor co-receptors as master regulators of the immune response. *Molecular Immunology* [Internet]. 2015;63(2):143–52. Available from: <http://dx.doi.org/10.1016/j.molimm.2014.05.008>
63. Fu R, Shen Q, Xu P, Luo JJ, Tang Y. Phagocytosis of microglia in the central nervous system diseases. *Molecular Neurobiology*. 2014;49(3):1422–34.
64. Fiebich BL, Ribeiro C, Batista A, Saliba SW. Role of Microglia TLRs in Neurodegeneration. 2018;12(October):1–10.
65. Ulvestad E. Reactive microglia in multiple sclerosis lesions have an increased expression of receptors for the Fc part of IgG. 1994;121:125–31.

66. Emmanuelle C, Alan H. Identification of Two Distinct Mechanisms of Phagocytosis Controlled by Different Rho GTPases. *Science* (1979) [Internet]. 1998 Nov 27;282(5394):1717–21. Available from: <https://doi.org/10.1126/science.282.5394.1717>
67. Schafer DP, Lehrman EK, Kautzman AG, Koyama R, Mardinly AR, Yamasaki R, et al. Microglia Sculpt Postnatal Neural Circuits in an Activity and Complement-Dependent Manner. *Neuron* [Internet]. 2012;74(4):691–705. Available from: <http://dx.doi.org/10.1016/j.neuron.2012.03.026>
68. Stevens B, Allen NJ, Vazquez LE, Howell GR, Christopherson KS, Nouri N, et al. The classical complement cascade mediates CNS synapse elimination. *Cell*. 2007 Dec;131(6):1164–78.
69. Hong S, Beja-glasser VF, Nfonoyim BM, Frouin A, Ramakrishnan S, Merry KM, et al. Complement and Microglia Mediate Early Synapse Loss in Alzheimer Mouse Models. *Science* (1979). 2016;352(6286):712–6.
70. Marín-Teva JL, Dusart I, Colin C, Gervais A, Van Rooijen N, Mallat M. Microglia Promote the Death of Developing Purkinje Cells. *Neuron*. 2004;41(4):535–47.
71. Cunningham CL, Martinez-Cerdeno V, Noctor SC. Microglia Regulate the Number of Neural Precursor Cells in the Developing Cerebral Cortex. *Journal of Neuroscience* [Internet]. 2013;33(10):4216–33. Available from: <http://www.jneurosci.org/cgi/doi/10.1523/JNEUROSCI.3441-12.2013>
72. Sierra A, Encinas JM, Deudero JJJP, Chancey JH, Enikolopov G, Overstreet-Wadiche LS, et al. Microglia shape adult hippocampal neurogenesis through apoptosis-coupled phagocytosis. *Cell Stem Cell*. 2010;7(4):483–95.
73. Ueno M, Fujita Y, Tanaka T, Nakamura Y, Kikuta J, Ishii M, et al. Layer v cortical neurons require microglial support for survival during postnatal development. *Nature Neuroscience*. 2013;16(5):543–51.
74. Sumi T, Harada K. Mechanism underlying hippocampal long-term potentiation and depression based on competition between endocytosis and exocytosis of AMPA receptors. *Scientific Reports* [Internet]. 2020;10(1):1–14. Available from: <https://doi.org/10.1038/s41598-020-71528-3>
75. Parkhurst CNN, Yang G, Ninan I, Savas JNN, Yates III JR, Lafaille JJJ, et al. Microglia Promote Learning-Dependent Synapse Formation through Brain-

- Derived Neurotrophic Factor. *Cell* [Internet]. 2013 Mar 23;155(7):1596–609. Available from: <http://dx.doi.org/10.1016/j.cell.2013.11.030>
76. Beattie EC, Stellwagen D, Morishita W, Bresnahan JC, Byeong KH, Von Zastrow M, et al. Control of synaptic strength by glial TNF α . *Science* (1979). 2002;
 77. Stellwagen D, Beattie EC, Seo JY, Malenka RC. Differential regulation of AMPA receptor and GABA receptor trafficking by tumor necrosis factor- α . *Journal of Neuroscience*. 2005;
 78. Rogers JT, Morganti JM, Bachstetter AD, Hudson CE, Peters MM, Grimmig BA, et al. CX3CR1 deficiency leads to impairment of hippocampal cognitive function and synaptic plasticity. *Journal of Neuroscience*. 2011;31(45):16241–50.
 79. Costello DA, Lyons A, Denieffe S, Browne TC, Cox FF, Lynch MA. Long term potentiation is impaired in membrane glycoprotein CD200-deficient mice: A role for toll-like receptor activation. *Journal of Biological Chemistry*. 2011;286(40):34722–32.
 80. Trapp BD, Wujek JR, Criste GA, Jalabi W, Yin X, Kidd GJ, et al. Evidence for Synaptic Stripping by Cortical Microglia. *GLIA*. 2007;55:360–8.
 81. Wake H, Moorhouse AJ, Jinno S, Kohsaka S, Nabekura J. Resting Microglia Directly Monitor the Functional State of Synapses In Vivo and Determine the Fate of Ischemic Terminals. *Journal of Neuroscience*. 2009;29(13):3974–80.
 82. Tremblay MÈ, Lowery RL, Majewska AK. Microglial Interactions with Synapses Are Modulated by Visual Experience. *PLOS Biology*. 2010 Nov 2;8(11):e1000527.
 83. Squarzoni P, Oller G, Hoeffel G, Pont-Lezica L, Rostaing P, Low D, et al. Microglia Modulate Wiring of the Embryonic Forebrain. *Cell Reports*. 2014;8(5):1271–9.
 84. Paolicelli RC, Bolasco G, Pagani F, Maggi L, Scianni M, Panzanelli P, et al. Synaptic pruning by microglia is necessary for normal brain development. *Science* (1979). 2011;333(6048):1456–8.
 85. Filipello F, Morini R, Corradini I, Zerbi V, Canzi A, Michalski B, et al. The Microglial Innate Immune Receptor TREM2 Is Required for Synapse Elimination and Normal Brain Connectivity. *Immunity* [Internet].

2018;48(5):979-991.e8. Available from:
<https://doi.org/10.1016/j.immuni.2018.04.016>

86. Lehrman EK, Wilton DK, Litvina EY, Welsh CA, Chang ST, Frouin A, et al. CD47 Protects Synapses from Excess Microglia-Mediated Pruning during Development. *Neuron* [Internet]. 2018;100(1):120-134.e6. Available from: <https://doi.org/10.1016/j.neuron.2018.09.017>
87. Pont-Lezica L, Beumer W, Colasse S, Drexhage H, Versnel M, Bessis A. Microglia shape corpus callosum axon tract fasciculation: Functional impact of prenatal inflammation. *European Journal of Neuroscience*. 2014;39(10):1551–7.
88. Kitayama M, Ueno M, Itakura T, Yamashita T. Activated microglia inhibit axonal growth through RGMa. *PLoS ONE*. 2011;6(9):1–9.
89. Gosselin D, Skola D, Coufal NG, Holtman IR, Schlachetzki JCM, Sajti E, et al. An environment-dependent transcriptional network specifies human microglia identity David. *Science* (1979). 2017;356(6344):1–28.
90. Bohlen CJ, Bennett FC, Tucker AF, Collins HY, Mulinyawe SB, Barres BA. Diverse Requirements for Microglial Survival, Specification, and Function Revealed by Defined-Medium Cultures. *Neuron* [Internet]. 2017;94(4):759-773.e8. Available from: <http://dx.doi.org/10.1016/j.neuron.2017.04.043>
91. Neumann H. Control of glial immune function by neurons. *Glia*. 2001;36(2):191–9.
92. Buttgerit A, Lelios I, Yu X, Vrohling M, Krakoski NR, Gautier EL, et al. Sall1 is a transcriptional regulator defining microglia identity and function. *Nature Immunology*. 2016 Dec;17(12):1397–406.
93. Deczkowska A, Matcovitch-Natan O, Tsitsou-Kampeli A, Ben-Hamo S, Dvir-Szternfeld R, Spinrad A, et al. Mef2C restrains microglial inflammatory response and is lost in brain ageing in an IFN-I-dependent manner. *Nature Communications*. 2017;8(1).
94. Hoek RH, Ruuls SR, Murphy CA, Wright GJ, Goddard R, Zurawski SM, et al. Down-regulation of the macrophage lineage through interaction with OX2 (CD200). *Science* (1979). 2000;

95. Zujovic V, Benavides J, Vigé X, Carter C, Taupin V. Fractalkine modulates TNF- α secretion and neurotoxicity induced by microglial activation. *Glia*. 2000;29(4):305–15.
96. Koning N, Swaab DF, Hoek RM, Huitinga I. Distribution of the immune inhibitory molecules CD200 and CD200R in the normal central nervous system and multiple sclerosis lesions suggests neuron-glia and glia-glia interactions. *Journal of Neuropathology and Experimental Neurology*. 2009;68(2):159–67.
97. Barclay AN, Wright GJ, Brooke G, Brown MH. CD200 and membrane protein interactions in the control of myeloid cells. *Trends in Immunology*. 2002;23(6):285–90.
98. Frank MG, Barrientos RM, Biedenkapp JC, Rudy JW, Watkins LR, Maier SF. mRNA up-regulation of MHC II and pivotal pro-inflammatory genes in normal brain aging. *Neurobiology of Aging*. 2006;27(5):717–22.
99. Wang XJ, Zhang S, Yan ZQ, Zhao YX, Zhou HY, Wang Y, et al. Impaired CD200-CD200R-mediated microglia silencing enhances midbrain dopaminergic neurodegeneration: Roles of aging, superoxide, NADPH oxidase, and p38 MAPK. *Free Radical Biology and Medicine* [Internet]. 2011;50(9):1094–106. Available from: <http://dx.doi.org/10.1016/j.freeradbiomed.2011.01.032>
100. Walker DG, Dalsing-Hernandez JE, Campbell NA, Lue LF. Decreased expression of CD200 and CD200 receptor in Alzheimer's disease: A potential mechanism leading to chronic inflammation. *Experimental Neurology* [Internet]. 2009;215(1):5–19. Available from: <http://dx.doi.org/10.1016/j.expneurol.2008.09.003>
101. Lyons A, McQuillan K, Deighan BF, O'Reilly JA, Downer EJ, Murphy AC, et al. Decreased neuronal CD200 expression in IL-4-deficient mice results in increased neuroinflammation in response to lipopolysaccharide. *Brain, Behavior, and Immunity* [Internet]. 2009;23(7):1020–7. Available from: <http://dx.doi.org/10.1016/j.bbi.2009.05.060>
102. Cox FF, Carney D, Miller AM, Lynch MA. CD200 fusion protein decreases microglial activation in the hippocampus of aged rats. *Brain, Behavior, and Immunity* [Internet]. 2012;26(5):789–96. Available from: <http://dx.doi.org/10.1016/j.bbi.2011.10.004>

103. Lyons A, Lynch AM, Downer EJ, Hanley R, O'Sullivan JB, Smith A, et al. Fractalkine-induced activation of the phosphatidylinositol-3 kinase pathway attenuates microglial activation in vivo and in vitro. *Journal of Neurochemistry*. 2009;110(5):1547–56.
104. Fenn AM, Smith KM, Lovett-Racke AE, Guerau-de-Arellano M, Whitacre CC, Godbout JP. Increased micro-RNA 29b in the aged brain correlates with the reduction of insulin-like growth factor-1 and fractalkine ligand. *Neurobiology of Aging*. 2013;34(12):2748–58.
105. Duan RS, Yang X, Chen ZG, Lu MO, Morris C, Winblad B, et al. Decreased fractalkine and increased IP-10 expression in aged brain of APPswe transgenic mice. *Neurochemical Research*. 2008;33(6):1085–9.
106. Cribbs DH, Berchtold NC, Perreau V, Coleman PD, Rogers J, Tenner AJ, et al. Extensive innate immune gene activation accompanies brain aging, increasing vulnerability to cognitive decline and neurodegeneration: A microarray study. *Journal of Neuroinflammation*. 2012;9:1–18.
107. Cardona AE, Pioro EP, Sasse ME, Kostenko V, Cardona SM, Dijkstra IM, et al. Control of microglial neurotoxicity by the fractalkine receptor. *Nature Neuroscience*. 2006;9(7):917–24.
108. Paglinawan R, Malipiero U, Schlapbach R, Frei K, Reith W, Fontana A. TGF β Directs Gene Expression of Activated Microglia to an Anti-Inflammatory Phenotype Strongly Focusing on Chemokine Genes and Cell Migratory Genes. *Glia*. 2003;44(3):219–31.
109. Butovsky O, Jedrychowski MP, Moore CS, Cialic R, Lanser AJ, Gabriely G, et al. Identification of a unique TGF- β -dependent molecular and functional signature in microglia. *Nature Neuroscience* [Internet]. 2014 Jan;17(1):131–43. Available from: <http://www.nature.com/doi/10.1038/nn.3599>
110. Stence N, Waite M, Dailey ME. Dynamics of microglial activation: a confocal time-lapse analysis in hippocampal slices. *Glia*. 2001 Mar;33(3):256–66.
111. Jurga AM, Paleczna M, Kuter KZ. Overview of General and Discriminating Markers of Differential Microglia Phenotypes. *Frontiers in Cellular Neuroscience*. 2020;14(August):1–18.
112. Ransohoff RM. A polarizing question: do M1 and M2 microglia exist? *Nature Neuroscience* [Internet]. 2016;19(8):987–91. Available from: <http://www.nature.com/doi/10.1038/nn.4338>

113. Wes PD, Holtman IR, Boddeke EWGM, Möller T, Eggen BJJ. Next generation transcriptomics and genomics elucidate biological complexity of microglia in health and disease. *Glia*. 2016;64(2):197–213.
114. Butovsky O, Jedrychowski MP, Moore CS, Cialic R, Lanser AJ, Gabriely G, et al. Identification of a unique TGF- β -dependent molecular and functional signature in microglia. *Nature Neuroscience* [Internet]. 2014;17(1):131–43. Available from: <http://www.nature.com/doi/10.1038/nn.3599>
115. Zhang Y, Chen K, Sloan SA, Bennett ML, Scholze AR, O’Keeffe S, et al. An RNA-sequencing transcriptome and splicing database of glia, neurons, and vascular cells of the cerebral cortex. *Journal of Neuroscience*. 2014;34(36):11929–47.
116. Hickman SE, Kingery ND, Ohsumi TK, Borowsky ML, Wang LC, Means TK, et al. The microglial sensome revealed by direct RNA sequencing. *Nature Neuroscience* [Internet]. 2013;16(12):1896–905. Available from: <http://dx.doi.org/10.1038/nn.3554>
117. Hirbec H, Marmai C, Duroux-Richard I, Roubert C, Esclangon A, Croze S, et al. The microglial reaction signature revealed by RNAseq from individual mice. *Glia*. 2018;66(5):971–86.
118. Rodrigues RJ, Tomé AR, Cunha RA. ATP as a multi-target danger signal in the brain. *Frontiers in Neuroscience*. 2015;9(APR):1–11.
119. Fields RD, Stevens-graham B. New Insights into Neuron-Glia Communication. 2002;298(October):556–63.
120. Haynes SE, Hollopeter G, Yang G, Kurpius D, Dailey ME, Gan WB, et al. The P2Y₁₂ receptor regulates microglial activation by extracellular nucleotides. *Nature Neuroscience*. 2006;9(12):1512–9.
121. Tvrdik P, Kalani MYS. In Vivo Imaging of Microglial Calcium Signaling in Brain Inflammation and Injury. *International Journal of Molecular Sciences*. 2017;18:2366.
122. Siddiqui TA, Lively S, Vincent C, Schlichter LC. Regulation of podosome formation , microglial migration and invasion by Ca²⁺ -signaling molecules expressed in podosomes. 2012;1–16.

123. Béchade C, Pascual O, Triller A, Bessis A. Nitric oxide regulates astrocyte maturation in the hippocampus: Involvement of NOS2. *Molecular and Cellular Neuroscience*. 2011;
124. Nakanishi M, Niidome T, Matsuda S, Akaike A, Kihara T, Sugimoto H. Microglia-derived interleukin-6 and leukaemia inhibitory factor promote astrocytic differentiation of neural stem/progenitor cells. *European Journal of Neuroscience*. 2007;
125. Giulian D, Young DG, Woodward J, Brown DC, Lachman LB. Interleukin-1 is an astroglial growth factor in the developing brain. *Journal of Neuroscience*. 1988;
126. Liddelow SA, Guttenplan KA, Clarke LE, Bennett FC, Bohlen CJ, Schirmer L, et al. Neurotoxic reactive astrocytes are induced by activated microglia. *Nature* [Internet]. 2017;541(7638):481–7. Available from: <http://dx.doi.org/10.1038/nature21029>
127. Pascual O, ben Achour S, Rostaing P, Triller A, Bessis A, Achour S ben, et al. Microglia activation triggers astrocyte-mediated modulation of excitatory neurotransmission. *Proc Natl Acad Sci U S A*. 2012 Jan;109(4):E197-205.
128. Wang Y, Qin ZH. Molecular and cellular mechanisms of excitotoxic neuronal death. *Apoptosis*. 2010;15(11):1382–402.
129. Rouach N, Avignone E, Mème W, Koulakoff A, Venance L, Blomstrand F, et al. Gap junctions and connexin expression in the normal and pathological central nervous system. *Biology of the Cell*. 2002.
130. Matejuk A, Ransohoff RM. Crosstalk Between Astrocytes and Microglia: An Overview. *Frontiers in Immunology*. 2020;11(July):1–11.
131. Vainchtein ID, Chin G, Cho FS, Kelley KW, Miller JG, Chien EC, et al. Astrocyte-derived interleukine-33 promotes microglial synapse engulfment adn neural circuit development. *Science* (1979) [Internet]. 2018;359(6381):1269–73. Available from: <http://science.sciencemag.org/content/early/2018/01/31/science.aal3589>
132. Hagemeyer N, Hanft KM, Akritidou MA, Unger N, Park ES, Stanley ER, et al. Microglia contribute to normal myelinogenesis and to oligodendrocyte progenitor maintenance during adulthood. *Acta Neuropathol*. 2017 Sep;134(3):441–58.

133. Wlodarczyk A, Holtman IR, Krueger M, Yogev N, Bruttger J, Khorrooshi R, et al. A novel microglial subset plays a key role in myelinogenesis in developing brain. *The EMBO Journal* [Internet]. 2017 Nov 15;36(22):3292–308. Available from: <http://www.ncbi.nlm.nih.gov/pmc/articles/PMC5686552/>
134. Lawson LJJ, Perry VHH, Dri P, Gordon S. Heterogeneity in the distribution and morphology of microglia in the normal adult mouse brain. *Neuroscience*. 1990;39(1):151–70.
135. Verdonk F, Roux P, Flamant P, Fiette L, Bozza FA, Simard S, et al. Phenotypic clustering: A novel method for microglial morphology analysis. *Journal of Neuroinflammation*. 2016;13(1).
136. Ribeiro Xavier AL, Kress BT, Goldman SA, De Lacerda Menezes JR, Nedergaard M. A distinct population of microglia supports adult neurogenesis in the subventricular zone. *Journal of Neuroscience*. 2015;35(34):11848–61.
137. Takagi S, Furube E, Nakano Y, Morita M, Miyata S. Microglia are continuously activated in the circumventricular organs of mouse brain. *Journal of Neuroimmunology*. 2019;331(October):74–86.
138. Stowell RD, Wong EL, Batchelor HN, Mendes MS, Lamantia CE, Whitelaw BS, et al. Cerebellar microglia are dynamically unique and survey Purkinje neurons in vivo. *Dev Neurobiol*. 2018;78(6):627–44.
139. de Haas AH, Boddeke HWGM, Biber K. Region-specific expression of immunoregulatory proteins on microglia in the healthy CNS. *Glia*. 2008;56(8):888–94.
140. Sharaf A, Krieglstein K, Spittau B. Distribution of microglia in the postnatal murine nigrostriatal system. *Cell and Tissue Research*. 2013;351(3):373–82.
141. Yang TT, Lin C, Hsu CT, Wang TF, Ke FY, Kuo YM. Differential distribution and activation of microglia in the brain of male C57BL/6J mice. *Brain Structure and Function*. 2013;218(4):1051–60.
142. Grabert K, Michael T, Karavolos MH, Clohisey S, Baillie JK, Stevens MP, et al. Microglial brain region-dependent diversity and selective regional sensitivities to aging. *Nature Neuroscience* [Internet]. 2016;19(3):504–16. Available from: <http://www.nature.com/doifinder/10.1038/nn.4222>

143. De Biase LM, Schuebel KE, Fusfeld ZH, Jair K, Hawes IA, Cimbri R, et al. Local Cues Establish and Maintain Region-Specific Phenotypes of Basal Ganglia Microglia. *Neuron*. 2017;95(2):341-356.e6.
144. Erö C, Gewaltig MO, Keller D, Markram H. A cell atlas for the mouse brain. *Frontiers in Neuroinformatics*. 2018;12(November):1–16.
145. Masuda T, Sankowski R, Staszewski O, Böttcher C, Amann L, Sagar, et al. Spatial and temporal heterogeneity of mouse and human microglia at single-cell resolution. *Nature*. 2019;566(7744):388–92.
146. Hammond TR, Dufort C, Dissing-Olesen L, Giera S, Young A, Wysoker A, et al. Single-Cell RNA Sequencing of Microglia throughout the Mouse Lifespan and in the Injured Brain Reveals Complex Cell-State Changes. *Immunity* [Internet]. 2019;50(1):253-271.e6. Available from: <https://doi.org/10.1016/j.immuni.2018.11.004>
147. Jordão MJC, Sankowski R, Brendecke SM, Sagar, Locatelli G, Tai YH, et al. Single-cell profiling identifies myeloid cell subsets with distinct fates during neuroinflammation. *Science (1979)*. 2019;363(6425).
148. Ayata P, Badimon A, Strasburger HJ, Duff MK, Montgomery SE, Loh YHE, et al. Epigenetic regulation of brain region-specific microglia clearance activity. *Nature Neuroscience* [Internet]. 2018;21(8):1049–60. Available from: <http://dx.doi.org/10.1038/s41593-018-0192-3>
149. Izzy S, Liu Q, Fang Z, Lule S, Wu L, Chung JY, et al. Time-Dependent Changes in Microglia Transcriptional Networks Following Traumatic Brain Injury. *Frontiers in Cellular Neuroscience*. 2019;13(August):1–16.
150. Wong WT. Microglial aging in the healthy CNS: Phenotypes, drivers, and rejuvenation. *Frontiers in Cellular Neuroscience*. 2013;7(MAR):1–13.
151. Hefendehl JK, Neher JJ, Sühs RB, Kohsaka S, Skodras A, Jucker M. Homeostatic and injury-induced microglia behavior in the aging brain. *Aging Cell*. 2014;13(1):60–9.
152. Hanamsagara R, Bilbo SD. Sex differences in neurodevelopmental and neurodegenerative disorders: Focus on microglial function and neuroinflammation during development. *J Steroid Biochem Mol Biol*. 2016;160:127–33.

153. Han J, Fan Y, Zhou K, Blomgren K, Harris RA. Uncovering sex differences of rodent microglia. *Journal of Neuroinflammation*. 2021;18(1):1–11.
154. Lars H. Nelson, Saulsbery AI, Lenz KM. Small cells with big implications: Microglia and sex differences in brain development, plasticity and behavioral health. *Prog Neurobiol*. 2019;176:103–19.
155. Guneykaya D, Ivanov A, Hernandez DP, Haage V, Wojtas B, Meyer N, et al. Transcriptional and Translational Differences of Microglia from Male and Female Brains. *Cell Reports*. 2018;24(10):2773-2783.e6.
156. Guillot-Sestier MV, Araiz AR, Mela V, Gaban AS, O'Neill E, Joshi L, et al. Microglial metabolism is a pivotal factor in sexual dimorphism in Alzheimer's disease. *Communications Biology* [Internet]. 2021;4(1). Available from: <http://dx.doi.org/10.1038/s42003-021-02259-y>
157. Hanamsagar R, Alter MD, Block CS, Sullivan H, Bolton JL, Bilbo SD. Generation of a microglial developmental index in mice and in humans reveals a sex difference in maturation and immune reactivity. *Glia*. 2017;65(9):460.
158. Weinhard L, Di Bartolomei G, Bolasco G, Machado P, Schieber NL, Neniskyte U, et al. Microglia remodel synapses by presynaptic trogocytosis and spine head filopodia induction. *Nature Communications*. 2018;9(1).
159. Ma L, Sun P, Zhang JC, Zhang Q, Yao SL. Proinflammatory effects of S100A8/A9 via TLR4 and RAGE signaling pathways in BV-2 microglial cells. *International Journal of Molecular Medicine*. 2017;40(1):31–8.
160. Thion MS, Low D, Silvin A, Pettersson S, Ginhoux F, Garel S, et al. Microbiome Influences Prenatal and Adult Microglia in a Sex-Specific Manner Article Microbiome Influences Prenatal and Adult Microglia in a Sex-Specific Manner. *Cell* [Internet]. 2018;172(3):500-507.e16. Available from: <https://doi.org/10.1016/j.cell.2017.11.042>
161. Villa A, Gelosa P, Castiglioni L, Cimino M, Rizzi N, Pepe G, et al. Sex-Specific Features of Microglia from Adult Mice. *Cell Reports*. 2018;23(12):3501–11.
162. Alzheimer's Disease International. World Alzheimer Report 2019. World Alzheimer Report 2019. 2019;100–1.

163. Stelzmann RA, Norman Schnitzlein H, Reed Murtagh F. An english translation of alzheimer's 1907 paper, "über eine eigenartige erkankung der hirnrinde." *Clinical Anatomy*. 1995;8(6):429–31.
164. Leng F, Edison P. Neuroinflammation and microglial activation in Alzheimer disease: where do we go from here? *Nature Reviews Neurology* [Internet]. 2021;17(3):157–72. Available from: <http://dx.doi.org/10.1038/s41582-020-00435-y>
165. Breijyeh Z, Karaman R. Comprehensive Review on Alzheimer's Disease: Causes and Treatment. *Molecules*. 2020;25(24):5789.
166. Nisticò R, Borg JJ. Aducanumab for Alzheimer's disease: A regulatory perspective. *Pharmacological Research*. 2021;171(June):2–4.
167. Walsh S, Merrick R, Milne R, Brayne C. Aducanumab for Alzheimer's disease? *The BMJ*. 2021;374:10–1.
168. Thinakaran G, Koo EH. Amyloid precursor protein trafficking, processing, and function. *Journal of Biological Chemistry*. 2008;283(44):29615–9.
169. Selkoe DJ. Alzheimer's disease: Genes, proteins, and therapy. *PHYSIOLOGICAL REVIEWS*. 2001;81(2).
170. van Helmond Z, Miners JS, Kehoe PG, Love S. Oligomeric A β in Alzheimer's disease: Relationship to plaque and tangle pathology, apoe genotype and cerebral amyloid angiopathy. *Brain Pathology*. 2010;20(2):468–80.
171. Kaye R, Lasagna-Reeves CA. Molecular mechanisms of amyloid oligomers toxicity. *Journal of Alzheimer's Disease*. 2013;33(SUPPL. 1).
172. Selkoe DJ. Soluble Oligomers of the Amyloid β -Protein Impair Synaptic.pdf. *Behavioural brain research*. 2008;192(1):106–13.
173. Hardy J, Selkoe DJ. The amyloid hypothesis of Alzheimer's disease: Progress and problems on the road to therapeutics. *Science* (1979). 2002;297(5580):353–6.
174. Wang Y, Mandelkow E. Tau in physiology and pathology. *Nature Reviews Neuroscience*. 2016;17(1):5–21.
175. Kametani F, Hasegawa M. Reconsideration of amyloid hypothesis and tau hypothesis in Alzheimer's disease. *Frontiers in Neuroscience*. 2018;12(JAN).

176. Gloria L, Nicholas C, Marc K. The Primary Structure and Heterogeneity of Tau Protein from Mouse Brain. *Science* (1979) [Internet]. 1988 Jan 15;239(4837):285–8. Available from: <https://doi.org/10.1126/science.3122323>
177. Barron MR, Gartlon J, Dawson LA, Atkinson PJ, Pardon MC. Increasing Tau 4R Tau Levels Exacerbates Hippocampal Tau Hyperphosphorylation in the hTau Model of Tauopathy but Also Tau Dephosphorylation Following Acute Systemic Inflammation. *Frontiers in Immunology*. 2020;11(March).
178. Fu H, Rodriguez GA, Herman M, Emrani S, Nahmani E, Barrett G, et al. Tau Pathology Induces Excitatory Neuron Loss, Grid Cell Dysfunction, and Spatial Memory Deficits Reminiscent of Early Alzheimer’s Disease. *Neuron* [Internet]. 2017;93(3):533-541.e5. Available from: <http://dx.doi.org/10.1016/j.neuron.2016.12.023>
179. Fu H, Hussaini SA, Wegmann S, Profaci C, Daniels JD, Herman M, et al. 3D Visualization of the temporal and spatial spread of tau pathology reveals extensive sites of tau accumulation associated with neuronal loss and recognition memory deficit in aged tau transgenic mice. *PLoS ONE*. 2016;11(7):1–20.
180. ROSSOR MN, NEWMAN S, FRACKOWIAK RSJ, LANTOS P, KENNEDY AM. Alzheimer’s Disease Families with Amyloid Precursor Protein Mutations. *Ann N Y Acad Sci*. 1993;695(1):198–202.
181. Sherrington R, Leresque G, Ikeda M, Ch H, Lin C, Holman K, et al. Cloning of a gene bearing missense mutations in early-onset familial Alzheimer’s disease. *Nature*. 1995;375(June):754–60.
182. Ephrat LL, Wilma W, Parvoneh P, M. RD, Junko O, H. PW, et al. Candidate Gene for the Chromosome 1 Familial Alzheimer’s Disease Locus. *Science* (1979) [Internet]. 1995 Aug 18;269(5226):973–7. Available from: <https://doi.org/10.1126/science.7638622>
183. Svedružić ŽM, Popović K, Smoljan I, Šendula-Jengiđ V. Modulation of γ -secretase activity by multiple enzyme-substrate interactions: Implications in pathogenesis of alzheimer’s disease. *PLoS ONE*. 2012;7(3).
184. John H, J. SD. The Amyloid Hypothesis of Alzheimer’s Disease: Progress and Problems on the Road to Therapeutics. *Science* (1979) [Internet]. 2002 Jul 19;297(5580):353–6. Available from: <https://doi.org/10.1126/science.1072994>

185. Kim J, Basak JM, Holtzman DM. The Role of Apolipoprotein E in Alzheimer's Disease. *Neuron*. 2009;63(3):287–303.
186. Slioter AJC, Cruts M, Kalmijn S, Hofman A, Breteler MMB, van Broeckhoven C, et al. Risk estimates of dementia by apolipoprotein E genotypes from a population-based incidence study: The Rotterdam study. *Archives of Neurology*. 1998;55(7):964–8.
187. W. MR. Apolipoprotein E: Cholesterol Transport Protein with Expanding Role in Cell Biology. *Science* (1979) [Internet]. 1988 Apr 29;240(4852):622–30. Available from: <https://doi.org/10.1126/science.3283935>
188. Krasemann S, Madore C, Cialic R, Baufeld C, Calcagno N, el Fatimy R, et al. The TREM2-APOE Pathway Drives the Transcriptional Phenotype of Dysfunctional Microglia in Neurodegenerative Diseases. *Immunity* [Internet]. 2017;47(3):566-581.e9. Available from: <http://dx.doi.org/10.1016/j.immuni.2017.08.008>
189. Andrews SJ, Fulton-Howard B, Goate A. Interpretation of risk loci from genome-wide association studies of Alzheimer's disease. *Lancet Neurol*. 2020 Apr;19(4):326–35.
190. Zou H, Wu LX, Tan L, Shang FF, Zhou HH. Significance of Single-Nucleotide Variants in Long Intergenic Non-protein Coding RNAs. *Frontiers in Cell and Developmental Biology*. 2020;8(May):1–14.
191. Novikova G, Andrews SJ, Renton AE, Marcora E. Beyond association: successes and challenges in linking non-coding genetic variation to functional consequences that modulate Alzheimer's disease risk. *Molecular Neurodegeneration*. 2021;16(1):1–13.
192. Sims R, van der Lee SJ, Naj AC, Bellenguez C, Badarinarayan N, Jakobsdottir J, et al. Rare coding variants in *PLCG2*, *ABI3*, and *TREM2* implicate microglial-mediated innate immunity in Alzheimer's disease. *Nature Genetics*. 2017;49:1373–1384.
193. Khani M, Gibbons E, Bras J, Guerreiro R. Challenge accepted: uncovering the role of rare genetic variants in Alzheimer's disease. *Molecular Neurodegeneration*. 2022;17(1):1–15.
194. Harold D, Abraham R, Hollingworth P, Sims R, Gerrish A, Hamshere ML, et al. Genome-wide association study identifies variants at *CLU* and *PICALM* associated with Alzheimer's disease. *Nat Genet*. 2009 Oct;41(10):1088–93.

195. Lambert JC, Heath S, Even G, Campion D, Sleegers K, Hiltunen M, et al. Genome-wide association study identifies variants at CLU and CR1 associated with Alzheimer's disease. *Nat Genet.* 2009 Oct;41(10):1094–9.
196. Iida K, Mornaghi R, Nussenzweig V. Complement receptor (CR1) deficiency in erythrocytes from patients with systemic lupus erythematosus. *Journal of Experimental Medicine.* 1982;155(5):1427–38.
197. Klickstein LB, Barbashov SF, Liu T, Jack RM, Nicholson-Weller A. Complement receptor type 1 (CR1, CD35) is a receptor for C1q. *Immunity.* 1997;7(3):345–55.
198. Crehan H, Hardy J, Pocock J. Blockage of CR1 prevents activation of rodent microglia. *Neurobiology of Disease* [Internet]. 2013;54:139–49. Available from: <http://dx.doi.org/10.1016/j.nbd.2013.02.003>
199. Velazquez P, Cribbs DH, Poulos TL, Tenner AJ. Aspartate residue 7 in amyloid B-protein is critical for classical complement pathway activation: Implications for Alzheimer's disease pathogenesis. *Nat Med.* 1997;3(1).
200. Cribbs DH, Velazquez P, Soreghan B, Glabe CG, Tenner AJ. Complement activation by cross-linked truncated and chimeric full-length β -amyloid. *NeuroReport* [Internet]. 1997;8(16). Available from: https://journals.lww.com/neuroreport/Fulltext/1997/11100/Complement_activation_by_cross_linked_truncated.9.aspx
201. Karch CM, Jeng AT, Nowotny P, Cady J, Cruchaga C, Goate AM. Expression of Novel Alzheimer's Disease Risk Genes in Control and Alzheimer's Disease Brains. *PLoS ONE.* 2012;7(11).
202. Huang K lin, Marcora E, Pimenova AA, Narzo AF di, Kapoor M, Jin SC, et al. A common haplotype lowers PU.1 expression in myeloid cells and delays onset of Alzheimer's disease. *Nat Neurosci.* 2017;20(8):1052–61.
203. Forabosco P, Ramasamy A, Trabzuni D, Walker R, Smith C, Bras J, et al. Insights into TREM2 biology by network analysis of human brain gene expression data. *Neurobiol Aging.* 2013 Dec;34(12):2699–714.
204. Lue LF, Schmitz C, Walker DG. What happens to microglial TREM2 in Alzheimer's disease: Immunoregulatory turned into immunopathogenic? *Neuroscience.* 2015 Aug;302:138–50.

205. Ma L, Allen M, Sakae N, Ertekin-Taner N, Graff-Radford NR, Dickson DW, et al. Expression and processing analyses of wild type and p.R47H TREM2 variant in Alzheimer's disease brains. *Molecular Neurodegeneration* [Internet]. 2016;11(1):72. Available from: <https://doi.org/10.1186/s13024-016-0137-9>
206. Kleinberger G, Yamanishi Y, Suárez-Calvet M, Czirr E, Lohmann E, Cuyvers E, et al. TREM2 mutations implicated in neurodegeneration impair cell surface transport and phagocytosis. *Science Translational Medicine* [Internet]. 2014;6(243):243ra86-243ra86. Available from: <https://www.science.org/doi/abs/10.1126/scitranslmed.3009093>
207. Kober DL, Alexander-Brett JM, Karch CM, Cruchaga C, Colonna M, Holtzman MJ, et al. Neurodegenerative disease mutations in TREM2 reveal a functional surface and distinct loss-of-function mechanisms. *Elife*. 2016 Dec;5.
208. Pillai S, Netravali IA, Cariappa A, Mattoo H. Siglecs and immune regulation. *Annu Rev Immunol* [Internet]. 2012/01/03. 2012;30:357–92. Available from: <https://pubmed.ncbi.nlm.nih.gov/22224769>
209. Bhattacharjee A, Rodrigues E, Jung J, Luzentales-Simpson M, Enterina JR, Galleguillos D, et al. Repression of phagocytosis by human CD33 is not conserved with mouse CD33. *Communications Biology* [Internet]. 2019;2(1):1–13. Available from: <http://dx.doi.org/10.1038/s42003-019-0698-6>
210. Naj AC, Jun G, Beecham GW, Wang LS, Vardarajan BN, Buross J, et al. Common variants at MS4A4/MS4A6E, CD2AP, CD33 and EPHA1 are associated with late-onset Alzheimer's disease. *Nat Genet*. 2011 May;43(5):436–41.
211. Zhao L. CD33 in Alzheimer's disease - Biology, pathogenesis, and therapeutics: A mini-review. *Gerontology*. 2019;65(4):323–31.
212. Escott-Price V, Sims R, Bannister C, Harold D, Vronskaya M, Majounie E, et al. Common polygenic variation enhances risk prediction for Alzheimer's disease. *Brain*. 2015 Dec;138(Pt 12):3673–84.
213. Euesden J, Lewis CM, O'Reilly PF. PRSice: Polygenic Risk Score software. *Bioinformatics*. 2015 May;31(9):1466–8.
214. Sims R, Hill M, Williams J. The multiplex model of the genetics of Alzheimer's disease. *Nature Neuroscience* [Internet]. 2020;23(3):311–22. Available from: <https://doi.org/10.1038/s41593-020-0599-5>

215. Bellenguez C, Küçükali F, Jansen IE, Kleindam L, Moreno-Grau S, Amin N, et al. New insights into the genetic etiology of Alzheimer's disease and related dementias. *Nat Genet.* 2022;54(4):412–36.
216. McGeer PL, Itagaki S, Tago H, McGeer EG. Reactive microglia in patients with senile dementia of the Alzheimer type are positive for the histocompatibility glycoprotein HLA-DR. *Neuroscience Letters.* 1987;
217. Itagaki S, McGeer PL, Akiyama H, Zhu S, Selkoe D. Relationship of microglia and astrocytes to amyloid deposits of Alzheimer disease. *Journal of Neuroimmunology* [Internet]. 1989;24(3):173–82. Available from: <http://www.sciencedirect.com/science/article/pii/016557288990115X>
218. Perlmutter LS, Barron E, Chui HC. Morphologic association between microglia and senile plaque amyloid in Alzheimer's disease. *Neuroscience Letters.* 1990;
219. Frautschy SA, Yang F, Irrizarry M, Hyman B, Saido TC, Hsiao K, et al. Microglial response to amyloid plaques in APPsw transgenic mice. *American Journal of Pathology.* 1998;
220. Heneka MT, Kummer MP, Stutz A, Delekate A, Schwartz S, Vieira-Saecker A, et al. NLRP3 is activated in Alzheimer's disease and contributes to pathology in APP/PS1 mice. *Nature.* 2013;493(7434):674–8.
221. Lambert JC, Ibrahim-Verbaas CA, Harold D, Naj AC, Sims R, Bellenguez C, et al. Meta-analysis of 74,046 individuals identifies 11 new susceptibility loci for Alzheimer's disease. *Nature Genetics.* 2013;45(12):1452–8.
222. Griffin WST, Liu L, Li Y, Mrak RE, Barger SW. Interleukin-1 mediates Alzheimer and Lewy body pathologies. *Journal of Neuroinflammation.* 2006;3:1–9.
223. Halle A, Hornung V, Petzold GC, Stewart CR, Monks BG, Reinheckel T, et al. The NALP3 inflammasome is involved in the innate immune response to amyloid- β . *Nature Immunology.* 2008;9(8):857–65.
224. Leger M, Quiedeville A, Bouet V, Haelewyn B, Boulouard M, Schumann-Bard P, et al. Object recognition test in mice. *Nature Protocols.* 2013;8(12):2531–7.
225. Vorhees C V, Williams MT. Morris water maze: procedures for assessing spatial and related forms of learning and memory. *Nat Protoc.* 2006;848–58.

226. Wang Y, Cella M, Mallinson K, Ulrich JD, Young KL, Robinette ML, et al. TREM2 lipid sensing sustains the microglial response in an Alzheimer's disease model. *Cell*. 2015;160(6):1061–71.
227. Gratuze M, Leyns CEG, Holtzman DM. New insights into the role of TREM2 in Alzheimer's disease. *Molecular Neurodegeneration*. 2018;13(1):1–16.
228. Yeh FL, Wang Y, Tom I, Gonzalez LC, Sheng M. TREM2 Binds to Apolipoproteins, Including APOE and CLU/APOJ, and Thereby Facilitates Uptake of Amyloid-Beta by Microglia. *Neuron* [Internet]. 2016;91(2):328–40. Available from: <http://dx.doi.org/10.1016/j.neuron.2016.06.015>
229. Griciuc A, Serrano-Pozo A, Parrado AR, Lesinski AN, Asselin CN, Mullin K, et al. Alzheimer's disease risk gene cd33 inhibits microglial uptake of amyloid beta. *Neuron*. 2013;78(4):631–43.
230. Bradshaw EM, Chibnik LB, Keenan BT, Ottoboni L, Raj T, Tang A, et al. CD33 Alzheimer's disease locus: Altered monocyte function and amyloid biology. *Nature Neuroscience*. 2013;16(7):848–50.
231. Siddiqui SS, Springer SA, Verhagen A, Sundaramurthy V, Alisson-Silva F, Jiang W, et al. The Alzheimer's Disease-protective CD33 splice variant mediates adaptive loss of function via diversion to an intracellular pool. *Journal of Biological Chemistry* [Internet]. 2017;292(37):15312–20. Available from: <http://dx.doi.org/10.1074/jbc.M117.799346>
232. Griciuc A, Patel S, Federico AN, Choi SH, Innes BJ, Oram MK, et al. TREM2 Acts Downstream of CD33 in Modulating Microglial Pathology in Alzheimer's Disease. *Neuron* [Internet]. 2019;103(5):820-835.e7. Available from: <https://doi.org/10.1016/j.neuron.2019.06.010>
233. Guillot-Sestier MV, Doty KR, Gate D, Rodriguez J, Leung BP, Rezai-Zadeh K, et al. IL10 deficiency rebalances innate immunity to mitigate Alzheimer-like pathology. *Neuron*. 2015;85(3):534–48.
234. Chakrabarty P, Li A, Das P, Golde TE, Chakrabarty P, Li A, et al. IL-10 Alters Immunoproteostasis in APP Mice , Increasing Plaque Burden and Worsening Cognitive Article IL-10 Alters Immunoproteostasis in APP Mice , Increasing Plaque Burden and Worsening Cognitive Behavior. *Neuron*. 2015;85(3):519–33.
235. He P, Zhong Z, Lindholm K, Berning L, Lee W, Lemere C, et al. Deletion of tumor necrosis factor death receptor inhibits amyloid β generation and

- prevents learning and memory deficits in Alzheimer's mice. 2007;178(5):829–41.
236. Mucke L, Masliah E, Yu GQ, Mallory M, Rockenstein EM, Tatsuno G, et al. High-level neuronal expression of abeta 1-42 in wild-type human amyloid protein precursor transgenic mice: synaptotoxicity without plaque formation. - PubMed - NCBI. *Journal of Neuroscience*. 2000;
 237. Spangenberg EE, Lee RJ, Najafi AR, Rice RA, Elmore MRP, Blurton-Jones M, et al. Eliminating microglia in Alzheimer's mice prevents neuronal loss without modulating amyloid- β pathology. *Brain*. 2016;139(4):1265–81.
 238. Sosna J, Philipp S, Iii RA, Reyes-ruiz JM, Baglietto-vargas D, Laferla FM, et al. Early long-term administration of the CSF1R inhibitor PLX3397 ablates microglia and reduces accumulation of intraneuronal amyloid, neuritic plaque deposition and pre-fibrillar oligomers in 5XFAD mouse model of Alzheimer's disease. *Molecular Neurodegeneration*. 2018;1–11.
 239. Son Y, Jeong YJ, Shin N rae, Oh SJ, Nam KR. Inhibition of Colony-Stimulating Factor 1 Receptor by PLX3397 Prevents Amyloid Beta Pathology and Rescues Dopaminergic Signaling in Aging 5xFAD Mice.
 240. Lee S, Xu G, Jay TR, Ransohoff RM, Lamb BT, Bhatta S, et al. Opposing effects of membrane-anchored CX3CL1 on amyloid and tau pathologies via the p38 MAPK pathway. *Journal of Neuroscience*. 2014;34(37):12538–46.
 241. Lee S, Varvel NH, Konerth ME, Xu G, Cardona AE, Ransohoff RM, et al. CX3CR1 deficiency alters microglial activation and reduces beta-amyloid deposition in two Alzheimer's disease mouse models. *American Journal of Pathology*. 2010;177(5):2549–62.
 242. Cho SH, Sun B, Zhou Y, Kauppinen TM, Halabisky B, Wes P, et al. CX3CR1 protein signaling modulates microglial activation and protects against plaque-independent cognitive deficits in a mouse model of Alzheimer disease. *Journal of Biological Chemistry* [Internet]. 2011;286(37):32713–22. Available from: <http://dx.doi.org/10.1074/jbc.M111.254268>
 243. Nash KR, Lee DC, Hunt JB, Morganti JM, Selenica ML, Moran P, et al. Fractalkine overexpression suppresses tau pathology in a mouse model of tauopathy. *Neurobiology of Aging* [Internet]. 2013;34(6):1540–8. Available from: <http://dx.doi.org/10.1016/j.neurobiolaging.2012.12.011>

244. Vlad SC, Miller DR, Kowall NW, Felson DT. Protective effects of NSAIDs on the development of Alzheimer disease. *Neurology*. 2008;
245. Chang KH, Hsu YC, Hsu CC, Lin CL, Hsu CY, Lee CY, et al. Prolong Exposure of NSAID in Patients With RA Will Decrease the Risk of Dementia: A Nationwide Population-Based Cohort Study. *Medicine*. 2016 Mar;95(10):e3056–e3056.
246. P.-F. M, J. TM, J. L, C. M, M.-E. LM, M. S, et al. A randomized trial of naproxen to slow progress of presymptomatic Alzheimer disease. *Neurology*. 2019;
247. Keren-Shaul H, Spinrad A, Weiner A, Matcovitch-Natan O, Dvir-Szternfeld R, Ulland TK, et al. A Unique Microglia Type Associated with Restricting Development of Alzheimer’s Disease. *Cell*. 2017;169(7):1276-1290.e17.
248. Mathys H, Adaikkan C, Gao F, Ransohoff RM, Regev A, Mathys H, et al. Temporal Tracking of Microglia Activation in Neurodegeneration at Single-Cell Resolution Article Temporal Tracking of Microglia Activation in Neurodegeneration at Single-Cell Resolution. *CellReports*. 2017;21(2):366–80.
249. Cruz JC, Tseng H chun, Goldman JA, Shih H, Tsai L huei. Aberrant Cdk5 Activation by p25 Triggers Pathological Events Leading to Neurodegeneration and Neurofibrillary Tangles. 2003;40:471–83.
250. Mathys H, Adaikkan C, Gao F, Young JZ, Hemberg M, Jager PL De, et al. Temporal Tracking of Microglia Activation in Neurodegeneration at Single-Cell Resolution. *Cell Rep*. 2017;21(2):366–80.
251. Sevenich L. Brain-Resident Microglia and Blood-Borne Macrophages Orchestrate Central Nervous System inflammation in Neurodegenerative Disorders and Brain Cancer. 2018;9(April):1–16.
252. Chen WT, Lu A, Craessaerts K, Pavie B, Sala Frigerio C, Corthout N, et al. Spatial Transcriptomics and In Situ Sequencing to Study Alzheimer’s Disease. *Cell*. 2020;182(4):976-991.e19.
253. Götz J, Bodea LG, Goedert M. Rodent models for Alzheimer disease. *Nature Reviews Neuroscience* [Internet]. 2018;19(10):583–98. Available from: <http://dx.doi.org/10.1038/s41583-018-0054-8>

254. Sasaguri H, Nilsson P, Hashimoto S, Nagata K, Saito T, de Strooper B, et al. APP mouse models for Alzheimer's disease preclinical studies. *The EMBO Journal* [Internet]. 2017;4621111:e201797397. Available from: <http://emboj.embopress.org/lookup/doi/10.15252/emboj.201797397>
255. Myers A, McGonigle P. Overview of Transgenic Mouse Models for Alzheimer's Disease. *Current Protocols in Neuroscience*. 2019;89(1):1–21.
256. Eriksen JL, Janus CG. Plaques, tangles, and memory loss in mouse models of neurodegeneration. *Behav Genet*. 2007 Jan;37(1):79–100.
257. Ameen-Ali KE, Wharton SB, Simpson JE, Heath PR, Sharp P, Berwick J. Review: Neuropathology and behavioural features of transgenic murine models of Alzheimer's disease. *Neuropathology and Applied Neurobiology*. 2017;43(7):553–70.
258. Oakley H, Cole SL, Logan S, Maus E, Shao P, Craft J, et al. Intraneuronal beta-amyloid aggregates, neurodegeneration, and neuron loss in transgenic mice with five familial Alzheimer's disease mutations: potential factors in amyloid plaque formation. *J Neurosci*. 2006 Oct;26(40):10129–40.
259. Oddo S, Caccamo A, Shepherd JD, Murphy MP, Golde TE, Kaye R, et al. Triple-transgenic model of Alzheimer's disease with plaques and tangles: intracellular Abeta and synaptic dysfunction. *Neuron* [Internet]. 2003;39. Available from: [https://doi.org/10.1016/S0896-6273\(03\)00434-3](https://doi.org/10.1016/S0896-6273(03)00434-3)
260. Saito T, Matsuba Y, Mihira N, Takano J, Nilsson P, Itohara S, et al. Single App knock-in mouse models of Alzheimer's disease. *Nature Neuroscience* [Internet]. 2014;17(5):661–3. Available from: <http://www.nature.com/doi/10.1038/nn.3697>
261. Sakakibara Y, Sekiya M, Saito T, Saido TC, Iijima KM. Amyloid- β plaque formation and reactive gliosis are required for induction of cognitive deficits in App knock-in mouse models of Alzheimer's disease. *BMC Neuroscience* [Internet]. 2019;20(1):1–14. Available from: <https://doi.org/10.1186/s12868-019-0496-6>
262. Jonsson F, Gurniak CB, Fleischer B, Kirfel G, Witke W. Immunological Responses and Actin Dynamics in Macrophages Are Controlled by N-Cofilin but Are Independent from ADF. 2012;7(4):1–12.

263. Iqbal AJ, Regan-komito D, Christou I, White GE, Mcneill E, Kenyon A, et al. A Real Time Chemotaxis Assay Unveils Unique Migratory Profiles amongst Different Primary Murine Macrophages. 2013;8(3).
264. Uhlemann R, Gertz K, Boehmerle W, Schwarz T, Nolte C, Freyer D, et al. Actin dynamics shape microglia effector functions. *Brain Structure and Function*. 2016;221(5):2717–34.
265. Hall A, Hall A. Rho GTPases and the Actin Cytoskeleton. 2012;509(1998).
266. Bishop AL, Hall A. Rho GTPases and their effector proteins. 2000;255:241–55.
267. Nobes CD, Hall A. Rho, Rac, and Cdc42 GTPases regulate the assembly of multimolecular focal complexes associated with actin stress fibers, lamellipodia, and filopodia. *Cell*. 1995;81(1):53–62.
268. Miki H, Suetsugu S, Takenawa T. WAVE , a novel WASP-family protein involved in actin reorganization induced by Rac. *EMBO Journal*. 1998;17(23):6932–41.
269. Suetsugu S, Miki H, Takenawa T. Identification of Two Human WAVE/SCAR Homologues as General Actin Regulatory Molecules Which Associate with the Arp2/3 Complex. *Biochemical and Biophysical Research Communications*. 1999;260(1):296–302.
270. Mullins RD, Heuser JA, Pollard TD. The interaction of Arp2/3 complex with actin: Nucleation, high affinity pointed end capping, and formation of branching networks of filaments. *Proc Natl Acad Sci USA*. 1998;95(May):6181–6.
271. Bailly M, Macaluso F, Cammer M, Chan A, Segall JE, Condeelis JS. Relationship between Arp2 / 3 Complex and the Barbed Ends of Actin Filaments at the Leading Edge of Carcinoma Cells after Epidermal Growth Factor Stimulation. 1999;145(2):331–45.
272. Higgs HN, Pollard TD. Regulation of Actin Complex and WASp / Scar Proteins *. :32531–5.
273. Weiner OD, Servant G, Welch MD, Mitchison TJ, John W, Bourne HR. Spatial control of actin polymerization during neutrophil chemotaxis. 2010;1(2):75–81.

274. Mendoza MC. Phosphoregulation of the WAVE Regulatory Complex and Signal Integration. *Semin Cell Dev Biol.* 2013;24(4):272–9.
275. Pantaloni D, Boujemaa R, Didry D, Gounon P, Carlier M France. The Arp2 / 3 complex branches filament barbed ends : functional antagonism with capping proteins. 2000;2(July):385–91.
276. Blanchoin L, Amann KJ, Higgs HN, Marchand J baptiste, Kaiser DA, Pollard TD. Direct observation of dendritic actin complex and WASP / Scar proteins. 2000;171(1994):1007–11.
277. Svitkina TM, Borisy GG. Organization and Treadmilling of Actin Filament Array in Lamellipodia. 1999;145(5):1009–26.
278. Suetsugu S, Yamazaki D, Kurisu S, Takenawa T. Differential Roles of WAVE1 and WAVE2 in Dorsal and Peripheral Ruffle Formation for Fibroblast Cell Migration. *Developmental Cell,*. 2003;5:595–609.
279. Kheir WA, Gevrey J claude, Yamaguchi H, Isaac B, Cox D. A WAVE2-Abi1 complex mediates CSF-1-induced F- actin-rich membrane protrusions and migration in macrophages. *Journal of Cell Science.* 2005;118:5369–79.
280. Gautreau A, Ho H yi H, Li J, Steen H, Gygi SP, Kirschner MW. Purification and architecture of the ubiquitous Wave complex. *Proc Natl Acad Sci U S A.* 2004 Mar;101(13):4379–83.
281. Chen Z, Borek D, Padrick SB, Gomez TS, Ismail A, Umetani J, et al. Structure and Control of the Actin Regulatory WAVE Complex. *Nature.* 2010;468(7323):533–8.
282. Hu K, Higgs HN, Pollard TD, Jacobi C, Aepfelbacher M, Linder S. The Verprolin-like Central (VC) Region of Wiskott-Aldrich Syndrome Protein Induces Arp2 / 3 Complex-dependent Actin Nucleation *. 2001;276(38):35761–7.
283. Rodal AA, Sokolova O, Robins DB, Daugherty KM, Hippenmeyer S, Riezman H, et al. Conformational changes in the Arp2 / 3 complex leading to actin nucleation. 2005;12(1):26–31.
284. Marchand J baptiste, Kaiser DA, Pollard TD, Higgs HN. Interaction of WASP / Scar proteins with actin and vertebrate Arp2 / 3 complex. 2001;3(JANUARY).

285. Oikawa T, Yamaguchi H, Itoh T, Kato M, Ijuin T, Yamazaki D, et al. PtdIns(3,4,5)P3 binding is necessary for WAVE2-induced formation of lamellipodia. *Nat Cell Biol.* 2004 May;6(5):420–6.
286. Stuart JR, Gonzalez FH, Kawai H, Yuan ZM. c-Abl interacts with the WAVE2 signaling complex to induce membrane ruffling and cell spreading. *Journal of Biological Chemistry.* 2006;281(42):31290–7.
287. Leng Y, Zhang J, Badour K, Arpaia E, Freeman S, Cheung P, et al. Abelson-interactor-1 promotes WAVE2 membrane translocation and Abelson-mediated tyrosine phosphorylation required for WAVE2 activation. *Proc Natl Acad Sci U S A.* 2005;102(4):1098–103.
288. Mendoza MC, Er EE, Zhang W, Ballif BA, Hunter L, Danuser G, et al. ERK-MAPK Drives Lamellipodia Protrusion by Activating the WAVE2 Regulatory Complex. 2012;41(6):661–71.
289. Danson CM, Pocha SM, Bloomberg GB, Cory GO. Phosphorylation of WAVE2 by MAP kinases regulates persistent cell migration and polarity. 2009;120(Pt 23):4144–54.
290. Nakanishi O, Suetsugu S, Yamazaki D, Takenawa T. Effect of WAVE2 Phosphorylation on Activation of the Arp2 / 3 Complex. 2007;325(IIm):319–25.
291. Heng TSP, Painter MW, Elpek K, Lukacs-Kornek V, Mauermann N, Turley SJ, et al. The immunological genome project: Networks of gene expression in immune cells. Vol. 9, *Nature Immunology.* 2008. p. 1091–1094.
292. Sjöstedt E, Fagerberg L, Hallström BM, Häggmark A, Mitsios N, Nilsson P, et al. Defining the Human Brain Proteome Using Transcriptomics and Antibody-Based Profiling with a Focus on the Cerebral Cortex. *PLOS ONE.* 2015;10(6):e0130028.
293. Patir A, Shih B, McColl BW, Freeman TC. A core transcriptional signature of human microglia: derivation and utility in describing region-dependent alterations associated with Alzheimer’s disease. *GLIA.* 2019;67(6):1240–53.
294. Sekino S, Kashiwagi Y, Kanazawa H, Takada K, Baba T, Sato S, et al. The NESH/Abi-3-based WAVE2 complex is functionally distinct from the Abi-1-based WAVE2 complex. *Cell Communication and Signaling.* 2015;13:41.

295. Hirao N, Sato S, Gotoh T, Maruoka M, Suzuki J, Matsuda S, et al. NESH (Abi-3) is present in the Abi/WAVE complex but does not promote c-Abl-mediated phosphorylation. *FEBS Letters*. 2006;580(27):6464–70.
296. Kotula L, Island S. Abi1, a critical molecule coordinating actin cytoskeleton reorganization with PI-3 kinase and growth signaling. *FEBS Letters*. 2012;586(17):2790–4.
297. Miyazaki K, Matsuda S, Ichigotani Y, Takenouchi Y, Hayashi K, Fukuda Y, et al. Isolation and characterization of a novel human gene (NESH) which encodes a putative signaling molecule similar to e3B1 protein. *Biochimica et Biophysica Acta - Gene Structure and Expression*. 2000;1493(1–2):237–41.
298. Ichigotani Y, Fujii K, Hamaguchi M, Matsuda S. In search of a function for the E3B1/Abi2/Argbp1/NESH family (Review). *Int J Mol Med*. 2002 Jun;9(6):591–5.
299. Ichigotani Y, Yokozaki S, Fukuda Y, Hamaguchi M, Matsuda S. Forced expression of NESH suppresses motility and metastatic dissemination of malignant cells. *Cancer Res*. 2002 Apr;62(8):2215–9.
300. Moraes L, Zanchin NIT, Cerutti JM, Moraes L, Zanchin NIT, Cerutti JM. ABI3, a component of the WAVE2 complex, is potentially regulated by PI3K/AKT pathway. *Oncotarget [Internet]*. 2017;5(0):67769–81. Available from: <http://www.oncotarget.com/fulltext/18840>
301. The Jackson Laboratory. B6N(Cg)-Abi3tm1.1(KOMP)Vlcg/J strain page.
302. Karahan H, Smith DC, Kim B, Dabin LC, Al-amin M, Wijeratne HRS, et al. Deletion of Abi3 gene locus exacerbates neuropathological features of Alzheimer's disease in a mouse model of A β amyloidosis. 2021;3954(November):1–20.
303. Ibanez KR, McFarland KN, Phillips J, Allen M, Lessard C, Zobel L, et al. Deletion of Abi3/Gngt2 influences age-progressive amyloid β and tau pathologies in distinctive ways. *bioRxiv*. 2021;
304. Ichigotani Y, Yokozaki S, Fukuda Y, Hamaguchi M, Matsuda S. Forced expression of NESH suppresses motility and metastatic dissemination of malignant cells. *Cancer Research*. 2002;62(8):2215–9.
305. Latini FRM, Hemerly JP, Oler G, Riggins GJ, Cerutti JM. Re-expression of ABI3-binding protein suppresses thyroid tumor growth by promoting

- senescence and inhibiting invasion. *Endocrine-Related Cancer*. 2008;15(3):787–99.
306. Latini FRM, Hemerly JP, Freitas BCG, Oler G, Riggins GJ, Cerutti JM. ABI3 ectopic expression reduces in vitro and in vivo cell growth properties while inducing senescence. *BMC Cancer*. 2011;11(1):11.
307. Bae J, Sung BH, Cho IH, Song WK. F-actin-dependent regulation of NESH dynamics in rat hippocampal neurons. *PLoS ONE*. 2012;7(4):e34514.
308. Bae J, Sung BH, Cho IH, Kim SM, Song WK. Nesh regulates dendritic spine morphology and synapse formation. *PLoS ONE*. 2012;7(4):e34677.
309. Yao Z, van Velthoven CTJ, Nguyen TN, Goldy J, Sedeno-Cortes AE, Baftizadeh F, et al. A taxonomy of transcriptomic cell types across the isocortex and hippocampal formation. *Cell [Internet]*. 2021;184(12):3222-3241.e26. Available from: <https://doi.org/10.1016/j.cell.2021.04.021>
310. Bennett ML, Bennett FC, Liddel SA, Ajami B, Zamanian JL, Fernhoff NB, et al. New tools for studying microglia in the mouse and human CNS. *Proceedings of the National Academy of Sciences [Internet]*. 2016;113(12):E1738–46. Available from: <http://www.pnas.org/lookup/doi/10.1073/pnas.1525528113>
311. Satoh J ichi, Kino Y, Yanaizu M, Tosaki Y, Sakai K, Ishida T, et al. Microglia express ABI3 in the brains of Alzheimer’s disease and Nasu-Hakola disease. *Intractable & Rare Diseases Research*. 2017;6(4):262–8.
312. Xia MQ, Bacskai BJ, Knowles RB, Qin SX, Hyman BT. Expression of the chemokine receptor CXCR3 on neurons and the elevated expression of its ligand IP-10 in reactive astrocytes: In vitro ERK1/2 activation and role in Alzheimer’s disease. *Journal of Neuroimmunology*. 2000;108(1–2):227–35.
313. Zaheer S, Thangavel R, Wu Y, Khan MM, Kempuraj D, Zaheer A. Enhanced expression of glia maturation factor correlates with glial activation in the brain of triple transgenic Alzheimer’s disease mice. *Neurochemical Research*. 2013;38(1):218–25.
314. Yin Z, Raj D, Saiepour N, van Dam D, Brouwer N, Holtman IR, et al. Immune hyperreactivity of A β plaque-associated microglia in Alzheimer’s disease. *Neurobiology of Aging [Internet]*. 2017;55:115–22. Available from: <http://dx.doi.org/10.1016/j.neurobiolaging.2017.03.021>

315. Man SM, Ma YR, Shang DS, Zhao WD, Li B, Guo DW, et al. Peripheral T cells overexpress MIP-1 α to enhance its transendothelial migration in Alzheimer's disease. *Neurobiology of Aging*. 2007;28(4):485–96.
316. Guedes JR, Lao T, Cardoso AL, el Khoury J. Roles of microglial and monocyte chemokines and their receptors in regulating Alzheimer's disease-associated amyloid- β and tau pathologies. *Frontiers in Neurology*. 2018;9(AUG):1–8.
317. Keren-Shaul H, Spinrad A, Weiner A, Matcovitch-Natan O, Dvir-Szternfeld R, Ulland TK, et al. A Unique Microglia Type Associated with Restricting Development of Alzheimer's Disease. *Cell* [Internet]. 2017;169(7):1276-1290.e17. Available from: <http://dx.doi.org/10.1016/j.cell.2017.05.018>
318. Ghaffari SD. Investigation of the ABI3 protein in microglia and its association with Alzheimer's disease in TgCRND8 mouse model. University of Cambridge, Cambridge; 2021.
319. Bai B, Wang X, Li Y, Chen PC, Yu K, Dey KK, et al. Deep Multilayer Brain Proteomics Identifies Molecular Networks in Alzheimer's Disease Progression. *Neuron* [Internet]. 2020;105(6):975-991.e7. Available from: <https://doi.org/10.1016/j.neuron.2019.12.015>
320. Das A, Kim SH, Arifuzzaman S, Yoon T, Chai JC, Lee YS, et al. Transcriptome sequencing reveals that LPS-triggered transcriptional responses in established microglia BV2 cell lines are poorly representative of primary microglia. *Journal of Neuroinflammation*. 2016;13(1):182.
321. Matsuda S, Ichigotani Y, Okumura N, Yoshida H, Kajiya Y, Kitagishi Y, et al. NESH protein expression switches to the adverse effect of imatinib mesylate. *Molecular Oncology*. 2008;2(1):16–9.
322. Shafiq CWNSSJRBA. Arp2/3 complex is required for macrophage integrin functions but is dispensable for FcR phagocytosis and in vivo motility. *Dev cell*. 2017;42(5):498–513.
323. Eswarappa SM, Pareek V, Chakravorty D. Role of actin cytoskeleton in LPS-induced NF- κ B activation and nitric oxide production in murine macrophages. *Innate Immunity*. 2008;14(5):309–18.
324. Lee CYD, Daggett A, Gu X, Jiang LL, Langfelder P, Li X, et al. Elevated TREM2 Gene Dosage Reprograms Microglia Responsivity and Ameliorates

- Pathological Phenotypes in Alzheimer's Disease Models. *Neuron*. 2018;97(5):1032-1048.e5.
325. Wang Y, Cella M, Mallinson K, Ulrich JD, Young KL, Robinette ML, et al. TREM2 lipid sensing sustains the microglial response in an Alzheimer's disease model. *Cell*. 2015;160(6):1061–71.
326. Wang Y, Ulland TK, Ulrich JD, Song W, Tzaferis JA, Hole JT, et al. TREM2-mediated early microglial response limits diffusion and toxicity of amyloid plaques. *Journal of Experimental Medicine* [Internet]. 2016;213(5):667–75. Available from: <http://jem.rupress.org/content/213/5/667>
327. Akama KT, Van Eldik LJ. β -Amyloid stimulation of inducible nitric-oxide synthase in astrocytes is interleukin-1 β - and tumor necrosis factor- α (TNF α)-dependent, and involves a TNF α receptor-associated factor- and NF κ B-inducing kinase- dependent signaling mechanism. *Journal of Biological Chemistry*. 2000;275(11):7918–24.
328. Martín-Sánchez A, Piñero J, Nonell L, Arnal M, Ribe EM, Nevado-Holgado A, et al. Comorbidity between Alzheimer's disease and major depression: a behavioural and transcriptomic characterization study in mice. *Alzheimer's Research and Therapy*. 2021;13(1):1–19.
329. Jones RE. Investigating how Alzheimer's Disease risk genes Spi1 and Abi3 modulate Macrophage physiology [PhD Thesis]. Cardiff University, Cardiff; 2019.
330. Jung S, Aliberti J, Graemmel P, Sunshine MJ, Kreutzberg GW, Sher A, et al. Analysis of Fractalkine Receptor CX3CR1 Function by Targeted Deletion and Green Fluorescent Protein Reporter Gene Insertion. *Molecular and Cellular Biology*. 2000;20(11):4106–14.
331. Wolf Y, Yona S, Kim K wook, Jung S. Microglia, seen from the CX 3 CR1 angle. 2013;7(March):1–9.
332. Todaro GJ, Green H. Quantitative studies of the growth of mouse embryo cells in culture and their development into established lines. *J Cell Biol* [Internet]. 1963 May;17(2):299–313. Available from: <https://pubmed.ncbi.nlm.nih.gov/13985244>
333. Rosas M, Osorio F, Robinson MJ, Davies LC, Dierkes N, Jones S a., et al. Hoxb8 conditionally immortalised macrophage lines model inflammatory

- monocytic cells with important similarity to dendritic cells. *European Journal of Immunology*. 2011;41(2):356–65.
334. Rosas M, Davies LC, Giles PJ, Liao CT, Kharfan B, Stone TC, et al. The transcription factor Gata6 links tissue macrophage phenotype and proliferative renewal. *Science* (1979) [Internet]. 2014;344(6184):645–8. Available from: <http://www.pubmedcentral.nih.gov/articlerender.fcgi?artid=4185421&tool=pmcentrez&rendertype=abstract>
335. Zhang G, Gurtu V, Kain SR. An enhanced green fluorescent protein allows sensitive detection of gene transfer in mammalian cells. *Biochem Biophys Res Commun*. 1996 Oct;227(3):707–11.
336. Liu Z, Chen O, Wall JBJ, Zheng M, Zhou Y, Wang L, et al. Systematic comparison of 2A peptides for cloning multi-genes in a polycistronic vector. *Sci Rep*. 2017 May;7(1):2193.
337. Daniels RW, Rossano AJ, Macleod GT, Ganetzky B. Expression of multiple transgenes from a single construct using viral 2A peptides in *Drosophila*. *PLoS One*. 2014;9(6):e100637.
338. Ramezani A, Hawley RG. Overview of the HIV-1 Lentiviral Vector System. *Current protocols in molecular biology* / edited by Frederick M Ausubel . [et al]. 2002;Chapter 16:1–15.
339. Ipseiz N, Czubala MA, Bart VMT, Davies LC, Jenkins RH, Brennan P, et al. Effective In Vivo Gene Modification in Mouse Tissue-Resident Peritoneal Macrophages by Intraperitoneal Delivery of Lentiviral Vectors. *Molecular Therapy - Methods & Clinical Development* [Internet]. 2020 Mar 13;16:21–31. Available from: <https://doi.org/10.1016/j.omtm.2019.10.004>
340. Pear WS, Nolan GP, Scott ML, Baltimore D. Production of high-titer helper-free retroviruses by transient transfection. *Proc Natl Acad Sci U S A*. 1993;90(18):8392–6.
341. Son KK, Patel DH, Tkach D, Park A. Cationic liposome and plasmid DNA complexes formed in serum-free medium under optimum transfection condition are negatively charged. *Biochim Biophys Acta*. 2000 Jun;1466(1–2):11–5.

342. Poznansky M, Lever A, Bergeron L, Haseltine W, Sodroski J. Gene transfer into human lymphocytes by a defective human immunodeficiency virus type 1 vector. *J Virol.* 1991 Jan;65(1):532–6.
343. Ipseiz N, Czubala MA, Bart VMT, Davies LC, Jenkins RH, Brennan P, et al. Effective *In Vivo* Gene Modification in Mouse Tissue-Resident Peritoneal Macrophages by Intraperitoneal Delivery of Lentiviral Vectors. *Molecular Therapy - Methods & Clinical Development* [Internet]. 2020 Mar 13;16:21–31. Available from: <https://doi.org/10.1016/j.omtm.2019.10.004>
344. Schindelin J, Arganda-Carreras I, Frise E, Kaynig V, Longair M, Pietzsch T, et al. Fiji: an open-source platform for biological-image analysis. *Nature Methods.* 2012;9(7):676–82.
345. ImageJ User Guide User Guide ImageJ. 2012;
346. Paxinos G, Franklin KBJ. *The Mouse Brain in Stereotaxic Coordinates.*
347. Zhang Z, Ma Z, Zou W, Guo H, Liu M, Ma Y, et al. The Appropriate Marker for Astrocytes: Comparing the Distribution and Expression of Three Astrocytic Markers in Different Mouse Cerebral Regions. Chiarini A, editor. *BioMed Research International* [Internet]. 2019;2019:9605265. Available from: <https://doi.org/10.1155/2019/9605265>
348. Tan YL, Yuan Y, Tian L. Microglial regional heterogeneity and its role in the brain. *Molecular Psychiatry.* 2020;25(2):351–67.
349. Bitplane AG. *Imaris Reference Manual 9.2.* 2018;(April). Available from: http://www.bitplane.com/download/manuals/ReferenceManual9_2_0.pdf
350. Clayton K, Delpech JC, Herron S, Iwahara N, Ericsson M, Saito T, et al. Plaque associated microglia hyper-secrete extracellular vesicles and accelerate tau propagation in a humanized APP mouse model. *Molecular Neurodegeneration.* 2021;16(1):1–16.
351. Goldey GJ, Roumis DK, Glickfeld LL, Kerlin AM, Reid RC, Bonin V, et al. Removable cranial windows for long-term imaging in awake mice. *Nature Protocols.* 2014;9(11):2515–38.
352. Lueptow LM. Novel Object Recognition Test for the Investigation of Learning and Memory in Mice. 2017;(August):1–9.

353. Liu MY, Yin CY, Zhu LJ, Zhu XH, Xu C, Luo CX, et al. Sucrose preference test for measurement of stress-induced anhedonia in mice. *Nature Protocols*. 2018;13(7):1686–98.
354. Gaskill BN, Karas AZ, Garner JP, Pritchett-Corning KR. Nest building as an indicator of health and welfare in laboratory mice. *J Vis Exp*. 2013;(82):51012.
355. Rougerie P, Miskolci V, Cox D. Generation of membrane structures during phagocytosis and chemotaxis of macrophages: Role and regulation of the actin cytoskeleton. *Immunol Rev*. 2013;256(1):222–39.
356. Horsthemke M, Bachg AC, Groll K, Moyzio S, Mütter B, Hemkemeyer SA, et al. Multiple roles of filopodial dynamics in particle capture and phagocytosis and phenotypes of Cdc42 and Myo10 deletion. *Journal of Biological Chemistry*. 2017;292(17):7258–73.
357. Mooren OL, Galletta BJ, Cooper JA. Roles for actin assembly in endocytosis. *Annual Review of Biochemistry*. 2012;81:661–86.
358. Kustermans G, El Benna J, Piette J, Legrand-Poels S. Perturbation of actin dynamics induces NF- κ B activation in myelomonocytic cells through an NADPH oxidase-dependent pathway. *Biochemical Journal*. 2005;387(2):531–40.
359. Papa R, Penco F, Volpi S, Gattorno M. Actin Remodeling Defects Leading to Autoinflammation and Immune Dysregulation. *Frontiers in Immunology*. 2021;11(January):1–11.
360. Fulga TA, Elson-Schwab I, Khurana V, Steinhilb ML, Spires TL, Hyman BT, et al. Abnormal bundling and accumulation of F-actin mediates tau-induced neuronal degeneration in vivo. *Nature Cell Biology*. 2007;9(2):139–48.
361. Henriques AG, Vieira SI, Da Cruz E Silva EF, Da Cruz E Silva OAB. A β promotes Alzheimer's disease-like cytoskeleton abnormalities with consequences to APP processing in neurons. *Journal of Neurochemistry*. 2010;113(3):761–71.
362. García-García E, Rosales C. Signal transduction during Fc receptor-mediated phagocytosis. *J Leukoc Biol*. 2002;72(6):1092–108.
363. Casella JF, Flanagan MD, Lin S. Cytochalasin D inhibits actin polymerization and induces depolymerization of actin filaments formed during platelet shape change. *Nature*. 1981;

364. Asai H, Ikezu S, Tsunoda S, Medalla M, Luebke J, Haydar T, et al. Depletion of microglia and inhibition of exosome synthesis halt tau propagation. *Nature Neuroscience*. 2015;18(11):1584–93.
365. Butterfield DA, Halliwell B. Oxidative stress, dysfunctional glucose metabolism and Alzheimer disease. *Nature Reviews Neuroscience*. 2019;20(3):148–60.
366. Bubb MR, Spector I, Beyer BB, Fosen KM. Effects of Jasplakinolide on the Kinetics of Actin Polymerization. *Journal of Biological Chemistry*. 2000;
367. Wilson MD, Sethi S, Lein PJ, Keil KP, States U, States U. Valid Statistical Approaches for Analyzing Sholl Data: Mixed Effects versus Simple Linear Models Mabelle. *J Neurosci Methods*. 2017;33–43.
368. Blanchoin L, Boujemaa-Paterski R, Sykes C, Plastino J. Actin dynamics, architecture, and mechanics in cell motility. *Physiological Reviews*. 2014;94(1):235–63.
369. Brown GD, Gordon S. Immune recognition. A new receptor for beta-glucans. *Nature*. 2001 Sep;413(6851):36–7.
370. Brown GD, Taylor PR, Reid DM, Willment JA, Williams DL, Martinez-Pomares L, et al. Dectin-1 is a major β -glucan receptor on macrophages. *Journal of Experimental Medicine*. 2002;196(3):407–12.
371. Underhill DM, Rosnagle E, Lowell CA, Simmons RM. Dectin-1 activates Syk tyrosine kinase in a dynamic subset of macrophages for reactive oxygen production. *Blood*. 2005;106(7):2543–50.
372. Diekmann D, Abo A, Johnston C, Segal AW, Hall A. Interaction of Rac with p67phox and regulation of phagocytic NADPH oxidase activity. *Science* (1979). 1994;265(5171):531–3.
373. Ridley AJ. Life at the leading edge. *Cell*. 2011;145(7):1012–22.
374. Acevedo A, González-Billault C. Crosstalk between Rac1-mediated actin regulation and ROS production. *Free Radical Biology and Medicine*. 2018;116(August 2017):101–13.
375. Morton WM, Ayscough KR, McLaughlin PJ. Latrunculin alters the actin-monomer subunit interface to prevent polymerization. *Nat Cell Biol*. 2000 Jun;2(6):376–8.

376. Wang GG, Calvo KR, Pasillas MP, Sykes DB, Häcker H, Kamps MP. Quantitative production of macrophages or neutrophils *ex vivo* using conditional Hoxb8. *Nature Methods*. 2006;3(4):287–93.
377. Lavin Y, Winter D, Blecher-Gonen R, David E, Keren-Shaul H, Merad M, et al. Tissue-resident macrophage enhancer landscapes are shaped by the local microenvironment. *Cell*. 2014;159(6):1312–26.
378. Friedman BA, Srinivasan K, Ayalon G, Meilandt WJ, Lin H, Huntley MA, et al. Diverse Brain Myeloid Expression Profiles Reveal Distinct Microglial Activation States and Aspects of Alzheimer’s Disease Not Evident in Mouse Models. *Cell Reports*. 2018;22(3):832–47.
379. Galatro TF, Holtman IR, Lerario AM, Vainchtein ID, Brouwer N, Sola PR, et al. Transcriptomic analysis of purified human cortical microglia reveals age-associated changes. *Nature Neuroscience*. 2017 Jul 3;20(July):1162.
380. Ormel PR, Vieira de Sá R, van Bodegraven EJ, Karst H, Harschnitz O, Sneebouer MAM, et al. Microglia innately develop within cerebral organoids. *Nature Communications* [Internet]. 2018;9(1). Available from: <http://dx.doi.org/10.1038/s41467-018-06684-2>
381. Shinozaki Y, Shibata K, Yoshida K, Shigetomi E, Gachet C, Ikenaka K, et al. Transformation of Astrocytes to a Neuroprotective Phenotype by Microglia via P2Y1 Receptor Downregulation. *Cell Reports* [Internet]. 2017;19(6):1151–64. Available from: <http://dx.doi.org/10.1016/j.celrep.2017.04.047>
382. Liddel SA, Guttenplan KA, Clarke LE, Bennett FC, Bohlen CJ, Schirmer L, et al. Neurotoxic reactive astrocytes are induced by activated microglia. *Nature* [Internet]. 2017;541(7638):481–7. Available from: <http://dx.doi.org/10.1038/nature21029>
383. Imai Y, Iwata I, Ito D, Ohsawa K, Kohsaka S. A Novel Gene *iba1* in the Major Histocompatibility Complex Class III Region Encoding an EF Hand Protein Expressed in a Monocytic Lineage 1. 1996;862:855–62.
384. Ott T, Nieder A. Dopamine and Cognitive Control in Prefrontal Cortex. *Trends in Cognitive Sciences*. 2019;23(3):213–34.
385. Morris RGM. Elements of a neurobiological theory of hippocampal function: the role of synaptic plasticity, synaptic tagging and schemas. Vol. 23, *Eur J Neurosci*. 2006. p. 2829–46.

386. Ohm TG. The dentate gyrus in Alzheimer's disease. *Progress in Brain Research*. 2007;163:723–40.
387. Grady CL, Furey ML, Pietrini P, Horwitz B, Rapoport SI. Altered brain functional connectivity and impaired short-term memory in Alzheimer's disease. *Brain*. 2001;124:739–56.
388. Falk T, Mai D, Bensch R, Çiçek Ö, Abdulkadir A, Marrakchi Y, et al. U-Net: deep learning for cell counting, detection, and morphometry. *Nature Methods*. 2019;16(1):67–70.
389. Salamanca L, Mechawar N, Murai KK, Balling R, Bouvier DS, Skupin A. MIC-MAC: An automated pipeline for high-throughput characterization and classification of three-dimensional microglia morphologies in mouse and human postmortem brain samples. *Glia*. 2019;67(8):1496–509.
390. Heindl S, Gesierich B, Benakis C, Llovera G, Duering M, Liesz A. Automated Morphological Analysis of Microglia After Stroke. *Front Cell Neurosci*. 2018 Apr 19;12:106.
391. Hanamsagar R, Alter MD, Block CS, Sullivan H, Bolton JL, Bilbo SD. Generation of a microglial developmental index in mice and in humans reveals a sex difference in maturation and immune reactivity: HANAMSAGAR et al. (*Glia*, (2017), 65, 9, (1504-1520), 10.1002/glia.23176). *Glia*. 2017;65:1504–20.
392. D. E, A.L. H de A, D. J, P. W, O. S, E. D, et al. Host microbiota constantly control maturation and function of microglia in the CNS. *Nat Neurosci*. 2015;18(7):965–77.
393. Elmore MRP, Lee RJ, West BL, Green KN. Characterizing newly repopulated microglia in the adult mouse: Impacts on animal behavior, cell morphology, and neuroinflammation. *PLoS ONE*. 2015;10(4):1–18.
394. García-Magro N, Martín YB, Palomino-Antolin A, Egea J, Negredo P, Avendaño C. Multiple Morphometric Assessment of Microglial Cells in Deafferented Spinal Trigeminal Nucleus. *Frontiers in Neuroanatomy*. 2020;13(January):1–13.
395. Hierro-bujalance C, Bacskai BJ, Garcia-alloza M. In Vivo Imaging of Microglia With Multiphoton Microscopy. 2018;10(July):1–14.

396. Walker DG, Lue LF. Immune phenotypes of microglia in human neurodegenerative disease: challenges to detecting microglial polarization in human brains. *Alzheimers Res Ther.* 2015 Aug;7(1):56.
397. Hopperton KE, Mohammad D, Trépanier MO, Giuliano V, Bazinet RP. Markers of microglia in post-mortem brain samples from patients with Alzheimer's disease: a systematic review. *Molecular Psychiatry* [Internet]. 2018;23(2):177–98. Available from: <https://doi.org/10.1038/mp.2017.246>
398. Jha MK, Jo M, Kim JH, Suk K. Microglia-Astrocyte Crosstalk: An Intimate Molecular Conversation. *The Neuroscientist.* 2019;25(3):227–40.
399. Schwarz1 JM, Sholar PW, Bilbo SD. Sex differences in microglial colonization of the developing rat brain. *J Neurochem.* 2012;948–63.
400. DeSantis DF, Smith CJ. Tetris in the Nervous System: What Principles of Neuronal Tiling Can Tell Us About How Glia Play the Game. *Frontiers in Cellular Neuroscience.* 2021;15(August):1–10.
401. Sasaki Y, Ohsawa K, Kanazawa H, Kohsaka S, Imai Y. Iba1 is an actin-cross-linking protein in macrophages/microglia. *Biochem Biophys Res Commun.* 2001 Aug;286(2):292–7.
402. Liddel SA, Barres BA. Reactive Astrocytes: Production, Function, and Therapeutic Potential. *Immunity* [Internet]. 2017;46(6):957–67. Available from: <http://dx.doi.org/10.1016/j.immuni.2017.06.006>
403. Marciniak E, Faivre E, Dutar P, Alves Pires C, Demeyer D, Caillierez R, et al. The Chemokine MIP-1 α /CCL3 impairs mouse hippocampal synaptic transmission, plasticity and memory. *Scientific Reports* [Internet]. 2015;5(October):1–11. Available from: <http://dx.doi.org/10.1038/srep15862>
404. Vlkolinský R, Siggins GR, Campbell IL, Krucker T. Acute exposure to CXC chemokine ligand 10, but not its chronic astroglial production, alters synaptic plasticity in mouse hippocampal slices. *J Neuroimmunol.* 2004 May;150(1–2):37–47.
405. Stowell RD, Sipe GO, Dawes RP, Batchelor HN, Lordy KA, Whitelaw BS, et al. Noradrenergic signaling in the wakeful state inhibits microglial surveillance and synaptic plasticity in the mouse visual cortex. *Nature Neuroscience* [Internet]. 2019;22(11):1782–92. Available from: <http://dx.doi.org/10.1038/s41593-019-0514-0>

406. Liu YU, Ying Y, Li Y, Eyo UB, Chen T, Zheng J, et al. Neuronal network activity controls microglial process surveillance in awake mice via norepinephrine signaling. *Nature Neuroscience* [Internet]. 2019;22(11):1771–81. Available from: <http://dx.doi.org/10.1038/s41593-019-0511-3>
407. Ji K, Akgul G, Wollmuth LP, Tsirka SE. Microglia Actively Regulate the Number of Functional Synapses. *PLoS ONE*. 2013;8(2).
408. Cheng C, Trzcinski O, Doering LC. Fluorescent labeling of dendritic spines in cell cultures with the carbocyanine dye “Dil.” *Frontiers in Neuroanatomy* [Internet]. 2014;8:30. Available from: <https://www.frontiersin.org/article/10.3389/fnana.2014.00030>
409. Zhang J, Malik A, Choi HB, Ko RWY, Dissing-Olesen L, MacVicar BA. Microglial CR3 activation triggers long-term synaptic depression in the hippocampus via NADPH oxidase. *Neuron*. 2014;82(1):195–207.
410. Riazi K, Galic MA, Kentner AC, Reid AY, Sharkey KA, Pittman QJ. Microglia-dependent alteration of glutamatergic synaptic transmission and plasticity in the hippocampus during peripheral inflammation. *Journal of Neuroscience*. 2015;35(12):4942–52.
411. Kemp A, Manahan-Vaughan D. Hippocampal long-term depression and long-term potentiation encode different aspects of novelty acquisition. *Proc Natl Acad Sci U S A*. 2004;101(21):8192–7.
412. Liu M, Li J, Dai P, Zhao F, Zheng G, Jing J, et al. Microglia activation regulates GluR1 phosphorylation in chronic unpredictable stress-induced cognitive dysfunction. *Stress*. 2015 Jan 2;18(1):96–106.
413. Ferrini F, De Koninck Y. Microglia control neuronal network excitability via BDNF signalling. *Neural Plasticity*. 2013;2013.
414. Parkhurst CNN, Yang G, Ninan I, Savas JNN, Yates III JR, Lafaille JJJ, et al. Microglia Promote Learning-Dependent Synapse Formation through Brain-Derived Neurotrophic Factor. *Cell*. 2013 Mar 23;155(7):1596–609.
415. Chen TW, Wardill TJ, Sun Y, Pulver SR, Renninger SL, Baohan A, et al. Ultrasensitive fluorescent proteins for imaging neuronal activity. *Nature*. 2013 Jul 18;499(7458):295–300.
416. Rajamohamedsait HB, Sigurdsson EM. Histological staining of amyloid and pre-amyloid peptides and proteins in mouse tissue. *Methods Mol Biol*

- [Internet]. 2012;849:411–24. Available from:
<https://pubmed.ncbi.nlm.nih.gov/22528106>
417. Mehla J, Lacoursiere SG, Lapointe V, McNaughton BL, Sutherland RJ, McDonald RJ, et al. Age-dependent behavioral and biochemical characterization of single APP knock-in mouse (APPNL-G-F/NL-G-F) model of Alzheimer's disease. *Neurobiology of Aging* [Internet]. 2019;75:25–37. Available from: <https://doi.org/10.1016/j.neurobiolaging.2018.10.026>
418. Sakakibara Y, Sekiya M, Saito T, Saido TC, Iijima KM. Cognitive and emotional alterations in App knock - in mouse models of A β amyloidosis. *BMC Neuroscience* [Internet]. 2018;1–17. Available from: <https://doi.org/10.1186/s12868-018-0446-8>
419. Pervolaraki E, Hall SP, Forestiere D, Saito T, Saido TC, Whittington MA, et al. Insoluble A β overexpression in an App knock-in mouse model alters microstructure and gamma oscillations in the prefrontal cortex, affecting anxiety-related behaviours. *DMM Disease Models and Mechanisms*. 2019;12(9).
420. Kundu P, Torres ERS, Stagaman K, Kasschau K, Okhovat M, Holden S, et al. Integrated analysis of behavioral, epigenetic, and gut microbiome analyses in App NL-G-F, App NL-F, and wild type mice. *Scientific Reports*. 2021;11(1):1–20.
421. Neely CLC, Pedemonte KA, Boggs KN, Flinn JM. Nest building behavior as an early indicator of behavioral deficits in mice. *Journal of Visualized Experiments*. 2019;2019(152):1–8.
422. Masuda A, Kobayashi Y, Kogo N, Saito T, Saido TC, Itohara S. Cognitive deficits in single App knock-in mouse models. *Neurobiology of Learning and Memory* [Internet]. 2016;135:73–82. Available from: <http://dx.doi.org/10.1016/j.nlm.2016.07.001>
423. Latif-Hernandez A, Sabanov V, Ahmed T, Craessaerts K, Saito T, Saido T, et al. The two faces of synaptic failure in App NL-G-Fknock-in mice. *Alzheimer's Research and Therapy*. 2020;12(1):1–15.
424. Dennison JL, Ricciardi NR, Lohse I, Volmar CH, Wahlestedt C. Sexual Dimorphism in the 3xTg-AD Mouse Model and Its Impact on Pre-Clinical Research. *J Alzheimers Dis*. 2021;80(1):41–52.

425. Couch BA, Kerrisk ME, Kaufman AC, Nygaard HB, Strittmatter SM, Koleske Brian AJ. Delayed Amyloid Plaque Deposition and Behavioral Deficits in Outcrossed A β PP/PS1 Mice. *J Comp Neurol* [Internet]. 2013;1395–408. Available from: <https://www.ncbi.nlm.nih.gov/pmc/articles/PMC3624763/pdf/nihms412728.pdf>
426. Arboleda-Velasquez JF, Lopera F, O'Hare M, Delgado-Tirado S, Marino C, Chmielewska N, et al. Resistance to autosomal dominant Alzheimer's disease in an APOE3 Christchurch homozygote: a case report. *Nature Medicine*. 2019;25(11):1680–3.
427. Mehta D, Jackson R, Paul G, Shi J, Sabbagh M, Network VH, et al. Why do trials for Alzheimer's disease drugs keep failing? *Expert Opin Investig Drugs*. 2017;26(6):735–9.
428. Pervolaraki E, Hall SP, Foresteire D, Saito T, Saido TC, Whittington MA, et al. Insoluble A β overexpression in an App knock-in mouse model alters microstructure and gamma oscillations in the prefrontal cortex, affecting anxiety-related behaviours. *DMM Disease Models and Mechanisms*. 2019;12(9).
429. Latif-Hernandez A, Shah D, Craessaerts K, Saido T, Saito T, de Strooper B, et al. Subtle behavioral changes and increased prefrontal-hippocampal network synchronicity in APP NL–G–F mice before prominent plaque deposition. *Behavioural Brain Research* [Internet]. 2019;364(November 2017):431–41. Available from: <https://doi.org/10.1016/j.bbr.2017.11.017>
430. Whyte LS, Hemsley KM, Lau AA, Saito T, Saido TC, Hopwood JJ, et al. Reduction in open field activity in the absence of memory deficits in the AppNL–G–F knock-in mouse model of Alzheimer's disease. *Behavioural Brain Research*. 2018;336(September 2017):177–81.
431. Lalonde R, Lewis TL, Strazielle C, Kim H, Fukuchi K. Transgenic mice expressing the bAPP695SWE mutation: effects on exploratory activity, anxiety, and motor coordination. *Brain Research*. 2003;977:38–45.
432. Cinalli DA, Cohen SJ, Guthrie K, Stackman RW. Object Recognition Memory: Distinct Yet Complementary Roles of the Mouse CA1 and Perirhinal Cortex. *Frontiers in Molecular Neuroscience*. 2020;13(October):1–16.
433. Mattapallil MJ, Wawrousek EF, Chan CC, Zhao H, Roychoudhury J, Ferguson TA, et al. The Rd8 mutation of the *Crb1* gene is present in vendor

- lines of C57BL/6N mice and embryonic stem cells, and confounds ocular induced mutant phenotypes. *Invest Ophthalmol Vis Sci.* 2012;53(6):2921–7.
434. Nolte ED, Nolte KA, Yan SS du. Anxiety and task performance changes in an aging mouse model. *Biochemical and Biophysical Research Communications* [Internet]. 2019;514(1):246–51. Available from: <https://doi.org/10.1016/j.bbrc.2019.04.049>
435. DeVito LM, Lykken C, Kanter BR, Eichenbaum H. Prefrontal cortex: Role in acquisition of overlapping associations and transitive inference. *Learning and Memory.* 2010;17(3):161–7.
436. Filali M, Lalonde R. Age-related cognitive decline and nesting behavior in an APPswe/PS1 bigenic model of Alzheimer's disease. *Brain Research* [Internet]. 2009;1292:93–9. Available from: <http://dx.doi.org/10.1016/j.brainres.2009.07.066>
437. Hefendehl JK, Wegenast-Braun BM, Liebig C, Eicke D, Milford D, Calhoun ME, et al. Long-term in vivo imaging of β -amyloid plaque appearance and growth in a mouse model of cerebral β -amyloidosis. *Journal of Neuroscience.* 2011;31(2):624–9.
438. Jung CKE, Keppler K, Steinbach S, Blazquez-Llorca L, Herms J. Fibrillar amyloid plaque formation precedes microglial activation. *PLoS ONE.* 2015;10(3):1–10.
439. Calvo-Rodriguez M, Hou SS, Snyder AC, Dujardin S, Shirani H, Nilsson KPR, et al. In vivo detection of tau fibrils and amyloid β aggregates with luminescent conjugated oligothiophenes and multiphoton microscopy. *Acta Neuropathol Commun.* 2019;7(1):171.
440. Conway OJ, Carrasquillo MM, Wang X, Bredenberg JM, Reddy JS, Strickland SL, et al. ABI3 and PLCG2 missense variants as risk factors for neurodegenerative diseases in Caucasians and African Americans. *Molecular Neurodegeneration.* 2018;13(1):1–12.
441. Dalmaso MC, Brusco LI, Olivar N, Muchnik C, Hanses C, Milz E, et al. Transethnic meta-analysis of rare coding variants in PLCG2, ABI3, and TREM2 supports their general contribution to Alzheimer's disease. *Translational Psychiatry* [Internet]. 2019;9(1):1–6. Available from: <http://dx.doi.org/10.1038/s41398-019-0394-9>

442. Jablonski KA, Amici SA, Webb LM, Ruiz-Rosado JDD, Popovich PG, Partida-Sanchez S, et al. Novel markers to delineate murine M1 and M2 macrophages. *PLoS ONE*. 2015;10(12):5–11.
443. Almanzar N, Antony J, Baghel AS, Bakerman I, Bansal I, Barres BA, et al. A single-cell transcriptomic atlas characterizes ageing tissues in the mouse. *Nature*. 2020;583(7817):590–5.
444. Karlsson M, Zhang C, Méar L, Zhong W, Digre A, Katona B, et al. A single-cell type transcriptomics map of human tissues. *Science Advances*. 2021;7(31):1–10.
445. Timmerman R, Burm SM, Bajramovic JJ. An overview of in vitro methods to study microglia. *Frontiers in Cellular Neuroscience*. 2018;12(August):1–12.
446. Kim KS, Marcogliese PC, Yang J, Callaghan SM, Resende V, Abdel-Messih E, et al. Regulation of myeloid cell phagocytosis by LRRK2 via WAVE2 complex stabilization is altered in Parkinson's disease. *Proceedings of the National Academy of Sciences [Internet]*. 2018;115(22):E5164–73. Available from: <http://www.pnas.org/lookup/doi/10.1073/pnas.1718946115>
447. Lancaster MA, Renner M, Martin CA, Wenzel D, Bicknell LS, Hurler ME, et al. Cerebral organoids model human brain development and microcephaly. *Nature*. 2013 Sep;501(7467):373–9.
448. Mancuso R, van den Daele J, Fattorelli N, Wolfs L, Balusu S, Burton O, et al. Stem-cell-derived human microglia transplanted in mouse brain to study human disease. *Nature Neuroscience [Internet]*. 2019;22(12):2111–6. Available from: <http://dx.doi.org/10.1038/s41593-019-0525-x>
449. Xu R, Li X, Boreland AJ, Posyton A, Kwan K, Hart RP, et al. Human iPSC-derived mature microglia retain their identity and functionally integrate in the chimeric mouse brain. *Nature Communications [Internet]*. 2020;11(1). Available from: <http://dx.doi.org/10.1038/s41467-020-15411-9>
450. Bernier LP, Bohlen CJ, York EM, Choi HB, Kamyabi A, Dissing-Olesen L, et al. Nanoscale Surveillance of the Brain by Microglia via cAMP-Regulated Filopodia. *Cell Reports [Internet]*. 2019;27(10):2895-2908.e4. Available from: <https://doi.org/10.1016/j.celrep.2019.05.010>
451. Guttenplan KA, Weigel MK, Prakash P, Wijewardhane PR, Hasel P, Rufen-Blanchette U, et al. Neurotoxic reactive astrocytes induce cell death via saturated lipids. *Nature*. 2021;599(7883):102–7.

452. Salas IH, Burgado J, Allen NJ. Glia: victims or villains of the aging brain? *Neurobiology of Disease*. 2020;143(February).
453. Chowen JA, Garcia-Segura LM. Role of glial cells in the generation of sex differences in neurodegenerative diseases and brain aging. *Mechanisms of Ageing and Development* [Internet]. 2021;196(March):111473. Available from: <https://doi.org/10.1016/j.mad.2021.111473>
454. Grosche A, Grosche J, Tackenberg M, Scheller D, Gerstner G, Gumprecht A, et al. Versatile and Simple Approach to Determine Astrocyte Territories in Mouse Neocortex and Hippocampus. *PLoS ONE*. 2013;8(7).
455. Rodríguez JJ, Yeh CY, Terzieva S, Olabarria M, Kulijewicz-Nawrot M, Verkhratsky A. Complex and region-specific changes in astroglial markers in the aging brain. *Neurobiology of Aging* [Internet]. 2014;35(1):15–23. Available from: <http://dx.doi.org/10.1016/j.neurobiolaging.2013.07.002>
456. Sierra A, Gottfried-Blackmore AC, McEwen BS, Bulloch K. Microglia Derived from Aging Mice Exhibit an Altered Inflammatory Profile. *Glia* [Internet]. 2007;55:412–24. Available from: <http://www.unscn.org/en/home/>
457. Matias I, Morgado J, Gomes FCA. Astrocyte Heterogeneity: Impact to Brain Aging and Disease. *Frontiers in Aging Neuroscience*. 2019;11(March):1–18.
458. Alasmari F, Alshammari MA, Alasmari AF, Alanazi WA, Alhazzani K. Neuroinflammatory Cytokines Induce Amyloid Beta Neurotoxicity through Modulating Amyloid Precursor Protein Levels/Metabolism. *BioMed Research International*. 2018;2018.
459. Yamamoto M, Kiyota T, Horiba M, Buescher JL, Walsh SM, Gendelman HE, et al. Interferon- γ and tumor necrosis factor- α regulate amyloid- β plaque deposition and β -secretase expression in Swedish mutant APP transgenic mice. *American Journal of Pathology*. 2007;170(2):680–92.
460. Liaoi YF, Wang BJ, Cheng HT, Kuo LH, Wolfe MS. Tumor necrosis factor- α , interleukin-1 β , and interferon- γ stimulate γ -secretase-mediated cleavage of amyloid precursor protein through a JNK-dependent MAPK pathway. *Journal of Biological Chemistry* [Internet]. 2004;279(47):49523–32. Available from: <http://dx.doi.org/10.1074/jbc.M402034200>
461. Dagher NN, Najafi AR, Kayala KMN, Elmore MRP, White TE, Medeiros R, et al. Colony-stimulating factor 1 receptor inhibition prevents microglial plaque association and improves cognition in 3xTg-AD mice. *Journal of*

Neuroinflammation [Internet]. 2015 Aug 1;12:139. Available from:
<http://www.ncbi.nlm.nih.gov/pmc/articles/PMC4522109/>

462. Azevedo EP, Ledo JH, Barbosa G, Sobrinho M, Diniz L, Fonseca ACC, et al. Activated microglia mediate synapse loss and short-term memory deficits in a mouse model of transthyretin-related oculoleptomeningeal amyloidosis. *Cell Death and Disease*. 2013;4(9).
463. Wang WY, Tan MS, Yu JT, Tan L. Role of pro-inflammatory cytokines released from microglia in Alzheimer's disease. *Annals of Translational Medicine*. 2015;3(10):1–15.
464. Reichwald J, Danner S, Wiederhold KH, Staufienbiel M. Expression of complement system components during aging and amyloid deposition in APP transgenic mice. *Journal of Neuroinflammation*. 2009;6:1–12.
465. Fonseca MI, Zhou J, Botto M, Tenner AJ. Absence of C1q leads to less neuropathology in transgenic mouse models of Alzheimer's disease. *Journal of Neuroscience*. 2004;24(29):6457–65.
466. Shi Q, Chowdhury S, Ma R, Le KX, Hong S, Caldarone BJ, et al. Complement C3 deficiency protects against neurodegeneration in aged plaque-rich APP/PS1 mice Qiaoqiao. *Sci Transl Med [Internet]*. 2017;9(392). Available from: <http://stm.sciencemag.org/content/9/392/eaaf6295>
467. Pchitskaya E, Bezprozvanny I. Dendritic Spines Shape Analysis—Classification or Clusterization? Perspective. *Frontiers in Synaptic Neuroscience*. 2020;12(September).
468. Mouzon BC, Bachmeier C, Ojo JO, Acker CM, Ferguson S, Paris D, et al. Lifelong behavioral and neuropathological consequences of repetitive mild traumatic brain injury. *Annals of Clinical and Translational Neurology*. 2018;5(1):64–80.
469. Howerton AR, Roland A v., Bale TL. Dorsal raphe neuroinflammation promotes dramatic behavioral stress dysregulation. *Journal of Neuroscience*. 2014;34(21):7113–23.
470. Chari T, Griswold S, Andrews NA, Fagiolini M. The Stage of the Estrus Cycle Is Critical for Interpretation of Female Mouse Social Interaction Behavior. *Frontiers in Behavioral Neuroscience*. 2020;14(June):1–9.

471. Rossi AF, Pessoa L, Desimone R, Ungerleider LG. The prefrontal cortex and the executive control of attention. *Exp Brain Res* [Internet]. 2009;192(3):489–97. Available from:
<https://www.ncbi.nlm.nih.gov/pmc/articles/PMC3624763/pdf/nihms412728.pdf>
472. Lang C, Campbell KR, Ryan BJ, Carling P, Attar M, Vowles J, et al. Single-Cell Sequencing of iPSC-Dopamine Neurons Reconstructs Disease Progression and Identifies HDAC4 as a Regulator of Parkinson Cell Phenotypes. *Cell Stem Cell* [Internet]. 2019;24(1):93-106.e6. Available from:
<https://doi.org/10.1016/j.stem.2018.10.023>

Appendices

Appendix 1

A



ELSEVIER

Dear Ms Elena Simonazzi

We hereby grant you permission to reprint the material below at no charge **in your thesis** subject to the following conditions:

RE: THE MOUSE BRAIN IN STEREOTAXIC COORDINATES, Second Edition, ISBN: 9780125476362, Paxinos et al, 2 Figures

B



ELSEVIER

Dear Ms Elena Simonazzi

We hereby grant you permission to reprint the material below at no charge **in your thesis** subject to the following conditions:

RE: THE MOUSE BRAIN IN STEREOTAXIC COORDINATES, Second Edition, ISBN: 9780125476362, Paxinos et al, 1 Figure

Appendix 1. Permission to use images from Paxinos et al. *Stereotaxic Atlas* (346). A) Permission to use 2 tables shown in Methods Figure 2.10. B) Permission to use 1 table shown in Methods Figure 2.15.

Appendix 2

The following code was used in Matlab to transform the raw data obtained from the two-photon microscope into TIFF files that could be used for downstream analysis. The code was developed by Dr. A. Ranson.

```
% get input of the number of frames per depth and number of depths
```

```

% load all frames from nth depth and register
function regZxT()

% Configuration:
framesPerDepth = 10;
nCh = 2;
plotReg = 0;
boxFilterSize = 10; % filter for spatial smoothing
downSampledFrameSize = 512; % size to reduce frame to
voxelSize = [.4,.4,2]; % x y z pixel size in microns

selpaths = {};
while true
    selpaths{end+1} = uigetdir;
    resp = questdlg('Add another folder?');
    if ~strcmp(resp,'Yes')
        break;
    end
end

for iExp = 1:length(selpaths)
    selpath = selpaths{iExp};
    %selpath = 'C:\temp\ministack';
    allFiles = dir(fullfile(selpath,'*.tif'));
    allFiles = {allFiles.name};

    boxFilter = ones(boxFilterSize,boxFilterSize,1,1);

    % load all frames
    if plotReg ; figure; end;

    % check if already registered
    % if exist(fullfile(selpath,'registered.mat'))
    %     resp = questdlg('Registered data exists... reregister?');
    % else
    %     resp = 'Yes';
    % end

    resp = 'Yes';

    if strcmp(resp,'Yes')
        % then register
        for iTif = 1:length(allFiles)
            disp(['Initial alignment
',num2str(iTif), '/', num2str(length(allFiles))]);
            tiffFilename = fullfile(selpath,allFiles{iTif});
            tiff = Tiff(tiffFilename,'r');
            frames = double(img.loadFrames(tiff));
            % remove red ch if needed
            if nCh == 2
                frames = frames(:,:,1:2:end);
            end

            numberOfDepths = size(frames,3)/framesPerDepth;

            % calculate frame number for each depth
            if iTif==1
                for iDepth = 1:numberOfDepths
                    startFrame = ((iDepth - 1) * framesPerDepth)+1;

```

```

        framesForDepth{iDepth} =
startFrame:(startFrame+framesPerDepth-1);
        end
    end

    % filter with boxFilter
    frames = convn(frames,boxFilter,'valid');
    % downsample image if requested
    frameSize = size(frames);
    framePix =
round(linspace(1,frameSize(1),downSampledFrameSize));
    frames = frames(framePix,framePix,:,:);
    % make space for registered data if it doesn't exist
    if ~exist('registeredData')
        registeredData =
zeros(size(frames,1),size(frames,2),numberOfDepths,length(allFiles))
;
        end
        % register frames from each depth to themselves
        for iDepth = 1:numberOfDepths
            targetFrame = frames(:, :, framesForDepth{iDepth}(1));
            [regFrames, x, y, dx, dy] =
rapidRegNonPar(frames(:, :, framesForDepth{iDepth}), targetFrame);
            % check number of frames where there is too much
movement and
            % exclude... compare each to the median of the
others?
            regFramesMedian = median(regFrames,3);
            registeredData(:, :, iDepth, iTif)=regFramesMedian;
        end
        tiff.close;

    end
    save(fullfile(selpath, 'registered.mat'), 'registeredData');
else
    disp('Loading already registered data');
    load (fullfile(selpath, 'registered.mat'));
end

% =====
% check if already registered
% if exist(fullfile(selpath, 'registered.mat'))
%     resp = questdlg('Registered data exists... reregister?');
% else
%     resp = 'Yes';
% end

% Register tn to t0
% Check each z position at each time point for its similarity to
all z
% positions from t0 (after registration) and thus build for each
z stack a
% median z offset (in units of depth)

% downsample frames for purpose of zalign
frameSize = size(registeredData);
downFrameSize = 100;
registeredDataDown =
registeredData(round(linspace(1,frameSize(1),downFrameSize)),round(1
inspace(1,frameSize(2),downFrameSize)),:,:);
% to measure progress

```



```

totalSteps = size(registeredData,4) * size(registeredData,3) *
size(registeredData,3);
currentStep = 1;
% to store corr(baseline,tn)
similarity =
zeros(size(registeredData,4),size(registeredData,3),size(registeredD
ata,3));
disp('=== Initial alignment complete===');
for iTimepoint = 1:size(registeredData,4)
    disp(['Calculating z drift... t =
',num2str(iTimepoint), '/', num2str(size(registeredData,4))]);
    for iDepth = 1:size(registeredData,3)
        for iDepthBaseline = 1:size(registeredData,3)
            currentStep = currentStep + 1;
            timepointImage =
registeredDataDown(:, :, iDepth, iTimepoint);
            baselineImage =
registeredDataDown(:, :, iDepthBaseline, 1);
            [timepointImageReg] =
rapidRegNonPar(timepointImage, baselineImage);
            % crop the images
            %baselineImage = baselineImage(50:150,50:150);
            %timepointImageReg =
timepointImageReg(50:150,50:150);
            similarity(iTimepoint, iDepth, iDepthBaseline) =
corr(timepointImageReg(:), baselineImage(:));
        end
    end
end

% for each timepoint calculate the best match of each depth to
the baseline
[~, bestMatches] = max(similarity(:, :, :), [], 3);
% calculate how much each depth is off
unMovingMatrix =
repmat(bestMatches(1, :), [size(registeredData,4), 1]);
offsetMatrix = bestMatches - unMovingMatrix;
offsetMeans = median(offsetMatrix, 2);
offsetErr = std(offsetMatrix, [], 2) / sqrt(size(offsetMatrix, 2));
% correct z drift by circ shifting the zstack by these amounts
shiftedRegisteredData = zeros(size(registeredData));
for iTimepoint = 1:size(registeredData,4)
    shiftedRegisteredData(:, :, :, iTimepoint) =
circshift(registeredData(:, :, :, iTimepoint), offsetMeans(iTimepoint)*1
, 3);
end

% remove wraparound of z registration
badZ = [abs(min(offsetMeans)); abs(max(offsetMeans))];
shiftedRegisteredData = shiftedRegisteredData(:, :, badZ(2)+1:end-
badZ(1), :);

% xy align every slice in the t=0 zstack to slice above
for iDepth = 2:size(shiftedRegisteredData,3)
    upperImage = shiftedRegisteredData(:, :, iDepth-1, 1);
    lowerImage = shiftedRegisteredData(:, :, iDepth, 1);
    shiftedRegisteredData(:, :, iDepth, iTimepoint) =
rapidRegNonPar(lowerImage, upperImage);
end

% xy align each timepoint to its starting point

```

```

    for iDepth = 1:size(shiftedRegisteredData,3)
        baselineImage = shiftedRegisteredData(:,:,iDepth,1);
        for iTimepoint = 2:size(registeredData,4)
            timepointImage =
shiftedRegisteredData(:,:,iDepth,iTimepoint);
            [shiftedRegisteredData(:,:,iDepth,iTimepoint)] =
rapidRegNonPar(timepointImage,baselineImage);
        end
    end

save(fullfile(selpath,'registered2.mat'),'shiftedRegisteredData','of
fsetMeans');
figure,errorbar(offsetMeans,offsetErr);
xlabel('Timepoint');
ylabel('Offset');

%     f2 = squeeze(shiftedRegisteredData(:,:,1,:));
%     data.vids.playVid(f2);

% add processed data directory
mkdir(fullfile(selpath,'processed'));
mkdir(fullfile(selpath,'processed','imaris'));
selpath = fullfile(selpath,'processed','imaris');

% save max intensity projection
zOut = squeeze(max(shiftedRegisteredData(:,:,:,:[1,3]),[]),3);
zOut = zOut - min(zOut(:));
maxVal = prctile(zOut(:),99);
zOut(zOut(:)>maxVal)=maxVal;
zOut = zOut/maxVal;
zOut = zOut * 2^15;
zOut = uint16(zOut);
img.saveFrames(zOut,fullfile(selpath,'max_projection.tif'));

% save stack with X x Y x t x Z
%     zOut = shiftedRegisteredData(:,:,:,);
%     zOut = permute(zOut,[1 2 4 3]);
%     zOut = zOut(:,:,:);
%     zOut = zOut - min(zOut(:));
%     maxVal = prctile(zOut(:),99);
%     zOut(zOut(:)>maxVal)=maxVal;
%     zOut = zOut/maxVal;
%     zOut = zOut * 2^15;
%     zOut = uint16(zOut);
%     saveFrames(zOut,fullfile(selpath,'zstackoption1.tif'));

% save stack with X x Y x Z x t
%     zOut = shiftedRegisteredData(:,:,:,);
%     zOut = zOut(:,:,:);
%     zOut = zOut - min(zOut(:));
%     maxVal = prctile(zOut(:),99);
%     zOut(zOut(:)>maxVal)=maxVal;
%     zOut = zOut/maxVal;
%     zOut = zOut * 2^15;
%     zOut = uint16(zOut);
%     saveFrames(zOut,fullfile(selpath,'zstackoption2.tif'));

% save stack with format expected by imaris
zOut = shiftedRegisteredData(:,:,:,);
zOut = zOut - min(zOut(:));
maxVal = prctile(zOut(:),99);

```

```

zOut(zOut(:)>maxVal)=maxVal;
zOut = zOut/maxVal;
zOut = zOut * 2^15;
zOut = uint16(zOut);
for iT = 1:size(zOut,4)
    zToSave = squeeze(zOut(:,:, :, iT));
    if iT <10
        outFilename =
fullfile(selpath, ['Stack_C01_T0', num2str(iT), '.tiff']);
    else
        outFilename =
fullfile(selpath, ['Stack_C01_T', num2str(iT), '.tiff']);
    end
    saveFrames(zToSave, outFilename, voxelSize);
end
% data.vids.playVid(zOut);
% % save example zstack from middle of time series
% midtime = round(size(shiftedRegisteredData,4)/2);
% zOut = (squeeze(shiftedRegisteredData(:,:, :, midtime)));
% zOut = zOut - min(zOut(:));
% maxVal = prctile(zOut(:), 99);
% zOut(zOut(:)>maxVal)=maxVal;
% zOut = zOut/maxVal;
% zOut = zOut * 2^15;
% zOut = uint16(zOut);
% img.saveFrames(zOut, fullfile(selpath, 'XxYxZ.tif'), 1);
% % save example time series from middle of z stack
% egZ = round(linspace(1, size(shiftedRegisteredData, 3), 5));
% for z = egZ
%     disp(['Saving timeseries ', num2str(z)]);
%     zOut = (squeeze(shiftedRegisteredData(:,:, z, :)));
%     zOut = zOut - min(zOut(:));
%     maxVal = prctile(zOut(:), 99);
%     zOut(zOut(:)>maxVal)=maxVal;
%     zOut = zOut/maxVal;
%     zOut = zOut * 2^15;
%     zOut = uint16(zOut);
%
img.saveFrames(zOut, fullfile(selpath, ['XxYxT_z', num2str(z), '.tif']),
1);
%     end
end
end

function [regMovie, x, y, dx, dy, target] = rapidRegNonPar(movie,
target, varargin)
% rapidReg Movie frame registration to a target frame using
parallelisation
% and array vectorisation for efficiency
%
% [REG, X, Y, DX, DY, TARGET] = rapidReg(MOVIE, TARGET,...)
register
% MOVIE (an (X,Y,T) array) to TARGET (either the target image
frame (X,Y)
% or 'auto', to find one automatically). Returns the registered
movie, REG,
% the x and y coordinates of the registered movies pixels relative
to the
% target (useful for when clipping is used), the translations
required to
% register each frame, DX and DY, and TAGRET, the target frame.

```

```

% Optionally takes, 'noparallel', meaning use single-threaded
codepath
% instead of parallel, and 'clip', meaning clip the output image
to keep
% only pixels that have valid info at all times (i.e. haven't
translated
% outside target).

% 2013-07 CB created (heavily plagiarised from Mario Dipoppa's
code)
% 2014-10 AR modified to use less memory. This version doesn't
perform
% the translation on the video, it just returns coordinates of
translation
% required. It does do the translation on a small subset of frames
in
% order to return a reference image.

[h, w, nFrames] = size(movie);

%% Setup
%convert movie data to an appropriate floating point type if
necessary
dataType = class(movie);
switch dataType
    case {'int8' 'int16' 'uint8' 'uint16' 'int32' 'uint32'}
        %convert all integer types up to 32-bits to single
        movie = single(movie);
        origTypeFun = str2func(dataType);
    case {'int64' 'uint64'}
        %convert 64-bit integer types to double
        movie = double(movie);
        origTypeFun = str2func(dataType);
    case {'single' 'double'}
        %no conversion
        origTypeFun = @identity;
    otherwise
        error(''%s'' is not a recognised data type', dataType);
end

%create a Gaussian filter for filtering frames
hGauss = 1;%fspecial('gaussian', [5 5], 3);
%look for flag on whether to use parallel codepath
% if any(cell2mat(strfind(varargin, 'nopar')) == 1)
% parallel = false;
% else
% parallel = true;
% end
parallel = false;
if length(varargin)>0
    for iArg = 1:2:length(varargin)
        argNames(ceil(iArg/2)) = varargin(iArg);
        argVales(ceil(iArg/2)) = varargin(iArg+1);
    end
else
    argNames = [];
    argVales = [];
end

if ismember('filter', lower(argNames))
    [~,idx] = ismember('filter', argNames);

```

```

    pair = cell2mat(argVals(idx));
    hGauss = pair;
end

if strcmpi(target, 'auto')
    %% Compute the best target frame
    %%first compute a smoothed mean of each frame
    meanF = smooth(mean(reshape(movie, h*w, nFrames)));
    %%now look in the middle third of the image frames for the
    minimum
    fromFrame = round(nFrames*1/3);
    toFrame = round(nFrames*2/3);
    [~, idx] = min(meanF(fromFrame:toFrame));
    minFrame = fromFrame + idx;
    %%Gaussian filter the target image
    target = imfilter(movie(:, :, minFrame), hGauss, 'same',
'replicate');
    %% AR added display output of which frame number is being used as
    target
    disp(['target frame is ', num2str(minFrame), '..']);
end

ftTarget = fft2(target);

%% Fourier transform the movie frames, unfiltered and filtered
ftMovie = fft2(movie);
movie = imfilter(movie, hGauss, 'same', 'replicate');

%% Compute required displacement and register each frame
dx = zeros(1, nFrames);
dy = zeros(1, nFrames);
nr = ifftshift((-fix(h/2):ceil(h/2) - 1));
nc = ifftshift((-fix(w/2):ceil(w/2) - 1));
[nc, nr] = meshgrid(nc, nr);
regMovie = zeros(h, w, nFrames, class(movie));

%% Register sequentially
for t = 1:nFrames
    %%find the best registration translation
    currentFrame = fft2(movie(:, :, t));
    output = dftregistration(fft2(target), currentFrame, 20);
    dx(t) = output(4);
    dy(t) = output(3);
    %%translate the original (i.e. unfiltered) frame
    ftRegFrame = ftMovie(:, :, t).*exp(sqrt(-1)*2*pi*(-dy(t)*nr/h -
dx(t)*nc/w));
    regMovie(:, :, t) = abs(ifft2(ftRegFrame));
end

%% %% If requested, clip the frames to the maximum fully valid region
% if any(cell2mat(strfind(varargin, 'clip')) == 1)
%     disp('clipping..');
%     dxMax = max(0, ceil(max(dx)));
%     dxMin = min(0, floor(min(dx)));
%     dyMax = max(0, ceil(max(dy)));
%     dyMin = min(0, floor(min(dy)));
%     x = (1 + dxMax):(h + dxMin);
%     y = (1 + dyMax):(h + dyMin);
%     regMovie = regMovie(y, x, :);

```

```

% else
x = 1:w;
y = 1:h;
% end

% regMovie = [];
end

function saveFrames(movie, fn, voxelSize)
%UNTITLED Summary of this function goes here
%

tiff = Tiff(fn, 'w');

[w, h, nFrames] = size(movie);

switch class(movie)
    %TODO: implement more cases as needed
    case 'uint16'
        bits = 16;
        format = 1;
    otherwise
        error('Unknown data type (''%s'') for inferring bits per
sample', class(movie));
end

tag.ImageWidth = w;
tag.ImageLength = h;
tag.SampleFormat = format;
tag.Photometric = Tiff.Photometric.MinIsBlack;
tag.BitsPerSample = bits;
tag.SamplesPerPixel = 1; %only luminance
tag.RowsPerStrip = 64;
tag.PlanarConfiguration = Tiff.PlanarConfiguration.Chunky;
tag.Compression = Tiff.Compression.Deflate;
tag.Software = 'MATLAB';
tag.XResolution = voxelSize(1);
tag.YResolution = voxelSize(3);

digitCount = 0;
for t = 1:nFrames
    fprintf([repmat('\b', 1, digitCount) '%i'], t);
    digitCount = length(num2str(t));

    setTag(tiff, tag);
    write(tiff, movie(:,:,t));
    if t < nFrames
        writeDirectory(tiff);
    end
end
fprintf(repmat('\b', 1, digitCount));
close(tiff);

end

```

Appendix 3

Appendix 3. Representative videos of two-photon imaging dataset. Video 3A, Abi3-WT. Video 3B, Abi3-KO.

Appendix 4

Set 1								
Animal	Object A	Object B	Total (s)	Absolute discrimination A	Discrimination index A	Absolute discrimination B	Discrimination index B	
1	22.52	23.16	45.68	-0.64	-0.01	0.64	0.01	
2	31.47	29.85	61.32	1.62	0.03	-1.62	-0.03	
3	19.93	23.01	42.94	-3.08	-0.07	3.08	0.07	
4	47.29	45.21	92.50	2.08	0.02	-2.08	-0.02	
5	27.94	31.54	59.48	-3.60	-0.06	3.6	0.06	
6	23.59	25.74	49.33	-2.15	-0.04	2.15	0.04	
7	45.65	47.25	92.90	-1.60	-0.02	1.6	0.02	
8	35.71	34.68	70.39	1.03	0.01	-1.03	-0.01	
9	22.64	18.99	41.63	3.65	0.09	-3.65	-0.09	
10	29.37	28.61	57.98	0.76	0.01	-0.76	-0.01	
					0.00	Average	0.00	

Set 2								
Animal	Object A	Object B	Total (s)	Absolute discrimination	Discrimination index	Absolute discrimination B	Discrimination index B	
1	31.58	35.65	67.23	-4.07	-0.06	4.07	0.06	
2	29.36	27.65	57.01	1.71	0.03	-1.71	-0.03	
3	20.12	22.94	43.02	-2.78	-0.06	2.78	0.06	
4	58.58	62.52	121.10	-3.94	-0.03	3.94	0.03	
5	45.2	42.98	88.18	2.22	0.03	-2.22	-0.03	
6	25.6	29.65	55.25	-4.05	-0.07	4.05	0.07	
7	38.52	41.88	80.32	-3.28	-0.04	3.28	0.04	
8	40.25	33.27	73.45	7.05	0.10	-7.05	-0.10	
9	30.56	23.22	53.78	7.34	0.14	-7.34	-0.14	
10	25.31	26.15	51.46	-0.84	-0.02	0.84	0.02	
					0.00	Average	0.00	

Appendix 4. Raw data from the pilot assessment of the objects used for the NOR task.